DETERMINING THE INDEX OF REFRACTION OF AN UNKNOWN OBJECT USING PASSIVE POLARIMETRIC IMAGERY DEGRADED BY ATMOSPHERIC TURBULENCE

DISSERTATION

Milo W. Hyde IV, Captain, USAF

AFIT/DEE/ENG/10-12

DEPARTMENT OF THE AIR FORCE
AIR UNIVERSITY

AIR FORCE INSTITUTE OF TECHNOLOGY

Wright-Patterson Air Force Base, Ohio

AFIT/DEE/ENG/10-12

DETERMINING THE INDEX OF REFRACTION
OF AN UNKNOWN OBJECT
USING PASSIVE POLARIMETRIC IMAGERY
DEGRADED BY ATMOSPHERIC TURBULENCE

DISSERTATION

Presented to the Faculty

Graduate School of Engineering and Management

Air Force Institute of Technology

Air University

Air Education and Training Command

in Partial Fulfillment of the Requirements for the

Degree of Doctor of Philosophy

Milo W. Hyde IV, B.S.E.E., M.S.E.E.

Captain, USAF

August 9, 2010

APPROVED FOR PUBLIC RELEASE; DISTRIBUTION UNLIMITED

DETERMINING THE INDEX OF REFRACTION

OF AN UNKNOWN OBJECT

USING PASSIVE POLARIMETRIC IMAGERY

DEGRADED BY ATMOSPHERIC TURBULENCE

Milo W. Hyde IV, B.S.E.E., M.S.E.E.
Captain, USAF

Approved:
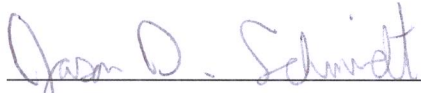
_____   30 July 2010
Maj Jason D. Schmidt, PhD (Chairman)   Date
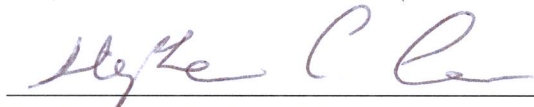
_____   30 July 2010
Dr. Stephen C. Cain (Member)   Date
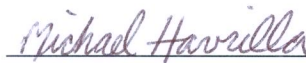
_____   30 July 2010
Dr. Michael J. Havrilla (Member)   Date

_____   30 Jul 10
Dr. Michael A. Marciniak (Member)   Date

Accepted:

_____   13 Aug 2010
M. U. Thomas   Date
Dean, Graduate School of
Engineering and Management

AFIT/DEE/ENG/10-12

Abstract

In this research, an algorithm is developed to estimate the index of refraction of an unknown object using passive polarimetric images degraded by atmospheric turbulence. The algorithm uses a variant of the maximum-likelihood blind-deconvolution algorithm developed by LeMaster and Cain to recover the true object (i.e., the first Stokes parameter), the degree of linear polarization, and the polarimetric-image point spread functions. Nonlinear least squares is then used to find the value of the complex index of refraction which best fits the theoretical degree of linear polarization, derived using a polarimetric bidirectional reflectance distribution function, to the turbulence-corrected degree of linear polarization. To verify the proposed material-characterization algorithm, experimental results of two painted metal samples are provided and analyzed. Possible uses of this novel algorithm include intelligence-gathering and nondestructive inspection/evaluation applications such as corrosion and crack detection/characterization.

Before the algorithm described above is implemented and experimentally verified, the results of two intermediate research steps are provided and discussed. The purpose of the first research step is to verify the accuracy of the polarimetric bidirectional reflectance distribution function chosen for this research. This is accomplished by comparing predictions made using the model to exact electromagnetic solutions of a rough perfect-reflecting surface and to experimental Mueller matrices of two rough metallic samples. In the second research step, the polarimetric bidirectional reflectance distribution function is used to create two material-classification algorithms which use turbulence-degraded polarimetric imagery. The first algorithm is a dielectric/metal classifier. It uses the blind-deconvolution algorithm mentioned above

iv

to remove atmospheric distortion and correctly classify the unknown object. The second classification algorithm, an enhanced version of the first, determines whether an object is composed of aluminum, iron, or dielectric materials. This enhanced material classification provides functional information about the unknown object. Experimental results of two dielectric and metallic samples are provided to validate the proposed classification algorithms. The results of these analyses are presented and discussed in this dissertation.

After results of the two intermediate research steps and the material-characterization algorithm have been analyzed, this dissertation is concluded. A summary of the work performed in this dissertation and a discussion of possible future research areas related to this work are provided.

To my wife

Acknowledgements

Table of Contents

List of Figures

List of Tables

List of Abbreviations

DETERMINING THE INDEX OF REFRACTION
OF AN UNKNOWN OBJECT
USING PASSIVE POLARIMETRIC IMAGERY
DEGRADED BY ATMOSPHERIC TURBULENCE

I. Introduction

Remote sensing is a collection of techniques whose purpose is to determine some piece of information about an object without physically handling the specimen. The specimen, or object of interest, could be any number of things—the ocean, the atmosphere, soils, tree canopies, an extrasolar planet, etc. Likewise, the desired information can vary as well. For instance, one might be interested in ocean wave height or current directions; another might be interested in detecting oil spills or levels of polar ice [63]. One of the most famous remote-sensing examples comes from the Cold War with the development of airborne sensors which could detect small amounts of radioactive isotopes in the atmosphere signaling the detonation of an atomic bomb [108]. Later, seismic detectors were developed to sense underground atomic tests [108]. These are but a few examples of the remote-sensing applications which exist in the literature.

In general, remote-sensing techniques can be divided into two categories—active and passive remote sensing. In active remote sensing, the object of interest is illuminated with some form of transmitted energy (electromagnetic or acoustic are the most common) which interacts with the object and then is measured by a sensor [63]. Common examples of active remote sensing are radio detection and ranging (RADAR), laser detection and ranging (LADAR), and sound navigation and ranging

(SONAR). In passive remote sensing, the illumination source is not controlled, i.e., the sensor must rely on a natural illumination source like the sun [63]. The atomic bomb detonation detectors discussed above are examples of passive remote sensors.

Another common passive remote-sensing technique is polarimetry. Polarimetry uses polarimetric images (images taken of an object through a linear polarizer and possibly also a retarder) to measure the polarization state of electromagnetic radiation (typically infrared or visible light). Polarimetry can be a powerful sensing tool since the manner in which light interacts with an object depends on the polarization state. Researchers have exploited this simple measurement to develop remote-sensing techniques which can detect objects hidden in clutter [51, 133], determine object surface orientations [123], determine the dielectric and metallic elements of an object [126, 141], and estimate the composition of an object [105, 123].

1.1 Research Goals

The goal of this research is to develop a method to determine the index of refraction of an unknown object using passive polarimetric imagery which has been degraded by atmospheric turbulence. This work differs from other remote-sensing material-characterization techniques, namely, Refs. [105, 123], in that it accounts for the deleterious effects atmospheric turbulence has on imaging. As a means of accomplishing the primary goal, two intermediate steps are required. The first is to verify the accuracy of the surface scattering model chosen for this research [139, 140] (see Chapter IV). This is accomplished in two ways. The first compares predictions made using the surface scattering model to exact electromagnetic solutions of a rough perfect-reflecting surface. The second uses a laboratory technique (ellipsometry) to measure the full Mueller matrices (described in subsequent chapters) of two rough metallic samples. The ellipsometric results are then compared to the surface

scattering model values to determine accuracy.

In the second step, the surface scattering model (having been verified in the first step) is used to create two material-classification algorithms. The first algorithm determines whether an object is composed of dielectric or metallic materials (see Chapter V). This work, while similar to Refs. [126, 141, 142, 143, 144], classifies an object using turbulence-degraded polarimetric imagery as opposed to diffraction-limited imagery. This novel algorithm makes use of a polarimetric blind-deconvolution algorithm (variant of the algorithm presented in Ref. [74]) to remove the deleterious effects of turbulence and make the classification decision. The second classification algorithm, an enhanced version of the first, determines whether an object is composed of aluminum, iron, or dielectric materials (see Chapter VI). Both classification algorithms are verified experimentally on objects consisting of dielectric and metallic materials.

Lastly, the full index-of-refraction algorithm is created (see Chapter VII). As is the case in the material-classification algorithms, a variant of the blind-deconvolution algorithm presented in Ref. [74] is used to remove the effects of turbulence. The efficacy of the proposed algorithm is tested experimentally on complex materials, i.e., objects composed of both dielectric and metallic materials.

Classifying or characterizing an unknown object remotely has obvious utility to the intelligence community. The polarimetric sensor utilized in this research is relatively simple (consists of a narrowband filter, linear polarizer, and a camera in its most basic form) and is easily miniaturized. In addition to intelligence gathering, the techniques developed in this research also have nondestructive inspection/evaluation (NDI/NDE) applications. For example, the methods presented in this dissertation could easily be adapted to nondestructively characterize corrosion on a metal surface, detect cracks in material coatings, etc.
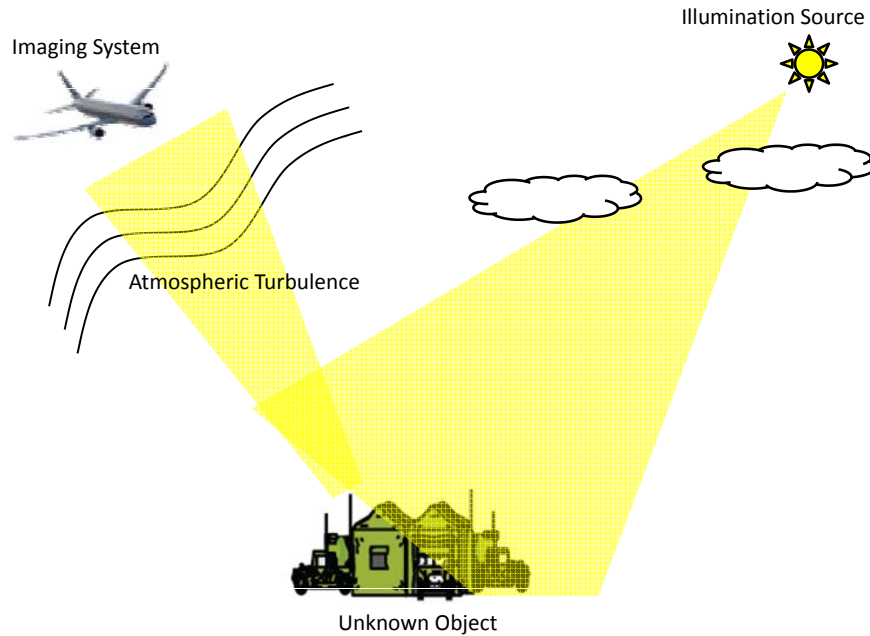
Figure 1. A hypothetical engagement scenario.

1.2 Scope and Assumptions

To demonstrate the difficulty of the remote-sensing material-characterization problem, consider the hypothetical engagement scenario shown in Fig. 1. The figure depicts an unknown object, illuminated with sunlight, being imaged by a passing aircraft. Note that a truly unknown object implies nothing is known about the object's surfaces, i.e., orientations, roughnesses, or compositions. Another unknown is the distortion in the collected images caused by atmospheric turbulence. The aggregate of all these unknowns is a highly complex, multidimensional problem space out of which a single solution (the index of refraction), amongst perhaps an infinite number, is sought. In order to make the goal of the proposed research achievable, the following six simplifying assumptions, described in the paragraphs below, are made.

The first assumption of this research, which is depicted in Fig. 1, is that the unknown object is illuminated with a natural (unpolarized, or randomly polarized) light source. Several researchers have found that the amount of circularly polarized

light, in light scattered from an object illuminated by a natural source, is extremely small [27, 85, 123]. Thus, the stated assumption allows one to disregard the possibility of receiving circularly polarized light. The implications of this assumption are significant. First, the polarimetric imaging sensor need only consist of a linear polarizer and a camera. Second, the Mueller matrices modeling reflection from a material surface can be reduced in dimension from 4×4 matrices to 3×3 matrices. Likewise, the Stokes vectors describing the polarization states of incident and reflected light can be reduced to length 3 vectors (from length 4 vectors). This assumption breaks down (of course) when the illumination source is not randomly polarized. Skylight is an example of an illumination source which is weakly polarized [27, 85]. Incorporating the effects of polarized illumination sources are left to future work.

The second assumption of this research is an assumption which is universal to remote-sensing material-classification and characterization techniques. Scatter from a surface is composed of weighted contributions of specularly scattered light and diffusely scattered light. As defined in subsequent chapters, specularly scattered light is light which obeys the law of reflection (angle of incidence equals angle of reflection). Since it is the result of a single surface reflection, specularly scattered light is assumed to be polarized as a consequence of the interaction with the material surface. Diffusely scattered light is light which is scattered evenly in all directions. Diffuse scattering arises from multiple surface reflections or volumetric scattering and is thus assumed to be unpolarized. From the definitions provided above, it is clear that meaningful polarimetric imagery of a surface is impossible if diffuse scattering dominates. Thus, a necessary condition for the polarimetric work presented in this research is that the light scattered from a surface possess a significant specular component.

Another assumption of this research is that the unknown object is composed of isotropic, nonmagnetic materials. As described in the next chapter, isotropic materi-

als are materials in which the index of refraction is independent of the polarization of the incident light. This assumption reduces the index of refraction from its most general form (a tensor) to a scalar. Nonmagnetic materials are materials which exhibit little tendency to becoming magnetically polarized when subjected to an external magnetic field. At optical frequencies, most materials are nonmagnetic. This assumption makes the permeability of the materials investigated in this research equal to that of vacuum. It also makes the index of refraction a function of permittivity alone.

In addition to the assumptions stated above, it is assumed that the rms surface height and surface correlation length are several times larger than the wavelength of the incident field. This condition is necessary for the validity of the chosen surface scattering model which is based on the geometrical optics (GO) approximation to scattering. This condition can be loosened somewhat if physical optics (PO) is used to model the surface scattering. This is left to future research.

Assumption number five is that the measured scattered light is obtained in the specular plane. The specular plane is the plane which contains the following three vectors: the vector modeling the direction of the incident light, the vector normal to the material's surface, and the vector modeling the direction of the reflected light. This assumption implies that one possesses *a priori* knowledge about the geometrical orientation of the object. This significantly reduces the dimensions of the problem space. It also simplifies the surface scattering model. In addition to generalizing the problem, out-of-specular-plane observation may permit one to sense other parameters in addition to the index of refraction. This is also left to future research.

Lastly, weak atmospheric turbulence is assumed throughout. In weak atmospheric turbulence, the atmosphere imparts random phase fluctuations to the passing light; whereas, in strong atmospheric turbulence, the atmosphere imparts random phase and

irradiance (called scintillation) fluctuations to the passing light. The atmospheric correction algorithm used in this research is incapable of correcting scintillation and thus, the proposed research is only applicable to weak atmospheric turbulence scenarios. In addition to the weak atmospheric turbulence requirement, the nature of the atmospheric turbulence is assumed to be statistically isotropic and homogeneous [5, 44]. This is a very common requirement in research involving atmospheric turbulence models.

1.3   Dissertation Organization

This dissertation is organized in the following manner. Chapter II provides the necessary theoretical background including a description of the electric and magnetic properties of materials, polarization of electromagnetic waves, electromagnetic scattering from material surfaces, and aspects of imaging. Chapter III presents a summary of the relevant published work including an overview of optical material-characterization (both laboratory and remote-sensing) techniques, a description of surface scattering models, and an explanation of two blind-deconvolution algorithms. Chapter IV presents the results of the first intermediate step of this research, namely, verification of the selected surface scattering model. Chapters V and VI present results of the two material-classification algorithms developed during step two of this research. Lastly, Chapter VII presents the results of the full index-of-refraction algorithm.

II. Theoretical Background

This chapter provides the background for the work presented in subsequent chapters. In this chapter, the electric and magnetic properties of materials, polarization of electromagnetic waves, electromagnetic scattering from material surfaces, and pertinent aspects of imaging are discussed.

2.1 Maxwell's Equations

Any study of light, be it microwaves, infrared, or visible light, begins with Maxwell's equations

$$\nabla \times \boldsymbol{E} = -\boldsymbol{\mathcal{M}} - \mathrm{j}\omega\boldsymbol{B}$$

$$\nabla \times \boldsymbol{H} = \boldsymbol{J} + \mathrm{j}\omega\boldsymbol{D}$$

$$\nabla \cdot \boldsymbol{D} = q_e$$

$$\nabla \cdot \boldsymbol{B} = q_m$$

$$(1)$$

represented here in time-harmonic form [9, 16, 45, 56, 63]. The top two expressions in Eq. (1) are known as Faraday's law and Ampere's law, respectively. Here, $\boldsymbol{E}$ is the electric field amplitude, $\boldsymbol{H}$ is the magnetic field amplitude, $\boldsymbol{\mathcal{M}}$ is the magnetic current density (nonphysical quantity), $\boldsymbol{J}$ is the electric current density, $\boldsymbol{B}$ is the magnetic flux density, $\boldsymbol{D}$ is the electric flux density, and ω is the angular frequency [9]. The bottom two expressions in Eq. (1) are known as Gauss' laws for electric and magnetic fields. Here, q_e is the electric charge density and q_m is the magnetic charge density (nonphysical quantity) [9]. The electric and magnetic flux densities are, in general, related to the electric and magnetic fields by tensor relations [9, 146]:

$$\boldsymbol{D} = \boldsymbol{\varepsilon} \cdot \boldsymbol{E}$$

$$\boldsymbol{B} = \boldsymbol{\mu} \cdot \boldsymbol{H}$$

$$(2)$$

where $\boldsymbol{\varepsilon}$ and $\boldsymbol{\mu}$ are the permittivity and permeability tensors of the medium, respectively. This research assumes that all media are linear, homogeneous, and isotropic thereby reducing the tensors to scalars, i.e.,

$$\begin{aligned} \boldsymbol{D} &= \varepsilon \boldsymbol{E} \\ \boldsymbol{B} &= \mu \boldsymbol{H} \end{aligned} . \tag{3}$$

Furthermore, all materials in this research are assumed to be nonmagnetic thereby making

$$\mu = \mu_0 \tag{4}$$

where μ_0 is the permeability of vacuum. Substituting Eqs. (3) and (4) into Eq. (1) produces

$$\begin{aligned} \nabla \times \boldsymbol{E} &= -\boldsymbol{\mathcal{M}} - \mathrm{j}\omega\mu_0 \boldsymbol{H} \\ \nabla \times \boldsymbol{H} &= \boldsymbol{J} + \mathrm{j}\omega\varepsilon \boldsymbol{E} \\ \nabla \cdot \boldsymbol{E} &= \frac{q_e}{\varepsilon} \\ \nabla \cdot \boldsymbol{H} &= \frac{q_m}{\mu_0} \end{aligned} . \tag{5}$$

2.2 Helmholtz Wave Equation

Using Eq. (5) to find the electric and magnetic fields of a system is rather difficult because the equations are first-order coupled partial differential equations. However, using the first-order coupled curl equations, a second-order uncoupled equation can be found which is more easily solved. The first step in deriving this expression is to take the curl of both sides of Faraday's law:

$$\nabla \times \nabla \times \boldsymbol{E} = -\nabla \times \boldsymbol{\mathcal{M}} - \mathrm{j}\omega\mu_0 \nabla \times \boldsymbol{H}. \tag{6}$$

Making use of the vector identity

$$\nabla \times \nabla \times \boldsymbol{A} = \nabla \left(\nabla \cdot \boldsymbol{A} \right) - \nabla^2 \boldsymbol{A} \tag{7}$$

and Ampere's law, Eq. (6) becomes

$$\nabla \left(\nabla \cdot \boldsymbol{E} \right) - \nabla^2 \boldsymbol{E} = -\nabla \times \boldsymbol{\mathcal{M}} - \mathrm{j}\omega\mu_0 \left(\boldsymbol{J} + \mathrm{j}\omega\varepsilon\boldsymbol{E} \right). \tag{8}$$

Substituting in Gauss' law for electric fields and rearranging terms results in the Helmholtz electric field wave equation

$$\nabla^2 \boldsymbol{E} + k^2 \boldsymbol{E} = \nabla \times \boldsymbol{\mathcal{M}} + \mathrm{j}\omega\mu_0 \boldsymbol{J} + \frac{1}{\varepsilon}\nabla q_e \tag{9}$$

where $k = \omega(\varepsilon\mu_0)^{1/2}$ is the wavenumber. If sources are not contained in the region of interest, Eq. (9) simplifies to the source-free Helmholtz wave equation:

$$\nabla^2 \boldsymbol{E} + k^2 \boldsymbol{E} = 0. \tag{10}$$

This form of the wave equation is the one most often seen in the literature.

Solving Eq. (10) is accomplished by first expanding the electric field into its components, namely

$$\nabla^2 \left(\hat{\boldsymbol{x}} E_x + \hat{\boldsymbol{y}} E_y + \hat{\boldsymbol{z}} E_z \right) + k^2 \left(\hat{\boldsymbol{x}} E_x + \hat{\boldsymbol{y}} E_y + \hat{\boldsymbol{z}} E_z \right) = 0. \tag{11}$$

Note that no coupling occurs between the components of the field, i.e., the x component of the field does not contribute to the other two orthogonal components. This

allows one to write Eq. (11) as three scalar equations of the form

$$\nabla^2 E_x + k^2 E_x = 0$$

$$\nabla^2 E_y + k^2 E_y = 0.$$ (12)

$$\nabla^2 E_z + k^2 E_z = 0$$

Note that all three scalar equations have the same mathematical form; therefore, their solutions have the same form. Expanding the scalar Laplacian operator in Eq. (12) produces

$$\frac{\partial^2}{\partial x^2} E_\alpha + \frac{\partial^2}{\partial y^2} E_\alpha + \frac{\partial^2}{\partial z^2} E_\alpha + k^2 E_\alpha = 0$$ (13)

where $\alpha = x, y, z$. Using separation of variables, i.e., the solution is assumed to be of the form

$$E_\alpha = f(x) g(y) h(z),$$ (14)

transforms Eq. (13) into

$$\frac{1}{f}\frac{d^2 f}{dx^2} + \frac{1}{g}\frac{d^2 g}{dy^2} + \frac{1}{h}\frac{d^2 h}{dz^2} = -k^2.$$ (15)

Since f, g, and h are functions of one variable independent of the other two, Eq. (15) can be further simplified to

$$\frac{1}{f}\frac{d^2 f}{dx^2} = -k_x^2$$

$$\frac{1}{g}\frac{d^2 g}{dy^2} = -k_y^2,$$ (16)

$$\frac{1}{h}\frac{d^2 h}{dz^2} = -k_z^2$$

where $k^2 = k_x^2 + k_y^2 + k_z^2$. The expressions in Eq. (16) are now second-order linear homogeneous differential equations and all have the solution

$$b(\alpha) = C_1 e^{-jk_\alpha \alpha} + C_2 e^{jk_\alpha \alpha}$$ (17)

11

where $b = f, g, h$ and, as before, $\alpha = x, y, z$. Substituting Eq. (17) into Eq. (14) produces the desired result

$$E_\alpha = \left(A_1 e^{-\mathrm{j}k_x x} + A_2 e^{\mathrm{j}k_x x}\right)\left(B_1 e^{-\mathrm{j}k_y y} + B_2 e^{\mathrm{j}k_y y}\right)\left(C_1 e^{-\mathrm{j}k_z z} + C_2 e^{\mathrm{j}k_z z}\right) \qquad (18)$$

where the coefficients, A_1, A_2, B_1, B_2, C_1, C_2, are found by enforcing the boundary conditions of the problem. The interested reader is referred to Ref. [9] for other solutions of the Helmholtz wave equation.

2.3 Transverse-Electromagnetic Waves

For electromagnetic wave propagation (far from the source) in free-space or infinite media, the field can be approximated as a plane wave in which the electric and magnetic fields are orthogonal to the direction of propagation and each other, i.e., $\boldsymbol{E} \perp \boldsymbol{H} \perp \boldsymbol{k}$. This arrangement is called transverse electromagnetic (TEM). In order to find expressions for the electric and magnetic fields of a TEM wave, a direction of propagation must be specified. This direction is of course arbitrary; however, for consistency, a wave propagating in the z direction is assumed. By specifying a z-directed wave, the electric and magnetic fields must now be confined to the xy plane, i.e.,

$$\begin{aligned}
E_x &= E_x^+ e^{-\mathrm{j}kz} + E_x^- e^{\mathrm{j}kz} \\
E_y &= E_y^+ e^{-\mathrm{j}kz} + E_y^- e^{\mathrm{j}kz} \\
H_x &= H_x^+ e^{-\mathrm{j}kz} + H_x^- e^{\mathrm{j}kz} \\
H_y &= H_y^+ e^{-\mathrm{j}kz} + H_y^- e^{\mathrm{j}kz}
\end{aligned} \qquad (19)$$

where the fields' time dependencies have been suppressed. Note that since the wave is z directed, $k = k_z$. This permits the coefficients in Eq. (18) to be combined producing Eq. (19). Expressions relating the electric and magnetic field amplitude coefficients

12

in Eq. (19) can be found using Faraday's law or Ampere's law. Substituting Eq. (19) into Ampere's law produces

$$
\begin{aligned}
H_x^+ &= -\frac{\omega\varepsilon}{k}E_y^+ \\
H_y^+ &= \frac{\omega\varepsilon}{k}E_x^+ \\
H_x^- &= \frac{\omega\varepsilon}{k}E_y^- \\
H_y^- &= -\frac{\omega\varepsilon}{k}E_x^-
\end{aligned}
\tag{20}
$$

or in a more general form

$$
\boldsymbol{H} = \frac{\omega\varepsilon}{k}\left(\hat{\boldsymbol{k}} \times \boldsymbol{E}\right) = \frac{1}{Z}\left(\hat{\boldsymbol{k}} \times \boldsymbol{E}\right)
\tag{21}
$$

where $\hat{\boldsymbol{k}}$ is the unit vector pointing in the direction of wave propagation and Z is the intrinsic impedance of the medium [9]. Inherent in Eq. (19) is the concept of field polarization which is discussed in detail later in this chapter.

2.4 Electric and Magnetic Properties of Materials

A material's response to electromagnetic waves can be characterized by three macroscopic parameters—permittivity, permeability, and conductance. This section introduces these three parameters and describes the physical processes which give rise to these quantities.

2.4.1 Permittivity.

Materials can be loosely divided into three categories—insulators (dielectrics), conductors, and magnetic materials. Dielectrics are defined as materials whose dominant charges in atoms and molecules are bound negative and positive charges that are held in place by atomic and molecular forces [9]. Dielectrics, therefore, do not conduct electric current. Common examples of dielectrics are acrylic, Teflon, glass,

distilled water, crystalline salt, lithium niobate, etc. When no field is applied, the electron clouds of the atoms making up the dielectric are, in general, symmetrically distributed about the nuclei. When an external field is applied, the dielectric's electron clouds shift in a direction related to the polarity of the applied field, thus creating numerous electric dipoles [9]. This interaction allows the dielectric to store energy, much like stretching a spring [9]. This storing of energy is quantitatively captured in the dielectric's permittivity value (also known as the dielectric constant). Permittivity, for natural materials, is a positive quantity and is typically represented as a value relative to the permittivity of vacuum, $\varepsilon_0 \approx 8.854 \times 10^{-12}$ F/m. For example, the static dc relative permittivity of water is 81 [9]. Water, therefore, possesses 81 times the energy storage capacity as that of vacuum. It is important to note that permittivity is a function of frequency or equivalently wavelength.

2.4.2 Conductance.

Materials which do not fit the definition of dielectrics are termed conductors. Conductors are materials whose atoms' outer electrons are loosely bound to their nuclei [9]. These electrons are therefore free to move [9]. When no field is applied, these free electrons move in random directions resulting in a zero net electric current [9]. When an external field is applied, the free electrons move in the opposite direction of the applied field generating a net current [9]. The measure of a conductor's ability to transmit electric current is called conductivity σ; its reciprocal is called resistivity. The conductivity of a material is always positive. A useful hypothetical material, called a perfect electrical conductor (PEC), has an infinite conductance. Natural conductors, like gold, silver, and copper, have very high but finite conductance values. Resistance to the flow of current, i.e., a finite conductance value, arises from crystal lattice vibrations in the material [9]. Since these lattice vibrations increase

as temperature increases, conductivity tends to decrease with rising temperature [9]. Like the permittivity of a material, conductivity is a function of the applied field's frequency.

2.4.3 Complex Permittivity.

For simplicity, the permittivity and conductance of a material are combined into a single complex quantity termed the complex permittivity. The form of a material's complex permittivity can be readily found by using Ampere's law Eq. (1):

$$\nabla \times \boldsymbol{H} = \sigma \boldsymbol{E} + \mathrm{j}\omega\varepsilon\boldsymbol{E} \tag{22}$$

where $\sigma\boldsymbol{E}$ has been substituted for the conduction current $\boldsymbol{J}$. Factoring out $\mathrm{j}\omega\boldsymbol{E}$ produces

$$\nabla \times \boldsymbol{H} = \mathrm{j}\omega\left(\varepsilon - \mathrm{j}\frac{\sigma}{\omega}\right)\boldsymbol{E}, \tag{23}$$

where $\varepsilon - \mathrm{j}\sigma/\omega$ is the material's complex permittivity. This quantity is typically represented in the literature as $\varepsilon' - \mathrm{j}\varepsilon''$ where ε' is the dielectric constant and ε'' is the dielectric loss. To see why the imaginary part of the complex permittivity represents energy dissipation or loss, $\varepsilon' - \mathrm{j}\varepsilon''$ must be substituted into the expression for the wavenumber k

$$k = \omega\sqrt{\mu_0\left(\varepsilon' - \mathrm{j}\varepsilon''\right)} = k' - \mathrm{j}k''. \tag{24}$$

Substituting Eq. (24) into the expression for a z-directed TEM wave, derived above, produces

$$E_\alpha = E_\alpha^+ e^{-\mathrm{j}(k' - \mathrm{j}k'')z} = E_\alpha^+ e^{-k''z}e^{-\mathrm{j}k'z}, \tag{25}$$

where $\alpha = x, y$. The first exponential term in Eq. (25) models a decaying wave envelope, thus showing that the imaginary part of the complex permittivity is a

measure of a material's loss.

2.4.4 Permeability.

The last broad category of material that exists is magnetic materials. Magnetic materials are materials which exhibit magnetic polarization when subjected to an external magnetic field [9]. Since the property of magnetism arises from orbiting and spinning electrons, all materials are somewhat magnetic [22]. Most natural materials are so magnetically weak that they can be safely approximated as nonmagnetic. For other materials, such as ferrites (contain iron, cobalt, or nickel), the magnetic property can be quite strong. The quantity which describes a material's response to an applied magnetic field is called permeability. Like permittivity, it is positive for natural materials and is typically represented as a quantity relative to the permeability of vacuum $\mu_0 = 4\pi \times 10^{-7}$ H/m. Materials which possess large permeabilities can be thought of as being composed of magnetic domains [22]. These domains are areas of the material in which the magnetic moments of the atoms are aligned in the same general direction [22]. When an external magnetic field is applied, all the domains which compose the material align with the field [22]. The result is a magnet. Making up rather large segments of the material, the domains cannot keep up with the oscillation of high frequency magnetic fields. Thus, materials which exhibit magnetic properties at optical frequencies are not common [22]. Like permittivity and conductivity, permeability is a function of frequency.

2.4.5 Complex Index of Refraction.

In optics, it is common to combine the permittivity, conductance, and permeability of a material into a single parameter called the complex index of refraction $\eta = n - j\kappa$ [22]. By definition, the real part of the complex index of refraction is the ratio

of the speed of light in vacuum to the speed of light in the material, i.e.,

$$n = \frac{c}{v} \tag{26}$$

where $c = 1/(\varepsilon_0\mu_0)^{1/2} = 2.998 \times 10^8$ m/s [22]. The imaginary part of the complex index of refraction κ is called the coefficient of extinction and, like the imaginary part of permittivity, is a measure of a material's loss [141]. The relation between the permittivity, conductance, and permeability of a material to its complex index of refraction can be found by applying Eq. (26), namely

$$\eta = \frac{1/\sqrt{\varepsilon_0\mu_0}}{1/\sqrt{\varepsilon\mu}} = \sqrt{\varepsilon_r\mu_r}, \tag{27}$$

where ε_r and μ_r are the relative complex permittivity and relative complex permeability, respectively [22]. For this research, all materials are assumed to be nonmagnetic; therefore $\mu_r = 1$. Substituting $\mu_r = 1$ and the expression for complex permittivity [Eq. (23)] into Eq. (27) and simplifying produces

$$
\begin{aligned}
\eta = n - \mathrm{j}\kappa &= \sqrt{\varepsilon_r} \\
&= \frac{1}{\sqrt{2}}\left[\left((\varepsilon'_r)^2 + \left(\frac{\sigma}{\omega\varepsilon_0}\right)^2\right)^{1/2} + \varepsilon'_r\right]^{1/2} \\
&\quad - \frac{\mathrm{j}}{\sqrt{2}}\left[\left((\varepsilon'_r)^2 + \left(\frac{\sigma}{\omega\varepsilon_0}\right)^2\right)^{1/2} - \varepsilon'_r\right]^{1/2}.
\end{aligned} \tag{28}
$$

Using the stated constraints on permittivity and conductance values of natural materials, it is clear from Eq. (28) that $n > 0$ and $\kappa \geq 0$.

It should be noted that the description for the electric and magnetic properties of materials given above is only accurate for isotropic, linear, and homogenous materials. In general, the manner in which materials respond to electromagnetic fields

depends on the intensity and polarization of the incident field. This transforms the permittivity, permeability, and conductance (as well as the index of refraction) into tensors which can become quite complicated [146]. A good example of a material which possesses a permittivity tensor is lithium niobate. Its crystalline structure gives it a dielectric constant which depends on the polarization of the incident field relative to its crystal axis.

2.5   Polarization

As referenced above, inherent in the TEM field expressions in Eq. (19) is the concept of polarization. Polarization, in essence, is the orientation of the electric field vector. There are four types of polarized light—linear, circular, elliptical, and unpolarized light. This section defines each polarization type and introduces two vector notations (Jones vectors and Stokes vectors) to handle polarized light.

2.5.1   Polarization Types.

Consider the TEM field expressions in Eq. (19):

$$\boldsymbol{E} = \left(\hat{\boldsymbol{x}} E_x + \hat{\boldsymbol{y}} E_y\right) e^{-\mathrm{j}kz} \tag{29}$$

where, for brevity, only the forward traveling wave is shown. The magnetic field is also removed since its orientation is irrelevant to this discussion on polarization [its direction can be found by applying Eq. (21)]. The values of the electric field coefficients in Eq. (29) determine the polarization state of the field. If both E_x and E_y are real, then the polarization state of the field is linear [56]. Figure 2 shows a plot of the path traced out by the electric field vector of a linear polarized wave. The angle the electric field vector makes with respect to the x or y axes is related to the relative amplitudes of E_x and E_y. There are two types of linear polarization—
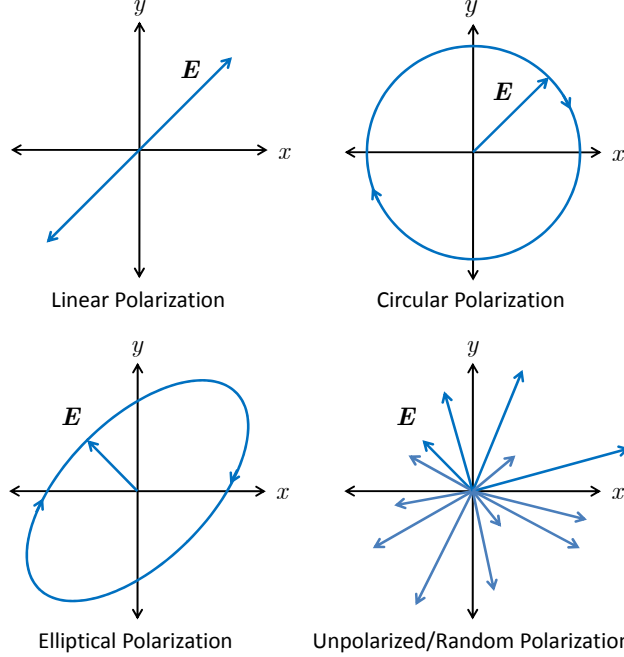
Figure 2. Linear, circular, elliptical, and random polarizations.

horizontal and vertical polarization. Horizontal polarization occurs when $E_y = 0$; vertical polarization occurs when $E_x = 0$.

If $|E_x| = |E_y|$, yet $|\angle E_x - \angle E_y| = 90°$, the result is a circularly polarized wave [56], i.e.,

$$\boldsymbol{E} = E_0 \left(\hat{\boldsymbol{x}} + \mathrm{j}\hat{\boldsymbol{y}} \right) e^{-\mathrm{j}kz}. \tag{30}$$

Figure 2 shows a plot of circular polarization. Note that the electric field vector appears to rotate either clockwise or counterclockwise depending on whether E_x leads or lags E_y. If E_x or E_y are complex and the above relationships do not hold, then the result is an elliptically polarized wave [56]. It is evident that linear polarization and circular polarization are just special cases of elliptical polarization. Figure 2 shows a plot of an elliptically polarized wave. The orientation of the ellipse mapped out by the electric field vector as well as the vector's rotation direction are determined by the relative amplitudes and phases of E_x and E_y.

The last polarization state of light (typically not considered a polarization state)

19

is called unpolarized light, or randomly polarized light. This polarization state arises from light's creation via spontaneous emission. Light emitted from an incandescent bulb, light emitting diode (LED), or the sun (i.e., natural light sources) is the result of a very large number of randomly orientated sources emitting light at random times [44, 56]. This results in rapidly changing, random field amplitude coefficients E_x and E_y [44, 56]. As described in Ref. [56], the term unpolarized light is a misnomer, since in actuality the light is composed of a rapidly varying succession of different polarization states. The polarization state changes occur so rapidly that attempts to resolve any single resultant polarization state are futile. Figure 2 shows a depiction of unpolarized light. States of polarization between unpolarized and fully polarized light are possible. The quantity degree of polarization is defined as the ratio of the fully polarized light power (irradiance) to the total light power [16, 44, 56]. It is formally introduced below.

2.5.2 Jones Vectors and Matrices.

Having introduced polarization, attention can now be turned to describing two formalisms developed to handle polarized light. The first formalism was introduced by R. Clark Jones in 1941 [56]. It was designed to handle polarized light only and therefore is not applicable to scenarios involving unpolarized light. Jones' formalism (also known as Jones vectors) is extremely straightforward. Light is represented as a 2×1 vector of x and y field component complex amplitudes, i.e.,

$$\boldsymbol{E} = \begin{bmatrix} E_x & E_y \end{bmatrix}^{\mathrm{T}}.$$

(31)

Common examples of Jones vectors are

$$
\begin{array}{ll}
\begin{bmatrix} 1 & 0 \end{bmatrix}^{\mathrm{T}} & \text{Horizontal polarization} \\[6pt]
\begin{bmatrix} 0 & 1 \end{bmatrix}^{\mathrm{T}} & \text{Vertical polarization} \\[6pt]
\begin{bmatrix} \cos\alpha & \sin\alpha \end{bmatrix}^{\mathrm{T}} & \text{Linear polarization at angle } \alpha \\[6pt]
\frac{1}{\sqrt{2}}\begin{bmatrix} 1 & \mathrm{j} \end{bmatrix}^{\mathrm{T}} & \text{Circular polarization}
\end{array}
\tag{32}
$$

Optical components which alter polarization state, like linear polarizers, wave plates, and material surfaces (discussed later), are represented as 2×2 matrices (known as Jones matrices). Some common examples are

$$
\begin{array}{ll}
\begin{bmatrix} 1 & 0 \\ 0 & 0 \end{bmatrix} & \text{Horizontal linear polarizer} \\[12pt]
\begin{bmatrix} 0 & 0 \\ 0 & 1 \end{bmatrix} & \text{Vertical linear polarizer} \\[12pt]
e^{\mathrm{j}\pi/4}\begin{bmatrix} 1 & 0 \\ 0 & -\mathrm{j} \end{bmatrix} & \text{Quarter-wave plate, fast axis vertical} \\[12pt]
\begin{bmatrix} \cos\alpha & \sin\alpha \\ -\sin\alpha & \cos\alpha \end{bmatrix} & \text{Rotation of angle } \alpha
\end{array}
\tag{33}
$$

Note that the Jones matrix for a linear polarizer (LP) or a quarter-wave plate (QWP) at any angle can be found by using the rotation matrix. For example, the Jones matrix

for a LP at α is

$$
\begin{aligned}
\mathbf{R}\left(-\alpha\right)\mathbf{J}_{\mathrm{hp}}\mathbf{R}\left(\alpha\right) &= \begin{bmatrix} \cos\alpha & -\sin\alpha \\ \sin\alpha & \cos\alpha \end{bmatrix} \begin{bmatrix} 1 & 0 \\ 0 & 0 \end{bmatrix} \begin{bmatrix} \cos\alpha & \sin\alpha \\ -\sin\alpha & \cos\alpha \end{bmatrix} \\
&= \begin{bmatrix} \cos^2\alpha & \cos\alpha\sin\alpha \\ \cos\alpha\sin\alpha & \sin^2\alpha \end{bmatrix}.
\end{aligned}
\tag{34}
$$

What makes Jones vectors/matrices particularly useful is how simple they make calculating the polarization state of light after it has encountered one or more optical components. For instance, suppose one is interested in the polarization state of light emerging from a QWP (fast axis vertical) immediately preceded by a LP at 45° given a horizontally polarized incident beam. The solution using Jones vectors/matrices is

$$
\begin{bmatrix} E_x \\ E_y \end{bmatrix} = e^{\mathrm{j}\pi/4} \begin{bmatrix} 1 & 0 \\ 0 & -\mathrm{j} \end{bmatrix} \frac{1}{2} \begin{bmatrix} 1 & 1 \\ 1 & 1 \end{bmatrix} \begin{bmatrix} 1 \\ 0 \end{bmatrix} = \frac{e^{\mathrm{j}\pi/4}}{2} \begin{bmatrix} 1 \\ -\mathrm{j} \end{bmatrix}
\tag{35}
$$

where the vectors/matrices from right to left represent the incident beam, the LP at 45° [obtained using Eq. (34)], and the QWP with fast axis vertical, respectively. One can see from Eq. (35) that the light exiting this optical system is circularly polarized.

2.5.3 Stokes Vectors and Mueller Matrices.

The last polarization formalism introduced here is called Stokes vectors. Stokes vectors were introduced by G. G. Stokes in 1852 [16, 56]. Unlike Jones vectors which deal directly with field amplitudes, Stokes vectors deal with field powers (or irradiances). Because of the way they are formulated, Stokes vectors can represent all

22

polarization states including unpolarized light. Stokes vectors are 4×1 vectors, i.e.,

$$\boldsymbol{S} = \begin{bmatrix} S_0 & S_1 & S_2 & S_3 \end{bmatrix}^{\mathrm{T}}. \tag{36}$$

The first element S_0 is equal to the total irradiance [16]. The parameter S_1 is equivalent to the difference between the irradiance of light passed by a horizontal polarizer and the irradiance of light passed by a vertical polarizer [16]. The parameter S_2 is equal to the difference between the irradiance of light passed by a polarizer at 45° and the irradiance of light passed by a polarizer at 135° (or equivalently -45°) [16]. Lastly, S_3 is equal to the excess in irradiance of light passed by a device which accepts right-handed circular polarization over that passed by a device which accepts left-handed circular polarization [16]. The elements of the Stokes vector are related to the Jones vector elements by

$$\begin{bmatrix} S_0 \\ S_1 \\ S_2 \\ S_3 \end{bmatrix} = \begin{bmatrix} \langle |E_x|^2 \rangle + \langle |E_y|^2 \rangle \\ \langle |E_x|^2 \rangle - \langle |E_y|^2 \rangle \\ 2 \langle |E_x| |E_y| \cos(\varphi_x - \varphi_y) \rangle \\ 2 \langle |E_x| |E_y| \sin(\varphi_x - \varphi_y) \rangle \end{bmatrix} \tag{37}$$

where $\langle \, \rangle$ represents the time average and φ_x and φ_y are the phases of the x and y field components, respectively [16]. Common Stokes vectors are

$$\begin{matrix} \begin{bmatrix} 1 & 0 & 0 & 0 \end{bmatrix}^{\mathrm{T}} & \text{Unpolarized} \\ \begin{bmatrix} 1 & 1 & 0 & 0 \end{bmatrix}^{\mathrm{T}} & \text{Horizontal polarization} \\ \begin{bmatrix} 1 & -1 & 0 & 0 \end{bmatrix}^{\mathrm{T}} & \text{Vertical polarization} \\ \begin{bmatrix} 1 & 0 & 0 & 1 \end{bmatrix}^{\mathrm{T}} & \text{Right circular polarization} \end{matrix} \tag{38}$$

Note that Stokes vectors are typically shown normalized to the S_0 parameter value. As in Jones' formalism, optical components which alter polarization state are represented as matrices (4×4). These matrices are called Mueller matrices. Mueller matrices were introduced by Hans Mueller in 1943 and operate on Stokes vectors [56]. The Mueller matrices for common optical components can be found in Refs. [14, 25, 56, 92, 116]. As an example of how Mueller matrices and Stokes vectors are used, consider the same example cited above—horizontally polarized light is incident on a LP at 45° immediately followed by a QWP (fast axis vertical):

$$
\boldsymbol{S}_{\mathrm{out}} =
\begin{bmatrix}
1 & 0 & 0 & 0 \\
0 & 1 & 0 & 0 \\
0 & 0 & 0 & -1 \\
0 & 0 & 1 & 0
\end{bmatrix}
\frac{1}{2}
\begin{bmatrix}
1 & 0 & 1 & 0 \\
0 & 0 & 0 & 0 \\
1 & 0 & 1 & 0 \\
0 & 0 & 0 & 0
\end{bmatrix}
\begin{bmatrix}
1 \\ 1 \\ 0 \\ 0
\end{bmatrix}
= \frac{1}{2}
\begin{bmatrix}
1 \\ 0 \\ 0 \\ 1
\end{bmatrix}. \tag{39}
$$

In Eq. (39), the vectors/matrices from right to left represent the incident beam, the LP at 45°, and the QWP with fast axis vertical, respectively. As expected, the result is a circularly polarized beam. Note that like Stokes vectors, it is common to normalize Mueller matrices to the m_{00} (or first row, first column) element value. Since Stokes vectors/Mueller matrices incorporate unpolarized light, it is possible to define the degree of polarization (DOP) of light in terms of Stokes parameters [16, 56, 85, 86]:

$$
\mathcal{P} = \frac{\sqrt{S_1^2 + S_2^2 + S_3^2}}{S_0}. \tag{40}
$$

Also of importance is the angle of polarization (AOP) [85, 86, 92, 116],

$$
\alpha = \frac{1}{2}\tan^{-1}\left(\frac{S_2}{S_1}\right). \tag{41}
$$

Note that α is undefined when dealing with circular polarization or unpolarized light.

2.6 TEM Waves at Smooth Boundaries

At material boundaries, light can be reflected (scattered) or transmitted. The amount of light scattered or transmitted depends on the index of refraction of the material and the polarization state of the incident field. It should be noted that the exact polarization state of light is rather arbitrary, i.e., one must fix an orthogonal coordinate system to the plane containing the electric and magnetic fields to define linear, circular, or elliptical polarization. The choice of coordinate system is arbitrary. When light encounters a material, it becomes convenient to let the vector normal to the material boundary be the z axis and the material's surface be the xy plane. The polarization state of light is then referenced to this coordinate system. The plane containing the material's surface normal (defined above to be $\hat{\boldsymbol{z}}$), the incident wave's direction vector $\boldsymbol{k}^i$, and the reflected wave's direction vector $\boldsymbol{k}^r$ is called the specular plane. The incident electric field vector component which resides in this plane is called the parallel field component because it lies parallel to the specular plane. The incident electric field vector component which resides in the plane orthogonal to the specular plane is called the perpendicular field component because it lies perpendicular to the specular plane. If the electric field vector lies completely in the specular plane, the polarization state of the incident light is referred to as parallel polarization, or p-pol. Likewise, if the electric field vector resides completely in the plane perpendicular to the specular plane, the polarization state of the incident light is referred to as perpendicular polarization, or s-pol (from the German word *senkrecht* meaning perpendicular). Derived below are the expressions for the reflection and transmission coefficients for both s- and p-pols as well as the Fresnel reflectances [16, 42, 56, 92, 116, 123]. Also shown are the Jones and Mueller matrices for reflection from a smooth material surface.
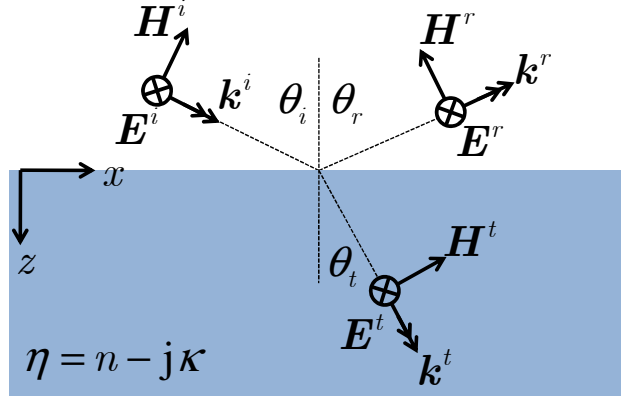
S-Pol
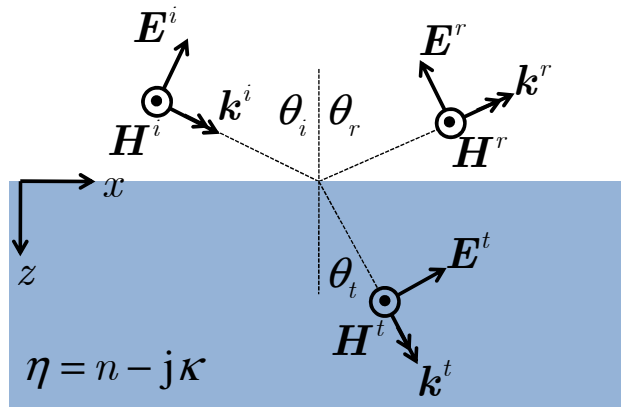
P-Pol

Figure 3. S-pol and p-pol scattering geometries.

2.6.1   S-Pol and P-Pol Fresnel Reflectances.

The s-pol and p-pol Fresnel reflectances are given in numerous references [16, 42, 56, 92, 116, 123]. The purpose of this section is to derive the expressions from electromagnetic field distributions. Consider the geometry shown in Fig. 3—a TEM wave is incident on an electrically large, planar conductive medium of complex index of refraction $\eta = n - \mathrm{j}\kappa$. The incident, reflected, and transmitted fields take the forms of the plane-wave solutions of Maxwell's equations, namely

$$\boldsymbol{E}^i = E_0 \begin{bmatrix} -\hat{\boldsymbol{y}} \\ \hat{\boldsymbol{x}} \cos\theta_i - \hat{\boldsymbol{z}} \sin\theta_i \end{bmatrix} e^{-\mathrm{j}k_0 x \sin\theta_i} e^{-\mathrm{j}k_0 z \cos\theta_i}$$

$$\boldsymbol{H}^i = \frac{E_0}{Z_0} \begin{bmatrix} \hat{\boldsymbol{x}} \cos\theta_i - \hat{\boldsymbol{z}} \sin\theta_i \\ \hat{\boldsymbol{y}} \end{bmatrix} e^{-\mathrm{j}k_0 x \sin\theta_i} e^{-\mathrm{j}k_0 z \cos\theta_i}$$

$$\boldsymbol{E}^r = E_0 \begin{bmatrix} -r_s \hat{\boldsymbol{y}} \\ -r_p \left(\hat{\boldsymbol{x}} \cos\theta_r + \hat{\boldsymbol{z}} \sin\theta_r \right) \end{bmatrix} e^{-\mathrm{j}k_0 x \sin\theta_r} e^{\mathrm{j}k_0 z \cos\theta_r}$$

$$\boldsymbol{H}^r = \frac{E_0}{Z_0} \begin{bmatrix} -r_s \left(\hat{\boldsymbol{x}} \cos\theta_r + \hat{\boldsymbol{z}} \sin\theta_r \right) \\ r_p \hat{\boldsymbol{y}} \end{bmatrix} e^{-\mathrm{j}k_0 x \sin\theta_r} e^{\mathrm{j}k_0 z \cos\theta_r}$$

$$\boldsymbol{E}^t = E_0 \begin{bmatrix} -t_s \hat{\boldsymbol{y}} \\ t_p \left(\hat{\boldsymbol{x}} \cos\theta_t - \hat{\boldsymbol{z}} \sin\theta_t \right) \end{bmatrix} e^{-\mathrm{j}k x \sin\theta_t} e^{-\mathrm{j}k z \cos\theta_t}$$

$$\boldsymbol{H}^t = \frac{E_0}{Z} \begin{bmatrix} t_s \left(\hat{\boldsymbol{x}} \cos\theta_t - \hat{\boldsymbol{z}} \sin\theta_t \right) \\ t_p \hat{\boldsymbol{y}} \end{bmatrix} e^{-\mathrm{j}k x \sin\theta_t} e^{-\mathrm{j}k z \cos\theta_t}$$

where E_0 is the amplitude of the incident field and Z_0 and Z are the intrinsic impedances of free space and the material, respectively [9]. Here a bracket notation is used to show both s- and p-pols—s-pol is the first row, p-pol is the second row. Enforcing the continuity of electric and magnetic fields tangential to the free-space/material interface results in

$$\begin{aligned} \begin{bmatrix} 1 \\ \cos\theta_i \end{bmatrix} e^{-\mathrm{j}k_0 x \sin\theta_i} + \begin{bmatrix} r_s \\ -r_p \cos\theta_r \end{bmatrix} e^{-\mathrm{j}k_0 x \sin\theta_r} &= \begin{bmatrix} t_s \\ t_p \cos\theta_t \end{bmatrix} e^{-\mathrm{j}k x \sin\theta_t} \\ \begin{bmatrix} \cos\theta_i \\ 1 \end{bmatrix} e^{-\mathrm{j}k_0 x \sin\theta_i} + \begin{bmatrix} -r_s \cos\theta_r \\ r_p \end{bmatrix} e^{-\mathrm{j}k_0 x \sin\theta_r} &= \frac{Z_0}{Z} \begin{bmatrix} t_s \cos\theta_t \\ t_p \end{bmatrix} e^{-\mathrm{j}k x \sin\theta_t} \end{aligned} \tag{42}$$

Expanding Eq. (42) into real and imaginary parts and algebraically combining the resulting expressions produces the law of reflection and Snell's law of refraction [9],

i.e.,

$$\theta_i = \theta_r$$
$$\sin \theta_i = \eta \sin \theta_t$$
(43)

Substituting Eq. (43) into Eq. (42) and simplifying produces

$$
\begin{bmatrix} 1 \\ \cos \theta_i \end{bmatrix} + \begin{bmatrix} r_s \\ -r_p \cos \theta_i \end{bmatrix} = \begin{bmatrix} t_s \\ t_p \cos \theta_t \end{bmatrix}
$$
$$
\begin{bmatrix} \cos \theta_i \\ 1 \end{bmatrix} + \begin{bmatrix} -r_s \cos \theta_i \\ r_p \end{bmatrix} = \frac{Z_0}{Z} \begin{bmatrix} t_s \cos \theta_t \\ t_p \end{bmatrix} .
$$
(44)

Solving Eq. (44) for r_s and r_p results in the s- and p-pol Fresnel reflection coefficients:

$$
r_s = \frac{Z \cos \theta_i - Z_0 \cos \theta_t}{Z \cos \theta_i + Z_0 \cos \theta_t} = \frac{\cos \theta_i - \eta \cos \theta_t}{\cos \theta_i + \eta \cos \theta_t}
$$
$$
r_p = \frac{Z_0 \cos \theta_i - Z \cos \theta_t}{Z_0 \cos \theta_i + Z \cos \theta_t} = \frac{\eta \cos \theta_i - \cos \theta_t}{\eta \cos \theta_i + \cos \theta_t} .
$$
(45)

Likewise, although not utilized in this research, solving Eq. (44) for t_s and t_p results in the s- and p-pol Fresnel transmission coefficients:

$$
t_s = \frac{2 \cos \theta_i}{\cos \theta_i + \eta \cos \theta_t}
$$
$$
t_p = \frac{2 \cos \theta_i}{\eta \cos \theta_i + \cos \theta_t} .
$$
(46)

In order to find expressions for the Fresnel reflectances in a form useful for remote-sensing applications, the angle of transmission θ_t must be removed from Eq. (45). Using the Pythagorean theorem and Snell's law of refraction, the s-pol reflection coefficient becomes

$$
r_s = \frac{\cos \theta_i - \sqrt{\eta^2 - \sin^2 \theta_i}}{\cos \theta_i + \sqrt{\eta^2 - \sin^2 \theta_i}} .
$$
(47)

Using the relation for the square root of a complex number [71],

$$\sqrt{a + \mathrm{j}b} = \sqrt{\frac{\sqrt{a^2 + b^2} + a}{2}} + \mathrm{jsgn}\,(b)\,\sqrt{\frac{\sqrt{a^2 + b^2} - a}{2}}, \tag{48}$$

results in

$$r_s = \frac{\cos\theta_i - (A - \mathrm{j}B)}{\cos\theta_i + (A - \mathrm{j}B)}$$

$$A = \sqrt{\frac{\sqrt{C} + D}{2}} \quad B = \sqrt{\frac{\sqrt{C} - D}{2}}. \tag{49}$$

$$C = 4n^2\kappa^2 + D^2$$

$$D = n^2 - \kappa^2 - \sin^2\theta_i$$

Taking the magnitude squared of Eq. (49) produces the s-pol Fresnel reflectance, namely,

$$R_s = |r_s|^2 = \frac{(\cos\theta_i - A)^2 + B^2}{(\cos\theta_i + A)^2 + B^2}. \tag{50}$$

The Fresnel reflectance for p-pol can be found in terms of R_s by noting that

$$r_p = \frac{\tan\,(\theta_i - \theta_t)}{\tan\,(\theta_i + \theta_t)} = -r_s \frac{\cos\,(\theta_i + \theta_t)}{\cos\,(\theta_i - \theta_t)}. \tag{51}$$

These expressions are easily found by using Snell's law of refraction and Eq. (45). Expanding Eq. (51) and substituting $\cos\theta_t = (A - \mathrm{j}B)/\eta$ and $\sin\theta_t = \sin\theta_i/\eta$ produces

$$r_p = -r_s \frac{\cos\theta_i\,(A - \mathrm{j}B) - \sin^2\theta_i}{\cos\theta_i\,(A - \mathrm{j}B) + \sin^2\theta_i} = -r_s \frac{A - \sin\theta_i\tan\theta_i - \mathrm{j}B}{A + \sin\theta_i\tan\theta_i - \mathrm{j}B}. \tag{52}$$

Taking the magnitude squared of Eq. (52) produces the desired result

$$R_p = |r_p|^2 = \frac{(A - \sin\theta_i\tan\theta_i)^2 + B^2}{(A + \sin\theta_i\tan\theta_i)^2 + B^2} R_s. \tag{53}$$

29

These exact forms of the s- and p-pol Fresnel reflectances appear in Refs. [42, 92, 116, 123].

2.6.2 Jones and Mueller Matrices for Reflection.

From the expressions derived above, Jones and Mueller matrices can be formed which model the behavior of light at a smooth material interface. The Jones matrix for light scattered from a smooth material boundary is simply

$$
\begin{bmatrix} E_s^r \\ E_p^r \end{bmatrix} = \begin{bmatrix} r_s & 0 \\ 0 & r_p \end{bmatrix} \begin{bmatrix} E_s^i \\ E_p^i \end{bmatrix}
\tag{54}
$$

where r_s and r_p are given in Eqs. (49) and (52), respectively [42, 92, 103, 104, 116]. From Eq. (54), the Mueller matrix for reflection from a smooth material surface can be derived. The general expressions relating Eq. (54) to the Mueller matrix elements are shown in the next chapter. For reflection from a smooth surface, the Mueller matrix takes the form

$$
\begin{bmatrix} S_0^r \\ S_1^r \\ S_2^r \\ S_3^r \end{bmatrix} = \frac{1}{2} \begin{bmatrix} R_s + R_p & R_s - R_p & 0 & 0 \\ R_s - R_p & R_s + R_p & 0 & 0 \\ 0 & 0 & 2\text{Re}\left\{r_s r_p^*\right\} & 2\text{Im}\left\{r_s r_p^*\right\} \\ 0 & 0 & -2\text{Im}\left\{r_s r_p^*\right\} & 2\text{Re}\left\{r_s r_p^*\right\} \end{bmatrix} \begin{bmatrix} S_0^i \\ S_1^i \\ S_2^i \\ S_3^i \end{bmatrix}
\tag{55}
$$

where R_s and R_p are given in Eqs. (50) and (53), respectively [42, 92, 103, 104, 116]. Here, Re { } and Im { } are the real and imaginary parts of the argument, respectively.

Before concluding, it is worth noting an important aspect of the ideas just presented. Figure 4 shows a plot of the s- and p-pol Fresnel reflectances for glass (amorphous SiO_2) and iron at a wavelength of 1 μm versus angle ($\theta_i = \theta_r$). Note that the s-pol reflectance is larger than the p-pol reflectance over nearly all angles. This
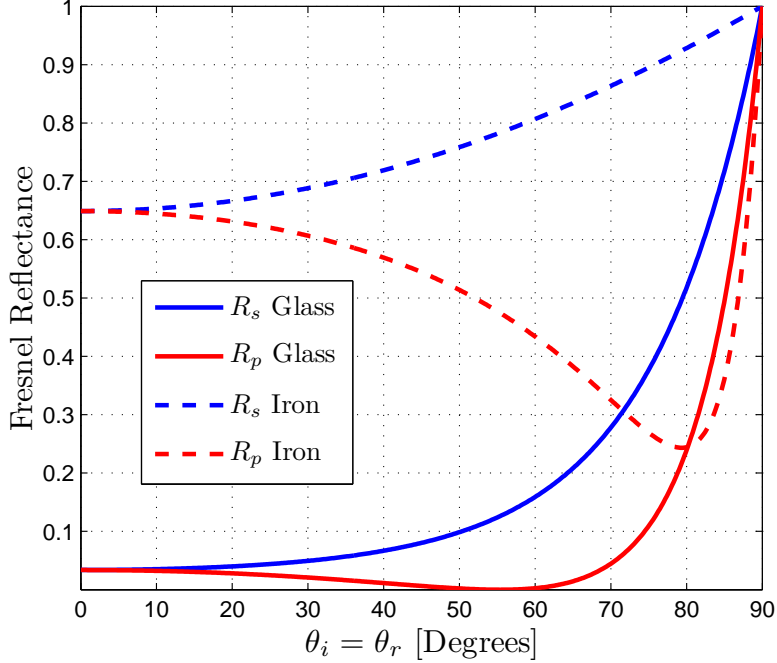
Figure 4. Fresnel reflectances of glass and iron at 1 μm versus angle. The index of refraction at 1 μm for glass is $1.45025 - j0$ [99] and iron is $3.23 - j4.35$ [100].

implies that unpolarized incident light, when scattered by a surface, becomes partially polarized and its plane of vibration is the s-pol plane. This is easy to verify mathematically using Stokes vectors/Mueller matrices:

$$\begin{bmatrix} S_0^r \\ S_1^r \\ S_2^r \\ S_3^r \end{bmatrix} = \frac{1}{2} \begin{bmatrix} R_s + R_p & R_s - R_p & 0 & 0 \\ R_s - R_p & R_s + R_p & 0 & 0 \\ 0 & 0 & 2\text{Re}\left\{r_s r_p^*\right\} & 2\text{Im}\left\{r_s r_p^*\right\} \\ 0 & 0 & -2\text{Im}\left\{r_s r_p^*\right\} & 2\text{Re}\left\{r_s r_p^*\right\} \end{bmatrix} \begin{bmatrix} 1 \\ 0 \\ 0 \\ 0 \end{bmatrix} = \frac{1}{2} \begin{bmatrix} R_s + R_p \\ R_s - R_p \\ 0 \\ 0 \end{bmatrix}. \tag{56}$$

The DOP and AOP, using Eqs. (40) and (41), are

$$\mathcal{P} = \frac{R_s - R_p}{R_s + R_p} \quad \alpha = 0. \tag{57}$$

Since $\mathcal{P}$ depends on the s- and p-pol reflectances and they, in turn, are functions of the material's complex index of refraction, $\mathcal{P}$ is a function of the index of refraction.

31

This observation and the manner in which unpolarized light scatters from a material surface are fundamental to this research.

2.7 Scattering from Rough Surfaces

The previous section described how light behaves when it encounters a smooth material boundary. Obviously, (perfectly) smooth material surfaces do not exist in nature. Whether the expressions derived above are sufficient to accurately model how light scatters from a boundary depends on the ratio of the wavelength of the incident light to the roughness of the surface. If the incident light's wavelength is several times the roughness of the surface, the Fresnel reflectances derived above should be sufficient. Physically, this implies that the incident light does not "see" the randomness of the material surface and thus the surface can be approximated as perfectly smooth. This scenario is often encountered in remote sensing using radio frequencies where wavelengths can range from centimeters to meters. On the other hand, if the incident light's wavelength is on the order of or smaller than the roughness of the surface, the Fresnel reflectances derived above must be altered to account for the randomness of the material surface. This scenario (applicable to this research) is encountered in remote sensing using infrared or optical frequencies where wavelengths range from hundreds of nanometers to microns. The purpose of this section is to define a framework for dealing with rough surface scattering. More details and descriptions of the framework utilized for this research are reserved for the next chapter.

2.7.1 Bidirectional Reflectance Distribution Functions.

Before introducing the theoretical framework used to deal with rough surface scattering, it is important to understand how surface roughness affects the scattering of light. Consider light reflected from a relatively smooth object like a mirror. The
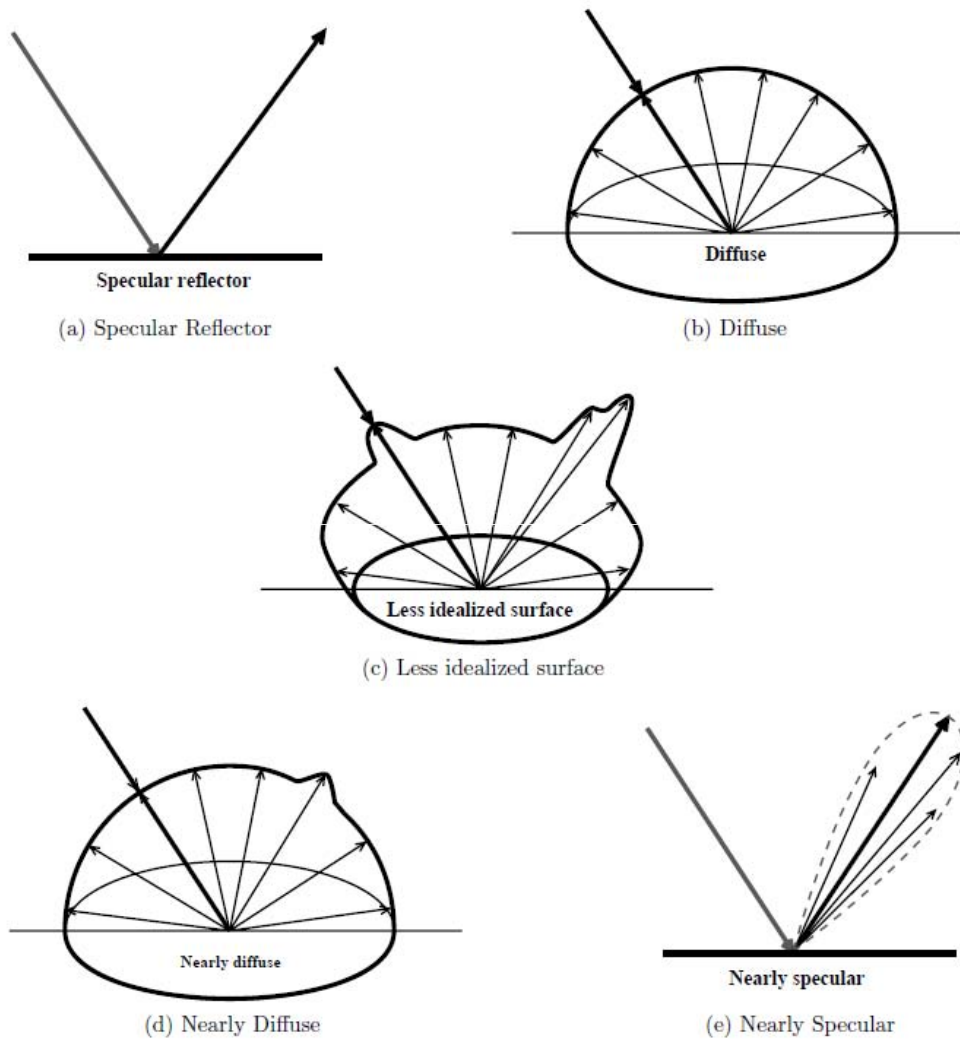
Figure 5. Radiance distributions for near-specular, diffuse, and generalized surfaces [92, 112].

scattered light from such a surface (a near-specular surface) obeys the law of reflection, i.e., the scattered light is nearly contained in the specular plane at the specular angle $(\theta_i = \theta_r)$. This is shown in Fig. 5. Contrast that mirror-like surface with a rough surface like a projector screen. The projector screen scatters light equally in all directions making the screen visible to anyone in the room (shown in Fig. 5). This type of surface is referred to as a diffuse or Lambertian surface. These two examples represent the extremes of surface roughness. Most surfaces lie somewhere in between these two extremes (shown in Fig. 5). In optics, scattering from rough surfaces is modeled using a bidirectional reflectance distribution function (BRDF). The BRDF is defined as the amount of light scattered into all directions from a surface illuminated by a source at an arbitrary position above the hemisphere of the material [116]. The BRDF is given by

$$f\left(\theta_i, \phi_i; \theta_r, \phi_r; \lambda\right) = \frac{dL_r\left(\theta_r, \phi_r\right)}{dE\left(\theta_i, \phi_i\right)} \quad \left[\text{sr}^{-1}\right] \tag{58}$$

where L_r is the radiance [W/(m^{2}sr)] leaving the surface and E is the incident irradiance [W/m^2] [42, 92, 96, 97, 116, 123]. The BRDF geometry is shown in Fig. 6 [123]. Most materials are azimuthally symmetric about the surface normal z; therefore, the azimuthal angles ϕ_i and ϕ_r can be combined into a single angle $\phi = |\phi_i - \phi_r|$ where $\phi = \pi$ (180°) corresponds to the forward scatter angle and defines the specular plane [42, 92, 116]. Another important quantity related to the BRDF is the directional hemispherical reflectance (DHR). The DHR is the ratio of the total energy reflected into the entire hemisphere above a material surface to the total energy incident from a particular direction [42, 92, 103, 104, 116, 139]:

$$\rho_{\text{DHR}}\left(\theta_i, \phi, \lambda\right) = \int_0^{2\pi} \int_0^{\pi/2} f\left(\theta_i; \theta_r; \phi; \lambda\right) \cos\left(\theta_r\right) \sin\left(\theta_r\right) d\theta_r d\phi. \tag{59}$$
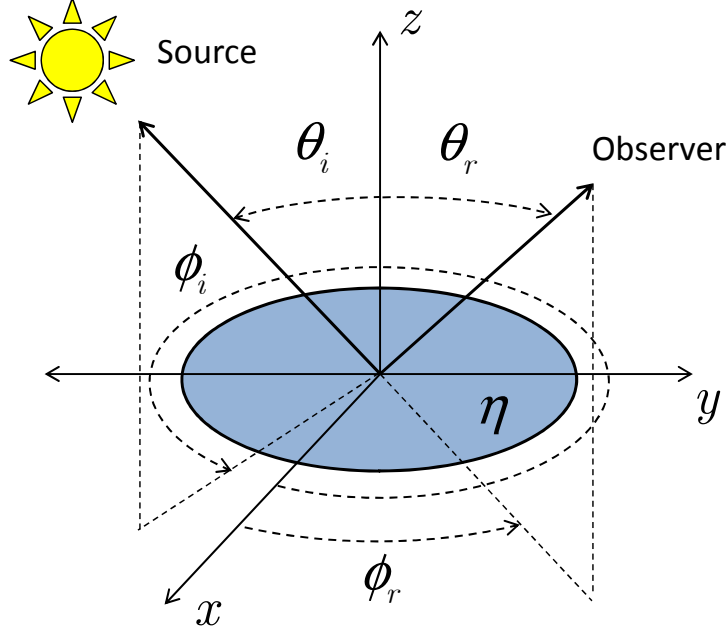
Figure 6. Bidirectional reflectance distribution function (BRDF) geometry [123].

For a perfect reflector (equivalently a PEC), ρ_{DHR} must be equal to 1 (conservation of energy) [139]. Easily derived from Eq. (59) is the BRDF for a diffuse or Lambertian surface. Recall that a diffuse surface scatters light equally in all directions; therefore, one expects the BRDF of such a surface to be completely independent of incident or observation angles, i.e.,

$$\rho_{\text{DHR}} = f \int_0^{2\pi} \int_0^{\pi/2} \cos(\theta_r) \sin(\theta_r) \, d\theta_r d\phi. \tag{60}$$

Carrying out the integration and solving for f produces [42, 92, 116]

$$f = \frac{\rho_{\text{DHR}}}{\pi}. \tag{61}$$

2.7.2   Polarimetric BRDF's.

A more general form of the scalar BRDF, defined in Eq. (58), is the polarimetric BRDF, or pBRDF. The pBRDF predicts the polarization effects of material surface

scattering as well as the amount of light scattered from a surface [42, 92, 116]. It is defined as

$$\mathbf{F}\left(\theta_i, \phi_i; \theta_r, \phi_r; \lambda\right) = \frac{d\boldsymbol{L}_r\left(\theta_r, \phi_r\right)}{d\boldsymbol{E}\left(\theta_i, \phi_i\right)}, \tag{62}$$

where $\boldsymbol{L}_r$ and $\boldsymbol{E}$ (same as above) are now Stokes vectors [42, 92, 116, 123] and the pBRDF $\mathbf{F}$ is a Mueller matrix. Note that the f_{00} element of Eq. (62) is equivalent to the scalar BRDF defined in Eq. (58) [42, 92, 116].

2.7.3 Types of BRDF's.

BRDF's come in two varieties—empirical and analytical BRDF's [116]. As the name implies, empirical BRDF's are BRDF's which arise from measurements. They are not of particular interest to this research and therefore are not discussed. Information regarding empirical BRDF's including measurement systems and techniques can be found in Ref. [116]. Analytical BRDF's are theoretical expressions derived from the physics of light's interaction with surfaces. They, in addition to being functions of incident and observation angles, are also functions of surface roughness and complex index of refraction. Analytical BRDF's can be divided into two types—PO- and GO-based models. PO BRDF's are based on the physical optics approximation of scattering [9, 11, 16, 136]. They tend to be more accurate than GO BRDF's; yet, they possess more complicated mathematical forms than their GO counterparts. The development and experimental verification of a PO BRDF is shown in Ref. [3]. GO BRDF's are based on the ray approximation of light [9, 16, 56]. While being less accurate than PO BRDF's, their simple mathematical forms make them especially attractive. The BRDF model chosen for this research (discussed in detail in the next chapter) is a GO BRDF.

2.8 Aspects of Imaging

This section gives the reader a brief background on the effects of aperture size and atmospheric turbulence on imaging. Excellent references discussing these topics in detail are [5, 44, 63, 111].

2.8.1 Diffraction-Limited Imaging.

The image produced by a camera is a measure of the irradiance of the light reflected or emitted by the object. The image received at the camera can be modeled as

$$i\left(\boldsymbol{y}\right) = \int\limits_{-\infty}^{\infty} o\left(\boldsymbol{x}\right) h\left(\boldsymbol{y} - \boldsymbol{x}\right) d\boldsymbol{x}, \tag{63}$$

or in the discrete case (applicable to modern digital cameras)

$$i\left(\boldsymbol{y}\right) = \sum_{\boldsymbol{x}} o\left(\boldsymbol{x}\right) h\left(\boldsymbol{y} - \boldsymbol{x}\right). \tag{64}$$

Here, $\boldsymbol{x}$ is the object-plane coordinate pair (or object-plane pixel pair), $\boldsymbol{y}$ is the image-plane coordinate pair (or image-plane pixel pair), o is the reflected irradiance of the object, h is the point spread function (PSF), and i is the received irradiance at the focal plane [45, 44, 74, 114]. Note that the received irradiance (or the image) is the object's irradiance convolved (two-dimensional convolution since $\boldsymbol{x}$ is a coordinate pair) with the PSF. In the case of a perfect image

$$h\left(\boldsymbol{y} - \boldsymbol{x}\right) = \delta\left(\boldsymbol{y} - \boldsymbol{x}\right), \tag{65}$$

where δ is the Dirac function. Real-world effects contribute to cause h to deviate from δ. Two main causes of this deviation are finite aperture size and atmospheric turbulence. Finite aperture size degrades image quality via diffraction. Diffraction
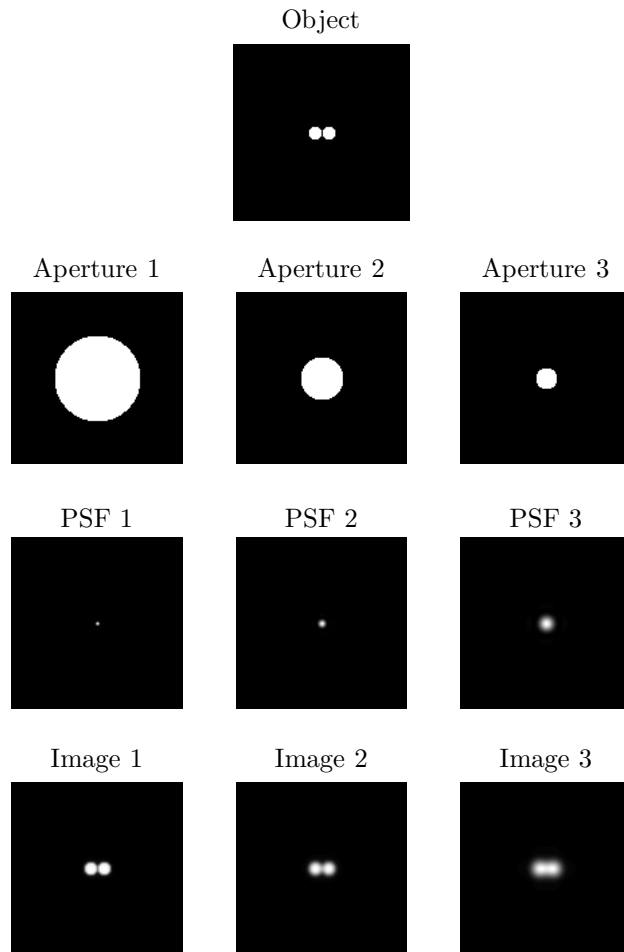
Figure 7. Diffraction-limited images (bottom row) of the object (top row) viewed through three differently-sized circular apertures (second row). Note that an increase in aperture size results in an increase in image resolution. The diffraction-limited PSF's are also shown (third row).

is an optical scattering effect in which light scattered from the edges of a collecting aperture interferes with the main lobe. The result is a limit in resolution. Figure 7 shows this effect for finite circular apertures of varying sizes. The PSF, incorporating the size and shape of the aperture, is

$$h\left(\boldsymbol{x}\right) = \left| \int_{-\infty}^{\infty} A\left(\boldsymbol{u}\right) e^{-\mathrm{j}2\pi\mathcal{K}\boldsymbol{x}\cdot\boldsymbol{u}} d\boldsymbol{u} \right|^2 \tag{66}$$

or in the discrete case

$$h\left(\boldsymbol{x}\right) = \left| \sum_{\boldsymbol{u}} A\left(\boldsymbol{u}\right) e^{-\mathrm{j}2\pi\mathcal{K}\boldsymbol{x}\cdot\boldsymbol{u}} \right|^2. \tag{67}$$

Here, $\boldsymbol{u}$ is the aperture-plane coordinate pair, $\mathcal{K}$ is a constant which depends on the wavelength and the distance to the image plane, and A is the aperture function [45, 74, 114].

2.8.2 Atmospheric Turbulence.

The second image degradation cause, atmospheric turbulence, is typically far more severe than the first. Atmospheric turbulence is caused by temperature and pressure gradients in the atmosphere. These gradients cause the index of refraction to vary randomly in both time and space [5, 44]. At point $\boldsymbol{r}$ and time t, the index of refraction of the atmosphere can be expressed as

$$n\left(\boldsymbol{r}, t\right) = n_0 + n_1\left(\boldsymbol{r}, t\right) \tag{68}$$

where $n_0 = \langle n\left(\boldsymbol{r}, t\right)\rangle \approx 1$ and $n_1\left(\boldsymbol{r}, t\right)$ represents the random deviation of $n\left(\boldsymbol{r}, t\right)$ from its mean value [5, 44]. In terms of temperature and pressure, the index of refraction is

$$n\left(\boldsymbol{r}, t\right) = 1 + 77.6 \times 10^{-6} \left(1 + 7.52 \times 10^{-3}\lambda^{-2}\right) \frac{P\left(\boldsymbol{r}, t\right)}{T\left(\boldsymbol{r}, t\right)} \tag{69}$$

39

where λ is the wavelength in microns, P is the atmospheric pressure in millibars, and T is the temperature in kelvin [5, 44].

Of particular relevance to the work presented here is the refractive-index power spectral density (PSD) developed by Kolmogorov. Kolmogorov reasoned that the PSD contained three regions demarcated by the smallest and largest sizes of turbulent "eddies" known as the inner (ℓ_0) and outer scales (L_0), respectively [5, 44]. Typical values for ℓ_0 and L_0 are a few millimeters and 1–100 m, respectively [44]. For turbulent eddy sizes lying in between the inner and outer scales (also known as the inertial subrange), i.e., $\ell_0 < L < L_0$, the Kolmogorov PSD takes the form

$$\Phi_n\left(\kappa_x, \kappa_y, z\right) = 0.033 C_n^2\left(z\right)\left(\kappa_x^2 + \kappa_y^2\right)^{-11/6} \tag{70}$$

where $\kappa_\alpha = 2\pi/\alpha$ $(\alpha = x, y)$, z is the propagation distance, and C_n^2 is the index-of-refraction structure constant which serves as a measure of the strength of index-of-refraction fluctuations [5, 44]. Several functional forms exist in the literature for C_n^2 (see Ref. [5] for discussions on these models). Note that the Kolmogorov PSD is only applicable for eddy sizes which reside in the inertial subrange. For eddy sizes which reside outside the inertial subrange another PSD must be used. Common examples of such PSD's are the von Kármán and the modified atmospheric PSD's [5, 44].

Atmospheric phase screens and phase wheels used in this research to model turbulence are created in the manner outlined by Frehlich:

$$\varphi\left(i\Delta x, l\Delta y\right) = \text{Re}\left\{\sum_{n=0}^{N_x}\sum_{m=0}^{N_y}\left[a\left(n, m\right) + jb\left(n, m\right)\right]\exp\left[\text{j}2\pi\left(\frac{in}{N_x} + \frac{lm}{N_y}\right)\right]\right\} \tag{71}$$

where Δx and Δy are the x and y grid spacings in the spatial domain, $a\left(n, m\right)$ and $b\left(n, m\right)$ are matrices of zero mean uncorrelated Gaussian random numbers, and N_x and N_y are the x and y lengths of $a\left(n, m\right)$ and $b\left(n, m\right)$ [39]. The variances of $a\left(n, m\right)$

and $b(n, m)$ are

$$\langle a^2(n, m) \rangle = \langle b^2(n, m) \rangle$$
$$= 2\pi \left(\frac{2\pi}{\lambda}\right)^2 \left(\frac{2\pi}{N_x \Delta x}\right) \left(\frac{2\pi}{N_y \Delta y}\right) \Phi_n \left(\frac{2\pi n}{N_x \Delta x}, \frac{2\pi m}{N_y \Delta y}, z\right), \tag{72}$$

where Δz is the phase screen thickness and Φ_n is the refractive-index PSD [39]. Substitution of the Kolmogorov PSD [Eq. (70)] into Eq. (72) produces

$$\langle a^2(n, m) \rangle = \langle b^2(n, m) \rangle$$
$$= 2\pi \Delta z \left(\frac{2\pi}{\lambda}\right)^2 \left(\frac{2\pi}{N_x \Delta x}\right) \left(\frac{2\pi}{N_y \Delta y}\right)$$
$$\left\{ 0.033 C_n^2 \left[\left(\frac{2\pi n}{N_x \Delta x}\right)^2 + \left(\frac{2\pi m}{N_y \Delta y}\right)^2 \right]^{-11/6} \right\} \tag{73}$$

where C_n^2 is assumed constant over the phase screen thickness Δz. At this point, it becomes convenient to introduce the atmospheric coherence width (or Fried's parameter) [5, 44, 111]:

$$r_0 = \left[0.423 \left(\frac{2\pi}{\lambda}\right)^2 \int\limits_0^{\Delta z} C_n^2(z) \, dz \right]^{-3/5} \tag{74}$$

where for small Δz

$$r_0 \approx \left[0.423 \left(\frac{2\pi}{\lambda}\right)^2 C_n^2 \Delta z \right]^{-3/5}. \tag{75}$$

The atmospheric coherence width is an extremely important parameter in imaging and serves as an "effective" pupil diameter when imaging in the presence of turbulence. This physical interpretation of r_0 is deduced by considering the Rayleigh resolution of a diffraction-limited imaging system utilizing a circular pupil:

$$\delta = 1.22 \frac{\lambda z_i}{D} \tag{76}$$

where D is the diameter of the imaging aperture and z_i is the image distance from the pupil [16, 56, 45]. Andrews and Phillips note that the resolution of an imaging system in the presence of atmospheric turbulence is [5]

$$\delta \approx 1.22\frac{\lambda z_i}{r_0}. \tag{77}$$

By comparing Eqs. (76) and (77), one can see that r_0 behaves as an "effective" aperture diameter. Note that the above equations imply that when imaging through turbulence, resolution is limited by r_0 and not D (assuming $D > r_0$ which is typically the case). Substituting Eq. (75) into Eq. (73) and simplifying yields

$$\langle a^2(n,m)\rangle = \langle b^2(n,m)\rangle$$
$$= \frac{0.0229}{N_x\Delta x N_y\Delta y}r_0^{-5/3}\left[\left(\frac{n}{N_x\Delta x}\right)^2 + \left(\frac{m}{N_y\Delta y}\right)^2\right]^{-11/6}. \tag{78}$$

If $N_x = N_y$ and $\Delta x = \Delta y$, then Eq. (78) simplifies to

$$\langle a^2(n,m)\rangle = \langle b^2(n,m)\rangle = 0.0229\left(\frac{D}{r_0}\right)^{5/3}\left(n^2 + m^2\right)^{-11/6}. \tag{79}$$

Phase screens and phase wheels can now be created by first generating two matrices of Gaussian random numbers. The Gaussian random numbers should be zero mean and have a variance given by Eq. (79). Utilizing Eq. (71) produces the desired result.

The effects of light propagating through the atmosphere are phase (occurs in weak and strong turbulence) and irradiance (occurs in strong turbulence) fluctuations in the field. The demarcation between weak and strong turbulence is determined by the

Rytov number or Rytov variance [5]. For a plane wave, the Rytov variance is [5]

$$\sigma_R^2(L) = 2.25 \left(\frac{2\pi}{\lambda}\right)^{7/6} L^{5/6} \int\limits_0^L C_n^2(z) \left(1 - \frac{z}{L}\right)^{5/6} dz. \tag{80}$$

Assuming constant C_n^2 and substituting in Eq. (75) produces

$$\sigma_R^2 = 2.91 \left[\frac{L}{(2\pi/\lambda) r_0^2}\right]^{5/6}. \tag{81}$$

Weak turbulence is loosely defined as turbulence in which $\sigma_R^2 < 0.2$; strong turbulence is defined as turbulence in which $\sigma_R^2 > 0.2$ [5]. Note that the values of σ_R^2 used in this research are much less than 0.2. Figure 8 shows the effects of weak atmospheric turbulence on the same object imaged in Fig. 7. Phase screens for this simulation are created as outlined above with $D/r_0 \approx 43$. Note, as implied by Eq. (77) and discussed above, an increase in aperture size does not improve the quality of the image. Incorporating atmospheric turbulence into the PSF [Eq. (66)] results in

$$h(\boldsymbol{x}) = \left|\int\limits_{-\infty}^{\infty} A(\boldsymbol{u}) e^{j\varphi(\boldsymbol{u})} e^{-j2\pi\mathcal{K}\boldsymbol{x}\cdot\boldsymbol{u}} d\boldsymbol{u}\right|^2 \tag{82}$$

or in the discrete case

$$h(\boldsymbol{x}) = \left|\sum_{\boldsymbol{u}} A(\boldsymbol{u}) e^{j\varphi(\boldsymbol{u})} e^{-j2\pi\mathcal{K}\boldsymbol{x}\cdot\boldsymbol{u}}\right|^2. \tag{83}$$

Here, φ models the random phase effects caused by propagation through the atmosphere [44, 74, 114]. Note that modeling turbulence in this manner is only accurate for $\sigma_R^2 \ll 0.2$. For strong turbulence scenarios, this model must be adapted. Note also that this model for the PSF is the same used by LeMaster and Cain and Schulz (discussed in more detail in the next chapter) [74, 114]. Image degradation caused

Object

Aperture 1   Aperture 2   Aperture 3

PSF 1   PSF 2   PSF 3

Image 1   Image 2   Image 3
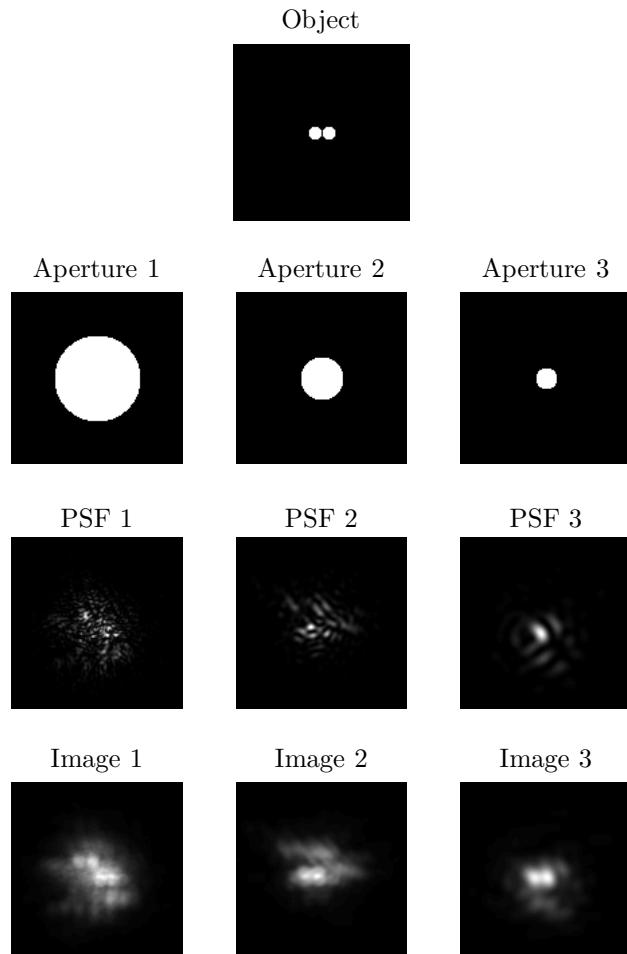
Figure 8. Turbulence-degraded images (bottom row) of the object (top row) viewed through three differently-sized circular apertures (second row). Note that an increase in aperture size does not improve image quality. The turbulence-degraded PSF's are also shown (third row).

by atmospheric turbulence is, at least in part, correctable. One technique used to remove atmospheric degradation is adaptive optics. Adaptive optics (AO) relies on a wavefront sensor and deformable mirror to correct phase aberrations caused by the atmosphere. References describing adaptive optics systems are [1, 75, 135]. The other technique, utilized in this research, is called blind deconvolution. Blind deconvolution is the process of recovering the true object, o in Eq. (64), from the degraded image having little or no information about h (PSF) or o [70]. Blind deconvolution is formally developed in the next chapter.

III. Summary of Published Research

This chapter provides a review of the relevant published work. Included in this literature summary is an overview of optical material-characterization (both laboratory and remote-sensing) techniques, a description of three BRDF's, and an explanation of two blind-deconvolution algorithms.

3.1 Optical Material Characterization

Material characterization requires one to solve forward and inverse problems. The forward problem involves finding theoretical expressions for the particular measurement geometry. In some instances, the forward problem can be algebraicly inverted resulting in direct closed-form expressions for index of refraction in terms of measurable quantities. However, in most circumstances, the inverse problem must be solved using numerical-inversion techniques such as the Newton-Raphson method, Gauss-Newton nonlinear least squares, or the Levenberg-Marquardt algorithm [79]. It is important to keep these two steps in mind as the following index-of-refraction measurement techniques are introduced. These two material-characterization problems form the basis of this research.

This section is organized in the following manner. Discussed first are laboratory material-characterization techniques followed by remote-sensing material-classification (defined below) and characterization algorithms. Note that many more techniques for determining the index of refraction exist in the literature [99, 100]. The techniques described below are chosen because they are the most popular and relevant to this research.

3.1.1 Laboratory Techniques.

The laboratory material-characterization techniques highlighted below are Brewster's-angle, minimum-deviation angle (prism methods), interferometric, and ellipsometric techniques. As stated above, this list is not all inclusive [99, 100].

3.1.1.1 Brewster's Angle.

The Brewster's-angle technique, along with the minimum-deviation angle method (discussed below), are the most mature optical material-characterization algorithms. The basic concept behind this measurement technique is accurately determining the Brewster's angle of a material. Recall the expression for the p-pol Fresnel reflectance given in Eq. (53):

$$
\begin{aligned}
R_p &= \left[\frac{(A - \sin\theta_i \tan\theta_i)^2 + B^2}{(A + \sin\theta_i \tan\theta_i)^2 + B^2} \right] \left[\frac{(\cos\theta_i - A)^2 + B^2}{(\cos\theta_i + A)^2 + B^2} \right] \\
A &= \sqrt{\tfrac{\sqrt{C}+D}{2}} \quad B = \sqrt{\tfrac{\sqrt{C}-D}{2}} \\
C &= 4n^2\kappa^2 + D^2 \\
D &= n^2 - \kappa^2 - \sin^2\theta_i
\end{aligned}
\tag{84}
$$

Note that for a lossless material, i.e., $\kappa = 0$, there exists an angle at which $R_p = 0$. This angle is called Brewster's angle θ_B [9, 16, 56]. Brewster's angle can be found in terms of index of refraction by making the necessary substitutions into Eq. (84):

$$
\theta_B = \tan^{-1}(n).
\tag{85}
$$

This expression can easily be inverted to produce a function of index of refraction in terms of Brewster's angle:

$$
n = \tan(\theta_B).
\tag{86}
$$
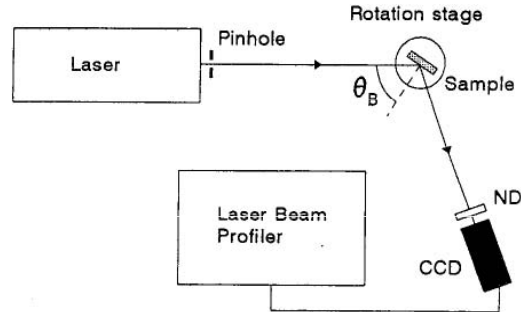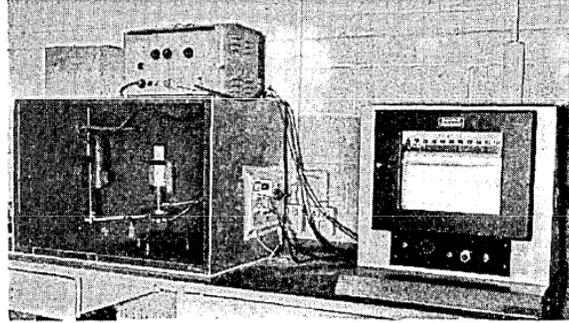
Figure 9. A photograph (top) of a goniophotometer used by Bell [12] and a schematic (bottom) of a goniophotometer used by Mian _et al._ [93].

It is important to understand physically what the mathematics above implies. P-pol light, which is incident at Brewster's angle, is completely transmitted (no reflection) into the material. Therefore, exposing an unknown material to p-pol incident light and finding the angle at which the scattered irradiance is a minimum provides a simple means of determining the index of refraction via Eq. (86). This process forms the basis of the material-measurement technique.

Brewster's angle is found experimentally using an instrument known as a goniophotometer [12]. A goniophotometer consists of two arms and a precision rotation stage (see Fig. 9). The first arm contains the light source (typically a laser) producing p-pol light; the second arm contains the optical detector (typically a camera). The rotation stage, which contains the sample, is situated immediately following the source arm. When searching for Brewster's angle, the movement of the detector arm must be coordinated with the movement of the rotation stage to ensure the detector remains in the specular direction. This is accomplished with mechanical gearing

which ensures the rotation stage moves at one-half the rate of rotation of the detector arm [12].

While being elegantly simple, this technique suffers from several shortcomings. The first is optical alignment. As stated above, the detector arm must be positioned in the specular direction for the technique to produce accurate index-of-refraction values. This is no small task. Both Bell [12] and Mian *et al.* [93] spend time discussing instrument alignment techniques in their respective papers. Next is specimen preparation. While, mathematically, p-pol incident light at Brewster's angle is not scattered, in actuality, some light is reflected from the material. This is caused by diffuse scattering from the surface of the material under test (MUT) [12]. Since diffuse scattering is caused by surface roughness, the surface of the MUT must be smooth enough to ensure specular scattering dominates. If the MUT's surface is too rough, such that diffuse scattering dominates, it is impossible to accurately determine the angle of minimum scattered irradiance. Lastly, the technique (as described) cannot be used to find the MUT's coefficient of extinction κ because it lacks a second independent measurement. This can be overcome by measuring the scattered irradiance at a second angle or by measuring the scattered irradiance at Brewster's angle when s-pol light is incident. These methods and several others are described in Ref. [99].

3.1.1.2 Minimum-Deviation Angle (Prism Techniques).

It has been known for centuries that when light passes through a prism, it bends. The degree to which the light bends depends on the index of refraction of the prism. This simple observation forms the basis of the minimum-deviation angle material-measurement technique. Figure 10 shows a diagram of the measurement geometry. Using Snell's law of refraction and some simple trigonometry, one can derive an expression for the deviation angle ψ in terms of the index of refraction and prism angle

49
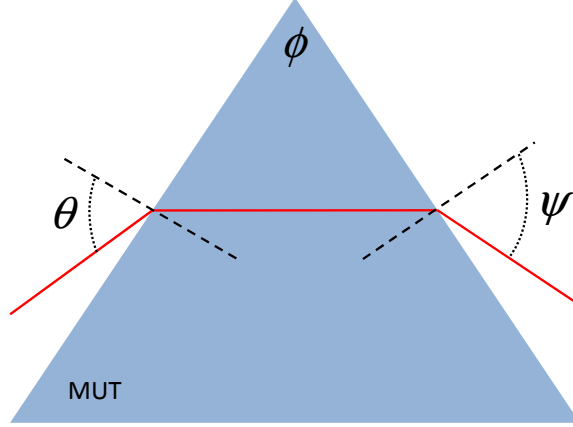
Figure 10. Minimum-deviation angle measurement geometry.

ϕ:

$$\psi = \sin^{-1}\left[n\sin\left(\phi - \sin^{-1}\left(\frac{\sin\theta}{n}\right)\right)\right] + \theta - \phi. \tag{87}$$

It can be shown that ψ is a minimum when the light ray passing through the prism is parallel to the prism's base. Solving for the index of refraction in terms of $\psi_{\min}$ results in

$$n = \frac{\sin\left[(\psi_{\min} + \phi)/2\right]}{\sin(\phi/2)}. \tag{88}$$

Finding the minimum deviation angle experimentally is accomplished using a device very similar to a goniophotometer (see Fig. 9). The measurement device consists of a light source (typically a laser) followed by a rotation stage, which holds the material prism, followed lastly by an optical detector. Since this technique relies on the light transmitted through the material, there is no need for the detector to move with the rotation stage. In order to measure the deviation angle, part of the source beam must be passed by the prism undeviated to provide a reference [58].

Several examples of this technique, or derivatives of it, exist in the literature [28, 29, 58, 88]. Three of the cited papers discuss measuring anisotropic materials at cryogenic temperatures [28, 29, 58]. It is worth discussing two of the issues with this measurement technique before concluding this summary. The first is that the
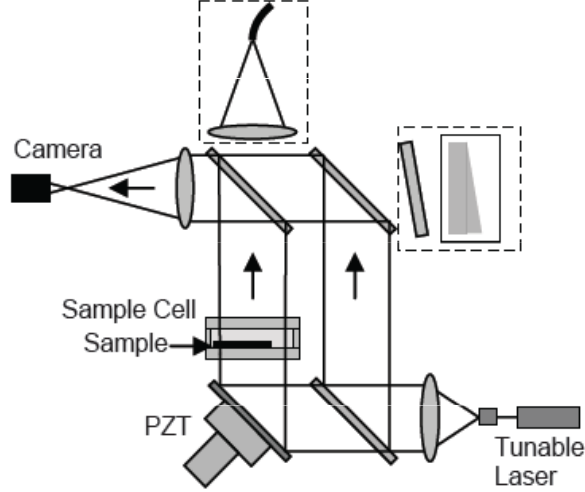
Figure 11. Schematic of a Mach-Zehnder interferometer used by Goodwin _et al._ [46].

minimum-deviation angle technique is a transmission measurement. While this certainly aids with optical alignment, it limits the applicability of this technique to low κ materials. The second measurement issue is specimen preparation. Like the Brewster's-angle technique, the faces of the MUT prism must be smooth enough to ensure light passes through the prism in the manner predicted by Snell's law. If the prism faces are too rough, light is transmitted at angles other than the Snell's law transmission angle (transmission equivalent of light being scattered in directions other than the specular direction). This makes finding $\psi_{\min}$ difficult. In addition to smooth prism faces, MUT prism construction can also be an issue. For an isotropic MUT, prism construction is less of a problem; however, for an anisotropic MUT, the prism faces must be correctly oriented relative to the MUT's crystal axes.

3.1.1.3 Interferometers.

Interferometric material-measurement techniques rely on the pattern formed when two light beams from the same source constructively and destructively interfere. Interferometers split light from a common source along two optical paths. The first path, known as the reference path, proceeds to the detector unimpeded. The second

path is sent through the MUT before interfering with the reference beam. The pattern produced on the optical detector is a series of peaks and nulls known as fringes. Figure 11 shows a schematic of a Mach-Zehnder interferometer which is commonly used for interferometric material measurements [46, 95] (for other interferometers see Refs. [19, 46, 89, 99]). The irradiance distribution detected by the camera is equal to the magnitude squared of the coherent sum of the two optical fields at the exit of the second beam splitter:

$$i = |u_1(t) + u_2(t)|^2 \tag{89}$$

where u_1 and u_2 represent the optical fields in the first (reference beam) and second arms of the interferometer, respectively. If the losses in the mirrors and beam splitters are assumed to be equal for both optical paths, then

$$u_1 = Ae^{\mathrm{j}\omega t}$$
$$u_2 = A\tau(n, \kappa; d)\, e^{\mathrm{j}\theta(n,\kappa;d)} e^{\mathrm{j}\omega t} e^{\mathrm{j}\phi} \tag{90}$$

where A is the amplitude of the field, $\tau \exp \mathrm{j}\theta$ is the complex field transmission coefficient (a function of n, κ, and the MUT thickness d), and ϕ is the controllable phase delay introduced by the adjustable mirror. Note that an expression for the field transmission coefficient can be found using electromagnetic theory. The transmission coefficient takes the form

$$\tau e^{\mathrm{j}\theta} = \frac{2\eta}{\mathrm{j}\eta^2 \sin\left(\frac{2\pi\eta}{\lambda}d\right) + 2\eta \cos\left(\frac{2\pi\eta}{\lambda}d\right) + \mathrm{j}\sin\left(\frac{2\pi\eta}{\lambda}d\right)} \tag{91}$$

where $\eta = n - \mathrm{j}\kappa$ is the complex index of refraction. Placing the above expression into magnitude and phase form is left to the reader. Substituting Eq. (90) into Eq. (89)

52

and simplifying produces

$$i\left(n, \kappa; \phi, d\right) = A^2 + A^2\tau^2 + 2A\tau \cos\left(\theta + \phi\right). \tag{92}$$

Note that if A and the thickness d are known, then only two measurements are necessary ($\phi = 0$ and $\pi/2$, for instance). If the field amplitude and the MUT thickness are unknown, then more measurements are needed [46, 99].

Like the other methods described above, interferometric material-measurement techniques are not perfect. MUT surface roughness and optical alignment are certainly issues that one must overcome when using an interferometric technique. Also, since interferometric material measurements are predominately transmission type measurements, the MUT must possess a low κ value (or be thin enough) to permit enough light through to noticeably interfere with the reference beam. This limitation can be overcome by redesigning the interferometer to operate in reflection mode. An example of such an instrument is a Kösters-prism interferometer. Details of its implementation can be found in Ref. [99]. Even with these limitations, interferometric techniques are very robust. They can be used to measure the thicknesses of thin films very accurately [99], to determine the index of refraction of ultrathin coal samples [89], to characterize gradient index materials (materials whose index of refraction changes along a direction) [95], and to measure the index of refraction of materials in wavelengths other than visible light (ultraviolet in this case) [19].

3.1.1.4 Ellipsometry.

Ellipsometry is the most powerful material-measurement technique of the methods described above. It makes use of the change in polarization state of light upon reflection in order to determine the material properties of the MUT. At the heart of ellipsometry is a device called an ellipsometer. While several different designs for
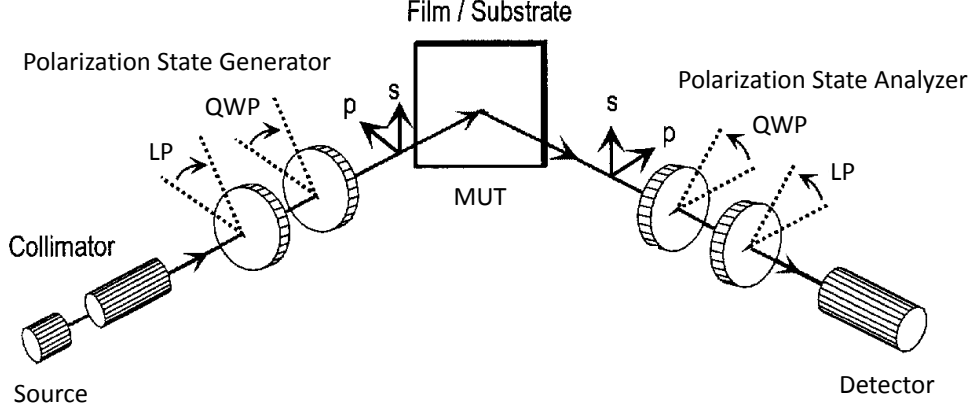
Figure 12. Schematic of a classic ellipsometer [127].

ellipsometers exist [14, 32, 73, 84, 118, 127, 133], the instrument described here is a classic ellipsometer. A classic ellipsometer consists of two arms—the polarization state generator (PSG) and the polarization state analyzer (PSA) [14, 25, 127]. The PSG consists of a light source followed by a linear polarizer (LP) and a quarter-wave plate (QWP) [14, 127]. The PSG is capable of producing four-independent polarization states [25]. The PSA consist of a QWP followed by a LP and an optical detector (essentially the mirror image of the PSG) [14, 127]. The MUT is placed in between the two arms of the ellipsometer (see Fig. 12). With this instrument, one is able to determine, unambiguously, the Mueller matrix of a sample. One can also determine, using an ellipsometer, the index of refraction (both the real and imaginary parts) and the thickness of the MUT (transmission ellipsometry).

In order to find the index of refraction of the MUT using an ellipsometer, a theoretical expression must be found for the irradiance received at the optical detector. This is best accomplished using Mueller matrices, i.e.,

$$S_0^{\text{out}} = \begin{bmatrix} 1 & 0 & 0 & 0 \end{bmatrix} \mathbf{P}(\zeta) \mathbf{Q}(\psi) \mathbf{M}(n, \kappa; \theta) \mathbf{Q}(\beta) \mathbf{P}(\alpha) \begin{bmatrix} S_0^{\text{in}} & 0 & 0 & 0 \end{bmatrix}^{\text{T}} \qquad (93)$$

where $\mathbf{P}$, $\mathbf{Q}$, and $\mathbf{M}$ are the Mueller matrices for a LP, a QWP, and reflection from a material, respectively (these matrices can be found in Ref. [14]). Here, ζ, ψ, β,

and α are angles measured with respect to the optic axis, θ is the angle of incidence (or reflection, since $\theta_i = \theta_r$) the light makes with the MUT, and S_0^{in} is the source irradiance. Note that with this ellipsometer, described mathematically in Eq. (93), 16-independent measurements are possible at each θ. If the source irradiance S_0^{in} is known, then only two of those 16 measurements are needed (else, three are required). This allows for the removal of the QWP's from the ellipsometer. It also allows the LP angles to be set equal ($\zeta = \alpha$). Making these simplifications and performing the matrix multiplication in Eq. (93) produces

$$
\begin{aligned}
S_0^{\text{out}} = \frac{S_0^{\text{in}}}{2} &\left[R_s + R_p + 2\left(R_s - R_p\right) \cos 2\alpha \right. \\
&\left. + \left(R_s + R_p\right) \cos^2 2\alpha + 2\text{Re}\left\{r_s r_p^*\right\} \sin^2 2\alpha \right].
\end{aligned}
\tag{94}
$$

Choosing two values for α ($\alpha = 0$ and $\pi/4$ are especially convenient) and a value for θ other than 0 or $\pi/2$ results in a system of nonlinear equations given by

$$
\begin{aligned}
S_0^{\text{out}}\left(\alpha = 0\right) &= 2 S_0^{\text{in}} R_s \\
S_0^{\text{out}}\left(\alpha = \pi/4\right) &= \frac{S_0^{\text{in}}}{2} \left[R_s + R_p + 2\text{Re}\left\{r_s r_p^*\right\} \right]
\end{aligned}
\tag{95}
$$

A two-dimensional Newton-Raphson search can be performed on Eq. (95) to find the index of refraction n and the coefficient of extinction κ. Note that although only two measurements are required to find n and κ all 16 could be used to provide an overdetermined system. Gauss-Newton nonlinear least squares could then be used to find the values for n and κ which best fit the measurements.

Ellipsometry suffers from two main sources of error. The first is optical alignment. In order for the ellipsometric measurement to be accurate, one must know precisely the orientation of the PSG and the PSA relative to the material's surface normal. This issue can be alleviated by operating the ellipsometer in trans-

mission mode [14, 25, 84, 133]; however, this limits MUT's to low κ or ultrathin materials. MUT surface roughness is less of an issue than the other techniques because pBRDF models can be incorporated into the theoretical ellipsometric expressions [103, 104, 123]. The second source of measurement error comes from the technique's use of polarization optics (LP's and QWP's). In the theoretical model for the received irradiance, these optical devices are assumed perfect. In actuality, a LP does allow light in the "blocked" polarization to pass, and a QWP does not exactly delay one polarization component a quarter-wave relative to the orthogonal component. In addition to these imperfections, LP's and QWP's are also dispersive (properties change with frequency); therefore, they must be changed (or theoretically accounted for) if one desires index-of-refraction values of the MUT at multiple wavelengths.

3.1.2 Remote-Sensing Techniques.

What separates remote-sensing material-measurement techniques from the laboratory methods described above is the inability to control certain variables. For instance, in remote sensing, transmission methods like minimum-deviation angle and interferometric techniques cannot be used because one cannot be certain of the observation geometry or that the MUT is translucent. Thus, one is relegated to a reflection-based technique. The Brewster's-angle technique could be used; however, not knowing the MUT geometry makes it difficult to ensure the MUT is illuminated with p-pol light. Ellipsometry presents the same problem as the Brewster's-angle technique, namely, the inability to control incident geometry and polarization state. On the other hand, it does permit the observer to control the measurement of the received polarization state via the PSA. Although not capable of 16-independent measurements like an ellipsometer, the PSA is capable of making 4-independent mea-
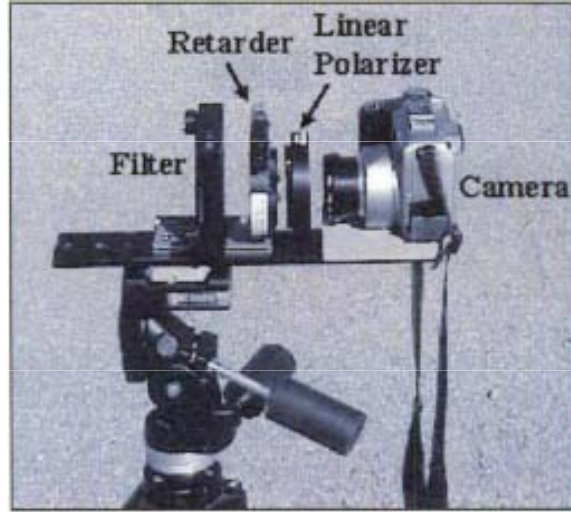
Figure 13. Photograph of the polarimeter used by Matchko and Gerhart [86].

surements, i.e., enough to deduce the Stokes vector. In remote sensing, this instrument, essentially one-half of an ellipsometer, is called a polarimeter. Described below are four remote-sensing applications which use this instrument. The first discusses methods for determining the DOP and AOP from passive polarimetric images, the second and third are passive material-classification algorithms, and the last is a passive material-characterization technique.

3.1.2.1 DOP and AOP Measurements.

The key to measuring the DOP and AOP of light reflected from an object is to determine the four Stokes parameters embedded in the polarimetric images. Once the Stokes parameters have been determined, the DOP and AOP can be found by using Eqs. (40) and (41), respectively. This research deals predominately with the DOP as a means of finding the index of refraction; therefore, not much emphasis is placed on measuring the AOP. Note that in future research on this subject, the AOP will be investigated. It provides a means of passively determining observation geometry [85].

Three papers are highlighted in this section on passive DOP and AOP measure-

ments. The first two are authored by Matchko and Gerhart [85, 86]. In the first paper, the authors measure the DOP and AOP of skylight [85]. In the second, the authors develop a technique to measure the DOP and AOP of an object using a commercial off-the-shelf (COTS) digital camera [86]. The instrument (polarimeter) used by the authors is shown in Fig. 13. It consists of a filter, retarder (ideally, a QWP), LP, and a digital camera. In order to find the Stokes parameters, four irradiance measurements are made: (1) LP at $0°$—I_1, (2) LP at $90°$—I_2, (3) LP at $45°$—I_3, and (4) retarder at $0°$ and LP at $45°$—I_4. Note that authors' polarimeter allowed for the precise movement of the retarder into and out of the optical path. This is why irradiance measurements (1)–(3) do not specify a retarder location. The Stokes parameters are related to the above irradiance measurements by

$$
\begin{aligned}
S_0 &= I_1 + I_2 \\
S_1 &= I_1 - I_2 \\
S_2 &= 2I_3 - S_0 \\
S_3 &= \frac{2I_4 - S_0 - S_2 \cos \epsilon}{\sin \epsilon}
\end{aligned}
\tag{96}
$$

where ϵ is the phase difference introduced by the retarder [86]. Note the ϵ is ideally $\pi/2$. It was necessary for the authors to include a variable retardance because they sought the Stokes parameters at wavelengths other than the optimal (tuned) wavelength of the retarder (see Ref. [86] for more details). Performing the above calculations for each pixel and using Eqs. (40) and (41), the authors formed DOP and AOP images of a vehicle under natural illumination (see Fig. 14). Note that the edges of the vehicle are clearly visible in the DOP image. The authors attribute this to the fact that at the time of day the images were taken, sunlight incident on the vehicle's panels was predominately scattered toward the ground. The vehicle's edges, being rounded, allowed sunlight to be scattered toward the detector. This explains
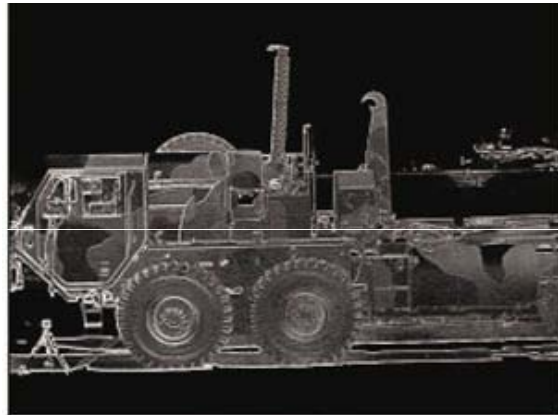
(a) P at 12:00
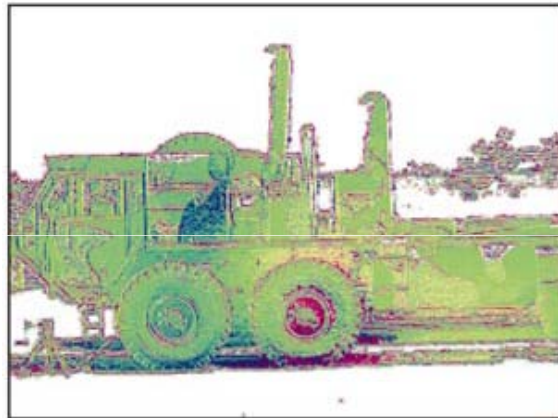
(b) ψ at 12:00

Figure 14. Measured DOP and AOP images of a scene published by Matchko and Gerhart [86].

the contrast difference between the vehicle's panels and edges in the DOP image [85]. Despite this, different paints are clearly visible in the image. Before concluding, it is worth noting one final observation made by the authors. The authors, along with Coulson and Thilak *et al.*, note that under natural sunlit conditions, the amount of reflected circularly polarized light is insignificant [27, 85, 123]. This implies that the fourth Stokes parameter (as well as the fourth row and fourth column of Mueller matrices) can be removed. This simplification is used throughout this research.

The third and final paper discussed in this section is research published by Goudail *et al.* [51]. The purpose of the paper was to demonstrate target detection using a liquid-crystal-based polarimeter. While Goudial *et al.* dedicate most of their paper to target detection, the section describing the workings of their polarimeter is interesting and relevant. The polarimeter used by Goudail *et al.* for their research consists of a filter, two liquid crystal retarders, a LP, and a camera. Goudail *et al.* determined the Stokes parameters of a scene by applying Stokes vectors/Mueller matrices, namely,

$$\boldsymbol{S}_{\text{out}} = \mathbf{M}_{\text{POL}}\mathbf{M}_{\text{R}}\left(\delta_1\right)\mathbf{M}_{\text{R}}\left(\delta_2\right)\boldsymbol{S}_{\text{in}} = \mathbf{M}_{\text{global}}\boldsymbol{S}_{\text{in}} \tag{97}$$

where $\mathbf{M}_{\text{POL}}$ is the Mueller matrix for a LP and $\mathbf{M}_{\text{R}}\left(\delta\right)$ is the Mueller matrix for a retarder with retardance δ [51]. Note that in this polarimeter, all elements remain stationary. The independent polarization state measurements are generated by a series of controllable phase differences introduced by the liquid crystal retarders. The irradiance detected at the camera is

$$I = S_0^{\text{out}} = A\left(\delta_1, \delta_2\right)S_0^{\text{in}} + B\left(\delta_1, \delta_2\right)S_1^{\text{in}} + C\left(\delta_1, \delta_2\right)S_2^{\text{in}} + D\left(\delta_1, \delta_2\right)S_3^{\text{in}} \tag{98}$$

where A, B, C, and D are the elements of the first row of $\mathbf{M}_{\text{global}}$. As stated above, 4 measurements are required to unambiguously resolve the Stokes parameters. How-
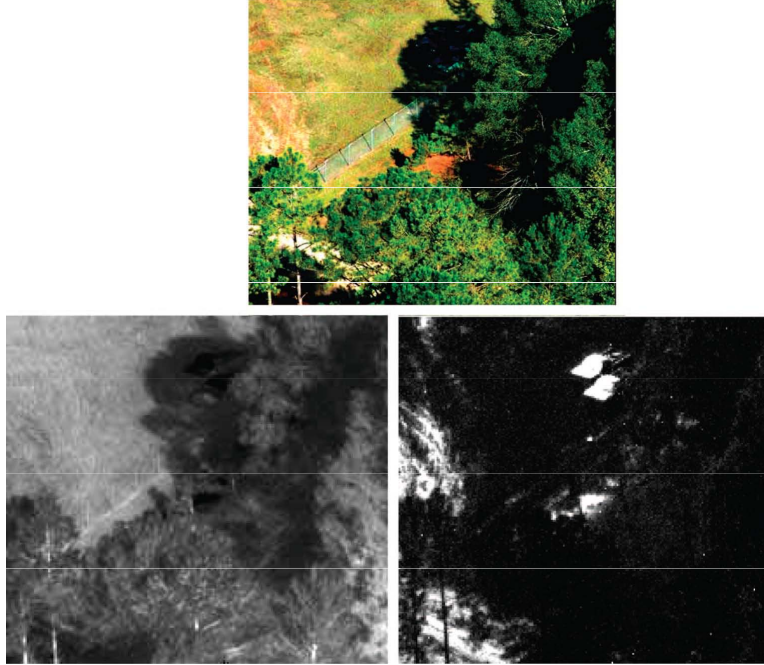
Figure 15. Visible image of two trucks in the shade (top), long-wave IR intensity image (bottom left), and long-wave IR polarization image (bottom right). Note that the trucks are visible in the polarimetric image [133].

ever, since the design of the authors' polarimeter makes collecting polarimetric images simple (does not require elements to be physically rotated), collecting more than four measurements is an easy task. Generalizing the above equation to multiple irradiance measurements produces

$$
\begin{bmatrix} I_1 \\ I_2 \\ \vdots \\ I_N \end{bmatrix} = \begin{bmatrix} A_1 & B_1 & C_1 & D_1 \\ A_2 & B_2 & C_2 & D_2 \\ \vdots & \vdots & \vdots & \vdots \\ A_N & B_N & C_N & D_N \end{bmatrix} \begin{bmatrix} S_0^{\text{in}} \\ S_1^{\text{in}} \\ S_2^{\text{in}} \\ S_3^{\text{in}} \end{bmatrix} \tag{99}
$$

where Eq. (99) is best solved using linear least squares when $N > 4$. The authors note that N should be at least 8 to ensure good results for the Stokes parameters [51]. In the remainder of the paper, the authors apply their polarimeter to target detection. While not relevant to this work, a few words on target detection using polarimetric

61

imagery are warranted. Polarimetric target detection is based on the premise that natural objects (tree canopies, for instance) tend to be diffuse scatterers. While manmade objects, like vehicles, aircraft, etc., tend to scatter polarized light. An example of target detection using passive polarimetric imagery is shown in Fig. 15. Note that the two trucks, hidden under the canopy, are visible in the polarimetric image. For more on polarimetric target detection see Ref. [51].

3.1.2.2 Material Classification.

Material classification differs from material characterization in one aspect—the inverse problem. Whereas material characterization requires one to solve forward and inverse problems, material classification only requires the solution to the forward problem. In material classification, a rule is deduced from the solution of the forward problem which discriminates one type of material from another. The parameter on which the rule is based is then measured and a choice is made between two (or more) possible outcomes based on the value of the measured parameter. In the two papers discussed below, dielectric materials are distinguished from metals based on the measured polarization Fresnel ratio (discussed below) and DOP, respectively.

In the first paper by Lawrence B. Wolff, the author develops a technique to classify dielectric and metallic objects in a scene using the polarization Fresnel ratio (also known as the Fresnel ratio) [141]. The polarization Fresnel ratio is defined as $F_\perp/F_\parallel$ where $F_\perp$ and $F_\parallel$ are the s- and p-pol Fresnel reflectances, respectively (using the author's notation). The author notes that a Fresnel ratio of greater than 2.0 is indicative of a dielectric surface; whereas, a Fresnel ratio of less than 2.0 is indicative of a metallic surface [141]. This simple thresholding scheme forms the basis of the classification algorithm.

Wolff models light scattered from a material surface using the microfacet model.

The microfacet model stipulates that a rough surface is composed of a large collection of randomly distributed facets each scattering light in the manner postulated by Fresnel's equations [103, 104]. Thus, light scattered from a surface is a combination of the following phenomena: (1) light waves which specularly reflect off a planar interface with the surface, significantly larger than the wavelength, a single time; (2) light waves which go through at least two specular reflections amongst multiple microfacets; (3) light waves which penetrate the top layer of the material surface, multiply refract, and then are reflected back out (volumetric scattering); and (4) light waves which diffract from interfaces with surface detail about the same size or smaller than the wavelength of the incident light wave [141]. Note that mechanism (1) is the specular component of reflection and mechanisms (2)–(4) combine to form the diffuse component of reflection (assumed to be unpolarized) [141]. Assuming unpolarized incident light and observation in the specular plane, Wolff's model for the received irradiance when viewed through a LP at angle θ relative to the specular plane (see Fig. 16) is

$$I(\theta) = \frac{1}{2}I_d + \frac{F_\parallel \cos^2\theta + F_\perp \sin^2\theta}{F_\parallel + F_\perp}I_s \tag{100}$$

where I_s and I_d are the specular and diffuse irradiances, respectively. Note that Eq. (100) sinusoidally varies between a maximum received irradiance value $I_{\max}$ when $\theta = \pi/2$ and a minimum received irradiance value $I_{\min}$ when $\theta = 0$:

$$\begin{aligned} I_{\max} &= \frac{1}{2}I_d + \frac{F_\perp}{F_\parallel + F_\perp}I_s \\ I_{\min} &= \frac{1}{2}I_d + \frac{F_\parallel}{F_\parallel + F_\perp}I_s \end{aligned}. \tag{101}$$

The Fresnel ratio is formed by algebraically manipulating these two equations such
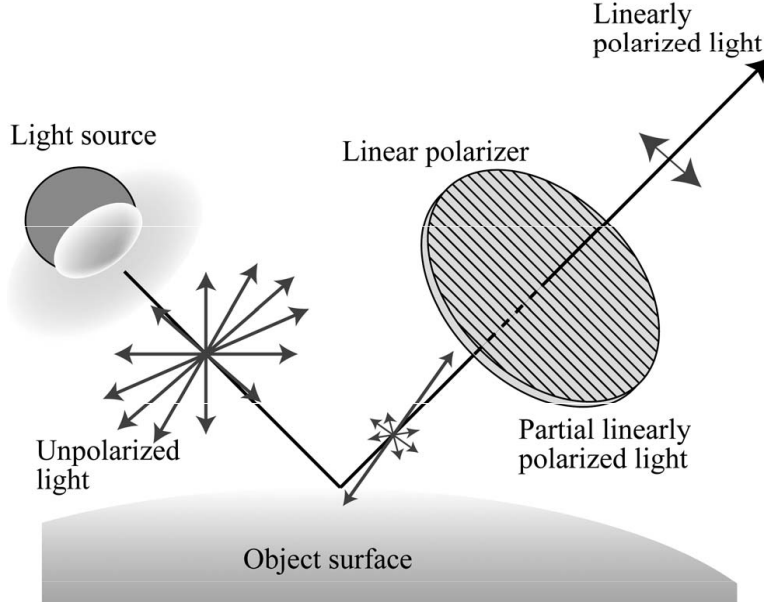
Figure 16. **Material classification geometry used by Wolff and Tominaga and Kimachi [126].**

that [141]

$$\frac{F_\perp}{F_\parallel} = \frac{I_{\max} - I_d/2}{I_{\min} - I_d/2}. \tag{102}$$

Wolff now makes two assumptions: (1) the specular component of reflection is far larger than the diffuse component of reflection (this implies $I_{\max} \gg I_d$) and (2) $I_{\min} \gg I_d$. Applying these assumptions to Eq. (102) produces Wolff's Fresnel ratio approximation, i.e.,

$$\frac{F_\perp}{F_\parallel} \approx \frac{I_{\max}}{I_{\min}}. \tag{103}$$

The author notes that this approximation always underestimates the true Fresnel ratio. This is especially evident near Brewster's angle when $F_\parallel$ for dielectric surfaces approaches zero. He also notes that the accuracy of the approximation depends on scattered light in which the specular component dominates. Note that this is a requirement for all polarimetric material-classification or characterization algorithms including the one developed in this research. Classification is achieved using Wolff's algorithm by first experimentally measuring $I_{\max}$ and $I_{\min}$. This is accomplished
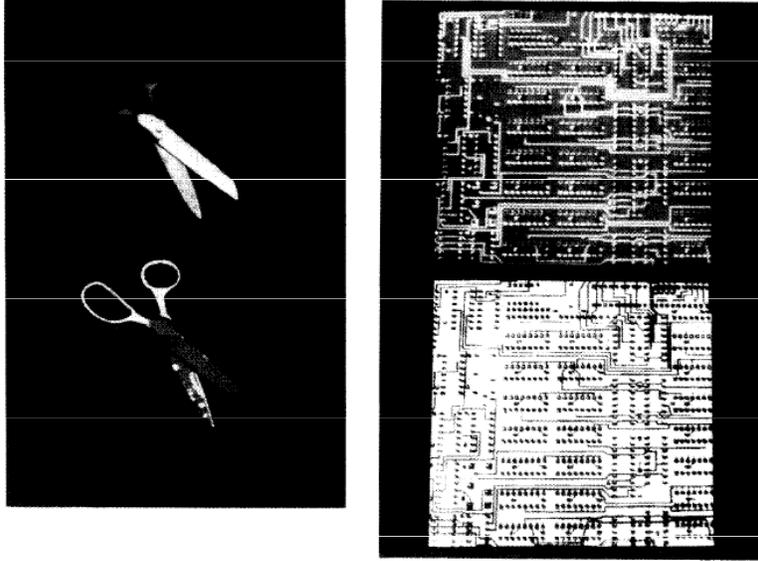
Figure 17. Results of Wolff's material-classification algorithm. The figure on the left is a pair of scissors. Clearly evident are the dielectric handles (bottom photo) and metallic blades (top photo). Also evident are the spots of corrosion (rust) on the blades (bottom photo). The figure on the right is a circuit board. The top picture contains the part of the circuit board classified metallic; the bottom picture contains the part of the circuit board classified as dielectric [141].

by making 4-irradiance measurements with the polarizer at 0°, 45°, 90°, and 135°, respectively. A sine curve is then fit to these values for each pixel in the image. $I_{\max}$ and $I_{\min}$ are then readily deduced. Lastly, Eq. (103) is applied to each pixel in the image and the following test applied

$$
\begin{aligned}
I_{\max}/I_{\min} \leq 2.0 \quad &\text{Metallic} \\
I_{\max}/I_{\min} > 2.0 \quad &\text{Dielectric}
\end{aligned}
\tag{104}
$$

Wolff concludes his paper by applying his classification technique to several different objects. Two of his results are shown in Fig. 17. The figure on the left is a pair of scissors. Note that the metallic blades (top photo) and dielectric handles (bottom photo) of the scissors are clearly visible. Note also that the algorithm correctly classifies corrosion (rust) on the blades as a dielectric (spots on the bottom photo). The figure on the right is a printed circuit board. The top picture contains the elements

of the circuit board which are classified as a metal; the bottom picture contains the elements of the circuit board which are classified as a dielectric [141].

The second and final material-classification paper presented is by Tominaga and Kimachi [126]. The authors use the DOP to discriminate dielectric and metallic objects in a scene. They accomplish this by observing the shape of the two-dimensional DOP surface (authors refer to it as a DOP map) around the specular highlight point of the material. The authors note that the DOP map becomes convex for dielectric materials and concave, or nearly flat, for metals (see Ref. [126] for detailed explanation of this phenomena). The concavity or convexity (i.e., the decision rule) of the DOP map is determined by calculating the second derivative (i.e., Laplacian) of the DOP map at the specular highlight point or by fitting a quadratic surface to the DOP map and noting the sign of the second-order coefficient. If the second derivative or the second-order fitted coefficient is positive, then the surface is categorized as a metal; else, the surface is categorized as a dielectric [126].

Tominaga and Kimachi assume the same measurement geometry as Wolff (see Fig. 16). Their model for received light is very similar as well, i.e.,

$$
\begin{aligned}
I\left(x,y,\theta\right) = {} & T_n I_d\left(x,y\right) \\
& + T_p \frac{F_\parallel\left(x,y\right)\sin^2\left(\theta-\theta_0\right) + F_\perp\left(x,y\right)\cos^2\left(\theta-\theta_0\right)}{F_\parallel\left(x,y\right) + F_\perp\left(x,y\right)} I_s\left(x,y\right)
\end{aligned}
\tag{105}
$$

where θ_0 denotes the direction of the s-pol plane, x and y are pixel coordinates, and T_p and T_n are the transmittances of the polarizer for linearly polarized and unpolarized light, respectively (ideally, $T_n = T_p/2$). The symbols I_d, I_s, $F_\parallel$, and $F_\perp$ have been defined previously. Note that Eq. (105) varies sinusoidally with a maximum $I_{\max}\left(x,y\right)$

at $\theta = \theta_0, \theta_0 + \pi$ and a minimum $I_{\min}(x, y)$ at $\theta = \theta_0 \pm \pi/2$ given by

$$\begin{aligned}
I_{\max}(x, y) &= \frac{F_\perp(x, y)}{F_\parallel(x, y) + F_\perp(x, y)} T_p I_s(x, y) + T_n I_d(x, y) \\
I_{\min}(x, y) &= \frac{F_\parallel(x, y)}{F_\parallel(x, y) + F_\perp(x, y)} T_p I_s(x, y) + T_n I_d(x, y)
\end{aligned}. \tag{106}$$

The difference between $I_{\max}(x, y)$ and $I_{\min}(x, y)$ equals the irradiance of received light which is completely polarized. The DOP can now be found by dividing this quantity by the total received irradiance, namely, (using the authors' notation)

$$\rho(x, y) = \frac{I_{\max}(x, y) - I_{\min}(x, y)}{I_{\max}(x, y) + I_{\min}(x, y)}. \tag{107}$$

Classification using Tominaga and Kimachi's algorithm begins in precisely the same manner as Wolff's, i.e., experimentally finding $I_{\max}(x, y)$ and $I_{\min}(x, y)$. Once that is achieved, Eq. (107) is applied to each pixel in the image, thus forming the DOP map. The following test is then applied

$$\begin{aligned}
\nabla^2 \rho(x, y)|_{\substack{x=x_0 \\ y=y_0}} &\geqslant 0 \quad \text{Metallic} \\
\nabla^2 \rho(x, y)|_{\substack{x=x_0 \\ y=y_0}} &< 0 \quad \text{Dielectric}
\end{aligned} \tag{108}$$

where (x_0, y_0) is the pixel coordinate corresponding to the specular highlight point.

Figure 18 shows some of the measurement results for the Tominaga and Kimachi material-classification algorithm. The top photographs show the MUT's—on the left is vinyl, on the right is copper. The bottom figures are the DOP maps for each MUT at 30° and 60° incident angles. The white dot in each figure marks the specular highlight point. The measured second derivatives at that point are −0.0072 and −0.0015 for vinyl and 0.0022 and 0.0021 for copper [126]. Both materials are classified correctly.
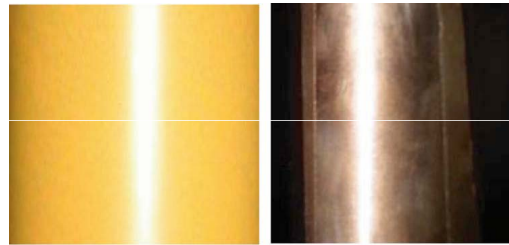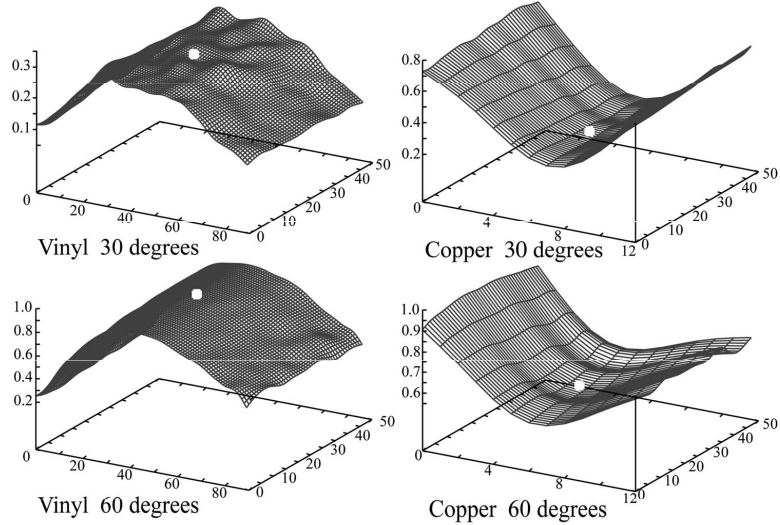
Figure 18. Results of Tominaga and Kimachi's material-classification algorithm. The top photographs show the materials classified using the algorithm. The image on the left is vinyl; the image on the right is copper. The bottom plots are the DOP maps for each material at 30° and 60° incident angles. The white dot in each plot is the specular highlight point [126].
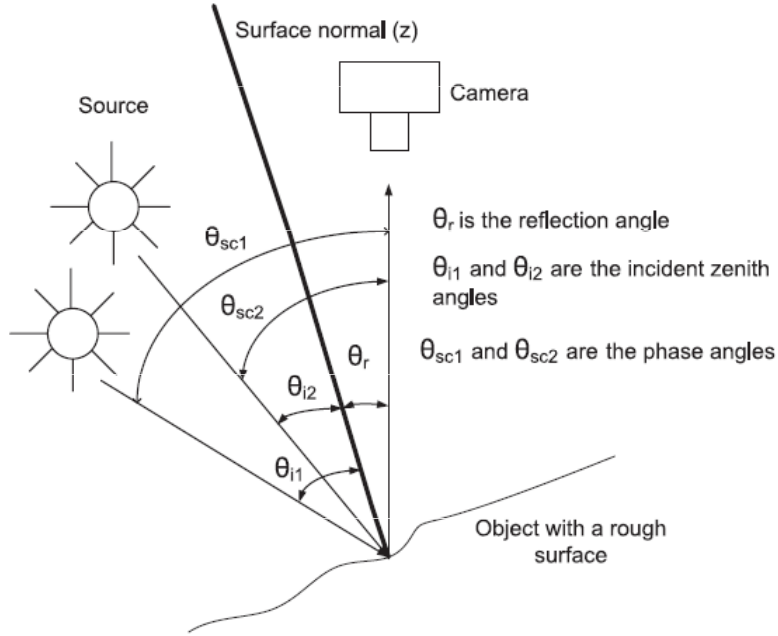
Figure 19. Measurement geometry used by Thilak *et al.* [123].

3.1.2.3 Material Characterization.

One of the few, if only, passive remote-sensing material-characterization papers is a paper by Thilak *et al.* [123]. The paper introduces a method to find the complex index of refraction and reflection angle of MUT's from DOP measurements made at several different incident angles. The authors' measurement geometry is shown in Fig. 19. The object is modeled using the Priest and Meier pBRDF (discussed in more detail in the next section) [104]. The authors make the following assumptions: (1) the object's position remains fixed; (2) the position of the unpolarized illumination source changes between measurements; (3) the source position with respect to the camera is known, i.e., θ_{sc1} and θ_{sc2} in Fig. 19 are known; (4) observation is restricted to the specular plane; and (5) in accordance with the findings of [27, 85], the amount of circularly polarized light in the reflected signal is negligible [123].

As stated above, the authors model scattering from the MUT using the Priest and

Meier pBRDF [104]. The form of this pBRDF is

$$f_{jl}\left(\theta_i, \theta_r, \phi\right) = \frac{1}{(2\pi)\left(4\sigma^2\right)\cos^4\theta} \frac{\exp\left[-\tan^2\theta/\left(2\sigma^2\right)\right]}{\cos\theta_r \cos\theta_i} m_{jl}\left(\theta_i, \theta_r, \phi\right) \qquad (109)$$

where f_{jl} is the element in the jth row, l^{th} column of the Mueller matrix pBRDF, m_{jl} is the element in the jth row, l^{th} column of the Mueller matrix for reflection [Eq. (55)], θ is the angle of orientation of microfacets relative to the mean surface normal, ϕ is the azimuth angle, and σ is the surface roughness parameter [123]. Note that since the amount of circularly polarized light in the reflected signal is assumed negligible, $j, l = 0, 1, 2$. The angle θ is related to the angles of incidence and reflection by [123]

$$\theta = \cos^{-1}\left(\frac{\cos\theta_i + \cos\theta_r}{2\cos\beta}\right) \qquad (110)$$

where

$$\cos 2\beta = \cos\theta_r \cos\theta_i + \sin\theta_r \sin\theta_i \cos\phi. \qquad (111)$$

Recall that for scattering in the specular plane $\phi = \pi$. This simplifies Eqs. (110) and (111) to

$$\theta = \left(\theta_r - \theta_i\right)/2 \quad \beta = \left(\theta_r + \theta_i\right)/2. \qquad (112)$$

Since the source is unpolarized, the scattered radiance is (using the authors' notation)

$$\begin{bmatrix} s_0^r \\ s_1^r \\ s_2^r \end{bmatrix} = \begin{bmatrix} f_{00} & f_{10} & 0 \\ f_{10} & f_{00} & 0 \\ 0 & 0 & f_{22} \end{bmatrix} \begin{bmatrix} 1 \\ 0 \\ 0 \end{bmatrix} = \begin{bmatrix} f_{00} \\ f_{10} \\ 0 \end{bmatrix}. \qquad (113)$$

Using Eq. (40), the DOP of the scattered light becomes

$$P = \frac{f_{10}}{f_{00}} = \frac{R_s - R_p}{R_s + R_p} \qquad (114)$$

70

where R_s and R_p are the s- and p-pol Fresnel reflectances, respectively. Substituting in R_s and R_p [given in Eqs. (50) and (53)] and Eq. (112) into Eq. (114) and simplifying produces the desired result

$$P\left(n, \kappa, \beta\right) = \frac{2A\sin^2\beta \cos\beta}{A^2\cos^2\beta + \sin^4\beta + B^2\cos^2\beta}$$

$$A = \sqrt{\frac{\sqrt{C}+D}{2}} \quad B = \sqrt{\frac{\sqrt{C}-D}{2}}$$

$$C = 4n^2\kappa^2 + D^2 \tag{115}$$

$$D = n^2 - \kappa^2 - \sin^2\beta$$

where the expressions for A, B, C, and D have been restated for convenience. Equation (115) is the solution to the forward problem in the authors' material-characterization algorithm [123].

The authors' inverse problem, the step necessary to find the desired parameters, is a two-step process [123]. In the first step, the authors use nonlinear least squares to find the values of n and κ which best fit Eq. (115) to DOP measurements. The angle β is assumed known:

$$P_j\left(n, \kappa\right) = \frac{2A_j\sin^2\beta_j \cos\beta_j}{A_j^2\cos^2\beta_j + \sin^4\beta_j + B_j^2\cos^2\beta_j} \tag{116}$$

where j corresponds to a measurement number, $j \in [1, 2, \cdots, T]$. Obviously T must be greater than or equal to 3 for a unique solution to exist. In the second step, the n and κ values found in the first step are incorporated into Eq. (115). The value of the reflection angle θ_r is then found (via nonlinear least squares) using the DOP measurements from the first step:

$$P_j\left(\theta_{ij}, \theta_r\right) = \frac{2A_j\sin^2\left(\frac{\theta_{ij}+\theta_r}{2}\right)\cos\left(\frac{\theta_{ij}+\theta_r}{2}\right)}{A_j^2\cos^2\left(\frac{\theta_{ij}+\theta_r}{2}\right) + \sin^4\left(\frac{\theta_{ij}+\theta_r}{2}\right) + B_j^2\cos^2\left(\frac{\theta_{ij}+\theta_r}{2}\right)}. \tag{117}$$

71

Table 1. "Low-noise" simulation results for copper published by Thilak *et al.* The true index of refraction is $n = 0.314$ and $\kappa = 3.544$ while the true reflection angle is $60°$. The results are obtained from 500 Monte Carlo trials [123].

Number of Measurements	$\hat{n}$	RMSE$_{\hat{n}}$	$\hat{\kappa}$	RMSE$_{\hat{\kappa}}$	$\hat{\theta}_r$ (°)	RMSE$_{\hat{\theta}_r}$
3 $(55° - 65°)$	2.479 ± 0.301	4.052	7.837 ± 0.595	8.254	60.039 ± 0.008	0.098
5 $(50° - 70°)$	1.474 ± 0.254	3.117	5.734 ± 0.482	5.911	59.823 ± 0.120	1.382
10 $(35° - 80°)$	0.421 ± 0.075	0.866	3.768 ± 0.164	1.822	59.695 ± 0.130	1.508

In order to verify the technique, the authors perform simulations as well as laboratory measurements. The simulated data sets are formed by using Eq. (115) with specific values for n, κ, and θ_r and a sequence of values for θ_i. Gaussian noise is then added to the data sets to simulate measurement noise. Two noise levels are considered—a "low-noise" scenario (defined to be Gaussian noise with a variance of 0.1% of the maximum DOP value) and a "high-noise" scenario (defined to be Gaussian noise with a variance of 1% of the maximum DOP value) [123]. Tables 1 and 2 show the results of the algorithm for a simulated copper $(0.314 - j3.554)$ surface—Table 1 is the "low-noise" scenario and Table 2 is the "high-noise" scenario. The authors note that the algorithm occasionally converges to physically unrealizable values, i.e., $n, \kappa < 0$, $\theta_r < 0°$, or $\theta_r > 90°$ [123]. When this occurs, the results are ignored and the algorithm is restarted. Note that the technique performs well.

Lastly, the authors verify the method experimentally. The authors use a polarimeter to form Stokes images. A single Stokes image is formed from ten polarimetric images collected with the polarizer rotated in $15°$ steps for each image [123]. The DOP values are calculated by averaging at least 100×100 pixels in the Stokes images [123]. Shown below is the published result for roughened copper (Table 3 and Fig. 20). More simulation and measurement results are available in Ref. [123].

Table 2. "High-noise" simulation results for copper published by Thilak *et al.* The true index of refraction is $n = 0.314$ and $\kappa = 3.544$ while the true reflection angle is 60°. The results are obtained from 200 Monte Carlo trials [123].

Number of Measurements	$\hat{n}$	RMSE$_{\hat{n}}$	$\hat{\kappa}$	RMSE$_{\hat{\kappa}}$	$\hat{\theta}_r$ (°)	RMSE$_{\hat{\theta}_r}$
3 (55° − 65°)	7.865 ± 0.826	9.610	15.669 ± 1.353	15.545	59.904 ± 0.195	1.409
5 (50° − 70°)	6.918 ± 0.964	9.580	13.321 ± 1.361	13.832	59.701 ± 0.339	2.461
10 (35° − 80°)	3.319 ± 0.822	6.637	8.031 ± 1.177	9.579	59.815 ± 0.210	1.525
19 (35° − 80°)	1.310 ± 0.449	3.378	5.373 ± 0.719	5.486	59.281 ± 0.776	5.629

Table 3. Measurement results for copper published by Thilak *et al.* The true index of refraction is $n = 0.4$ and $\kappa = 2.95$. The angle of incidence is varied in steps of 5° [123].

Angle of Incidence (°)	Reflection Angle (°)	$\hat{n}$	$\hat{\kappa}$	$\hat{\theta}_r$ (°)
35 − 70	60	0.54	3.19	59.51
35 − 70	55	0.53	3.26	54.63
35 − 70	50	0.53	3.32	49.62
35 − 70	45	0.51	3.37	44.85
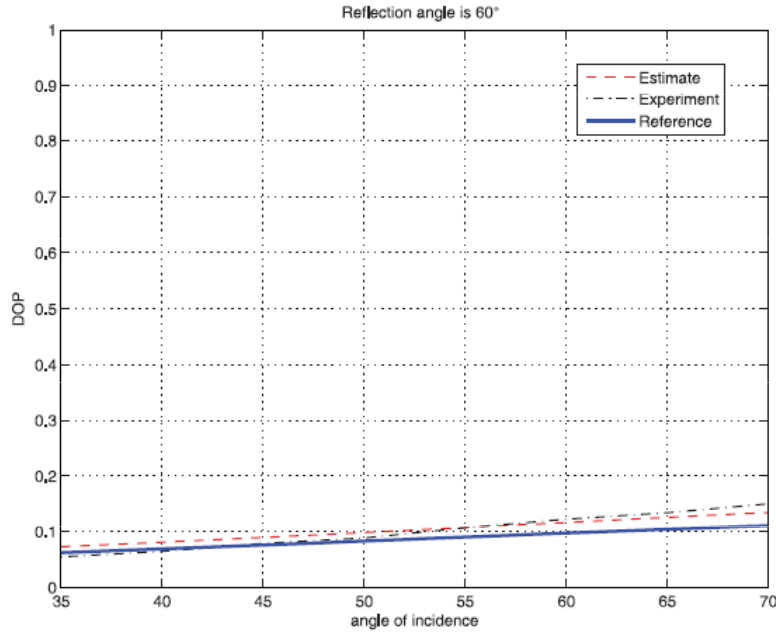
Figure 20. Measurement results for copper published by Thilak *et al.* [123].

3.1.2.4 Other Papers.

A couple of other papers are worth mentioning before proceeding to the pertinent literature on BRDF's. The first is a paper by Terrier *et al.* in which an algorithm is developed which discriminates objects in a scene based on their roughness [120]. The technique uses a polarimetric version of the Torrance and Sparrow BRDF [128] (discussed below) to predict the scattered Stokes parameters from a material surface. The index of refraction of the material is estimated first by minimizing the difference between the measured S_2/S_1 and the theoretical S_2/S_1 at multiple incident angles via nonlinear least squares. Lastly, the surface roughness is estimated (again via nonlinear least squares) using the measured and theoretical specular component of reflection. The technique is very similar in nature to that of Thilak *et al.*; however, the technique utilizes a more accurate pBRDF (discussed below) as well as an active source (i.e., polarization state of source is controlled).

The other is a paper by Hong in which a technique is proposed to estimate the refractive index of specular surfaces at a given view angle by direct inversion of Fresnel's equations [60]. Note that in general R_s and R_p are transcendental expressions of η; however, under specific circumstances (see Ref. [60]) closed-form analytical expressions can be found for n and κ in terms of R_s and R_p. The author uses these expressions along with a related approximation developed in the paper to estimate the index of refraction of water from ultraviolet (200 nm) to microwave (18.75 cm) wavelengths. Details can be found in Ref. [60].

3.2 BRDF's

This section deals with three BRDF's each one building on the one that preceded it. The last BRDF introduced in this section is the one chosen for this research. Note that many other BRDF's exists (see Refs. [3, 42, 87, 92, 116]). The three described
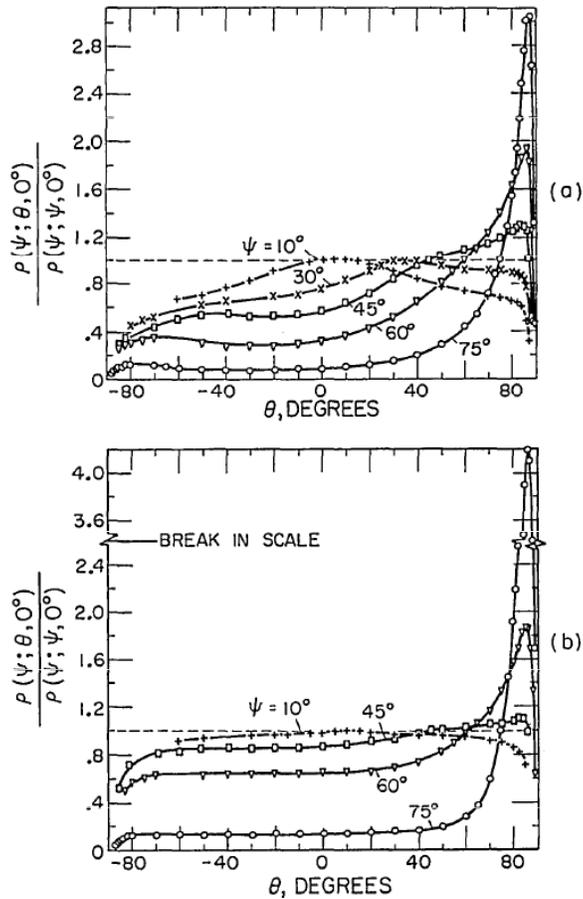
Figure 21. **Measurement results for aluminum and magnesium oxide ceramic at** $\lambda = 0.5$ μm **published by Torrance and Sparrow. The top subfigure shows the results for aluminum,** $\sigma_m = 1.3$ μm. **The bottom subfigure shows the results for magnesium oxide ceramic,** $\sigma_m = 1.9$ μm. **Note that the values for reflectance are normalized to the reflectance value at the specular angle. Off-specular peaks occur when the plotted values become greater than unity; they are visible at angles greater than** $40°$ **[128].**

below are the most relevant to this research.

3.2.1 Torrance and Sparrow.

Torrance and Sparrow's 1967 paper is the seminal paper for GO BRDF's [128]. The authors were motivated to describe mathematically the scattering phenomena known as off-specular peaks. An off-specular peak is a maximum in reflected irradiance which occurs at an angle larger than the specular angle [128]. Off-specular peaks commonly appear in measured data for both metallic and dielectric surfaces
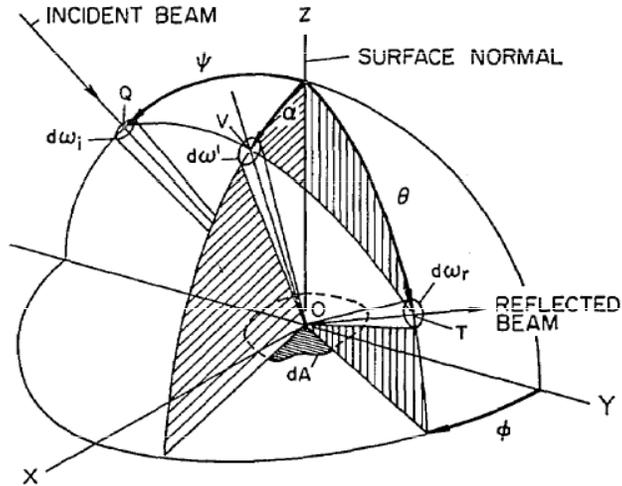
Figure 22. Scattering geometry used by Torrance and Sparrow. The figure shows a light beam (incident at angle ψ and of solid angle $d\omega_i$) incident on a small area of material dA. The reflected light, scattered from microfacets whose normals are inclined at angle α from the z axis, is scattered at polar angle θ and azimuth angle ϕ [128].

(see Fig. 21). Empirical evidence predicts their appearance when the rms surface roughness σ_m is on the order of or greater than the wavelength of the incident field, i.e., $\sigma_m/\lambda \geq 1$ [128]. Note that electromagnetic theory states that all scattering occurs in the specular direction for surfaces much larger than the wavelength of the incident field; therefore, this phenomenon must be related to surface roughness. Researchers, prior to Torrance and Sparrow, understood this; however, none could formulate an expression to accurately model off-specular peaks. BRDF's (prior to Torrance and Sparrow) either predicted infinite scattered irradiance as the incident angle approached grazing or did not predict the feature at all [128]. Needless to say, the work of Torrance and Sparrow remedied this problem.

Torrance and Sparrow's initial premise is that light reflected from a rough surface is composed of two components—a specular component and a diffuse component, i.e.,

$$dN_r\left(\psi;\theta,\phi\right) = dN_{r,s}\left(\psi;\theta,\phi\right) + dN_{r,d}\left(\psi\right) \tag{118}$$

where ψ is the angle of incidence (source angle), θ is the angle of observation (re-

flection angle), and ϕ is the azimuth angle (rotational symmetry is assumed). The Torrance and Sparrow scattering geometry is shown in Fig. 22. Note that the authors' notation is used throughout. In accordance with the microfacet surface model (on which the Torrance and Sparrow BRDF is based), the specular component of the scattered irradiance is the result of specular reflections (obeying Fresnel's equations) from a large number of small mirror-like facets which compose the surface [103, 104, 128]. These facets are assumed to distributed symmetrically about the mean surface normal according to a slope distribution function [104]. Torrance and Sparrow utilize Gaussian-shaped distribution, namely,

$$P\left(\alpha\right) = b \exp\left(-c^2\alpha^2\right) \tag{119}$$

where α is the angle between the facet surface normal and the mean surface normal and b and c are fit parameters. Torrance and Sparrow's expression for the specular component of the scattered irradiance is

$$dN_{r,s}\left(\psi; \theta, \phi\right) = \left(f N_i d\omega_i / 4\right) F\left(\psi', \hat{n}\right) \left[G\left(\psi_p, \theta_p\right)/\cos\theta\right] P\left(\alpha\right). \tag{120}$$

where f is the area of a facet, N_i is the incident flux, $d\omega_i$ is the solid angle subtended

by the source, and F is the Fresnel reflectance (either s- or p-pol). Also in Eq. (120),

$$\psi' = \frac{1}{2}\cos^{-1}\left(\cos\theta\cos\psi - \sin\theta\sin\psi\cos\phi\right)$$

$$\alpha = \cos^{-1}\left(\cos\psi\cos\psi' + \sin\psi\sin\psi'\cos\beta_1\right)$$

$$\psi_p = \tan^{-1}\left(\cos\beta_2\tan\psi\right)$$

$$\theta_p = \psi_p + 2\alpha \qquad\qquad . \qquad (121)$$

$$\beta_1 = \sin^{-1}\left(\sin\phi\sin\theta/\sin 2\psi'\right)$$

$$\beta_2 = \pi - \sin^{-1}\left(\sin\beta_1\sin\psi'/\sin\alpha\right)$$

$$\hat{n} = n - \mathrm{j}\kappa$$

The only term not formally defined in Eq. (120) is the function G. Its significance is discussed later. The diffuse component of the scattered irradiance arises from multiple reflections among facets and from internal scattering (volumetric scattering) [128]. The form chosen by Torrance and Sparrow for the diffuse component of the scattered irradiance is

$$dN_{r,d}\left(\psi\right) = aN_i\cos\psi \qquad (122)$$

where a is a fit parameter. Putting Eqs. (120) and (122) together produces the Torrance and Sparrow BRDF, i.e.,

$$\begin{aligned}\rho &= \frac{dN_r\left(\psi;\theta,\phi\right)}{N_i\cos\psi d\omega_i} \\ &= \frac{bfF\left(\psi',\hat{n}\right)G\left(\psi_p,\theta_p\right)\exp\left(-c^2\alpha^2\right)}{4\cos\psi\cos\theta} + \frac{a}{d\omega_i}\end{aligned} . \qquad (123)$$

What truly separates the Torrance and Sparrow BRDF from previous BRDF's is the function G. Mathematically, G is the fraction of an illuminated facet that contributes to the scattered irradiance [128]. Physically, it models the shadowing and masking of a facet by an adjacent facet [128]. Torrance and Sparrow call this

78
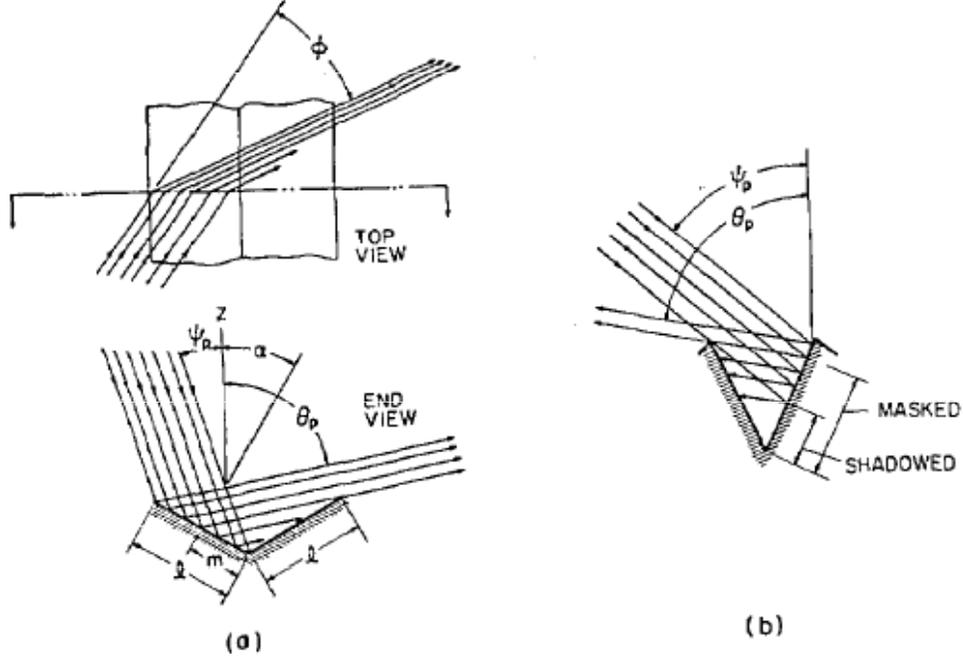
Figure 23. V-groove cavity geometry used by Torrance and Sparrow [128].

term the geometrical attenuation factor. The form of the geometrical attenuation factor is derived under the following assumptions: (1) each specularly reflecting facet comprises one side of a symmetric V-groove cavity; (2) the longitudinal axis of the cavity is parallel to the plane of the mean surface; (3) all azimuthal orientations of the longitudinal axis of the cavity are assumed equally probable; (4) all masking and shadowing effects take place within cavities; this is equivalent to assuming that the upper edges of all V-groove cavities lie in the same plane; (5) only the first reflection of an incident beam is added to the specularly reflected flux; (6) all multiple reflections are assumed to be perfectly diffuse [128]. The V-groove cavity geometry is shown in Fig. 23. After much trigonometry (details can be found in Ref. [128]), Torrance and Sparrow derive the geometrical attenuation factor

$$G\left(\psi_p, \theta_p\right) = 1 - \frac{1 - \sqrt{1 - A^2}}{A} \tag{124}$$

where

$$A = \frac{\sin^2\theta_p - \cos^2\left[(\theta_p - \psi_p)/2\right]}{\cos^2\left[(\theta_p - \psi_p)/2\right] - \cos\left(\theta_p - \psi_p\right)\sin^2\theta_p}. \tag{125}$$

The authors also include a table stipulating how it should be used (see Table I in Ref. [128]). It should be noted that Blinn derived an easier method for determining its value [15]. Blinn found that the value for the geometrical attenuation factor is the minimum of G_a, G_b, and G_c, namely

$$G = \min\left(G_a, G_b, G_c\right)$$
$$G_a = 1 \quad G_b = \frac{2\cos\alpha\cos\theta}{\cos\psi'} \quad G_c = \frac{2\cos\alpha\cos\psi}{\cos\psi'}. \tag{126}$$

The geometrical attenuation factor is vital because it serves to attenuate the scattered irradiance at angles near grazing [128]. This keeps the Torrance and Sparrow BRDF from asymptotically approaching infinity as the incident or observation angles approach 90°. In addition to keeping the Torrance and Sparrow BRDF well behaved near the grazing angles, the geometrical attenuation factor also serves to accurately predict the position and magnitude (parameter fitting is required to ensure this) of off-specular peaks. Note that G is a function of geometry, i.e., it depends on the angles of incidence, observation, and azimuth, and not a function of material parameters $n-\mathrm{j}\kappa$ [128]. This aspect of G is in accordance with intuition and experiment. Torrance and Sparrow conclude their paper by comparing predictions made using their BRDF to the aluminum and magnesium oxide ceramic measurement results shown above. Figure 24 shows their results. Note the accurate prediction of the off-specular peaks.

3.2.2   Priest and Germer.

In 2000, Priest and Germer developed a polarized version of the Torrance and Sparrow BRDF [103]. Note that in 2002, Priest and Meier published this pBRDF and

80
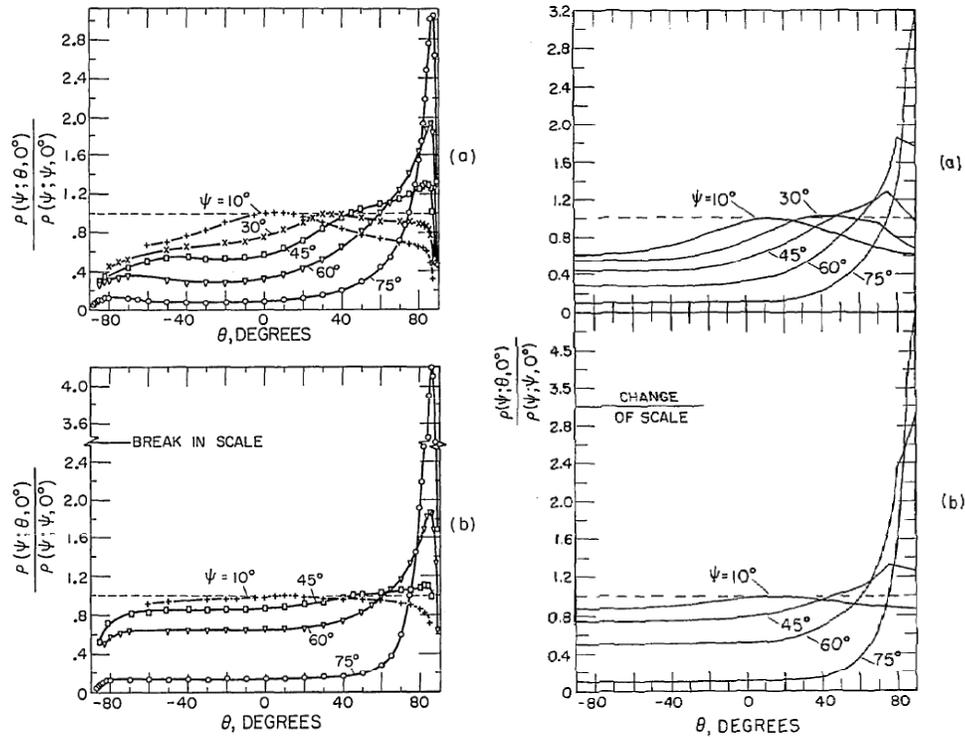
Figure 24. Predicted results (rightmost figures) for aluminum and magnesium oxide ceramic at $\lambda = 0.5$ μm published by Torrance and Sparrow. The top subfigure shows the results for aluminum. The bottom subfigure shows the results for magnesium oxide ceramic. For ease of comparison, the measurement results (shown in Fig. 21) are reproduced here (leftmost figures). Note that the Torrance and Sparrow BRDF accurately predicts the off-specular peaks. Information regarding the values of the fit parameters can be found in Ref. [128].

presented measurement results [104]. Both papers (the first a conference proceeding, the second a journal article) are very similar. Much of the information presented below comes from the 2002 Priest and Meier journal paper. Note that the Priest and Germer pBRDF and the Priest and Meier pBRDF are identical. Both terms are used interchangeably in this research.

Like the Torrance and Sparrow BRDF, the Priest and Germer pBRDF is based on the microfacet surface model. The microfacet model postulates that a rough surface is composed of a large number of small mirror-like facets each obeying Fresnel's equations [103, 104]. These facets are symmetrically distributed about the mean surface normal according to a distribution function [103, 104]. The most common distribution used (and the one used by Priest and Germer) is a Gaussian distribution [11], i.e.,

$$p(\theta) = \frac{1}{2\pi\sigma^2\cos^3\theta} \exp\left(\frac{-\tan^2\theta}{2\sigma^2}\right) \tag{127}$$

where θ is the angle between the mean surface normal and the facet normal and σ^2 is the slope variance. Note that Beckmann provides a more physical definition for the slope variance:

$$\sigma^2 = \frac{2\sigma_h^2}{\ell^2} \tag{128}$$

where σ_h is the rms surface height and ℓ is the surface correlation length [11]. With a Gaussian facet distribution, the expression for the Priest and Germer scalar BRDF is

$$f = \frac{1}{2\pi} \frac{1}{4\sigma^2} \frac{1}{\cos^4\theta} \frac{\exp\left[-\tan^2\theta/\left(2\sigma^2\right)\right]}{\cos\theta_r \cos\theta_i} \rho(\beta). \tag{129}$$

For brevity, the derivation of Eq. (129) is not shown. References detailing its derivation can be found in [103, 104, 119]. In Eq. (129), β is the angle of incidence onto or angle of reflection from a facet, θ_i is the angle of incidence with the respect to the mean surface normal, θ_r is the angle of reflection with respect to the mean sur-
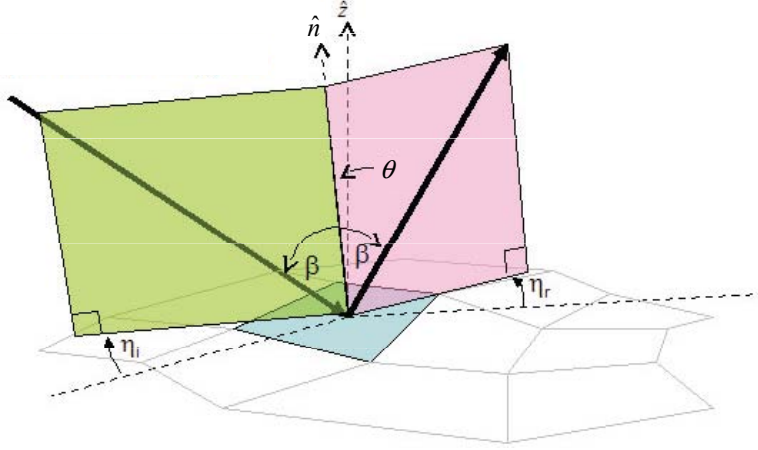
Figure 25. Microfacet scattering geometry used by Priest and Germer [42].

face normal, and ρ is the applicable Fresnel reflectance (either s- or p-pol). Using trigonometry, expressions can be found relating θ and β to θ_i, θ_r, and ϕ, namely,

$$\cos \theta = \frac{\cos \theta_i + \cos \theta_r}{2 \cos \beta}$$

$$\cos 2\beta = \cos \theta_i \cos \theta_r + \sin \theta_i \sin \theta_r \cos \phi$$

(130)

In order to generalize Eq. (129) to the case of polarized light, the authors use a Jones matrix approach [103, 104]. Consider the microfacet scattering geometry shown in Fig. 25. Only microfacets aligned at angle θ scatter light in the manner depicted. The angle η_i is the angle between the plane of incidence as defined by the incident light ray and mean surface normal (macro plane of incidence) and the plane of incidence as defined by the incident light ray and the microfacet surface normal (micro plane of incidence) [42]. Likewise, the angle η_r is the angle between the plane of reflection as defined by the reflected light ray and mean surface normal (macro plane of reflection) and the plane of reflection as defined by the reflected light ray and the microfacet surface normal (micro plane of reflection) [42]. The angles η_i and

η_r are related to θ_i, θ_r, and ϕ by

$$
\begin{aligned}
\cos \eta_i &= \frac{\cos \theta - \cos \theta_i \cos \beta}{\sin \theta_i \sin \beta} \\
\cos \eta_r &= \frac{\cos \theta - \cos \theta_r \cos \beta}{\sin \theta_r \sin \beta}
\end{aligned}
\tag{131}
$$

derived using trigonometry [103, 104]. In accordance with the microfacet surface model, the Jones matrix for light scattered from a microfacet is given by Eq. (54). This expression, however, is referenced to the local s- and p-pol geometry of a microfacet. Thus, two coordinate rotations are required to model the scattering depicted in Fig. 25. The first rotates the macro plane of incidence to align with the micro plane of incidence; the second rotates the micro plane of reflection to align with the macro plane of reflection. The Jones vector/matrix formalism modeling this process is

$$
\begin{aligned}
\begin{bmatrix} E_s^r \\ E_p^r \end{bmatrix} &= \begin{bmatrix} \cos \eta_r & \sin \eta_r \\ -\sin \eta_r & \cos \eta_r \end{bmatrix} \begin{bmatrix} r_s & 0 \\ 0 & r_p \end{bmatrix} \begin{bmatrix} \cos \eta_i & -\sin \eta_i \\ \sin \eta_i & \cos \eta_i \end{bmatrix} \begin{bmatrix} E_s^i \\ E_p^i \end{bmatrix} \\
&= \begin{bmatrix} T_{ss} & T_{ps} \\ T_{sp} & T_{pp} \end{bmatrix} \begin{bmatrix} E_s^i \\ E_p^i \end{bmatrix}
\end{aligned}
\tag{132}
$$

where r_s and r_p are the s- and p-pol Fresnel reflection coefficients [Eqs. (49) and (51)], respectively [103, 104]. In order to arrive at the desired Mueller matrix representation, expressions are required which relate the Jones matrix elements (derived above) to the Mueller matrix elements. These expressions are given in Refs. [103, 104] and

shown here

$$m_{00} = \frac{1}{2} \left(|T_{ss}|^2 + |T_{sp}|^2 + |T_{ps}|^2 + |T_{pp}|^2 \right)$$

$$m_{01} = \frac{1}{2} \left(|T_{ss}|^2 + |T_{sp}|^2 - |T_{ps}|^2 - |T_{pp}|^2 \right)$$

$$m_{02} = \frac{1}{2} \left(T_{ss}T_{ps}^* + T_{ss}^*T_{ps} + T_{sp}T_{pp}^* + T_{sp}^*T_{pp} \right)$$

$$m_{03} = \frac{1}{2} \left[\mathrm{j} \left(T_{ps}T_{ss}^* - T_{ps}^*T_{ss} \right) + \mathrm{j} \left(T_{pp}T_{sp}^* - T_{pp}^*T_{sp} \right) \right]$$

$$m_{10} = \frac{1}{2} \left(|T_{ss}|^2 - |T_{sp}|^2 + |T_{ps}|^2 - |T_{pp}|^2 \right)$$

$$m_{11} = \frac{1}{2} \left(|T_{ss}|^2 - |T_{sp}|^2 - |T_{ps}|^2 + |T_{pp}|^2 \right)$$

$$m_{12} = \frac{1}{2} \left[\left(T_{ss}T_{ps}^* + T_{ss}^*T_{ps} \right) - \left(T_{sp}T_{pp}^* + T_{sp}^*T_{pp} \right) \right]$$

$$m_{13} = \frac{1}{2} \left[\mathrm{j} \left(T_{ps}T_{ss}^* - T_{ps}^*T_{ss} \right) - \mathrm{j} \left(T_{pp}T_{sp}^* - T_{pp}^*T_{sp} \right) \right] \qquad (133)$$

$$m_{20} = \frac{1}{2} \left(T_{ss}T_{sp}^* + T_{ss}^*T_{sp} + T_{ps}T_{pp}^* + T_{ps}^*T_{pp} \right)$$

$$m_{21} = \frac{1}{2} \left[\left(T_{ss}T_{sp}^* + T_{ss}^*T_{sp} \right) - \left(T_{ps}T_{pp}^* + T_{ps}^*T_{pp} \right) \right]$$

$$m_{22} = \frac{1}{2} \left(T_{ss}T_{pp}^* + T_{ss}^*T_{pp} + T_{ps}T_{sp}^* + T_{ps}^*T_{sp} \right)$$

$$m_{23} = \frac{1}{2} \left[\mathrm{j} \left(T_{ps}T_{sp}^* - T_{ps}^*T_{sp} \right) - \mathrm{j} \left(T_{ss}T_{pp}^* - T_{ss}^*T_{pp} \right) \right]$$

$$m_{30} = \frac{1}{2} \left[\mathrm{j} \left(T_{ss}T_{sp}^* - T_{ss}^*T_{sp} \right) + \mathrm{j} \left(T_{ps}T_{pp}^* - T_{ps}^*T_{pp} \right) \right]$$

$$m_{31} = \frac{1}{2} \left[\mathrm{j} \left(T_{ss}T_{sp}^* - T_{ss}^*T_{sp} \right) - \mathrm{j} \left(T_{ps}T_{pp}^* - T_{ps}^*T_{pp} \right) \right]$$

$$m_{32} = \frac{1}{2} \left[\mathrm{j} \left(T_{ss}T_{pp}^* - T_{ss}^*T_{pp} \right) + \mathrm{j} \left(T_{ps}T_{sp}^* - T_{ps}^*T_{sp} \right) \right]$$

$$m_{33} = \frac{1}{2} \left[\left(T_{ss}T_{pp}^* + T_{ss}^*T_{pp} \right) - \left(T_{ps}T_{sp}^* + T_{ps}^*T_{sp} \right) \right]$$

Here, $*$ is the complex conjugate operation. Substituting Eq. (133) into Eq. (129) for ρ produces the desired result, i.e.,

$$f_{jk} \left(\theta_i, \theta_r, \phi \right) = \frac{1}{2\pi} \frac{1}{4\sigma^2} \frac{1}{\cos^4\theta} \frac{\exp\left[-\tan^2\theta / \left(2\sigma^2 \right) \right]}{\cos\theta_r \cos\theta_i} m_{jk} \left(\theta_i, \theta_r, \phi \right) \qquad (134)$$

where j and k can take any integer value between 0 and 3 [103, 104]. Note that for

in-plane scattering (i.e., $\phi = \pi$)

$$m_{00} = m_{11}$$

$$m_{01} = m_{10}$$

$$m_{22} = m_{33} \tag{135}$$

$$m_{23} = -m_{32}$$

producing the Mueller matrix for reflection given in Eq. (55).

It is worth discussing the measurement results published by Priest and Meier and a few aspects of their pBRDF before concluding. Figure 26 shows Mueller matrix measurement results compared to theoretical predictions made using Eq. (134) for two material samples. The top subfigure shows the results for Enhanced Martin Black (an anodized aluminum, dyed-black coating on an aluminum substrate) [104]. Enhanced Martin Black is a rough highly-absorbing material. The bottom subfigure shows the results for LabSphere Infragold [72] (plasma sprayed copper overcoated with electroplated gold on an aluminum substrate) [104]. LabSphere Infragold is a rough highly-reflective material. Both material samples were measured at 3.39 μm. The Mueller matrices for these samples were collected at in-plane scattering conditions ($\phi = \pi$) and at the specular angle ($\theta_i = \theta_r$). Note that for the Enhanced Martin Black sample, the Priest and Germer pBRDF performs admirably; however, discrepancies exist between the Priest and Germer pBRDF predictions and the measurement results for LabSphere Infragold. The authors interpret these results to mean that reflection from a highly-absorbing surface (like Enhanced Martin Black) leaves the surface after a single bounce. The remaining light is absorbed. For scattering from a highly-reflective surface (like LabSphere Infragold), the reflected light is a product of numerous random reflections which depolarize the light. This results in a significant diffuse contribution to the scattered light. The pBRDF given in Eq. (134)
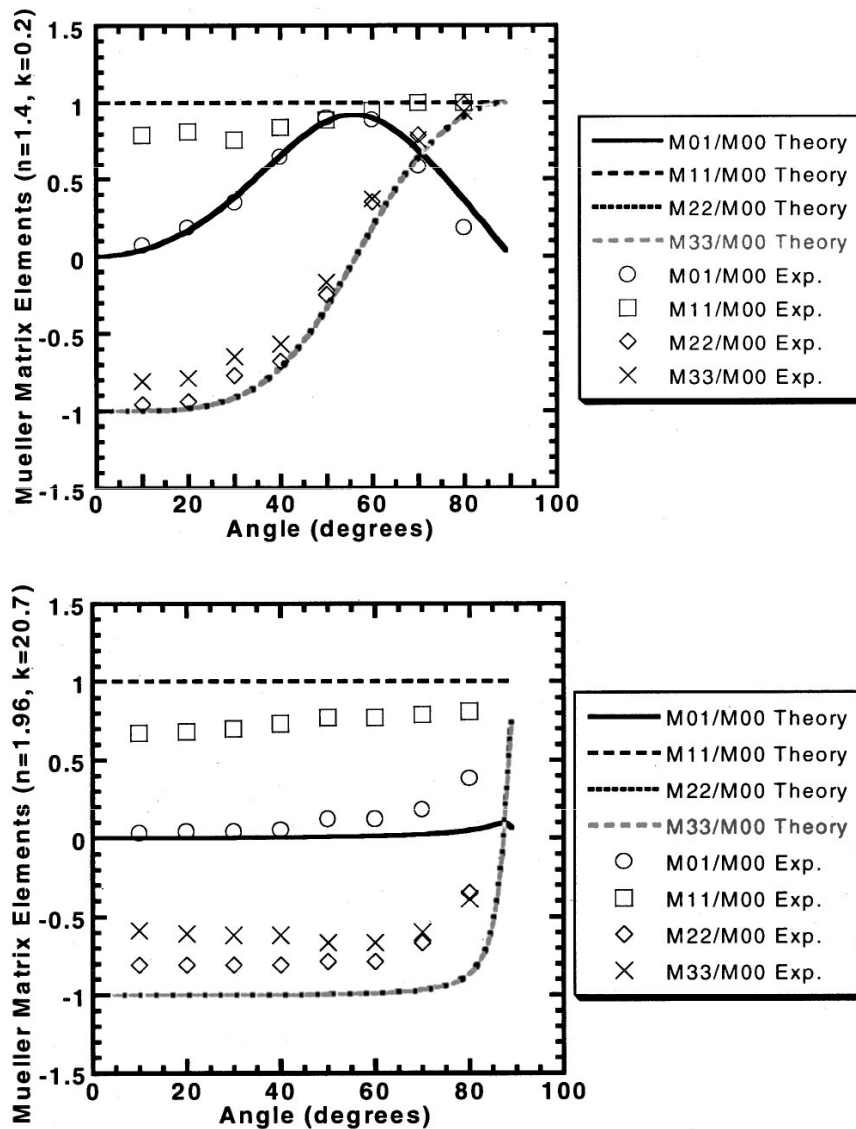
Figure 26. Mueller matrix measurement results comparing predictions made by the Priest and Germer pBRDF to experimental data. The top subfigure shows the results for Enhanced Martin Black; the bottom subfigure shows the results for LabSphere Infragold. Both material samples were measured at 3.39 μm. The Mueller matrices for both samples were collected at in-plane scattering conditions and at the specular angle [104].
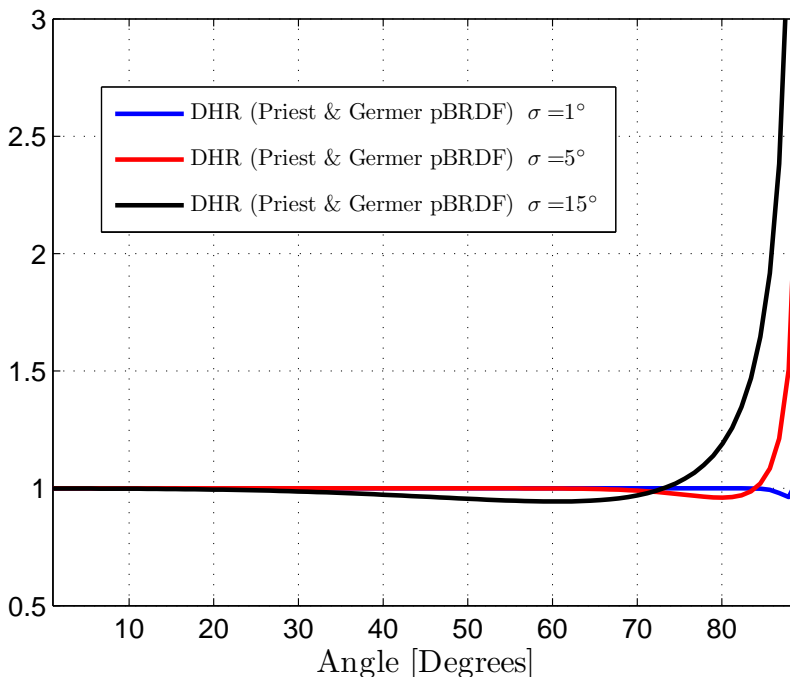
Figure 27. DHR's calculated using the Priest and Germer pBRDF for three PEC surfaces of differing surface roughness (1°, 5°, and 15° rms slope roughnesses).

includes no depolarizing or diffuse term and therefore suffers when trying to accurately predict the scattering from highly-reflective surfaces. The authors propose how a diffuse BRDF component could be derived; however, they do not include it in the paper [103, 104]. Wellems *et al.* include this term in their pBRDF (discussed below) [139]. In addition to the diffuse component of scatter, the Priest and Germer pBRDF does not include the geometrical attenuation factor derived by Torrance and Sparrow. While the full impact of this omission is demonstrated below, the lack of the geometrical attenuation factor causes the Priest and Germer pBRDF to asymptotically approach infinity as the angle of incidence or observation approaches grazing. Thus, for large angles of incidence (or observation), the Priest and Germer pBRDF does not obey the conservation of energy.

3.2.3   Wellems *et al.*.

While the Priest and Germer pBRDF is elegantly simple, it predicts nonphysical scattering results for angles approaching grazing. This is because the model does not conserve energy. Recall from the previous chapter that the DHR for a PEC surface must equal 1. In other words, all light incident on a PEC surface, regardless of roughness, is scattered back into the hemisphere containing the incident light. Collection of this scattered light (via integration) over the entire hemisphere should result in a scattered energy value equal to the amount of incident energy. Shown in Fig. 27 are the DHR's for a 1°, 5°, and 15° rms surface roughness PEC. The DHR's in the figure are calculated using the Priest and Germer pBRDF. Note that the DHR's are calculated by integrating over the whole sphere, not just the upper hemisphere [103, 104]. According to Priest and Germer, the physical meaning of this is that their pBRDF allows light to be scattered below the surface. Obviously, a PEC does not permit light to enter. This "transmitted" light is actually a result of multiple facet reflections and thus can serve as a depolarizing (diffuse) contribution to the Priest and Germer pBRDF [103, 104]. In order to incorporate the diffuse term, as suggested by Refs. [103, 104], the pBRDF must first be made to obey the conservation of energy ($\rho_{\mathrm{DHR}} \leq 1$). This was achieved by Wellems *et al.*

The two key additions of Wellems *et al.* to the Priest and Germer pBRDF were the inclusion of the Torrance and Sparrow geometrical attenuation factor and the derivation of a simple diffuse component to the pBRDF [139]. As discussed above, Torrance and Sparrow's geometrical attenuation factor serves a vital function. It attenuates the amount of scattered irradiance at angles near-grazing causing the BRDF to remain bounded. The inclusion of this term causes the Priest and Germer pBRDF to obey the conservation of energy [139]. Figure 28 shows the DHR, calculating using the Priest and Germer pBRDF (unshadowed Priest and Germer pBRDF), for a PEC
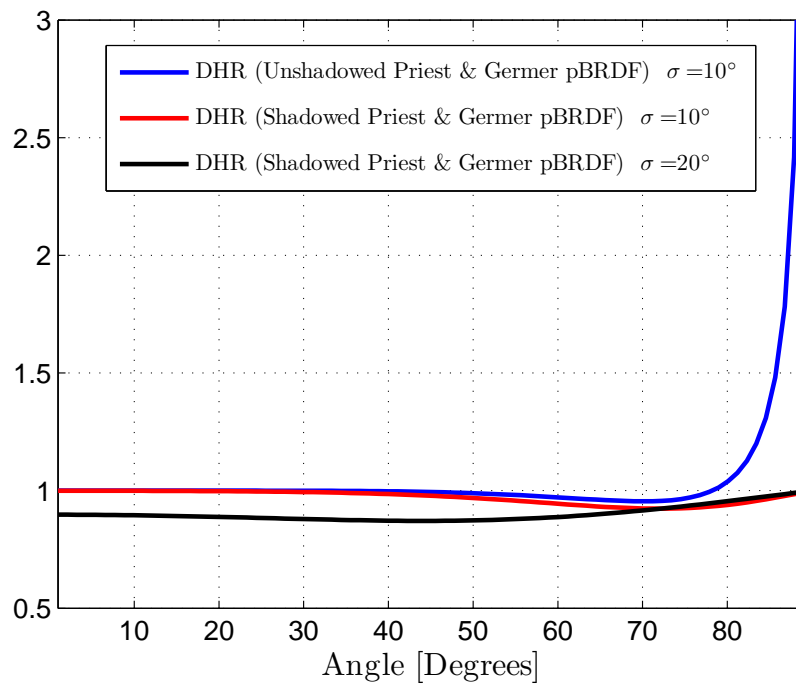
Figure 28. DHR, calculated using the unshadowed Priest and Germer pBRDF, for a PEC surface with a 10° rms slope roughness compared to the DHR's, calculated using the shadowed Priest and Germer pBRDF, for two PEC surfaces with 10° and 20° rms slope roughnesses, respectively.

surface with a 10° rms slope roughness compared to the DHR's, calculated using the Priest and Germer pBRDF with the geometrical attenuation factor included (shadowed Priest and Germer pBRDF), for two PEC surfaces with 10° and 20° rms slope roughnesses, respectively. Note that the DHR's calculated using the shadowed Priest and Germer pBRDF are never greater than 1.

Since inclusion of the Torrance and Sparrow geometrical attenuation factor into the Priest and Germer pBRDF results in a pBRDF which obeys the conservation of energy, attention can now be turned to deriving a diffuse component to the Priest and Germer pBRDF. Wellems *et al.* state that the diffuse component to the pBRDF is simply the difference between 1 (i.e., the correct conservation of energy value) and the calculated DHR value divided by π:

$$f^{\text{diff}} = \frac{1 - \rho_{\text{DHR}}}{\pi}. \tag{136}$$

To understand the factor of $1/\pi$, see the derivation of the Lambertian BRDF in the previous chapter. The Wellems pBRDF is now formed by adding the shadowed Priest and Germer pBRDF to the diffuse component, i.e.,

$$f_{jk}(\theta_i, \theta_r, \phi, \sigma) = f_{jk}^{\text{spec}}(\theta_i, \theta_r, \phi, \sigma) + f_{jk}^{\text{diff}}(\theta_i, \theta_r, \phi, \sigma) \tag{137}$$

where

$$f_{jk}^{\text{spec}}(\theta_i, \theta_r, \phi, \sigma) = \frac{G(\theta_i, \theta_r, \phi)}{(2\pi)(4\sigma^2)\cos^4\theta} \frac{\exp\left[-\tan^2\theta/(2\sigma^2)\right]}{\cos\theta_r \cos\theta_i} m_{jk}(\theta_i, \theta_r, \phi)$$

$$f_{jk}^{\text{diff}}(\theta_i, \theta_r, \phi, \sigma) = \begin{cases} [1 - \rho_{\text{DHR}}(\theta_i, \sigma)] \, m_{00}(\theta_i, \theta_r, \phi)/\pi & j = 0, \, k = 0 \\ \\ 0 & \text{else} \end{cases} \tag{138}$$

$$\rho_{\text{DHR}}(\theta_i, \sigma) = \int\limits_{0}^{2\pi} \int\limits_{0}^{\pi/2} \frac{G(\theta_i, \theta_r, \phi)}{(2\pi)(4\sigma^2)\cos^4\theta} \frac{\exp\left[-\tan^2\theta/(2\sigma^2)\right]}{\cos\theta_r \cos\theta_i} \cos\theta_r \sin\theta_r d\theta_r d\phi$$
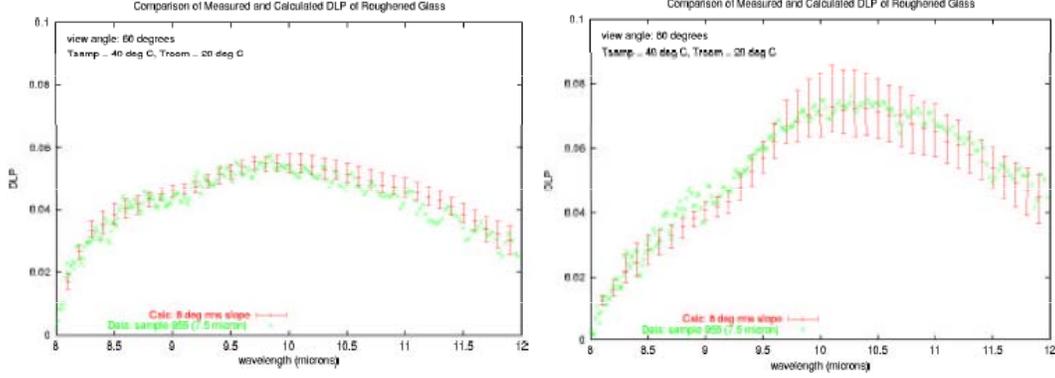
Figure 29. Measurement results of roughened glass published by Wellems *et al.* The figures compare measurements of $|S_1/S_0|$ to predictions made using the Wellems pBRDF. The figure on the left shows the results for a 60° view angle. The figure on the right shows the results for an 80° view angle. The green curve is the measurement; the red curve is the prediction. The error bars on the red curve are the result of an uncertainty in the index of refraction of glass [139].

Note that, in accordance with intuition, the only Mueller matrix element the diffuse component contributes to is the m_{00} element. Equation (137) is the BRDF that is used in this research.

Wellems *et al.* conclude their paper by comparing $|S_1/S_0|$ measurements of roughened glass to $|S_1/S_0|$ predictions made using their pBRDF. Figure 29 shows the results for 60° (left) and 80° (right) view angles. The green curve is the measurement; the red curve is the prediction. The error bars on the red curve are the result of an uncertainty in the index of refraction of glass (see Ref. [139] for more details). Note that the Wellems pBRDF performs well at both angles; its performance at 80° is especially impressive.

Another reference which discusses this pBRDF is Ref. [140]. In the paper, Wellems *et al.* present a two-parameter hyper-Cauchy facet distribution function. Numerous experimental results of $(S_1^2 + S_2^2)^{1/2}/S_0$ and S_2/S_1 at 8.5–9.5 μm of roughened glass and unprepared metal and painted surfaces are presented demonstrating the flexibility of the new facet distribution function.

3.3 Blind Deconvolution

Recall from the previous chapter the definition of blind deconvolution: blind deconvolution is the process of recovering the true object from the degraded image having little or no information about the PSF or the true object [70]. Two blind-deconvolution papers are reviewed in this section. The first by Schulz (an improvement on the work of Holmes [59]) presents a method for estimating the PSF's and the true object from images degraded by atmospheric turbulence. The second paper by LeMaster and Cain estimates the polarized and unpolarized components of scene, as well as the AOP and PSF's, from polarimetric images degraded by atmospheric turbulence. Both papers employ the maximum-likelihood (ML) estimation approach. ML estimation is a means of estimating a set of parameters $\boldsymbol{\theta} = [\theta_1, \theta_2, \cdots, \theta_m]^{\mathrm{T}}$ of a statistical distribution based upon data $\boldsymbol{x} = [x_1, x_2, \cdots, x_n]^{\mathrm{T}}$ drawn according to that distribution [94]. The goal of ML estimation is to determine values of $\boldsymbol{\theta}$ which maximize the probability of observing $\boldsymbol{x}$, i.e.,

$$\boldsymbol{\theta}_{\mathrm{ML}} = \arg \max_{\boldsymbol{\theta}} f\left(\boldsymbol{x} \mid \boldsymbol{\theta}\right) = \arg \max_{\boldsymbol{\theta}} l_x\left(\boldsymbol{\theta}\right) \tag{139}$$

where f is the probability density function (PDF) of the data $\boldsymbol{x}$ conditioned on the sought parameters $\boldsymbol{\theta}$ [94]. Here, l_x is referred to as the likelihood function. Note that in many instances, especially when dealing with exponential-type statistical distributions (Poisson, Gaussian, exponential, Rayleigh, etc.), it is convenient to work with the log of the likelihood function. Since the log function is monotonically increasing, maximizing the likelihood function is equal to maximizing the log-likelihood function [94]. Finding $\boldsymbol{\theta}_{\mathrm{ML}}$ involves solving the system of nonlinear equations shown

here [94]

$$\frac{\partial}{\partial \theta_1} l_x\left(\theta_1, \theta_2, \cdots, \theta_m\right) = 0$$
$$\frac{\partial}{\partial \theta_2} l_x\left(\theta_1, \theta_2, \cdots, \theta_m\right) = 0$$
$$\vdots$$
$$\frac{\partial}{\partial \theta_m} l_x\left(\theta_1, \theta_2, \cdots, \theta_m\right) = 0$$

$$(140)$$

While techniques such as the Newton-Raphson method can be used, a simpler alternative known as the expectation-maximization (EM), or generalized expectation-maximization (GEM) algorithm can be used [70]. This is the technique employed by the authors of the two papers discussed below. The EM algorithm is an iterative technique which consists of two steps from which it derives its name—the expectation step and the maximization step. In the expectation step, the observed data $\boldsymbol{x}$ (called the incomplete data) are represented as the aggregate of some underlying distribution (called the complete data $\boldsymbol{y}$) [74]. Note that the complete data are not observed directly, nor do they need to have any physical significance [74, 94]. They do, however, need to have the same statistical distribution as the incomplete data [74]. The expectation step gets its name from the calculation of the expectation of the complete-data log-likelihood function when conditioned upon the incomplete data and the most recent parameter estimates $\boldsymbol{\theta}^{(k)}$ [74, 94]:

$$Q\left(\boldsymbol{\theta} \mid \boldsymbol{\theta}^{(k)}\right) = \mathrm{E}\left\{\ln\left[f\left(\boldsymbol{y} \mid \boldsymbol{\theta}\right)\right]\mid \boldsymbol{x}, \boldsymbol{\theta}^{(k)}\right\}. \tag{141}$$

The function Q is called the objective function [74]. In the final step of the EM algorithm (the maximization step), the values of the estimated parameters are found such that the objective function is maximized or (at least) increased in value [74, 94]:

$$\boldsymbol{\theta}^{(k+1)} = \arg\max_{\boldsymbol{\theta}} Q\left(\boldsymbol{\theta} \mid \boldsymbol{\theta}^{(k)}\right). \tag{142}$$

The EM algorithm is then iterated until the sought parameters satisfy an arbitrary stopping criterion [74, 94]. Having provided the necessary background, attention can now be turned to reviews of the research published by Schulz and LeMaster and Cain.

3.3.1 Schulz.

One drawback of the unconstrained ML estimation approach to blind deconvolution is its tendency to produce a trivial estimate [114]. The trivial estimate is obtained when the object is estimated as a point source and the PSF as the measured data [114]. The purpose of Schulz's paper is to present methods for overcoming this shortfall. Two such techniques are presented. The first is a penalized-ML estimator. This technique adds a penalty term to the standard log-likelihood function which discourages object estimates which resemble a point source [114]. The second method is an ML estimator in which the PSF's are parameterized by phase errors distributed over the imaging aperture [114]. This technique, being the most relevant to this research, is the one highlighted. Information regarding Schulz's penalized-ML estimator can be found in Ref. [114].

Recall from the previous chapter the expression for the detected irradiance, i.e., Eq. (64). If K images are collected, Eq. (64) becomes

$$i_k\left(\boldsymbol{y};\, o,\, h_k\right) = \sum_{\boldsymbol{x}} o\left(\boldsymbol{x}\right) h_k\left(\boldsymbol{y} - \boldsymbol{x}\right) \tag{143}$$

where the index $k = 1, \cdots, K$. As previously defined, $\boldsymbol{x}$ is the object-plane coordinate pair, $\boldsymbol{y}$ is the image-plane coordinate pair, o is the true object, and h_k is the PSF for the kth captured frame. Note that the measurement of i_k is never perfect. Several noise sources are responsible for its corruption. The two most common are readout noise and shot, or photon noise. The assumption made by Schulz is that shot noise is the dominant noise source [114]. Shot noise is caused by the random arrival times

of individual photons at the camera's detector array [44]. The number of photons which arrive in a given time is Poisson distributed; thus, the photon count (related to the detected irradiance) at a certain location in the camera's detector array is a Poisson random variable [44, 114]. Schulz defines the photon count at location $\boldsymbol{y}$ in the kth frame as $d_k(\boldsymbol{y})$ where $d_k(\boldsymbol{y})$ is a Poisson random variable with mean equal to i_k [114]:

$$i_k(\boldsymbol{y};\, o,\, h_k) = \mathrm{E}\left[d_k(\boldsymbol{y})\right]. \tag{144}$$

The log-likelihood function based on the Poisson distribution is

$$L(o,\, h) = \sum_{k=1}^{K}\left\{-\sum_{\boldsymbol{y}} i_k(\boldsymbol{y};\, o,\, h_k) + \sum_{\boldsymbol{y}} d_k(\boldsymbol{y})\ln\left[i_k(\boldsymbol{y};\, o,\, h_k)\right]\right\} + \mathrm{A.T.} \tag{145}$$

where A.T. is another term that depends on neither o nor h_k and thus does not affect the maximization [114].

This is the point at which Schulz introduces the parameterized form of the PSF. The expression is very similar to Eq. (83):

$$h_k(\boldsymbol{y} - \boldsymbol{x};\, \alpha_k,\, \theta_k) = \alpha_k\left|\sum_{\boldsymbol{u}} A(\boldsymbol{u})\, e^{\mathrm{j}\theta_k(\boldsymbol{u})} e^{-\mathrm{j}2\pi\mathcal{K}\boldsymbol{u}\cdot(\boldsymbol{y}-\boldsymbol{x})}\right|^2 = \alpha_k g(\boldsymbol{y} - \boldsymbol{x};\, \theta_k) \tag{146}$$

where, as before, A is the aperture function of the imaging system and θ_k models the random phase effects caused by propagation through the atmosphere. Note that the phase effects are permitted to differ from frame to frame. The new variables in Eq. (146) not yet defined are α_k, which models the gain of the kth PSF, and $\mathcal{K}$, which is a constant whose value depends primarily on the sample spacing used to perform the discrete Fourier transform (DFT) [114]. Substitution of Eq. (146) into Eq. (145)

produces the log-likelihood function

$$L\left(o, h\right) = -\sum_k \sum_{\boldsymbol{y}} \sum_{\boldsymbol{x}} \alpha_k g\left(\boldsymbol{y} - \boldsymbol{x};\, \theta_k\right) o\left(\boldsymbol{x}\right) + \sum_k \sum_{\boldsymbol{y}} d_k\left(\boldsymbol{y}\right) \ln \alpha_k$$
$$+ \sum_k \sum_{\boldsymbol{y}} d_k\left(\boldsymbol{y}\right) \ln \left[\sum_{\boldsymbol{x}} g\left(\boldsymbol{y} - \boldsymbol{x};\, \theta_k\right) o\left(\boldsymbol{x}\right)\right] \tag{147}$$

Differentiating the above expression with respect to α_k, setting the subsequent equation equal to zero, and solving yields the ML estimate for α_k, namely,

$$\hat{\alpha}_k = D_k/G$$
$$D_k = \sum_{\boldsymbol{y}} d_k\left(\boldsymbol{y}\right) \quad G = \sum_{\boldsymbol{x}} g\left(\boldsymbol{x};\, \theta_k\right) \tag{148}$$

The estimates (actually, the update equations) for the other parameters θ_k and o are found using the EM algorithm. For the sake of brevity, the details are not shown. They can be found in Ref. [114]. The update equations for θ_k and o are

$$o^{\text{new}}\left(\boldsymbol{x}\right) = \frac{1}{\sum_k D_k} o^{\text{old}}\left(\boldsymbol{x}\right) \sum_k \sum_{\boldsymbol{y}} \frac{\hat{\alpha}_k g\left(\boldsymbol{y} - \boldsymbol{x};\, \theta_k^{\text{old}}\right)}{i_k\left(\boldsymbol{y};\, o^{\text{old}};\, h_k^{\text{old}}\right)} d_k\left(\boldsymbol{y}\right)$$

$$\theta_k^{\text{new}}\left(\boldsymbol{u}\right) = \begin{cases} \tilde{\theta}\left(\boldsymbol{u}\right) & \sum_{\boldsymbol{x}} \xi\left(\boldsymbol{x};\, \theta_k^{\text{old}}\right) \ln g\left(\boldsymbol{x};\, \tilde{\theta}\right) \geq \sum_{\boldsymbol{x}} \xi\left(\boldsymbol{x};\, \theta_k^{\text{old}}\right) \ln g\left(\boldsymbol{x};\, \theta_k^{\text{old}}\right) \\ \theta_k^{\text{old}}\left(\boldsymbol{u}\right) & \text{else} \end{cases} \tag{149}$$

where

$$\xi\left(\boldsymbol{x};\, \theta_k^{\text{old}}\right) = g\left(\boldsymbol{x};\, \theta_k^{\text{old}}\right) \left[\sum_{\boldsymbol{y}} \frac{o^{\text{old}}\left(\boldsymbol{y} - \boldsymbol{x}\right)}{i_k\left(\boldsymbol{y};\, o^{\text{old}};\, h_k^{\text{old}}\right)} d_k\left(\boldsymbol{y}\right)\right]$$
$$\tilde{\theta}\left(\boldsymbol{u}\right) = \text{phase}\left\{F_{\boldsymbol{x}}^{-1}\left\{\sqrt{\xi\left(\boldsymbol{x};\, \theta_k^{\text{old}}\right)} \exp\left\{\text{jphase}\left[\tilde{g}\left(\boldsymbol{x};\, \theta_k^{\text{old}}\right)\right]\right\}\right\}\right\} \tag{150}$$
$$\tilde{g}\left(\boldsymbol{x};\, \theta_k^{\text{old}}\right) = F_{\boldsymbol{u}}\left\{A\left(\boldsymbol{u}\right) \exp\left[\text{j}\theta_k^{\text{old}}\left(\boldsymbol{u}\right)\right]\right\}$$

Note that the update for θ_k is accomplished using one, or more, iterations of the

Gerchberg-Saxton (GS) phase retrieval algorithm [43]. This completes the review of Schultz's ML blind-deconvolution algorithm.

Figure 30 shows simulation results performed using Schulz's algorithm. The simulated data sets are produced by convolving two PSF's (second row) with the object (top row). The resulting images are then corrupted with shot noise (simulated) so that each image contains approximately 1,000,000 photons (third row). The estimated PSF's (fourth row) and object (last row) are obtained after 1,000 iterations of the algorithm. Note that the object is recovered.

3.3.2 LeMaster and Cain.

This section presents a polarimetric version of Schulz's blind-deconvolution algorithm. The technique, published by LeMaster and Cain, decomposes Schulz's polarization-insensitive complete-data formulation into polarized and unpolarized components [74]. From polarimetric images of a scene, the algorithm returns estimates of the polarized and unpolarized image components as well as the AOP and polarimetric channel PSF's. A close variant of this algorithm is used in this research.

As stated above, LeMaster and Cain's polarimetric ML blind-deconvolution algorithm is very similar to Schulz's. The measured polarimetric images (incomplete data) d_c are assumed to be Poisson random variables, such that the mean of d_c is i_c:

$$\mathrm{E}\left[d_c\left(\boldsymbol{y}\right)\right] = i_c\left(\boldsymbol{y}\right) = \sum_{\boldsymbol{x}} o_c\left(\boldsymbol{x}\right) h_c\left(\boldsymbol{y} - \boldsymbol{x}\right). \tag{151}$$

This expression is the same as Eq. (143) with the exception that the object o_c is permitted to vary between polarimetric images. LeMaster and Cain model the object

Actual Object

Actual PSF 1   Actual PSF 2

Image 1   Image 2

Estimated PSF 1   Estimated PSF 2

Estimated Object
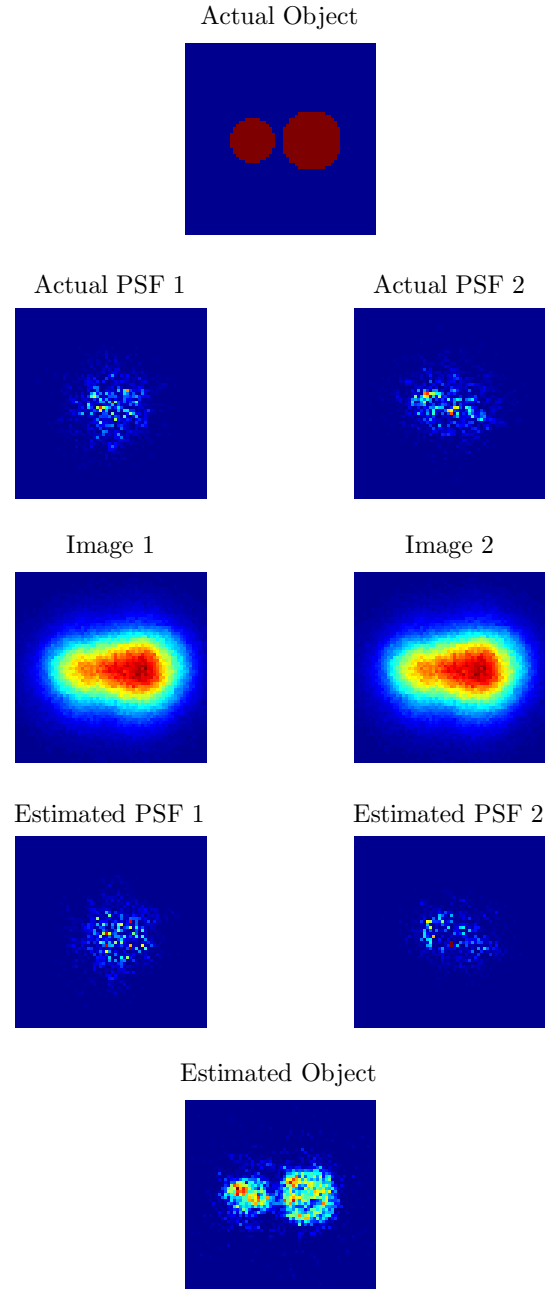
Figure 30. Simulation results using Schulz's ML blind-deconvolution algorithm. The simulated images are produced by convolving two PSF's (second row) with the object (top row). The images are then corrupted with simulated shot noise so that each image contains approximately 1,000,000 photons (third row). The estimated PSF's (fourth row) and object (last row) are obtained after 1,000 iterations of the algorithm.

99

in channel c as

$$o_c (\boldsymbol{x}) = \frac{1}{2} [1 - \mathcal{P} (\boldsymbol{x})] S_0 (\boldsymbol{x}) + \mathcal{P} (\boldsymbol{x}) S_0 (\boldsymbol{x}) \cos^2 [\alpha (\boldsymbol{x}) - \theta_c]$$
$$= \frac{1}{2} \lambda_u (\boldsymbol{x}) + \lambda_p (\boldsymbol{x}) \cos^2 [\alpha (\boldsymbol{x}) - \theta_c]$$

(152)

where S_0 is the total irradiance (i.e., the first Stokes parameter), $\mathcal{P}$ is the DOP, α is the AOP, and θ_c is the angular orientation of the LP with respect to the optic axis [74]. The terms λ_u and λ_p are the unpolarized and polarized components of the object irradiance, respectively. These are the images which are estimated by the algorithm.

LeMaster and Cain split each d_c into polarized and unpolarized components, $\tilde{d}_{pc} (\boldsymbol{y}, \boldsymbol{x})$ and $\tilde{d}_{uc} (\boldsymbol{y}, \boldsymbol{x})$, which in accordance with the requirements of the EM algorithm become the complete data:

$$d_c (\boldsymbol{y}) = \sum_{\boldsymbol{x}} \tilde{d}_{uc} (\boldsymbol{y}, \boldsymbol{x}) + \sum_{\boldsymbol{x}} \tilde{d}_{pc} (\boldsymbol{y}, \boldsymbol{x})$$

$$\mathrm{E} \left[\tilde{d}_{uc} (\boldsymbol{y}, \boldsymbol{x}) \right] = \frac{1}{2} \lambda_u (\boldsymbol{x}) h_c (\boldsymbol{y} - \boldsymbol{x})$$

(153)

$$\mathrm{E} \left[\tilde{d}_{pc} (\boldsymbol{y}, \boldsymbol{x}) \right] = \lambda_p (\boldsymbol{x}) \cos^2 [\alpha (\boldsymbol{x}) - \theta_c] h_c (\boldsymbol{y} - \boldsymbol{x})$$

The expression for the log-likelihood function becomes

$$L (\lambda_u, \lambda_p, \alpha, h_c) = \sum_c \sum_{\boldsymbol{y}} \sum_{\boldsymbol{x}} \left[\tilde{d}_{uc} \ln \left(\tfrac{1}{2} \lambda_u h_c \right) - \tfrac{1}{2} \lambda_u h_c \right]$$
$$+ \sum_c \sum_{\boldsymbol{y}} \sum_{\boldsymbol{x}} \left\{ \tilde{d}_{pc} \ln [\lambda_p \cos^2 (\alpha - \theta_c) h_c] - \lambda_p \cos^2 (\alpha - \theta_c) h_c \right\}$$

(154)

where, for brevity, the functional dependencies of $\tilde{d}_{pc}$, $\tilde{d}_{uc}$, λ_p, λ_u, α, and h_c have been omitted [74]. The first step of the EM algorithm, the expectation step, is accomplished by calculating the conditional expectation of the complete-data log-likelihood function

[Eq. (154)], i.e.,

$$Q^{n+1}\left(\lambda_u,\ \lambda_p,\ \alpha,\ h_c\right)=\mathrm{E}\left[L\left(\lambda_u,\ \lambda_p,\ \alpha,\ h_c\right)\middle|\,d_c,\ \lambda_u^n,\ \lambda_p^n,\ \alpha^n,\ h_c^n\right].\tag{155}$$

Calculating the expectation produces the objective function given by

$$\begin{aligned}
Q^{n+1}\left(\lambda_u,\ \lambda_p,\ \alpha,\ h_c\right)=&\sum_c\sum_{\boldsymbol{y}}\sum_{\boldsymbol{x}}\left[\psi_{uc}^{n+1}\ln\left(\tfrac{1}{2}\lambda_u h_c\right)-\tfrac{1}{2}\lambda_u h_c\right]\\
&+\sum_c\sum_{\boldsymbol{y}}\sum_{\boldsymbol{x}}\left\{\psi_{pc}^{n+1}\ln\left[\lambda_p\cos^2\left(\alpha-\theta_c\right)h_c\right]-\lambda_p\cos^2\left(\alpha-\theta_c\right)h_c\right\}
\end{aligned}\tag{156}$$

where

$$\begin{aligned}
\psi_{uc}^{n+1}\left(\boldsymbol{y},\boldsymbol{x}\right)&=\frac{1}{2}\frac{d_c\left(\boldsymbol{y}\right)}{i_c^n\left(\boldsymbol{y}\right)}\lambda_u^n\left(\boldsymbol{x}\right)h_c^n\left(\boldsymbol{y}-\boldsymbol{x}\right)\\
\psi_{pc}^{n+1}\left(\boldsymbol{y},\boldsymbol{x}\right)&=\frac{d_c\left(\boldsymbol{y}\right)}{i_c^n\left(\boldsymbol{y}\right)}\lambda_p^n\left(\boldsymbol{x}\right)\cos^2\left[\alpha^n\left(\boldsymbol{x}\right)-\theta_c\right]h_c^n\left(\boldsymbol{y}-\boldsymbol{x}\right)
\end{aligned}\tag{157}$$

With the expectation step complete, attention is now turned to the maximization step. Taking derivatives of Eq. (156) with respect to λ_p, λ_u, α, and h_c and setting those expressions equal to zero yields

$$\begin{aligned}
\frac{\partial Q^{n+1}}{\partial\lambda_p\left(\boldsymbol{x}_0\right)}&=0=\sum_c\sum_{\boldsymbol{y}}\frac{\psi_{pc}^{n+1}\left(\boldsymbol{y},\boldsymbol{x}_0\right)}{\lambda_p\left(\boldsymbol{x}_0\right)}-\sum_c\cos^2\left[\alpha\left(\boldsymbol{x}_0\right)-\theta_c\right]\\
\frac{\partial Q^{n+1}}{\partial\lambda_u\left(\boldsymbol{x}_0\right)}&=0=\sum_c\sum_{\boldsymbol{y}}\frac{\psi_{uc}^{n+1}\left(\boldsymbol{y},\boldsymbol{x}_0\right)}{\lambda_u\left(\boldsymbol{x}_0\right)}-\frac{c}{2}\\
\frac{\partial Q^{n+1}}{\partial\alpha\left(\boldsymbol{x}_0\right)}&=0=-2\sum_c\sum_{\boldsymbol{y}}\psi_{pc}^{n+1}\left(\boldsymbol{y},\boldsymbol{x}_0\right)\tan\left[\alpha\left(\boldsymbol{x}_0\right)-\theta_c\right]\\
&\qquad\qquad+\sum_c\lambda_p\left(\boldsymbol{x}_0\right)\sin\left\{2\left[\alpha\left(\boldsymbol{x}_0\right)-\theta_c\right]\right\}\\
\frac{\partial Q^{n+1}}{\partial h_c\left(\boldsymbol{z}\right)}&=0=\sum_{\boldsymbol{y}}\frac{\psi_{pc}^{n+1}\left(\boldsymbol{y},\boldsymbol{y}-\boldsymbol{z}\right)+\psi_{uc}^{n+1}\left(\boldsymbol{y},\boldsymbol{y}-\boldsymbol{z}\right)}{h_c\left(\boldsymbol{z}\right)}-\sum_{\boldsymbol{y}}o_c^{n+1}\left(\boldsymbol{y}-\boldsymbol{z}\right)
\end{aligned}\tag{158}$$

where $\boldsymbol{z}=\boldsymbol{y}-\boldsymbol{x}_0$ has been substituted into the maximization equation for h_c [74]. Note that the update equation for h_c is precisely the same as Schulz's and thus can be directly incorporated. This result makes physical sense since one does not expect

atmospheric turbulence to affect the polarization state of passing light . The authors also note that if the orientations of the LP are chosen wisely, i.e., in a manner such that θ_c is evenly distributed over all possible linear polarization states (0°, 60°, and -60° for the three channel scenario), then

$$\sum_c \cos^2\left(\alpha - \theta_c\right) = \frac{c}{2}$$

$$\sum_c \sin\left[2\left(\alpha - \theta_c\right)\right] = 0$$

(159)

no matter the value of α [74]. Note that this arrangement of LP measurements has been shown to maximizes signal-to-noise ratio (SNR) [132]. This simplification has the effect of completely decoupling the above update equations so that

$$\lambda_p^{n+1}\left(\boldsymbol{x}_0\right) = \frac{2}{c} \sum_c \sum_{\boldsymbol{y}} \psi_{pc}^{n+1}\left(\boldsymbol{y}, \boldsymbol{x}_0\right)$$

$$\lambda_u^{n+1}\left(\boldsymbol{x}_0\right) = \frac{2}{c} \sum_c \sum_{\boldsymbol{y}} \psi_{uc}^{n+1}\left(\boldsymbol{y}, \boldsymbol{x}_0\right).$$

(160)

$$\alpha^{n+1}\left(\boldsymbol{x}_0\right) = \frac{1}{2}\tan^{-1}\frac{S_2^{n+1}\left(\boldsymbol{x}_0\right)}{S_1^{n+1}\left(\boldsymbol{x}_0\right)}$$

Here, S_1^{n+1} and S_2^{n+1} are intermediate Stokes parameters. Their derivations can be found in Appendix A of Ref. [74].

With the derivation complete, LeMaster and Cain present measurement results using their algorithm. The object utilized by LeMaster and Cain consists of two fully polarized bars back illuminated by a 660 nm diode. The AOP's of the two bars are 2° for the top bar and -83° for the bottom bar. Three polarimetric images are collected—the first with the polarizer at 0°, the second with the polarizer at 60°, and the third with the polarizer at -60°. A phase screen is placed at the imaging aperture for the 60° and -60° polarimetric images to simulate atmospheric turbulence. The published results are shown in Figs. 31–33. Figure 31 shows the 0° (top left), 60° (top
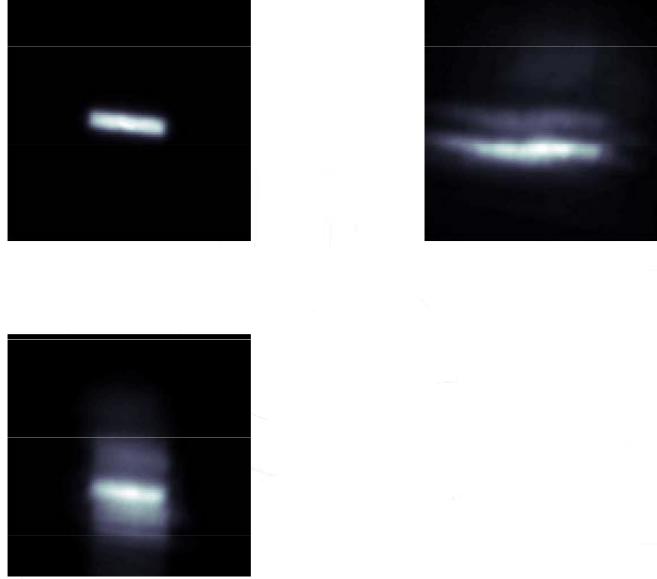
Figure 31. Measured polarimetric images published by LeMaster and Cain. The object is a set of two back illuminated bars. The top bar is polarized at an angle of 2°; the bottom bar is polarized at an angle of -83°. The leftmost figure on the top row is an image of the object taken through a LP orientated at an angle of 0°. The rightmost figure on the top row is an image of the object taken through a LP orientated at 60°. The figure on the bottom row is an image of the object taken through a LP orientated at -60° [74].

right), and -60° (bottom left) polarimetric images. The top row of Fig. 32 (from left to right) shows the initial guesses for λ_u and λ_p. The bottom row shows the estimates for λ_u and λ_p after 500 iterations of the algorithm. Note that the λ_u estimate is nearly all dark as one would expect for this fully polarized object. Lastly, Fig. 33 shows the results for the AOP estimate. The estimated angles are -8° for the top bar and -72° for the bottom bar. For a discussion on possible sources of error, see Ref. [74].
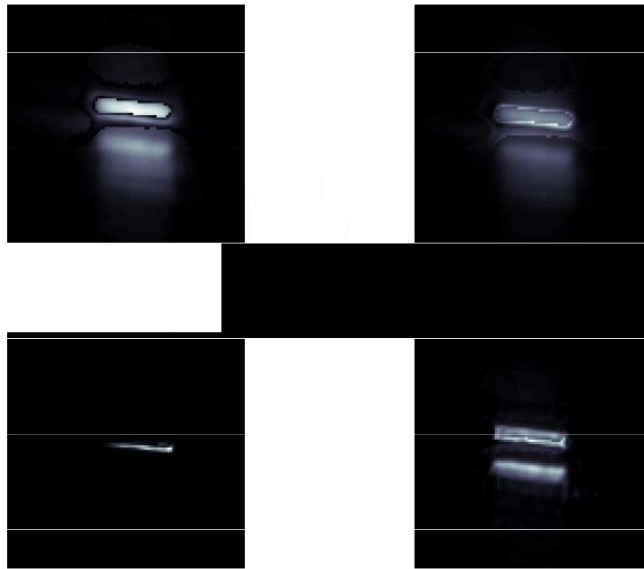
Figure 32. Estimation results published by LeMaster and Cain. The images on the top row (from left to right) are the initial guesses for λ_u and λ_p. The images on the bottom row (from left to right) are the estimates for λ_u and λ_p after 500 iterations of the algorithm [74].
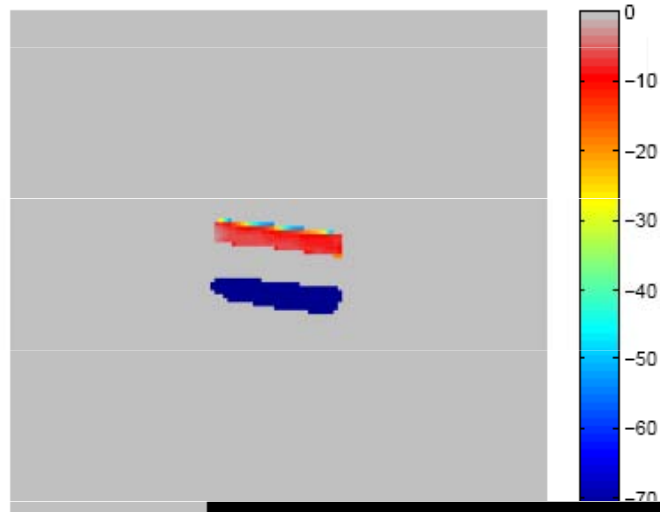
Figure 33. Estimation results published by LeMaster and Cain. This figure shows the result of the AOP estimate [74].

IV. pBRDF Verification

The contents of this chapter were published in *Optics Express*, vol. 17, no. 24 on 18 Nov 2009.

4.1 Introduction

Rough surface scattering has been an active area of research for nearly half a century. One of the early areas of research dealt with radio [10] and acoustic [31, 54] wave scatter from the ocean surface. Measurement of this scatter led to methods for sensing ocean wave heights [69]. In another application, in preparation for the NASA Apollo missions, analysis of light scattered from the lunar surface led researchers to conclude that the moon's surface is composed of a particulate material [53]. Study of the scattering from rough surfaces has also been applied to predict reflections from tree canopies [57, 68], biological/medical sensing [145, 148], and computer/video graphics [15, 26, 55].

Scattering from a rough surface is typically modeled using a bidirectional reflectance distribution function (BRDF) or its polarimetric counterpart, a polarimetric BRDF. BRDF's are generally classified in two main types—empirical and analytical BRDF's. As the name implies, empirical BRDF's are formulated from measurements. An example of such a BRDF can be found in Ref. [52]. Analytical BRDF's are typically derived using either physical optics or geometrical optics. Physical optics BRDF's rely on the electromagnetic physical optics approximation [16, 136] (known as the Kirchoff approximation in optics) to predict the scatter from rough surfaces. The seminal work in this type of BRDF is that of Beckmann and Spizzichino [11]. Another work which presents an excellent description of the Kirchoff approximation of rough surface scattering is that of Ishimaru [63]. More recently, Beckmann and

Spizzichino's BRDF has been extended to include shadowing (described below) and polarization [3, 55]. Geometrical optics BRDF's rely on the ray approximation of light [16, 91]. The seminal paper in this BRDF genre is that of Torrance and Sparrow [128]. Since Torrance and Sparrow, numerous geometrical optics BRDF's have been developed. These include BRDF's specialized to predict IR signatures of aircraft [110], full polarimetric geometrical optics BRDF's [34, 103, 104, 139, 140], and BRDF's derived to predict scatter from multilayer coatings [33]. Both types of analytical BRDF's discussed here require the surface roughness features to be several times larger than the wavelength of the incident light. Since physical optics BRDF's are based on a more sound approximation, they tend to be more accurate than geometrical optics BRDF's. However, geometrical optics BRDF's tend to be simpler in mathematical form and thus more numerically efficient. They also tend to be more physically intuitive than their physical optics counterparts.

The geometrical optics BRDF introduced here is a full polarimetric BRDF (pBRDF). It is very similar in form to the pBRDF introduced by Priest and Germer [103, 104]; however, this pBRDF includes a shadowing function (in particular, the Torrance and Sparrow [128] shadowing function) and a Lambertian (diffuse) pBRDF component. It is shown that the pBRDF satisfies reciprocity and conserves energy. Section 4.2 introduces the theoretical form of the pBRDF. Section 4.3 compares the pBRDF prediction of the scatter from a rough perfectly-reflecting surface to that of an exact electromagnetic solution. In Section 4.4, Mueller matrix predictions are made using the pBRDF and compared to measurements made using a Mueller matrix ellipsometer [127] in order to validate the model. Lastly, the chapter is concluded with a summary of the work presented.
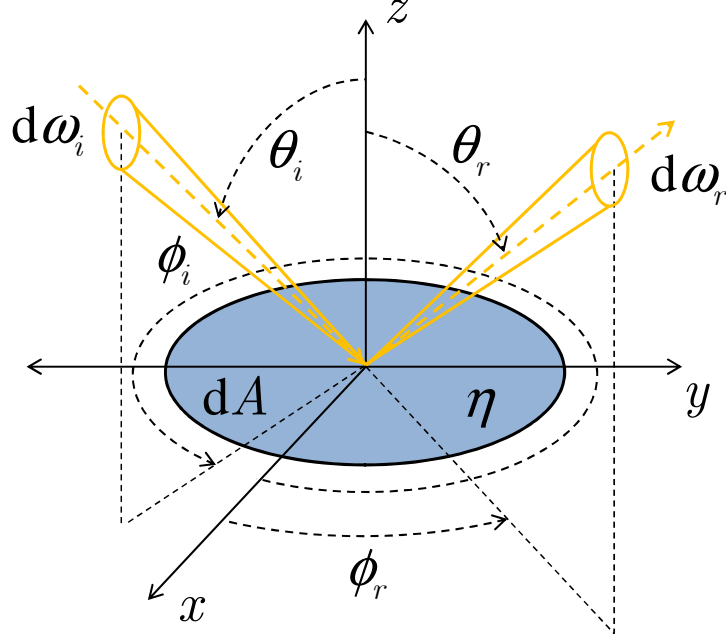
Figure 34. Macroscopic surface scattering geometry. Light subtending solid angle dω_i is incident from the (θ_i, ϕ_i) direction on a small area dA of a much larger rough surface with complex index of refraction $\eta = n - \mathrm{j}\kappa$. Light is scattered and observed within solid angle dω_r in the (θ_r, ϕ_r) direction.

4.2 Methodology

Consider the scattering geometry shown in Fig. 34. Light, subtending solid angle dω_i and centered on polar angle θ_i and azimuth angle ϕ_i, is incident on a small area dA of a larger rough surface with complex index of refraction $\eta = n - \mathrm{j}\kappa$. Light is scattered from the surface and observed within solid angle dω_r at polar angle θ_r and azimuth angle ϕ_r. The BRDF is defined as the ratio of the scattered radiance to the incident irradiance:

$$f(\theta_i, \theta_r, \phi) = \frac{\mathrm{d}L_r(\theta_r, \phi)}{\mathrm{d}E_i(\theta_i)} = \frac{\mathrm{d}L_r(\theta_r, \phi)}{L_i(\theta_i)\cos\theta_i \mathrm{d}\omega_i} \tag{161}$$

where dL_r is the scattered radiance, dE_i is the incident irradiance, and $\phi = |\phi_r - \phi_i|$ (i.e., surface is isotropic and homogeneous). Note that the incident irradiance is equivalent to the product of the incident radiance and the projected solid angle

$\cos \theta_i \mathrm{d}\omega_i$ [4, 38, 96, 97, 112, 116, 119, 128]. In the general polarimetric case, the scattered radiance and incident irradiance are replaced by Stokes vectors and the BRDF (now a pBRDF) by a Mueller matrix, i.e. [4, 14, 38, 41, 103, 104, 112, 116, 139],

$$\mathbf{F}\left(\theta_i, \theta_r, \phi\right) = \frac{\mathrm{d}\mathbf{L}_r\left(\theta_r, \phi\right)}{\mathbf{L}_i\left(\theta_i\right)\cos\theta_i\mathrm{d}\omega_i}. \tag{162}$$

Note that f of Eq. (161) equals F_{00} where the subscript 00 is the element in the first row and first column of the pBRDF Mueller matrix [112, 116]. It is common in literature to express the scattered radiance as the sum of the radiance which leaves the surface after one reflection and the radiance which leaves the surface after multiple reflections [26, 33, 41, 87, 112, 116, 119, 128, 139, 140]:

$$\mathbf{L}_r\left(\theta_r, \phi\right) = \mathbf{L}_r^{\text{single}}\left(\theta_r, \phi\right) + \mathbf{L}_r^{\text{multiple}}\left(\theta_r, \phi\right) \tag{163}$$

implying that

$$\mathbf{F} = \mathbf{F}^{\text{single}} + \mathbf{F}^{\text{multiple}}. \tag{164}$$

It follows that light leaving the surface after a single scattering event (for convenience termed the first reflection) models the specular component of reflection. This component carries with it all polarimetric information gained from interaction with the material surface. The multiple scattering term models the diffuse, or Lambertian component of reflection. One can glean this by considering the effect on polarization after multiple random surface reflections. In general, the first reflection is partially polarized and directed in the specular direction relative to the local surface normal of the illuminated area. If a portion of the first reflection is incident on another part of the material surface, the second reflection is a partially polarized version of the first, directed, once again, in the specular direction relative to the local surface normal of that illuminated area. This being repeated numerous times results in scatter which
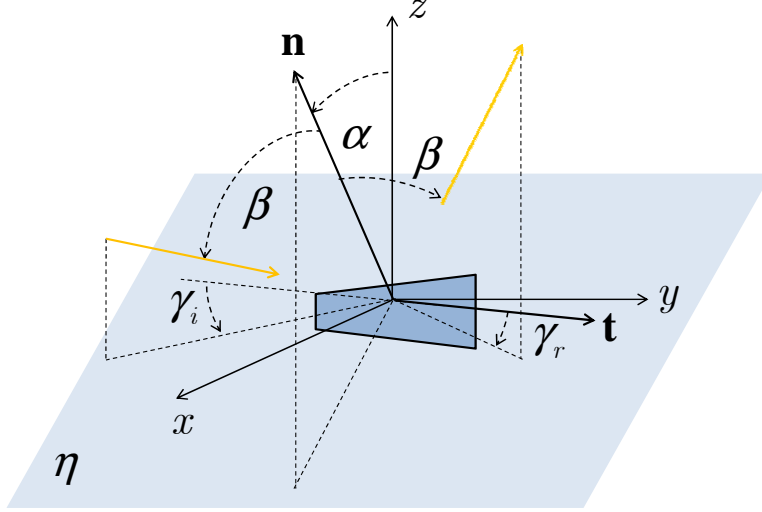
Figure 35. Scattering geometry of a single microfacet. The angle α is the polar angle from the mean surface normal to the microfacet normal n. The angle β is the incident angle onto and reflected angle from a microfacet as measured from the microfacet normal. The angle γ_i is the angle between the macroscopic plane of incidence and the scattering plane of the microfacet (depicted in the figure as the plane containing the vectors n and t). Likewise, the angle γ_r is the angle between the macroscopic plane of reflection and the scattering plane of the microfacet.

is unpolarized and of uniform radiance throughout the scattering hemisphere. Therefore, a pBRDF can be expressed as the sum of a polarized specular component and of an unpolarized diffuse component [26, 41, 87, 112, 116, 119, 128, 139, 140]:

$$\mathbf{F}^{\mathrm{s}} = \mathbf{F}^{\mathrm{single}}, \quad \mathbf{F}^{\mathrm{d}} = \mathbf{F}^{\mathrm{multiple}}$$
$$\mathbf{F} = \mathbf{F}^{\mathrm{s}} + \mathbf{F}^{\mathrm{d}} \tag{165}$$

As noted by Sun [119], Maxwell and Beard [87], and Ellis [33], this assumption is not always valid; however, it is an assumption which is very common in literature and, for the purpose of keeping the mathematical form of the pBRDF simple, is utilized here. In the next subsection, the form of the specular pBRDF component is shown and discussed.

4.2.1 Specular pBRDF Component.

The pBRDF here makes use of the microfacet surface model introduced by Torrance and Sparrow [128]. The model assumes that a rough surface is composed of a collection of randomly (according to some distribution) oriented facets each scattering light in the manner stipulated by Fresnel's equations (see Fig. 35). For Fresnel's equations to be an accurate model for reflection from the surface of a microfacet, the size of the facet must be large compared to the incident wavelength λ. This implies that the "roughness" of the macroscopic surface should be large compared to λ. As discussed by Sun [119], the microfacet surface model can be considered accurate when the surface height standard deviation σ_h and the surface correlation length ℓ are large compared to λ, i.e., $\sigma_h, \ell \gg \lambda$. The specular component of a microfacet model-based pBRDF takes the form

$$\mathbf{F}^s\left(\theta_i, \theta_r, \phi; \sigma_h, \ell; \eta\right) = \frac{P\left(\alpha; \sigma_h, \ell\right) \mathbf{M}\left(\beta; \eta\right) G\left(\theta_i, \theta_r, \phi\right)}{4 \cos\theta_i \cos\theta_r \cos\alpha} \tag{166}$$

where P is the distribution function modeling the orientation of the facets around the mean surface normal (z direction in Figs. 34 and 35), $\mathbf{M}$ is the Mueller matrix modeling the polarimetric scattering from the material surface, and G is the visibility function (shadowing/masking factor) [103, 104, 112, 116, 119, 139, 140]. Note that the angles α and β are derived using spherical trigonometry:

$$\begin{aligned} \cos\alpha &= \left(\cos\theta_i + \cos\theta_r\right) / \left(2\cos\beta\right) \\ \cos 2\beta &= \cos\theta_i \cos\theta_r + \sin\theta_i \sin\theta_r \cos\phi \end{aligned} \tag{167}$$

For the sake of brevity, the derivation of Eq. (166) is not shown. A full derivation of the expression can be found in Ref. [119]. It should be noted that Eq. (166) differs from that given in Refs. [112, 116] by a factor of $\cos\alpha$ in the denominator. Shell [116]

notes that the impact of this factor is minimal since the BRDF magnitude rapidly decreases with increasing α such that division by a decreasing $\cos\alpha$ is negligible.

Since the height distributions of most natural surfaces are Gaussian [119], the facet distribution function utilized in this pBRDF is that of Beckmann [11]:

$$P\left(\alpha;\sigma_h,\ell\right) = \frac{\ell^2 \exp\left[-\ell^2 \tan^2\alpha / \left(4\sigma_h^2\right)\right]}{4\pi\sigma_h^2\cos^3\alpha}. \tag{168}$$

Note that while this facet distribution function is very common, utilized in Refs. [26, 103, 104, 119, 139], other facet distributions do exist. For example, Torrance and Sparrow [128] utilize a simpler unnormalized distribution function of Gaussian shape, Shell [116] and Gartley [42] discuss Cauchy facet distribution functions in their research, and Wellems *et al.* [140] introduce a two-parameter hyper-Cauchy facet distribution function in their work.

The elements of the Mueller matrix $\mathbf{M}$ in Eq. (166) can be found by starting with Jones vectors and matrices, i.e.,

$$\begin{bmatrix} E_r^s \\ E_r^p \end{bmatrix} = \begin{bmatrix} \cos\gamma_r & \sin\gamma_r \\ -\sin\gamma_r & \cos\gamma_r \end{bmatrix} \begin{bmatrix} r_s & 0 \\ 0 & r_p \end{bmatrix} \begin{bmatrix} \cos\gamma_i & -\sin\gamma_i \\ \sin\gamma_i & \cos\gamma_i \end{bmatrix} \begin{bmatrix} E_i^s \\ E_i^p \end{bmatrix}$$
$$\begin{bmatrix} E_r^s \\ E_r^p \end{bmatrix} = \begin{bmatrix} T_{ss} & T_{ps} \\ T_{sp} & T_{pp} \end{bmatrix} \begin{bmatrix} E_i^s \\ E_i^p \end{bmatrix} \tag{169}$$

where E_i^s and E_r^s are the s-pol (perpendicular polarization), incident and reflected, complex electric field components, E_i^p and E_r^p are the p-pol (parallel polarization), incident and reflected, complex electric field components, and r_s and r_p are the complex Fresnel field reflection coefficients for the s- and p-pol, respectively [42, 103, 104, 112, 116, 139, 140]. Note that s- and p-polarization for E_i^s, E_r^s, E_i^p, and E_r^p are defined with respect to the macroscopic coordinate system (see Fig. 34); however, the

111

complex Fresnel field reflection coefficients are defined with respect to the microfacet coordinate system (see Fig. 35). Thus, it is necessary to perform coordinate system rotations to align the macroscopic planes of incidence and reflection with the microfacet planes of incidence and reflection. This fact explains the rotation matrices in Eq. (169). Relating the angles γ_i and γ_r to the macroscopic angles is, once again, accomplished using trigonometry [42, 103, 104, 112, 116, 139, 140]:

$$
\begin{aligned}
\cos\gamma_i &= (\cos\alpha - \cos\theta_i\cos\beta)/(\sin\theta_i\sin\beta) \\
\cos\gamma_r &= (\cos\alpha - \cos\theta_r\cos\beta)/(\sin\theta_r\sin\beta)
\end{aligned}
\tag{170}
$$

Before converting the Jones matrix into a Mueller matrix, it is important to discuss briefly the physical interpretation of the Jones scattering matrix in Eq. (169). The Jones matrix elements, T_{ss}, T_{ps}, T_{sp}, and T_{pp}, can be interpreted as modeling how s- or p-pol incident light couples into s- or p-pol reflected light. For instance, the T_{ps} element models how incident s-pol light couples into p-pol reflected light. The other elements can be interpreted in a similar manner. For scattering in the specular plane (i.e., $\phi = \pi$), intuition leads one to conclude that the Jones scattering matrix in Eq. (169) becomes diagonal, i.e., incident s-pol and incident p-pol couple into reflected s-pol and reflected p-pol, respectively. This conclusion is easily confirmed by substituting $\phi = \pi$ into Eq. (170). Converting the Jones matrix in Eq. (169) to a

Mueller matrix is performed using the analysis in Ref. [38]:

$$\mathbf{M} = \frac{1}{2} \begin{bmatrix} M_{00} & M_{01} & 0 & 0 \\ M_{01} & M_{00} & 0 & 0 \\ 0 & 0 & M_{22} & jM_{23} \\ 0 & 0 & -jM_{23} & M_{22} \end{bmatrix}$$

$$M_{00} = |T_{ss}|^2 + |T_{sp}|^2 + |T_{ps}|^2 + |T_{pp}|^2$$

$$M_{01} = |T_{ss}|^2 + |T_{sp}|^2 - |T_{ps}|^2 - |T_{pp}|^2$$

$$M_{22} = T_{ss}T_{pp}^* + T_{ss}^*T_{pp} + T_{ps}T_{sp}^* + T_{ps}^*T_{sp}$$

$$M_{23} = T_{ps}T_{sp}^* - T_{ps}^*T_{sp} - T_{ss}T_{pp}^* + T_{ss}^*T_{pp}$$

$$(171)$$

where $*$ is the complex conjugate operation. For the sake of brevity, the expressions for all 16 elements are not shown. The Mueller matrix represented in Eq. (171) occurs when observation is confined to the specular plane as is done for the measurement results presented in Section 4.4. The full expressions can be found in Refs. [42, 103, 104, 112, 116, 139, 140]. Note that the Mueller matrix in Eq. (171) has a similar physical interpretation as the Jones scattering matrix discussed above. For instance, the M_{23} element of the above Mueller matrix models how the fourth Stokes parameter (circular polarization) couples into the third Stokes parameter (linear polarization) upon reflection.

The shadowing/masking function utilized in this pBRDF is that derived by Torrance and Sparrow [128] and simplified by Blinn [15]:

$$G(\theta_i, \theta_r, \phi) = \min\left(1; \frac{2\cos\alpha\cos\theta_r}{\cos\beta}; \frac{2\cos\alpha\cos\theta_i}{\cos\beta}\right). \quad (172)$$

This expression is derived assuming that each microfacet comprises one side of a symmetric v-shaped groove (see Fig. 36). Mathematically, G determines the fraction of
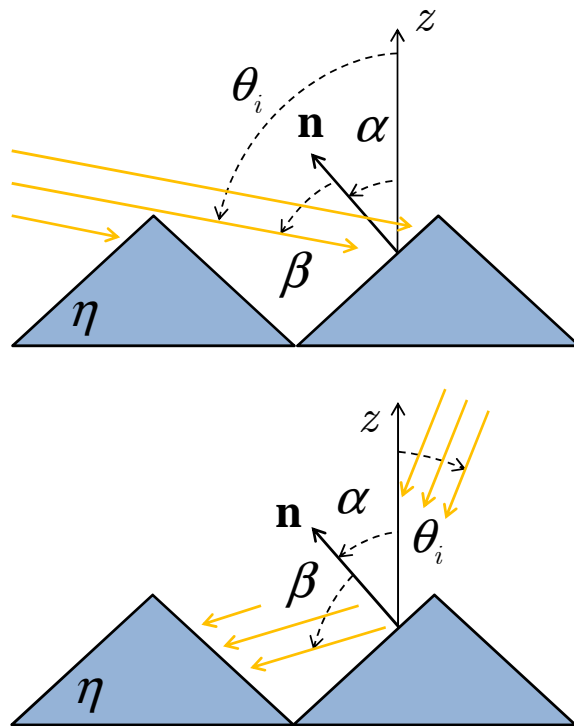
Figure 36. Scattering geometry of a v-shaped groove. The top subfigure depicts shadowing while the bottom subfigure depicts masking. Shadowing occurs when the angle of incidence approaches grazing. Similarly, masking occurs when the angle of observation nears grazing.
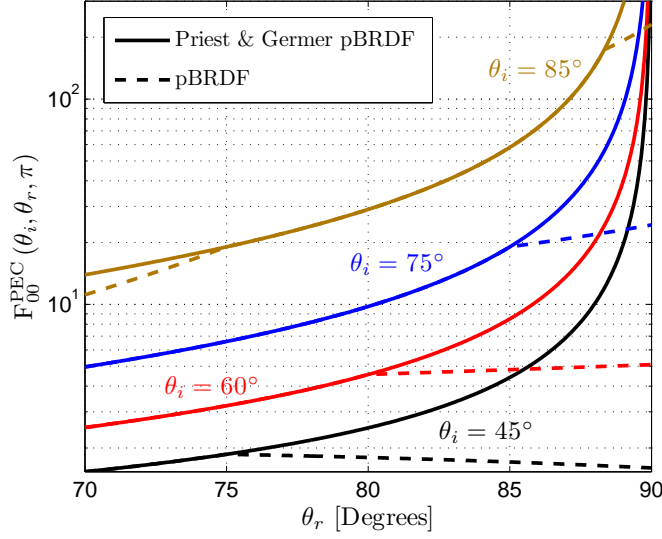
Figure 37. Comparisons of the $\mathbf{F}_{00}$ elements of the Priest and Germer pBRDF [103, 104] and the pBRDF in Eq. (173) for $\theta_i = 45°$, $60°$, $75°$, and $85°$ with $2^{1/2}\sigma_h/\ell = 0.3$. The pBRDF's are evaluated in the specular plane ($\phi = \pi$) and using a perfect reflecting surface.

an illuminated microfacet which contributes to the scattered radiance. Physically, as is evident from Fig. 36, G models the incident and reflected light blocked by adjacent microfacets. Most of the BRDF's/pBRDF's in literature include a shadowing/masking function of some form [26, 87, 119, 128, 139, 140]. The function is instrumental in keeping the BRDF bounded and thus satisfying the conservation of energy. A notable exception to this is the pBRDF of Priest and Germer [103, 104]. The lack of G causes their pBRDF to asymptotically approach infinity as the angle of incidence or observation approaches grazing [139, 140].

The desired specular component of the pBRDF can now be formed by substituting the facet distribution function P [Eq. (168)], the Mueller matrix $\mathbf{M}$ [Eq. (171)], and the shadowing/masking function G [Eq. (172)] into Eq. (166) [139, 140]:

$$\mathrm{F}_{jk}^s\left(\theta_i, \theta_r, \phi; \sigma_h, \ell; \eta\right) = \frac{\ell^2 \exp\left[-\ell^2 \tan^2\alpha/\left(4\sigma_h^2\right)\right]}{16\pi\sigma_h^2 \cos\theta_i \cos\theta_r \cos^4\alpha} G\left(\theta_i, \theta_r, \phi\right) \mathrm{M}_{jk}\left(\beta; \eta\right). \qquad (173)$$

115

Note that the form of Eq. (173) is very similar to that of Priest and Germer [103, 104] with the important difference being the addition of the shadowing/masking function G in Eq. (173). As is stated above, G plays a critical role in keeping the pBRDF bounded and thus a realistic physical model. In order to demonstrate the function's importance, consider the pBRDF predictions shown in Fig. 37. The figure shows traces comparing the F_{00} elements of the Priest and Germer pBRDF [103, 104] and the pBRDF in Eq. (173) for $\theta_i = 45°$, $60°$, $75°$, and $85°$ with $2^{1/2}\sigma_h/\ell = 0.3$. The pBRDF's are evaluated in the specular plane ($\phi = \pi$) and using a perfect reflecting surface, i.e., a perfect electric conductor (PEC). The figure clearly shows that the pBRDF in Eq. (173) remains bounded while the Priest and Germer pBRDF diverges as θ_r approaches $90°$. Having developed and discussed the specular pBRDF component, attention can now be turned to the diffuse component.

4.2.2 Diffuse pBRDF Component.

Before the diffuse component of the pBRDF can be developed, the concept of directional hemispherical reflectance (DHR) must be reviewed. The DHR is defined as the ratio of the total energy reflected into the entire hemisphere above a material surface to the total energy incident from a particular direction [38, 42, 103, 104, 112, 116, 119, 139, 140]:

$$\rho_{\text{DHR}}\left(\theta_i; \sigma_h, \ell\right) = \int\limits_{0}^{2\pi} \int\limits_{0}^{\pi/2} F_{00}\left(\theta_i, \theta_r, \phi; \sigma_h, \ell; \eta\right) \cos\theta_r \sin\theta_r \mathrm{d}\theta_r \mathrm{d}\phi. \qquad (174)$$

Note that $\rho_{\text{DHR}} \leqslant 1$, otherwise the pBRDF violates the conservation of energy (assuming a passive material). The stated condition becomes an equality when the surface is a PEC. Substituting Eq. (165) into the DHR expression and applying the

equality condition (a PEC surface) produces

$$1 = \int_0^{2\pi}\int_0^{\pi/2} F_{00}^{\text{s, PEC}} \cos\theta_r \sin\theta_r \mathrm{d}\theta_r \mathrm{d}\phi + \int_0^{2\pi}\int_0^{\pi/2} F_{00}^{\text{d, PEC}} \cos\theta_r \sin\theta_r \mathrm{d}\theta_r \mathrm{d}\phi. \qquad (175)$$

Note that Eq. (175) is a statement of the conservation of energy. The diffuse term is assumed to obey Lambert's law; thus,

$$F_{00}^{\text{d, PEC}}(\theta_i; \sigma_h, \ell) = \frac{1}{\pi}\left(1 - \int_0^{2\pi}\int_0^{\pi/2} F_{00}^{\text{s, PEC}} \cos\theta_r \sin\theta_r \mathrm{d}\theta_r \mathrm{d}\phi\right).$$

$$F_{00}^{\text{d, PEC}}(\theta_i; \sigma_h, \ell) = \frac{1}{\pi}\left[1 - \rho_{\text{DHR}}^{\text{s, PEC}}(\theta_i; \sigma_h, \ell)\right] \qquad (176)$$

Note that Eq. (176) represents the fraction of scattered light not comprising the specular lobe, or equivalently, the fraction of light which is scattered multiple times. Therefore, generalizing Eq. (176) to a surface other than a PEC is simply a matter of multiplying $F_{00}^{\text{d, PEC}}$ times M_{00} [139, 140]. Eq. (176) possesses two notable characteristics which make it an attractive model for the diffuse pBRDF component. First, it depends only on the angle of incidence and the statistical properties of the rough surface. One's intuition dictates that for a "smooth" surface light leaves the surface after a single reflection and therefore most of the scattered radiance is contained within the specular lobe. This can be verified mathematically by noting that as $\sigma_h \to 0$, the facet distribution function in Eq. (173) becomes a Dirac delta function. Substituting this expression into Eq. (176) results in $F_{00}^{\text{d}} = 0$. Likewise, as surface roughness increases, one would expect light to be scattered multiple times before leaving the material surface. Mathematically this can be verified by observing that $F_{00}^{\text{s}} \to 0$ as $\sigma_h \to \infty$. Substituting $F_{00}^{\text{s}} = 0$ into Eq. (176) produces the trivial result $F_{00}^{\text{d}} = 1/\pi$ (i.e., pure diffuse scattering). The second characteristic of note in favor of modeling the diffuse pBRDF component in the manner outlined above is that no fitted coeffi-

cients are required to model the strength of the diffuse pBRDF component. The use of coefficients, whose values are determined by fitting the BRDF to measured data, is a common feature in other BRDF's [26, 41, 42, 87, 112, 116, 128].

4.2.3 Summary of Theory.

Combining the specular pBRDF term [Eq. (173)] and the diffuse pBRDF term [Eq. (176)] produces the desired result [139, 140]

$$
\begin{aligned}
\mathrm{F}_{00}\left(\theta_{i}, \theta_{r}, \phi ; \sigma_{h}, \ell ; \eta\right) &= \mathrm{F}_{00}^{\mathrm{s}}\left(\theta_{i}, \theta_{r}, \phi ; \sigma_{h}, \ell ; \eta\right) + \frac{1}{\pi}\left[1 - \rho_{\mathrm{DHR}}^{\mathrm{s,\ PEC}}\left(\theta_{i} ; \sigma_{h}, \ell\right)\right] \mathrm{M}_{00}\left(\beta ; \eta\right) \\
\mathrm{F}_{jk}\left(\theta_{i}, \theta_{r}, \phi ; \sigma_{h}, \ell ; \eta\right) &= \mathrm{F}_{jk}^{\mathrm{s}}\left(\theta_{i}, \theta_{r}, \phi ; \sigma_{h}, \ell ; \eta\right) \quad j, k \neq 0
\end{aligned}
$$

$$(177)$$

Note that since it is assumed to be unpolarized, the diffuse component only contributes to the F_{00} element of the pBRDF Mueller matrix.

In order to show that the above expression satisfies electromagnetic reciprocity, θ_{i} and ϕ_{i} must be switched with θ_{r} and ϕ_{r}. It is easy to show that doing so produces the same expression as that in Eq. (177); thus, the pBRDF satisfies the reciprocity condition. Proving that Eq. (177) conserves energy requires one to show that $\rho_{\mathrm{DHR}} \leqslant 1$. Note that the conservation of energy is enforced when finding the value of the diffuse pBRDF component (detailed above). Therefore, Eq. (177) conserves energy as well.

Summarizing the theory, Eq. (177) possesses two characteristics which distinguishes it from existing geometrical optics pBRDF's in literature. The first is the addition of the shadowing/masking function G. As discussed above, G keeps Eq. (177) bounded and thus a realistic physical model. The second is the development of a diffuse pBRDF component. As previously stated, this component depends only on physical parameters and does not need to be fit to measured data. In the next section, predictions made using Eq. (177) of a rough PEC surface are compared to Method of
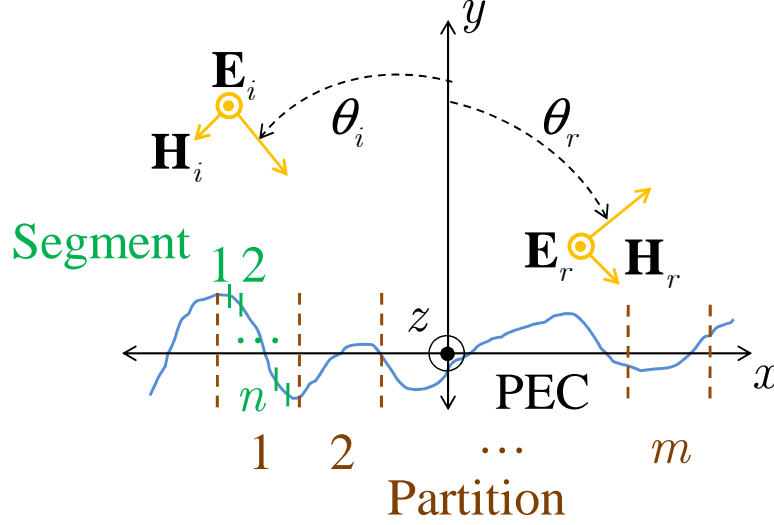
Figure 38. Scattering geometry of the MoM solutions. The surface is a $15,000\lambda$ long random (surface height is Gaussian distributed) PEC surface. The surface is assumed to be invariant in the z direction.

Moments [101] (MoM) solutions for the purpose of validating the model.

4.3   Simulation

Before analyzing the simulation results, a brief background on the MoM is warranted. The MoM is a technique to solve integral equations which arise frequently in electromagnetics. The problem of interest here is a $15,000\lambda$ long random (surface height is Gaussian distributed) PEC surface. The surface is invariant in the z direction (see Fig. 38) significantly reducing the number of unknowns in the problem. Also, as is shown in Fig. 38, only s-pol is considered here. The electric field integral equation (EFIE) for the scattering problem depicted in Fig. 38 (assuming plane wave excitation) is formulated by applying the transverse electric field boundary condition at the random PEC surface, i.e., $E_r^z = -E_i^z$:

$$\frac{\pi Z_0}{2\lambda} \int_{C'} J^z\left(\boldsymbol{\rho'}\right) H_0^{(2)}\left(\frac{2\pi}{\lambda}\left|\boldsymbol{\rho} - \boldsymbol{\rho'}\right|\right) \mathrm{d}C' = \exp\left[-\mathrm{j}\frac{2\pi}{\lambda}\left(\mathbf{k}_i \cdot \boldsymbol{\rho}\right)\right] \quad \boldsymbol{\rho} \in C' \qquad (178)$$

119

where Z_0 is the intrinsic impedance of free-space (approximately $377\,\Omega$), $\boldsymbol{\rho} = \mathbf{x}x + \mathbf{y}y$ is the observation vector, $\boldsymbol{\rho}' = \mathbf{x}x' + \mathbf{y}y'$ is the source vector, $\mathbf{k}_i = \mathbf{x}\sin\theta_i - \mathbf{y}\cos\theta_i$ is the propagation vector of the incident field, J^z is the current induced on the PEC surface by the field, and $H_0^{(2)}$ is a zeroth order Hankel function of the second kind. Note that the integral in Eq. (178) is over the parameterized surface contour denoted by C'. The unknown in Eq. (178) is the surface current J^z. Note that assuming $\mathbf{J} = 2\mathbf{n} \times \mathbf{H}_i$ forms the basis of the physical optics, or Kirchoff approximation [11, 16, 63, 136]. In the MoM, J^z is expanded in a set of basis functions (in this case, fixed width pulses):

$$J^z\left(\boldsymbol{\rho}'\right) = \sum_{n=1}^{N} \alpha_n p_n\left(\boldsymbol{\rho}'\right). \tag{179}$$

After simplification, the resulting expression is then tested using another set of functions (in this case, Dirac delta functions located at the center of each pulse) to produce an $N \times N$ matrix equation where N is the number of unknowns, i.e.,

$$\begin{bmatrix} a_{11} & a_{12} & \cdots & a_{1N} \\ a_{21} & a_{22} & \cdots & a_{2N} \\ \vdots & \vdots & \ddots & \vdots \\ a_{N1} & a_{N2} & \cdots & a_{NN} \end{bmatrix} \begin{bmatrix} \alpha_1 \\ \alpha_2 \\ \vdots \\ \alpha_N \end{bmatrix} = \begin{bmatrix} E_{i,1}^z \\ E_{i,2}^z \\ \vdots \\ E_{i,N}^z \end{bmatrix}. \tag{180}$$

Note, for example, that the $2N$ element of the MoM matrix shown above models how the Nth source current segment contributes to the scattered field at the 2nd observation segment. The other elements of the MoM matrix can be interpreted in a similar manner. Solving Eq. (180) yields the unknown current. Once J^z is computed,

the scattered field can be found at any observation point by

$$E_r^z(x, y) = \frac{\pi Z_0}{2\lambda} \sum_{n=1}^{N} \alpha_n \int_{C_n'} H_0^{(2)} \left(\frac{2\pi}{\lambda} |\boldsymbol{\rho} - \boldsymbol{\rho}'| \right) dC_n'$$

$$\lim_{\rho \to \infty} E_r^z(\rho, \theta_r) = \frac{Z_0}{2\sqrt{\rho\lambda}} \exp\left[-j \left(\frac{2\pi}{\lambda} \rho - \frac{\pi}{4} \right) \right] \tag{181}$$

$$\sum_{n=1}^{N} \alpha_n \int_{C_n'} \exp\left[j\frac{2\pi}{\lambda} (x' \sin \theta_r + y' \cos \theta_r) \right] dC_n'$$

where C_n' is the segment of the parameterized contour represented by the nth pulse and $\rho = (x^2 + y^2)^{1/2}$ is the Euclidean distance from the origin. The second line of the above expression assumes that the observation point ρ is in the far-field as defined by Fraunhofer [16]. Note that the MoM solution shown above is a coherent field solution. Since the incoherent solution is the one desired, the $15,000\lambda$ surface is divided up into $M = 100$ partitions and the scattered field from each partition is summed incoherently [6, 23, 40, 125]. Also, in order to minimize the effect of edge diffraction from the surface partitions, i.e., approximate an infinite surface, J^z is windowed using a Gaussian taper:

$$W_m(x) = \exp\left[-\left(\frac{x - x_m}{w} \right)^2 \right], \tag{182}$$

where the index m represents the mth surface partition, x_m is the center of the mth partition, and w is the taper width [6, 23, 40, 125]. The incoherent far-field reflectance distribution can now be found from

$$\sigma(\theta_r) = \frac{1}{w\sqrt{\pi/2}} \left(\frac{1}{M} \lim_{\rho \to \infty} 2\pi\rho \sum_{m=1}^{M} \left| E_{r,m}^z \right|^2 \right), \tag{183}$$

where $E_{r,m}^z$ is the scattered field from the mth partition [6, 23, 40, 125]. Note that the above expression is the average incoherent radar cross section (RCS) of the random
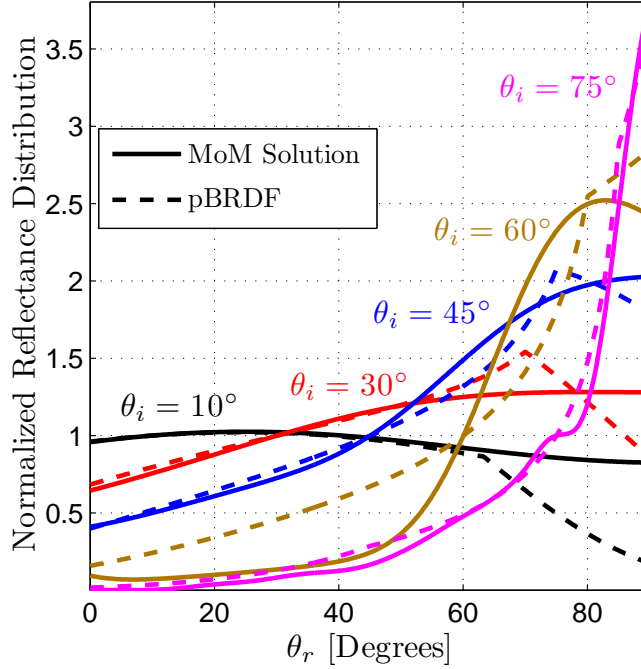
Figure 39. Comparisons of the reflectance distributions predicted by MoM solutions of a $15,000\lambda$ long random (surface height is Gaussian distributed) PEC surface with those of the pBRDF in Eq. (177) for $\theta_i = 10°$, $30°$, $45°$, $60°$, and $75°$ and $2^{1/2}\sigma_h/\ell = 0.3$. Note that the reflectance distributions in the figure are normalized with respect to their values at the specular angles $(\theta_i = \theta_r)$. Observation for both the MoM and the pBRDF predictions is in the specular plane $(\phi = \pi)$.

PEC surface normalized by the effective illumination length. Detailed analysis of these steps can be found in Refs. [6, 23, 40, 125]. Having provided the necessary background on the MoM, attention can now be turned to the simulation results.

The simulation results are shown in Fig. 39. As mentioned above, the simulation surface is a $15,000\lambda$ long random (surface height is Gaussian distributed) PEC surface. The Gaussian surface is generated as shown in Ref. [40] with roughness equal to $2^{1/2}\sigma_h/\ell = 0.3$. The traces on the figure are far-field reflectance distributions for $\theta_i = 10°$, $30°$, $45°$, $60°$, and $75°$. Note that the reflectance distributions in the figure are normalized with respect to their values at the specular angles $(\theta_i = \theta_r)$, and observation for both the MoM and pBRDF predictions is in the specular plane $(\phi = \pi)$. Overall, the pBRDF predictions match very well with the exact MoM

solutions. At some incident angles, the pBRDF predictions deviate from the MoM solutions; however, there is almost unanimous agreement between the pBRDF and MoM solutions on the locations and magnitudes of reflectance maxima. Note that ripples are visible in the MoM solution traces for $\theta_i = 45°$, $60°$, and $75°$. These ripples are caused by constructive and destructive interference in the scattered field. Incoherent scatter should not interfere; however, as discussed above, the MoM solution is coherent. The incoherent scatter is being approximated by summing the scattered field incoherently over 100 partitions of the entire $15,000\lambda$ surface. Although this should be sufficient [6], some interference is still occurring. Summing the scattered field incoherently over more partitions should lessen the interference ripples; however, the cost is a longer simulation run time. The results shown here are sufficient to demonstrate the validity of the pBRDF. In the next section, Mueller matrix element predictions made using Eq. (177) are compared to experimental measurement results in order to further validate the pBRDF.

4.4   Mueller Matrix Measurement Results

The instrument used to collect the Mueller matrix data presented here is an ellipsometer [127] at the Air Force Research Laboratory (AFRL), Wright-Patterson Air Force Base, Ohio. A photograph of the ellipsometer is shown in Fig. 40. It, like all ellipsometers, consists of two arms—the polarization state generator (PSG) and the polarization state analyzer (PSA). The material under test (MUT) is placed in between the PSG and PSA in a sample holder which is able to rotate. The PSG of the instrument shown in Fig. 40 consists of a 1064 nm laser followed by polarization optics mounted on a stationary optical rail. Note that the polarization state of the laser is set using a polarizing beam splitter. The PSG polarization optics consist of two half-wave plates (HWP) and a quarter-wave plate (QWP). They are contained
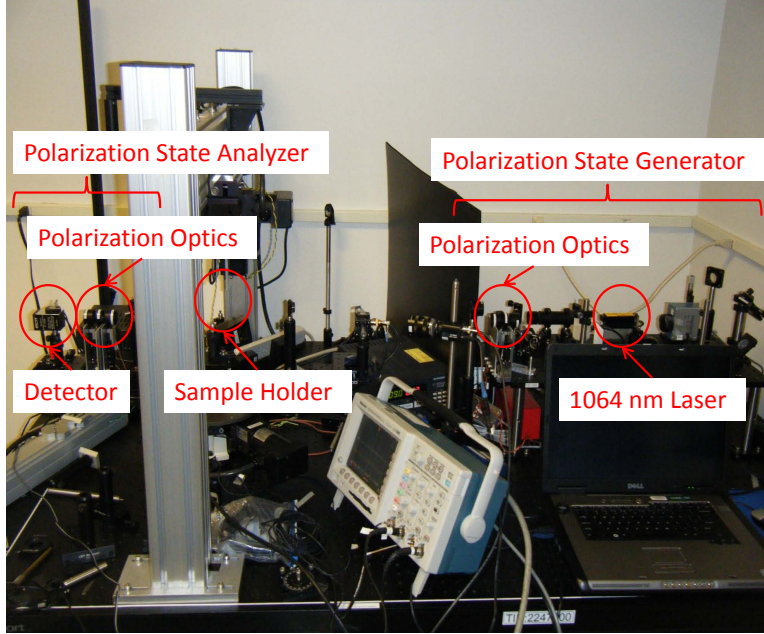
Figure 40. Photograph of the Mueller matrix ellipsometer used in this experiment. The ellipsometer is located at the Air Force Research Laboratory, Wright-Patterson Air Force Base, Ohio.

within a mechanical housing which allows them to be moved precisely into and out of the source beam. This allows the PSG to generate four-independent polarization states to interrogate the MUT. As is common, the PSA of the ellipsometer shown in Fig. 40 is a mirror image of the PSG. It consists of a set of polarization optics followed by a horizontal linear polarizer and a detector mounted on a rotating base. The PSA is able to rotate independently of the MUT sample holder, thus allowing any (θ_i, θ_r) to be measured. The polarization optics used in the PSA are identical to and are contained within the same type of mechanical housing as that of the PSG. This allows the PSA to analyze four-independent polarization states. Overall, the instrument is able to make 16-independent polarimetric measurements of a MUT, thereby providing all the necessary information to deduce the MUT's Mueller matrix.

Before the MUT is measured, the instrument is calibrated using the Eigenvalue Calibration Method (ECM) [25]. The ECM is a calibration technique developed by Compain *et al.* [25] in which the Mueller matrices of a set of known standards are
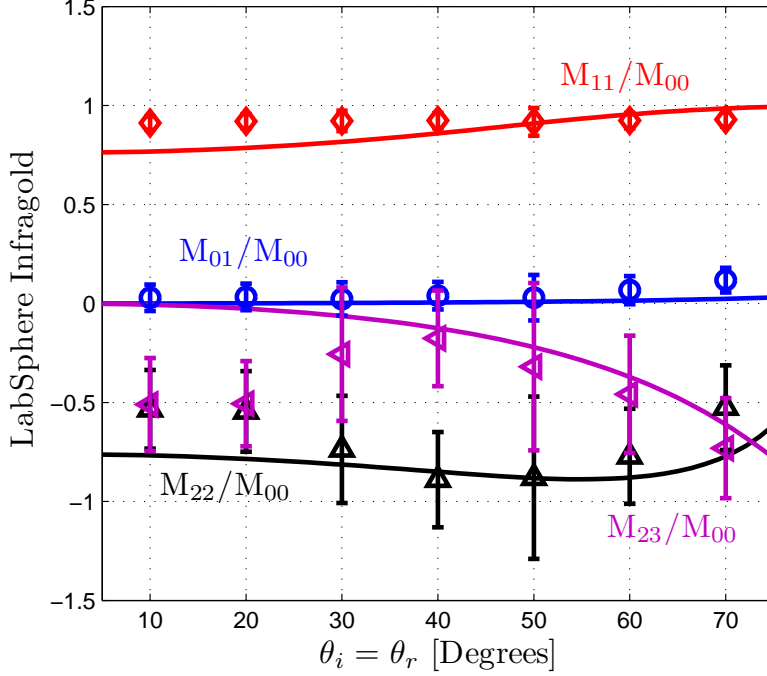
Figure 41. Mueller matrix measurement results for LabSphere Infragold [72] compared to predictions made using the pBRDF. The measurement results are plotted as symbols; the pBRDF predictions are plotted as solid lines. Note that the measurements are made in the specular plane ($\phi = \pi$). The complex index of refraction used for gold is $\eta = 0.285 - j7.3523$ [76] and $2^{1/2}\sigma_h/\ell = 0.44$. The plotted values for the measured Mueller matrix elements of LabSphere Infragold are the means of 256 irradiance measurements. The bars on the figure represent $\pm 1\sigma$, i.e., one standard deviation of those 256 measurements.

measured in order to compute the experimental Mueller matrices for the PSG and PSA. Once these matrices have been determined (see Ref. [25] for details), the desired Mueller matrix of the MUT can be found by

$$\mathbf{M} = \mathbf{A}^{-1}\mathbf{S}\mathbf{W}^{-1} \tag{184}$$

where $\mathbf{S}$ is a 4×4 matrix of measured (ellipsometric) irradiances, $\mathbf{W}$ is the experimental Mueller matrix of the PSG, and $\mathbf{A}$ is the experimental Mueller matrix of the PSA. In the measurement results presented here, the standards used to calibrate the ellipsometer are a no sample measurement, a linear polarizer (LP), and a QWP. The LP is measured at 0°, 60°, and 120°; the QWP is measured at 45°.
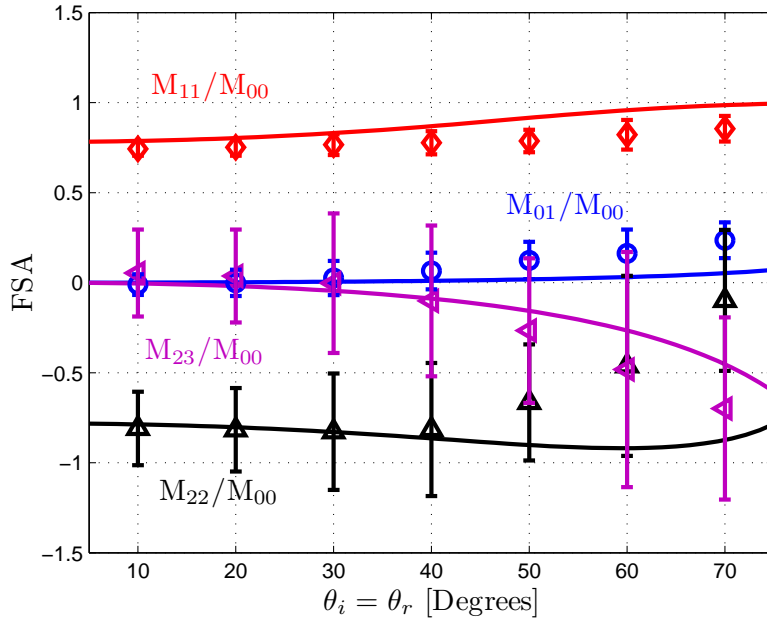
Figure 42. Mueller matrix measurement results for flame sprayed aluminum (FSA) compared to predictions made using the pBRDF. The measurement results are plotted as symbols; the pBRDF predictions are plotted as solid lines. Note that the measurements are made in the specular plane ($\phi = \pi$). The complex index of refraction used for aluminum is $\eta = 1.226 - \mathbf{j}10.413$ [76] and $2^{1/2}\sigma_h/\ell = 0.43$. The plotted values for the measured Mueller matrix elements of FSA are the means of 256 irradiance measurements. The bars on the figure represent $\pm 1\sigma$, i.e., one standard deviation of those 256 measurements.

126

The Mueller matrix measurement results are shown in Figs. 41 and 42. Figure 41 shows the Mueller matrix measurement results for LabSphere Infragold [72]. The complex index of refraction for gold ($\eta = 0.285 - j7.3523$) is obtained from Ref. [76]. The figure shows the experimental M_{01}, M_{11}, M_{22}, and M_{23} elements compared to predictions made using the pBRDF in Eq. (177). Note that all measurements are made in the specular plane ($\phi = \pi$), and the Mueller matrix elements are normalized with respect to the M_{00} element as annotated on the figure. The plotted values for the measured Mueller matrix elements of LabSphere Infragold are the means of 256 irradiance measurements. The bars on the figure represent $\pm 1\sigma$, i.e., one standard deviation of those 256 measurements. Note that the LabSphere Infragold results are consistent with those published by Priest and Meier [104]. Although there are discrepancies between the measured Mueller matrix elements and the pBRDF (especially at 10° and 20°), the pBRDF predictions agree well with the measurements. The most important aspect of the results is that the pBRDF captures the trend of the data (i.e., the physics of the material surface interaction) as the observation angle (or equivalently incident angle) approaches grazing.

Figure 42 shows the Mueller matrix measurement results for flame sprayed aluminum (FSA). The complex index of refraction for aluminum is $\eta = 1.226 - j10.413$ [76]. Shown in the figure are the same Mueller matrix elements as Fig. 41. As before, all measurements are made in the specular plane ($\phi = \pi$), and the Mueller matrix elements are normalized with respect to the M_{00} element. Once again, the plotted values for the measured Mueller matrix elements of FSA are the means of 256 irradiance measurements. The bars on the figure represent $\pm 1\sigma$ of those 256 measurements. As is the case in Fig. 41, discrepancies do exist between the measured data and the pBRDF predictions; however, the pBRDF, once again, captures the trend of the measured data.

Before concluding, it is worth discussing a possible cause of the discrepancies observed in Figs. 41 and 42. It is assumed that the published values of η for gold and aluminum are accurate for the LabSphere Infragold and FSA samples measured in this experiment. As noted in Ref. [76], the value of η can vary greatly depending on sample quality, sample preparation, or measurement technique. If, instead of using the published values for η, the best values for η are found via nonlinear least squares, one obtains for LabSphere Infragold $\eta = 0.4364 - j5.2526$ and for FSA $\eta = 0.8886 - j3.4602$. While it is possible that the best-fit index for LabSphere Infragold could be more representative of the true η value for the specimen (considering how LabSphere Infragold is manufactured [72]), the best-fit FSA index is more difficult to explain. One possibility is that the FSA specimen used in this experiment is slightly oxidized (i.e., a thin coating of Al_2O_3). This hypothesis would explain the sharper than predicted rise in the measured M_{22}/M_{00} element in Fig. 42.

4.5   Conclusion

In this chapter, a geometrical optics pBRDF is presented. As discussed, the pBRDF is composed of a specular (single reflection) component and a diffuse (multiple reflection) component. The specular component, derived using the microfacet surface model [128], is shown to consist of a facet distribution function, a Mueller matrix modeling the polarimetric scattering from the material surface, and a visibility (shadowing/masking) function. Each one of these constituent functions is discussed in detail. The diffuse component is derived using the DHR and the conservation of energy. It is shown that a diffuse pBRDF component derived in this fashion depends only on geometrical parameters (angle of incidence, surface height standard deviation, and surface correlation length) and does not require coefficients fit to measured data. Taken as a whole (i.e., adding the specular and diffuse components), the pBRDF is

shown to satisfy electromagnetic reciprocity and the conservation of energy. Lastly, in order to validate the pBRDF, predictions made using the pBRDF are compared to MoM solutions of a rough PEC surface and experimental Mueller matrix data for two rough metallic samples. It is shown, via these results, that the pBRDF accurately models the physics of the light/material surface interaction.

The pBRDF presented in this chapter possesses two characteristics which distinguishes it from existing geometrical optics pBRDF's in literature. The first is the addition of the visibility (shadowing/masking) function. As shown and discussed, the visibility function keeps the pBRDF bounded and thus a realistic physical model. The second is the development of a diffuse pBRDF component. This component allows for better modeling of rough reflective surfaces which tend to depolarize light via multiple surface reflections.

V. Material Classification Using Polarimetric Imagery Degraded by Atmospheric Turbulence

The contents of this chapter were accepted for publication in *IEEE Transactions on Geoscience and Remote Sensing* on 13 June 2010.

5.1 Introduction

Polarization-based material-classification techniques can generally be divided into two types—active polarimetric and passive polarimetric techniques. Active polarimetry is the measure of the polarization state of scattered light when the source excitation is controlled. Examples of material-classification (and characterization) techniques using active polarimetry can be found in Refs. [21, 48, 49, 81, 82, 83, 90, 98, 102, 113, 120, 124, 127, 129, 131, 134]. Passive polarimetry, most relevant to the work presented here, is the measure of the polarization state of scattered light when the source excitation is uncontrolled. In most cases, the source excitation is considered to be spatially incoherent and unpolarized, e.g., the sun. Since this scenario is the one most often encountered in remote sensing, there is a great deal of research in this area. A review of the available research yields index-of-refraction-based material-classification (and characterization) techniques [122, 123], a degree-of-linear-polarization (DOLP)-based method [126], algorithms based on the measured Fresnel ratio [141, 142, 143, 144], and multispectral polarimetric methods [17, 20, 66, 147]. While an extensive body of material-classification research and techniques exists, to the author's knowledge a solution to the problem of polarization-based material classification using images degraded by atmospheric turbulence has not been proposed.

In this chapter, a material-classification technique using polarimetric imagery degraded by atmospheric turbulence is presented (see Fig. 43). The classification tech-

nique described here determines whether an object is composed of dielectric or metallic materials. The technique uses a variant of the polarimetric maximum-likelihood blind-deconvolution algorithm developed by LeMaster and Cain [74] to recover the true object's irradiance (i.e., the first Stokes parameter), the DOLP, the angle of polarization (AOP), and the polarimetric-image point spread functions (PSF's) from turbulence-degraded imagery. Added to LeMaster and Cain's algorithm are two novel DOLP priors (defined and discussed later), one representative of a dielectric and the other representative of a metal. The DOLP estimate which maximizes the log-likelihood function determines whether the image pixel is classified as a dielectric or a metal. The proposed material-classification technique assumes that the object is illuminated with spatially incoherent and unpolarized light (i.e, passive polarimetry) as depicted in Fig. 43. As a result of this assumption, circular polarization can generally be ignored [27]. It should be noted that this assumption is invalid when dealing with circularly dichroic materials which are encountered in biological applications [2, 30]. Another assumption of this work is that the unknown material must be able to produce polarized scatter from unpolarized illumination, i.e., the material must have some diattenuation. The proposed technique is not designed to handle diffuse scatterers or materials which are purely retarding. This assumption limits the location of the observer to somewhere near the specular plane (defined and explained below). In addition to this observational requirement, the proposed technique also requires that the incident θ_i and observation θ_r angles be off normal, i.e., $\theta_i, \theta_r > 30°$. This is due to the fact that natural materials weakly polarize scattered light at near-normal collection geometries. This limitation of the proposed technique is discussed in more detail below. Note that these assumptions are common in existing polarimetric material-classification techniques [20, 122, 123, 126, 141, 142, 143, 144, 147].
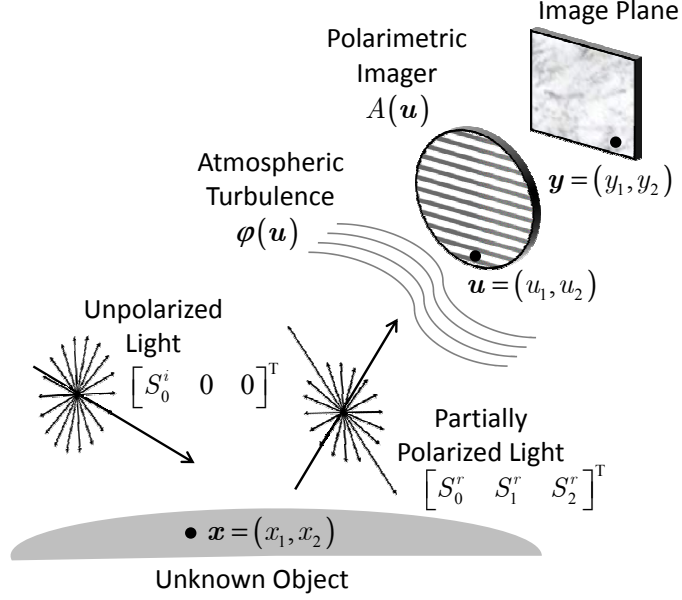
Figure 43. Measurement geometry of proposed material-classification technique. Unpolarized light with Stokes vector $\begin{bmatrix} S_0^i & 0 & 0 \end{bmatrix}^{\mathbf{T}}$ illuminates an unknown object. Upon reflection, the light is partially polarized with Stokes vector $\begin{bmatrix} S_0^r & S_1^r & S_2^r \end{bmatrix}^{\mathbf{T}}$, is distorted by atmospheric turbulence with random phase distribution $\varphi(u)$, and is received by a polarimetric sensor of aperture $A(u)$.

In the next section, the LeMaster and Cain algorithm is reviewed. The modified form of the LeMaster and Cain algorithm necessary for this research effort is also presented and discussed. In addition to presenting the blind-deconvolution algorithm, a discussion of the novel dielectric and metallic DOLP priors, particulary, how they are formed and their mathematical representations is presented. In Section 5.3, experimental results of the material-classification technique are presented and discussed in order to validate the algorithm. Lastly, the chapter is concluded with a summary of the research presented.

5.2 Theory

This section provides a review of the LeMaster and Cain [74] blind-deconvolution algorithm which is an integral part of the material-classification technique. The algorithm is a maximum-likelihood blind-deconvolution algorithm (see Ref. [70] for back-

ground) for spatially incoherent polarimetric imagery and is a generalization of the multiframe blind-deconvolution algorithm developed by Schulz [114]. The algorithm, as presented in Ref. [74] and in Chapter III, estimates the polarized and unpolarized image components of a scene, as well as the AOP and polarimetric-image PSF's [44]. For use in the proposed classification technique, it is more convenient to have the algorithm estimate the first Stokes parameter S_0, the DOLP, the AOP, and the image PSF's. This form of the LeMaster and Cain algorithm is the one discussed below. In addition to the algorithm review, modification of the LeMaster and Cain algorithm to include a DOLP prior is also shown and discussed. Subsection 5.2.2 provides the physical insight and discusses the mathematical forms of the dielectric and metallic DOLP priors used to make the classification decision. Lastly, this section concludes with a summary of the theoretical work presented.

It should be noted before beginning the deconvolution algorithm review that if the inner scale of atmospheric turbulence (typically a few millimeters) is much larger than the wavelength of the field, the polarization state of the transmitted field is not affected [5, 63, 111]. For optical wavelengths, this is typically the case. The negligible effect of atmospheric turbulence on polarization state was recently verified experimentally by Toyoshima *et al.* [130]. Although turbulence does not alter the polarization state of passing light, it does have the effect of mixing scattered light from different parts of the object of interest (i.e., blurring). LeMaster and Cain's deconvolution algorithm serves to demix the scattered light.

5.2.1 Review of LeMaster and Cain's Polarimetric Blind-Deconvolution Algorithm.

It is easily shown that the irradiance received through a linear polarizer is

$$
\begin{aligned}
I\left(\theta\right) &= \frac{1}{2}S_0 + \frac{1}{2}S_1\cos 2\theta + \frac{1}{2}S_2\sin 2\theta \\
&= \frac{1}{2}\left(1 - \mathcal{P}\right)S_0 + \mathcal{P}S_0\cos^2\left(\alpha - \theta\right)
\end{aligned}
\tag{185}
$$

where S_0, S_1, and S_2 are the first three Stokes parameters, $\mathcal{P}$ is the DOLP, α is the AOP, and θ is the angular orientation of the linear polarizer [16]. Note that the first and second terms on line 2 of Eq. (185) are the unpolarized and polarized contributions to the irradiance, respectively. Incorporating the effects of the viewing aperture and the atmosphere is accomplished via the parameterized form of the PSF:

$$
h\left(\boldsymbol{y} - \boldsymbol{x}\right) = \left|\sum_{\boldsymbol{u}} A\left(\boldsymbol{u}\right)\exp\left[\mathrm{j}\varphi\left(\boldsymbol{u}\right)\right]e^{-\mathrm{j}2\pi\kappa\boldsymbol{u}\cdot\left(\boldsymbol{y}-\boldsymbol{x}\right)}\right|^2
\tag{186}
$$

where $\varphi\left(\boldsymbol{u}\right)$ models the random phase effects caused by propagation through the atmosphere, $A\left(\boldsymbol{u}\right)$ is the aperture function of the imaging system (radius r)

$$
A\left(\boldsymbol{u}\right) = \begin{cases} 1 & |\boldsymbol{u}| \leqslant r \\ 0 & |\boldsymbol{u}| > r \end{cases},
\tag{187}
$$

and κ is a constant related to the wavelength and the spatial sampling frequency (i.e., the spatial wavenumber). Since modern cameras collect data over a discrete grid and solutions are formed on a digital computer, the above expression for the PSF [Eq. (186)] is represented as a discrete sum rather than an integral [114]. Note that $\boldsymbol{x}$ represents an object-plane pixel pair (x_1, x_2), $\boldsymbol{y}$ represents an image-plane pixel pair (y_1, y_2), and $\boldsymbol{u}$ represents an aperture-plane pixel pair (u_1, u_2) as depicted

in Fig. 43. The noiseless image, or irradiance received at the camera, is the irradiance received through a linear polarizer [Eq. (185)] convolved with the PSF [Eq. (186)]:

$$
\begin{aligned}
i_n\left(\boldsymbol{y}\right) = & \sum_{\boldsymbol{x}} \frac{1}{2}\left[1 - \mathcal{P}\left(\boldsymbol{x}\right)\right] S_0\left(\boldsymbol{x}\right) h_n\left(\boldsymbol{y} - \boldsymbol{x}\right) \\
& + \sum_{\boldsymbol{x}} \mathcal{P}\left(\boldsymbol{x}\right) S_0\left(\boldsymbol{x}\right) \cos^2\left[\alpha\left(\boldsymbol{x}\right) - \theta_n\right] h_n\left(\boldsymbol{y} - \boldsymbol{x}\right)
\end{aligned}
\tag{188}
$$

where the index n is introduced to represent the nth of N total polarimetric images. The index is included on the PSF h to allow for the possibility that the turbulence varies from polarimetric image to polarimetric image. Note that Eq. (188), being noiseless, is never attained experimentally. Two of the more common camera noise sources responsible for its corruption are readout noise and shot, or photon noise. In LeMaster and Cain's algorithm, shot noise is assumed to be the dominant noise source [74]. Shot noise is caused by the random arrival times of individual photons at the camera's detector array [44]. The number of photons which arrive in a given time is Poisson distributed; thus, the photon count at a certain grid location in the camera's detector array is a Poisson random variable [44]. Let $d_n\left(\boldsymbol{y}\right)$ (i.e., the measured polarimetric images) be defined as the photon count at location $\boldsymbol{y}$ in the nth polarimetric image. Note that $d_n\left(\boldsymbol{y}\right)$ is a Poisson random variable with mean equal to i_n, namely,

$$
\mathrm{E}\left[d_n\left(\boldsymbol{y}\right)\right] = i_n\left(\boldsymbol{y}\right)
\tag{189}
$$

where $i_n\left(\boldsymbol{y}\right)$ is assumed to be in units of photon counts.

Maximizing the likelihood of $d_n\left(\boldsymbol{y}\right)$ directly is impractical [74]; thus, the problem is reformulated using the expectation-maximization (EM) algorithm (see Ref. [94] for details). In accordance with the requirements of the algorithm, the incomplete data $d_n\left(\boldsymbol{y}\right)$ (the measured images themselves) are represented as the aggregate of the complete data. In this case, the complete data are the unpolarized and polarized

components, $\tilde{d}_{un}(\boldsymbol{y}, \boldsymbol{x})$ and $\tilde{d}_{pn}(\boldsymbol{y}, \boldsymbol{x})$, of $d_n(\boldsymbol{y})$ such that

$$
\begin{aligned}
d_n(\boldsymbol{y}) &= \sum_{\boldsymbol{x}} \tilde{d}_{un}(\boldsymbol{y}, \boldsymbol{x}) + \sum_{\boldsymbol{x}} \tilde{d}_{pn}(\boldsymbol{y}, \boldsymbol{x}) \\
\mathrm{E}\left[\tilde{d}_{un}\right] &= \frac{1}{2}(1 - \mathcal{P}) S_0 h_n \\
\mathrm{E}\left[\tilde{d}_{pn}\right] &= \mathcal{P} S_0 \cos^2(\alpha - \theta_n) h_n
\end{aligned}
\tag{190}
$$

where, for notational convenience, the variable dependencies in the bottom two expressions of Eq. (190) are omitted. Note that $\tilde{d}_{un}(\boldsymbol{y}, \boldsymbol{x})$ and $\tilde{d}_{pn}(\boldsymbol{y}, \boldsymbol{x})$ are also Poisson distributed. Hence, the complete-data log-likelihood function is

$$
\begin{aligned}
L^{\mathrm{CD}} &= L_u^{\mathrm{CD}}(\mathcal{P}, S_0, h_n) + L_p^{\mathrm{CD}}(\mathcal{P}, S_0, \alpha, h_n) + L_{\mathrm{prior}}^{\mathrm{CD}}(\mathcal{P}) \\
L_u^{\mathrm{CD}} &= \sum_n \sum_{\boldsymbol{y}} \sum_{\boldsymbol{x}} \tilde{d}_{un} \ln\left[\frac{1}{2}(1 - \mathcal{P}) S_0 h_n\right] \\
&\quad - \sum_n \sum_{\boldsymbol{y}} \sum_{\boldsymbol{x}} \frac{1}{2}(1 - \mathcal{P}) S_0 h_n \\
L_p^{\mathrm{CD}} &= \sum_n \sum_{\boldsymbol{y}} \sum_{\boldsymbol{x}} \tilde{d}_{pn} \ln\left[\mathcal{P} S_0 \cos^2(\alpha - \theta_n) h_n\right] \\
&\quad - \sum_n \sum_{\boldsymbol{y}} \sum_{\boldsymbol{x}} \mathcal{P} S_0 \cos^2(\alpha - \theta_n) h_n \\
L_{\mathrm{prior}}^{\mathrm{CD}} &= \sum_n \sum_{\boldsymbol{y}} \sum_{\boldsymbol{x}} \ln\left[\Pi(\mathcal{P})\right]
\end{aligned}
\tag{191}
$$

The function Π is the polarization prior and does not appear in LeMaster and Cain's complete-data log-likelihood function. It is formulated in the next subsection. In Eq. (191), $\mathcal{P}$, S_0, α, and h_n are the desired parameters; they are considered to be deterministic. The random quantities in Eq. (191) are the complete data $\tilde{d}_{un}(\boldsymbol{y}, \boldsymbol{x})$ and $\tilde{d}_{pn}(\boldsymbol{y}, \boldsymbol{x})$.

It should be noted that adding the polarization prior onto LeMaster and Cain's log-likelihood function, as is done in Eq. (191), changes the $\mathcal{P}$ estimate from an ML

estimate to a maximum *a posteriori* (MAP) estimate [137]. In MAP estimation, the log-likelihood function is generally the sum of two PDF's (actually, the natural logs of the PDF's) [137]. The first PDF is the probability density function of the measured data conditioned on the sought parameter. In Eq. (191), this PDF is the sum of the L_u^{CD} and L_p^{CD} terms. The second PDF is the probability density function of the sought parameter. This is the polarization prior term in Eq. (191). If $\Pi(\mathcal{P}) = 0$, the MAP $\mathcal{P}$ estimate becomes an ML estimate as originally presented in LeMaster and Cain [74]. The reader is referred to Ref. [137] for more information on MAP estimation.

Calculating the conditional expectation of the complete-data log-likelihood (i.e, the first step of the EM algorithm),

$$Q^{i+1}(\mathcal{P}, S_0, \alpha, h_n) = \\ \mathrm{E}\left[L^{\mathrm{CD}}(\mathcal{P}, S_0, \alpha, h_n)\,|d_n, \mathcal{P}^i, S_0^i, \alpha^i, h_n^i\right] \tag{192}$$

produces the objective function Q. The index i represents the EM algorithm iteration count; thus, $\mathcal{P}^i$ is the estimated DOLP value after the ith iteration. Note, as mentioned above, the only random quantities in the log-likelihood function [Eq. (191)] are the complete data. Therefore, the expectation in Eq. (192) can be brought inside the summations and applied to the complete data:

$$\mathrm{E}\left[\tilde{d}_{un}|d_n, \mathcal{P}^i, S_0^i, \alpha^i, h_n^i\right] = \psi_{un}^{i+1}(\boldsymbol{y}, \boldsymbol{x}) \\ = \frac{1}{2}\frac{d_n}{i_n^i}\left(1 - \mathcal{P}^i\right)S_0^i h_n^i \\ \mathrm{E}\left[\tilde{d}_{pn}|d_n, \mathcal{P}^i, S_0^i, \alpha^i, h_n^i\right] = \psi_{pn}^{i+1}(\boldsymbol{y}, \boldsymbol{x}) \\ = \frac{d_n}{i_n^i}\mathcal{P}^i S_0^i \cos^2\left(\alpha^i - \theta_n\right)h_n^i \tag{193}$$

where, for brevity, $\psi_{un}^{i+1}(\boldsymbol{y}, \boldsymbol{x})$ and $\psi_{pn}^{i+1}(\boldsymbol{y}, \boldsymbol{x})$ are introduced to represent the condi-

tional expectations. The full expression for the objective function Q can be formed by substituting the above expressions into Eq. (191) for the complete data $\tilde{d}_{un}(\boldsymbol{y}, \boldsymbol{x})$ and $\tilde{d}_{pn}(\boldsymbol{y}, \boldsymbol{x})$. For the sake of brevity, the full functional form of Q is not shown here.

Maximizing Q with respect to the estimated parameters $\mathcal{P}$, S_0, α, and h_n (i.e., step two of the EM algorithm) at pixel location $\boldsymbol{x}_0$ produces

$$0 = \mathcal{P}(1-\mathcal{P})\sum_n \sum_{\boldsymbol{y}} \frac{1}{\Pi(\mathcal{P})} \frac{\mathrm{d}\Pi(\mathcal{P})}{\mathrm{d}\mathcal{P}}$$

$$-\mathcal{P}\sum_n \sum_{\boldsymbol{y}} \left(\psi_{un}^{i+1} + \psi_{pn}^{i+1}\right) + \sum_n \sum_{\boldsymbol{y}} \psi_{pn}^{i+1}$$

$$S_0 = \frac{2}{N} \sum_n \sum_{\boldsymbol{y}} \left(\psi_{un}^{i+1} + \psi_{pn}^{i+1}\right) \qquad (194)$$

$$0 = \sum_n \sum_{\boldsymbol{y}} \psi_{pn}^{i+1} \tan(\alpha - \theta_n)$$

$$h_n(\boldsymbol{z}) = \frac{1}{D_n} \sum_{\boldsymbol{y}} \left[\psi_{un}^{i+1}(\boldsymbol{y}, \boldsymbol{y} - \boldsymbol{z}) + \psi_{pn}^{i+1}(\boldsymbol{y}, \boldsymbol{y} - \boldsymbol{z})\right]$$

where $\boldsymbol{z} = \boldsymbol{y} - \boldsymbol{x}_0$ has been substituted into the update equation for h_n and $D_n = \sum_{\boldsymbol{y}} d_n(\boldsymbol{y})$. Note that to arrive at the above expressions, the polarizer angles θ_n must be chosen such that they are evenly spaced between $0°$ and $180°$. As discussed in Ref. [132], this set of polarimeter measurements optimizes SNR. The update equations for an arbitrary set of polarizer angles are given in Ref. [74] and in Chapter III. Note that these expressions are coupled among the parameters of interest, namely, S_0, $\mathcal{P}$, α, and h_n, and are more difficult to solve. Also inherent in the above expressions is the requirement that $\sum_{\boldsymbol{x}} h_n(\boldsymbol{x}) = 1$. Note that the update equation for h_n is equivalent to that derived by Schulz (Eq. (43) in Ref. [114] and Eqs. (149) and (150) in Chapter III); thus, Schulz's PSF estimator is directly incorporated. A more explicit form for the AOP update equation [third expression in Eq. (194)] can be found in Ref. [74] and in Chapter III. To arrive at that form requires more algorithm background, which

for the sake of brevity, is not included here. This concludes the summary and DOLP prior modification of LeMaster and Cain's blind-deconvolution algorithm. In the next subsection, the mathematical expressions of the novel DOLP priors are presented and discussed.

5.2.2 DOLP Priors.

A prior, in essence, is information one possesses about the solution of an estimated parameter. A prior serves to weight certain estimates more than others, thereby steering the estimation algorithm to search for solutions in certain regions of the parameter space. In this subsection, two priors for the DOLP estimate are formulated—one physically representative of the DOLP values obtained from dielectric materials and the other physically representative of the DOLP values obtained from metallic materials. To formulate these priors, one must understand how these materials polarize light. In very general terms, dielectrics strongly polarize scattered light, whereas metals weakly polarize scattered light. This simple observation forms the basis of several other material-classification techniques [21, 126, 141, 142, 143, 144].

To derive mathematical expressions for the DOLP priors of these material classes, the DOLP's for a representative sample of metals and dielectrics are predicted using a pBRDF [62, 139, 140] (see Chapter IV). Using a pBRDF to predict the DOLP's permits several different variables, like surface roughness $2^{1/2}\sigma_h/\ell$ (defined in Chapter IV), lighting (source) direction θ_i, and observation direction (θ_r, ϕ), to be considered. Figure 44 shows the pBRDF (Eq. (177) in Chapter IV) calculated DOLP's for aluminum (Figs. 44a and 44b), iron (Figs. 44c and 44d), glass (Figs. 44e and 44f), and Teflon (Figs. 44g and 44h). The angle of incidence θ_i in all the figures is 45°. The leftmost figures, Figs. 44a, 44c, 44e, and 44g, show the calculated DOLP's when the surface roughness is $2^{1/2}\sigma_h/\ell = 0.1$. The rightmost figures, Figs. 44b, 44d, 44f, and 44h,
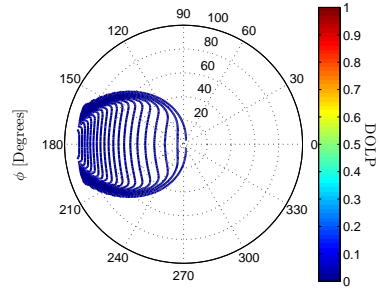
(a) DOLP of Al, $2^{1/2}\sigma_h/\ell = 0.1$.
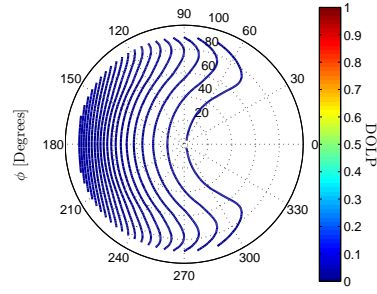
(b) DOLP of Al, $2^{1/2}\sigma_h/\ell = 0.6$.
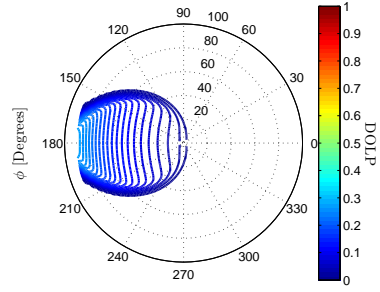
(c) DOLP of Fe, $2^{1/2}\sigma_h/\ell = 0.1$.
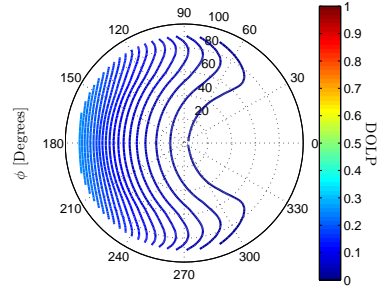
(d) DOLP of Fe, $2^{1/2}\sigma_h/\ell = 0.6$.
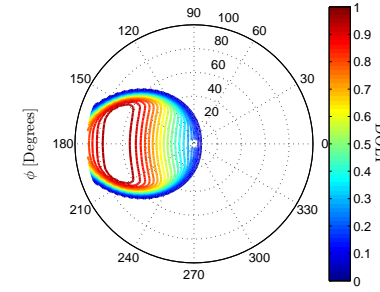
(e) DOLP of glass, $2^{1/2}\sigma_h/\ell = 0.1$.
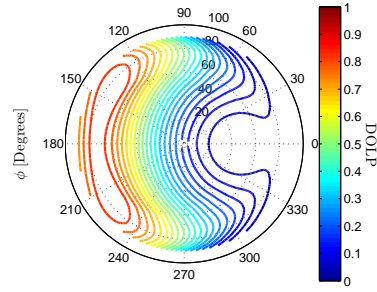
(f) DOLP of glass, $2^{1/2}\sigma_h/\ell = 0.6$.
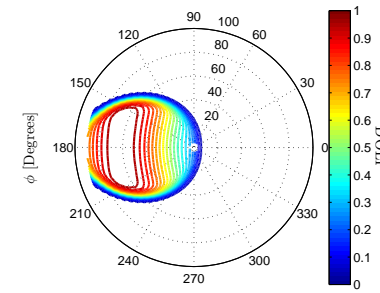
(g) DOLP of Teflon, $2^{1/2}\sigma_h/\ell = 0.1$.
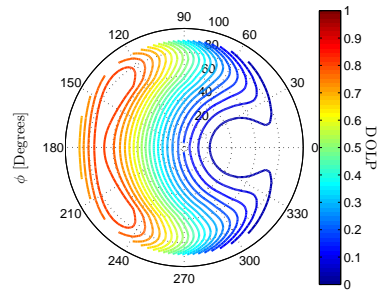
(h) DOLP of Teflon, $2^{1/2}\sigma_h/\ell = 0.6$.

Figure 44. DOLP contour plots of aluminum, iron, glass, and Teflon versus azimuth angle ϕ and polar angle θ_r (the radial direction in the figures) predicted using a pBRDF. The incident angle θ_i in all the figures is $45°$. Note that the complex indices of refraction (at 1550 nm) used for aluminum, iron, glass, and Teflon are $1.44 - \mathbf{j}16$, $3.60 - \mathbf{j}5.88$, $1.44 - \mathbf{j}0.0$, and $1.35 - \mathbf{j}0.0$, respectively [76].

show the calculated DOLP's when the surface roughness is $2^{1/2}\sigma_h/\ell = 0.6$. Viewing the DOLP's in this manner allows one to gain an understanding of how observation geometry (θ_r, ϕ) and surface roughness affect the DOLP of scattered light. Note that for a relatively "smooth" surface, $2^{1/2}\sigma_h/\ell = 0.1$, most of the observable DOLP is contained in a small lobe in the specular plane (i.e., $\phi = |\phi_r - \phi_i| = \pi$). As the surface becomes rough, $2^{1/2}\sigma_h/\ell = 0.6$, the observable DOLP spreads out from the specular plane but also loses magnitude. Physically, this is the result of two effects caused by surface roughness—the broadening of the specular lobe and the increase in diffuse scattering. Note that this necessitates the assumption that the observer's location be near the specular plane. The largest DOLP value obtained in Fig. 44 is approximately 1 (diffuse scattering prevents this from ever being exactly 1) by both glass and Teflon at an observation angle of approximately $60°$. Note that this maximum in DOLP occurs at Brewster's angle and is characteristic of dielectric materials. The largest DOLP value obtained by the metals is approximately 0.3 by iron at pseudo-Brewster's angle, which is near grazing for most metals at optical wavelengths [65]. Note that the largest DOLP value obtained by aluminum is roughly an order of magnitude less than that of iron at approximately the same observation angle. Other common metals with DOLP's similar to iron are titanium, chromium, and nickel. Metals with DOLP's similar to aluminum are copper, gold, and silver. Note that these metal relationships hold for visual and near-infrared optical wavelengths. Dispersion may cause these relationships to break down for other electromagnetic bands.

From the calculated DOLP traces shown in Fig. 44, a metal DOLP prior in the shape of a uniform probability density centered at a DOLP value of 0.15 and extending to 0 and 0.3 would capture the range of DOLP values shown in Fig. 44. A uniform probability density also serves to model the uncertainty in collection geometry as generally as possible (with the exception that θ_i and θ_r be off normal, as

discussed previously). Unfortunately, utilizing a uniform density for the metal DOLP prior is problematic because the distribution is not differentiable as required in the DOLP update equation [Eq. (194)]. It is convenient (shown and discussed below) to approximate a uniform distribution using a super-Gaussian distribution:

$$\Pi\left(\mathcal{P}\right) = c_1 \exp\left\{-\left[c_2\left(\mathcal{P} - c_3\right)\right]^m\right\}, \tag{195}$$

where c_1 is a constant which ensures the above expression integrates to unity, c_2 is a constant which behaves as a "variance" term for the super Gaussian (i.e., controls the width of the distribution), c_3 is a constant which controls where the distribution is centered, and m is an even integer [64]. It is clear from the form of Eq. (195) that the prior density approaches a uniform probability as m approaches infinity. Letting $c_1 = 1$, $c_2 = 7.2$, $c_3 = 0.15$, and $m = 10$ produces the metal DOLP prior depicted in Fig. 45.

A mathematical form for the dielectric DOLP prior can be found in the same manner as the metal DOLP prior just discussed. From the calculated DOLP traces shown in Fig. 44, it is evident that DOLP values for dielectric materials extend from 0 to approximately 1. While it is possible to develop a DOLP prior which covers this entire range of DOLP values, it would be ineffective for classification purposes because it encapsulates the metal DOLP prior. Thus, it is necessary to formulate the dielectric DOLP prior in a manner such that it excludes the metal DOLP prior. Note that a dielectric DOLP prior in the shape of a uniform probability centered at a DOLP value of 0.65 and extending to 0.3 and 1 would capture a vast majority of the observable dielectric DOLP values shown in Fig. 44. As is the case for the metal DOLP prior (and for the same reason), this uniform probability is approximated using a super-Gaussian distribution of the form shown in Eq. (195). Letting $c_1 = 1$, $c_2 = 3.1$, $c_3 = 0.65$, and $m = 10$ produces the dielectric DOLP prior depicted in
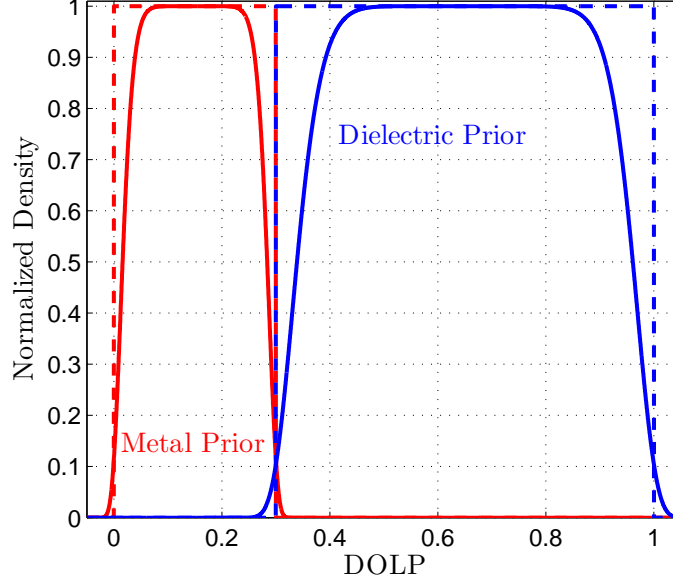
Figure 45. Metal DOLP prior, obtained by setting $c_1 = 1$, $c_2 = 7.2$, $c_3 = 0.15$, and $m = 10$ in Eq. (195), and the dielectric DOLP prior, obtained by setting $c_1 = 1$, $c_2 = 3.1$, $c_3 = 0.65$, and $m = 10$ in Eq. (195).

Fig. 45.

It must be stated that the DOLP priors just introduced are not universally applicable. Since DOLP is a function of index of refraction (itself a function of wavelength [60, 115]) and observation geometry, dispersion and collection geometry have a major impact on the expected DOLP from a material surface. For most applications, wavelength and observation geometry can, at the very least, be estimated and a set of DOLP priors can be formed in the manner outlined above. The DOLP priors, as defined above, are applicable to visual/near-infrared wavelengths and incident and observation angles θ_i and $\theta_r > 30°$. Note that this technique as a whole will have difficulty accurately classifying materials at near-normal incident angles regardless of wavelength or θ_r. This is because materials polarize scattered light very weakly at near-normal incident angles. Thus, the technique, as proposed and under these conditions, can be expected to poorly classify dielectric materials.

5.2.3 Summary of Theory.

Before presenting measurement results, it is necessary to show the new DOLP update equation when the general form of the DOLP priors [Eq. (195)] is substituted into Eq. (194):

$$
\begin{aligned}
0 = {}& m c_2^m \mathcal{P}^2 (\mathcal{P} - c_3)^{m-1} - m c_2^m \mathcal{P} (\mathcal{P} - c_3)^{m-1} \\
& - \mathcal{P} \sum_n \sum_{\boldsymbol{y}} \left(\psi_{un}^{i+1} + \psi_{pn}^{i+1} \right) + \sum_n \sum_{\boldsymbol{y}} \psi_{pn}^{i+1}
\end{aligned}
. \tag{196}
$$

Note that Eq. (196) is a $(m+1)$-order polynomial equation where only one of the roots is physically realizable, i.e., $0 \leqslant \mathcal{P}(\boldsymbol{x}_0) \leqslant 1$ [64]. This is an attractive feature of choosing super-Gaussian priors because the roots of polynomials can be found quickly (requiring no *a priori* knowledge unlike other nonlinear root finders, e.g., Newton's method) using the companion matrix method [138].

Summarizing the technique, the material-classification algorithm introduced here (shown as a flowchart in Fig. 46) determines whether an unknown object is composed of dielectric or metallic materials using passive polarimetric imagery degraded by atmospheric turbulence. The technique uses a variant of the polarimetric blind-deconvolution algorithm developed by LeMaster and Cain [74] to recover the true object S_0, the DOLP $\mathcal{P}$, the AOP α, and the PSF's h_n (reviewed above). Incorporated into the blind-deconvolution algorithm are two novel DOLP priors, one representative of a dielectric, the other representative of a metal (discussed in the previous subsection). The DOLP update [Eq. (196)] resulting from each prior is substituted into the log-likelihood function [Eq. (191)]. The DOLP update (either the update resulting from the dielectric DOLP prior or the update resulting from the metal DOLP prior) which maximizes the log-likelihood function determines whether that pixel in the image is classified as a dielectric or a metal. The algorithm is iterated until the stopping
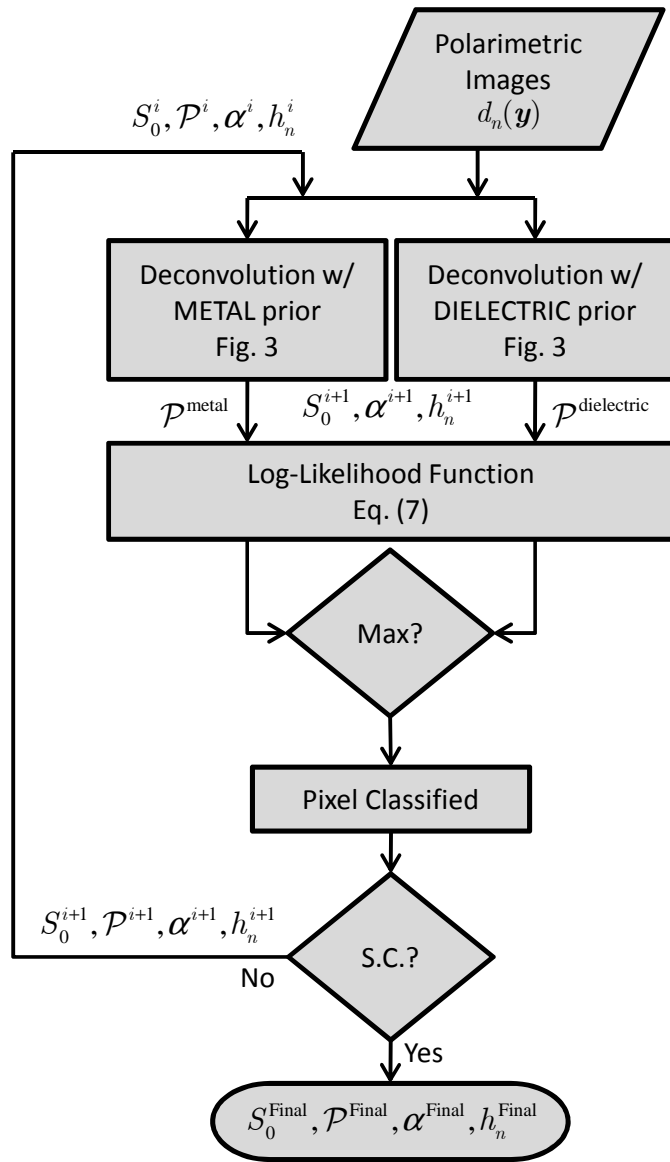
Figure 46. Flowchart of proposed material-classification algorithm, i^{th} iteration. S.C. represents the stopping criterion.

criterion is met. Iteration count is used as the stopping criterion in this research. Another stopping criterion based on the variance difference between the estimated and measured images is presented in Ref. [78]. In the next section, measurement results using the proposed material-classification algorithm are presented to validate the technique.

5.3 Experimental Verification

5.3.1 Instrument Description.

The instrument used to collect the Stokes imagery presented here is a Stokes polarimeter in the Optical Turbulence Estimation, Compensation, and Simulation (OPTECS) laboratory at the Air Force Institute of Technology. A photograph of the instrument is shown in Fig. 47. The instrument consists of three main sections—the source/sample section, the atmospheric turbulence simulator (ATS) [13] section, and the polarimetric imager (analyzer) section. The first section, the source/sample section, consists of two precision rotation stages. The lower rotation stage holds the source, a 1550 nm light emitting diode (LED), and the upper rotation stage, which holds the sample. By rotating the lower stage in combination with the upper rotation stage, any in-specular-plane incident/observation geometry $\theta_i + \theta_r \geq 48°$ is possible. The second section of the Stokes polarimeter shown in Fig. 47 is the ATS section [13]. The ATS section comprises three sets of doublet lenses and a rotating phase wheel. The phase wheel has a pattern machined into it that has phase properties consistent with Kolmogorov turbulence [5, 44, 63, 111] and is located between the second and third set of doublet lenses. By changing its location between the set of doublets, the atmospheric turbulence coherence diameter (Fried's parameter) r_0 [5, 44, 111] can be precisely controlled. Rotating the phase wheel allows one to model the temporal effects of atmospheric turbulence, i.e., the Tyler and Greenwood

146
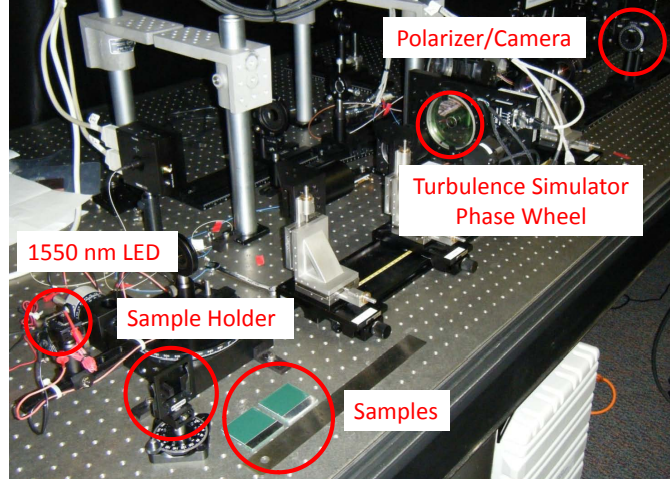
Figure 47. Photograph of the Stokes polarimeter, including painted steel and aluminum samples, used in this experiment.

time constants [5, 111]. Several independent experiments have been performed to verify the realism of the ATS by comparing measured turbulence parameters to the theoretical expressions. In regards to this experiment, modulation transfer functions (MTF's) were measured and compared to the theoretical short-exposure MTF's [44] to determine the r_0 values at different phase wheel locations. Excellent fits were obtained between the experimental and theoretical MTF's (see Fig. 48). Mantravadi *et al.* [80] and Rhoadarmer and Angel [107], the designers of the ATS, report similar results comparing the experimental phase structure function D_ϕ to the theoretical D_ϕ. The last section of the instrument is the polarimetric imager, or analyzer section. The analyzer section consists of a lens for imaging (aperture sized to $r = 12.5$ mm to ensure proper pupil-plane sampling for the deconvolution algorithm), a linear polarizer, and a FLIR Systems Alpha VisGaAs digital camera [35, 36]. The size of the Alpha VisGaAs's focal-plane array is 250×316 with a 30 μm pitch [35, 36]. The lenses in the ATS and analyzer sections of the Stokes polarimeter are such that the magnification is 2.25; thus, the resulting image represents a region on the sample approximately 3.33 mm $\times$ 4.21 mm at normal incidence.
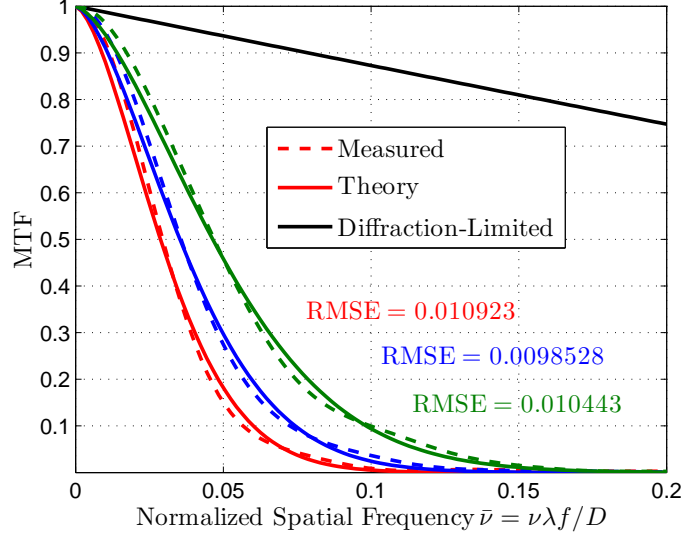
Figure 48. Experimental modulation transfer functions (MTF's) compared to theoretical MTF's for three different phase wheel locations. The root-mean-square errors (RMSE's) of the fits are annotated on the figure.

5.3.2 Experimental Procedure.

For the measurement results presented here, Stokes images, i.e., S_0, S_1, and S_2, are created from four polarimetric images, $\theta = 0°$, $45°$, $90°$, and $135°$, respectively [47, 50, 132]:

$$\frac{1}{2} \begin{bmatrix} 1 & 1 & 0 \\ 1 & 0 & 1 \\ 1 & -1 & 0 \\ 1 & 0 & -1 \end{bmatrix} \begin{bmatrix} S_0 \\ S_1 \\ S_2 \end{bmatrix} = \begin{bmatrix} I\left(0°\right) \\ I\left(45°\right) \\ I\left(90°\right) \\ I\left(135°\right) \end{bmatrix}. \tag{197}$$

Dark-frame images, images taken with the camera's lens cap on, are also collected and subtracted from the raw polarimetric images prior to converting to Stokes images. In this experiment, the phase wheel locations are chosen such that the ratio of the aperture diameter D to Fried's parameter r_0 is approximately $D/r_0 \approx 7.9, 10.5$, and 12.9. Note that these values were experimentally determined by fitting the theoretical short-exposure MTF to the measured MTF as discussed above and shown in Fig. 48.

The phase wheel is not rotated between polarimetric images; thus, each polarimet-

ric image experiences the same atmospheric turbulence. The purpose for not rotating the phase wheel between polarimetric images is to avoid pixel misregistration, a well documented issue in Stokes polarimetry [112, 133]. Traditionally, pixel misregistration arises from the movement of the object or the imager between polarimetric images. Since Stokes polarimetry requires multiple images (or measurements) and analysis performed on a per-pixel basis, any motion of the object or sensor produces errors in the resulting Stokes images [112]. Atmospheric turbulence tends to exacerbate this problem via random wavefront inclination, or tilt. Tilt has the effect of "steering" the resulting image to different parts of the focal plane (in the case of strong tilt, off the focal plane entirely). Therefore, even in a scenario in which traditional misregistration is not a concern (i.e., object and sensor do not move between polarimetric images), misregistration still occurs if the turbulence (in particular, the tilt) changes between polarimetric measurements. Interestingly, the Stokes polarimeter architectures designed to combat traditional misregistration should be effective against tilt misregistration. Two architectures which are commonly utilized for this purpose are the division of amplitude polarimeter (DoAmP) and the division of aperture polarimeter [112, 133]. In the experimental results to follow, the *a priori* knowledge that each polarimetric channel experiences the same turbulence is included in the deconvolution algorithm. In this way, a DoAmP is modeled. Even if a DoAmP or a division of aperture polarimeter is used, it may be advantageous to assume no relation exists between the polarimetric-channel PSF's and allow the deconvolution algorithm to estimate them independently. This would allow differences in aberrations among optical paths (also known as non-common optical path aberrations) to be corrected. Note that experimental results were also obtained operating the algorithm assuming no relation exists between channel PSF's. The results are very similar to those shown below.

The painted aluminum and steel (behaves like iron) samples used in this experiment (see Fig. 47) were first cleaned with acetone. A layer of Rust-Oleum White Primer [109] was applied followed lastly by a coat of KRYLON® gloss Hunter Green [121]. Sections of each sample were left unpainted (i.e., bare metal) to test the technique on an object consisting of both dielectric and metallic parts. Prior to performing the deconvolution, the raw polarimetric images were tiled to 512 pixel × 512 pixel images. The resulting tiled images were then spatially windowed using a super-Gaussian window to mitigate the ringing artifacts caused by the fast Fourier transforms executed in the deconvolution algorithm [106]. Initial guesses input into the deconvolution algorithm for S_0, $\mathcal{P}$, and α are an image whose pixel values are one, an image whose pixels values are $1/2$, and an image whose pixel values are zero, respectively. The initial guess for h is a randomly drawn Kolmogorov phase screen ($D/r_0 = 10$), with piston and tilt removed, created in the manner described in Ref. [39].

5.3.3 Classification Results.

In Fig. 49, Figs. 49a, 49d, and 49g show the no-turbulence, turbulence-degraded, and estimated (after 250 algorithm iterations) S_0 images for the painted aluminum sample collected at $\theta_i = \theta_r = 50°$, respectively. The no-turbulence, turbulence-degraded, and estimated DOLP images for the painted aluminum sample are shown in Figs. 49b, 49e, and 49h. Figures 49c, 49f, and 49i show the classification results. The no-turbulence and turbulence-degraded material-classification results are computed from a simple DOLP-thresholding scheme, i.e., $\mathcal{P} < 0.30$ implies metal, $\mathcal{P} \geq 0.30$ implies dielectric. This threshold is the DOLP value of equal probability between the metal and dielectric DOLP priors. The experimental results for the painted steel sample are shown in Fig. 50 and are orientated in the same manner as just described.

(a) No-turbulence S_0.

(b) No-turbulence $\mathcal{P}$.

(c) No-turbulence classification.

(d) Turbulence-degraded S_0.

(e) Turbulence-degraded $\mathcal{P}$.

(f) Turbulence-degraded classification.

(g) Estimated S_0.

(h) Estimated $\mathcal{P}$.

(i) Estimated classification.
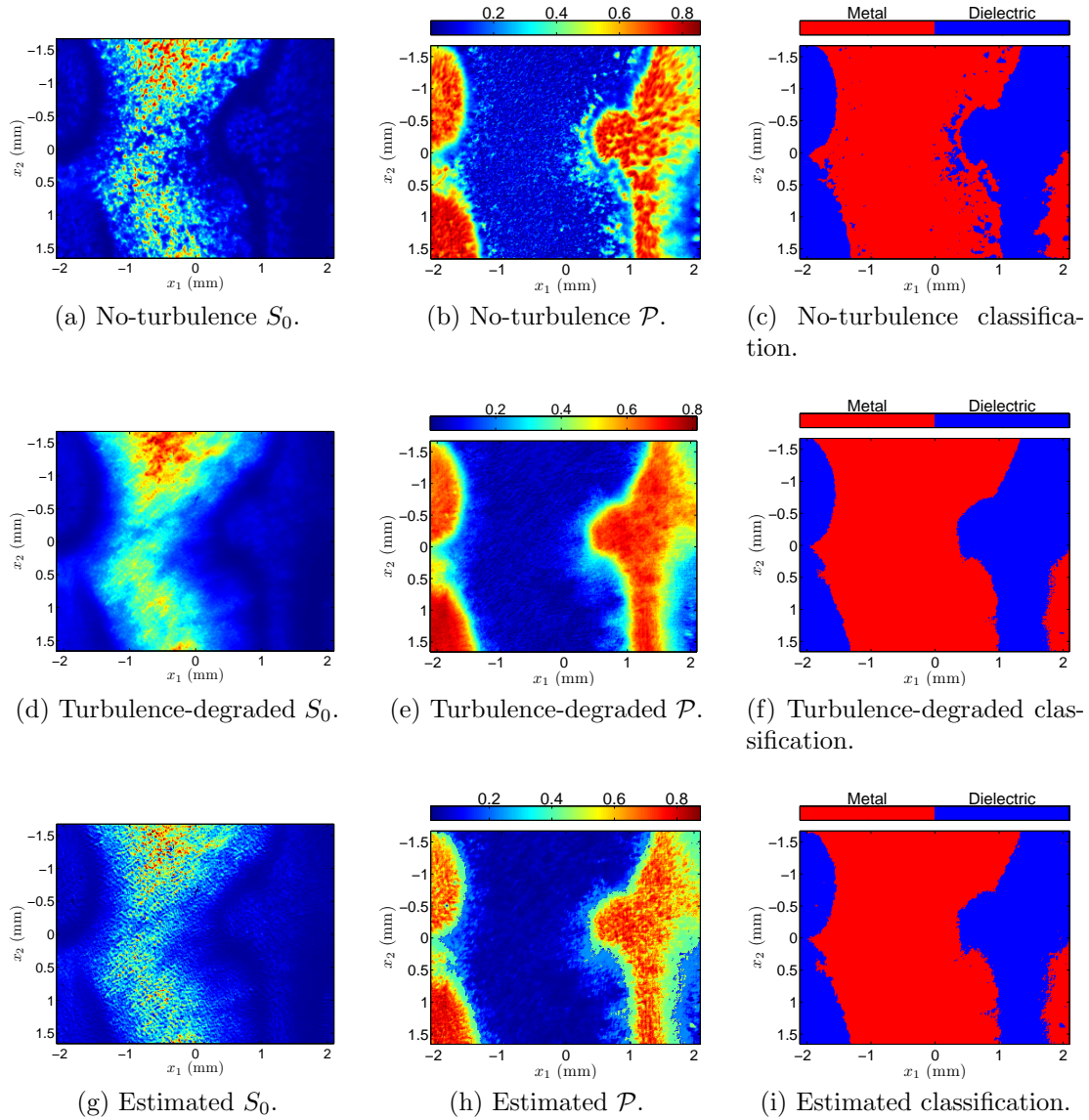
Figure 49. Experimental results of the material-classification algorithm for the painted aluminum ($D/r_0 \approx 12.9$) sample (see Fig. 47). The images depict the right side of the letter s and the left side of the letter t formed using a template. The collection geometry is $\theta_i = \theta_r = 50°$. The dimensions annotated on the figures are object coordinates $x = (x_1, x_2)$ at normal incidence. For the no-turbulence and turbulence-degraded classification results, $\mathcal{P} < 0.30$ implies metal, $\mathcal{P} \geq 0.30$ implies dielectric. The estimated classification result uses the metal and dielectric DOLP priors derived in Section 5.2.2.

(a) No-turbulence S_0.

(b) No-turbulence $\mathcal{P}$.

(c) No-turbulence classification.

(d) Turbulence-degraded S_0.

(e) Turbulence-degraded $\mathcal{P}$.

(f) Turbulence-degraded classification.

(g) Estimated S_0.

(h) Estimated $\mathcal{P}$.

(i) Estimated classification.
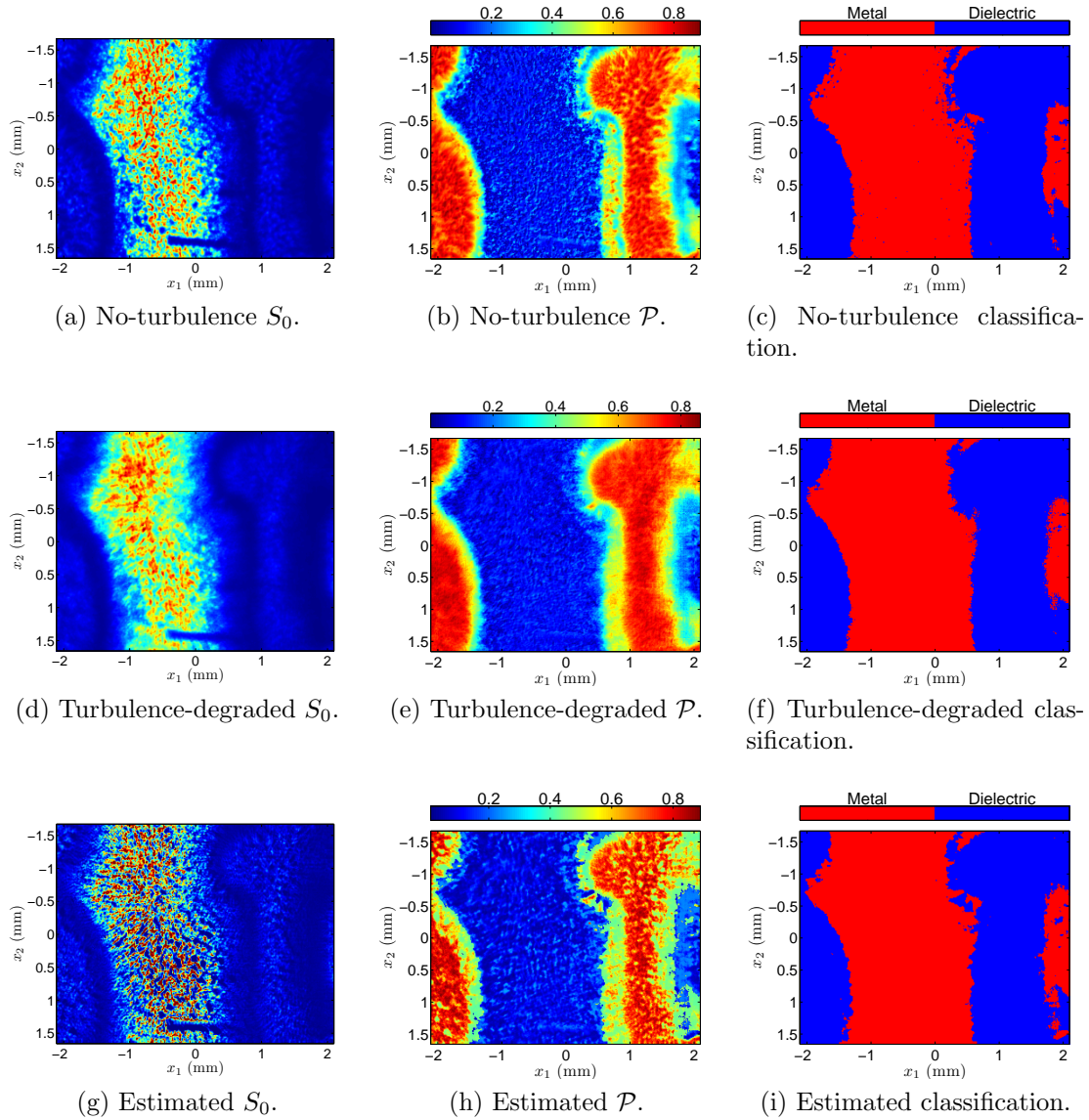
Figure 50. Experimental results of the material-classification algorithm for the painted steel ($D/r_0 \approx 7.9$) sample (see Fig. 47). The images depict the right side of the letter s and the left side of the letter t formed using a template. The collection geometry is $\theta_i = \theta_r = 50°$. The dimensions annotated on the figures are object coordinates $x = (x_1, x_2)$ at normal incidence. For the no-turbulence and turbulence-degraded classification results, $\mathcal{P} < 0.30$ implies metal, $\mathcal{P} \geq 0.30$ implies dielectric. The estimated classification result uses the metal and dielectric DOLP priors derived in Section 5.2.2.

Note that the algorithm accurately classifies both the aluminum and steel samples and recovers object features lost in the turbulence-degraded images, especially small features along the metal/paint boundaries. These features are evident in the DOLP images in Figs. 49 and 50. They are difficult to discern in the S_0 images because of the irradiance contrast between the metal and painted regions of the objects. Spatial (correlation coefficient and RMSE) and histogram image similarity metrics calculated in the frequency domain generally show that the spectrums of the estimated images better match (convincingly so, depending on the metric) the no-turbulence image spectrums than that of their turbulence-degraded counterparts. Note that the algorithm was experimentally tested on other scenes, specifically, half-painted half-metal objects. The algorithm clearly recovered small scratches and nicks in the metal portions of the objects lost in the turbulence-degraded images. In some cases, the scratches were so clearly resolved by the algorithm that they were misclassified as dielectric due to the fact that more light is scattered in the polarization state parallel to the scratches than in the orthogonal polarization state (i.e., the scattering phenomenon exploited to create wire-grid polarizers and polarimetric edge-detection algorithms).

Table 5 shows the results of the classification quantitatively. Columns 1–3 report the fractions of pixels incorrectly classified as metal, the fractions of pixels incorrectly classified as dielectric, and the total pixels incorrectly classified, respectively, using the no-turbulence classification results as truths. The fourth column reports the correlation coefficients for the turbulence-degraded and estimated classification images correlated with the no-turbulence classification images. The fifth column reports the root-mean-square errors (RMSE's) for the turbulence-degraded and estimated classification images using the no-turbulence classification images as truths. Note that the algorithm outperforms the turbulence-degraded (no-correction) case in classifying

153

Table 4. **Material-classification results for the painted aluminum and painted steel samples at** $\theta_i = \theta_r = 50°$.

	Aluminum Sample				
	Frac. Incor. M	Frac. Incor. D	Frac. Incor. Tot.	Corr. Coef.	RMSE
Turb. $D/r_0 \approx 7.9$	0.0322	0.0709	0.0476	0.9005	0.2183
Est. $D/r_0 \approx 7.9$	0.0244	0.0835	0.0480	0.8999	0.2190
Turb. $D/r_0 \approx 10.5$	0.0332	0.0898	0.0558	0.8834	0.2362
Est. $D/r_0 \approx 10.5$	0.0264	0.0992	0.0555	0.8843	0.2355
Turb. $D/r_0 \approx 12.9$	0.0339	0.0950	0.0583	0.8782	0.2414
Est. $D/r_0 \approx 12.9$	0.0293	0.0971	0.0564	0.8823	0.2374

	Steel Sample				
	Frac. Incor. M	Frac. Incor. D	Frac. Incor. Tot.	Corr. Coef.	RMSE
Turb. $D/r_0 \approx 7.9$	0.0236	0.0571	0.0402	0.9200	0.2005
Est. $D/r_0 \approx 7.9$	0.0147	0.0708	0.0424	0.9165	0.2060
Turb. $D/r_0 \approx 10.5$	0.0227	0.0776	0.0498	0.9015	0.2233
Est. $D/r_0 \approx 10.5$	0.0164	0.0724	0.0441	0.9131	0.2100
Turb. $D/r_0 \approx 12.9$	0.0236	0.0911	0.0570	0.8879	0.2387
Est. $D/r_0 \approx 12.9$	0.0209	0.0847	0.0524	0.8968	0.2290

the metal portions of the object. Performance of the algorithm also improves as the atmospheric phase fluctuations become stronger (i.e., D/r_0 increases). For the D/r_0 values and scenes used in this experiment, the quantitative improvement is marginal for the spatially-based image metrics reported in Table 5. It is expected that the classification improvement provided by using the algorithm will become more apparent for larger D/r_0 values or a more complex scene.

5.3.4 Limitations.

Figures 51 and 52 show the results of the material-classification algorithm for $\theta_i = \theta_r = 24°$. The layouts of the figures are exactly the same as Figs. 49 and 50. The no-turbulence (Figs. 51c and 52c) and turbulence-degraded (Figs. 51f and 52f) classification results are computed using the same DOLP-thresholding scheme as above with the threshold value equal to 0.08 (determined by inspecting the histogram of the no-turbulence DOLP). To demonstrate a key limitation of the proposed technique, the estimated classification results (Figs. 51i and 52i) are computed using the DOLP

(a) No-turbulence S_0.

(b) No-turbulence $\mathcal{P}$.

(c) No-turbulence classification.

(d) Turbulence-degraded S_0.

(e) Turbulence-degraded $\mathcal{P}$.

(f) Turbulence-degraded classification.

(g) Estimated S_0.

(h) Estimated $\mathcal{P}$.

(i) Estimated classification.
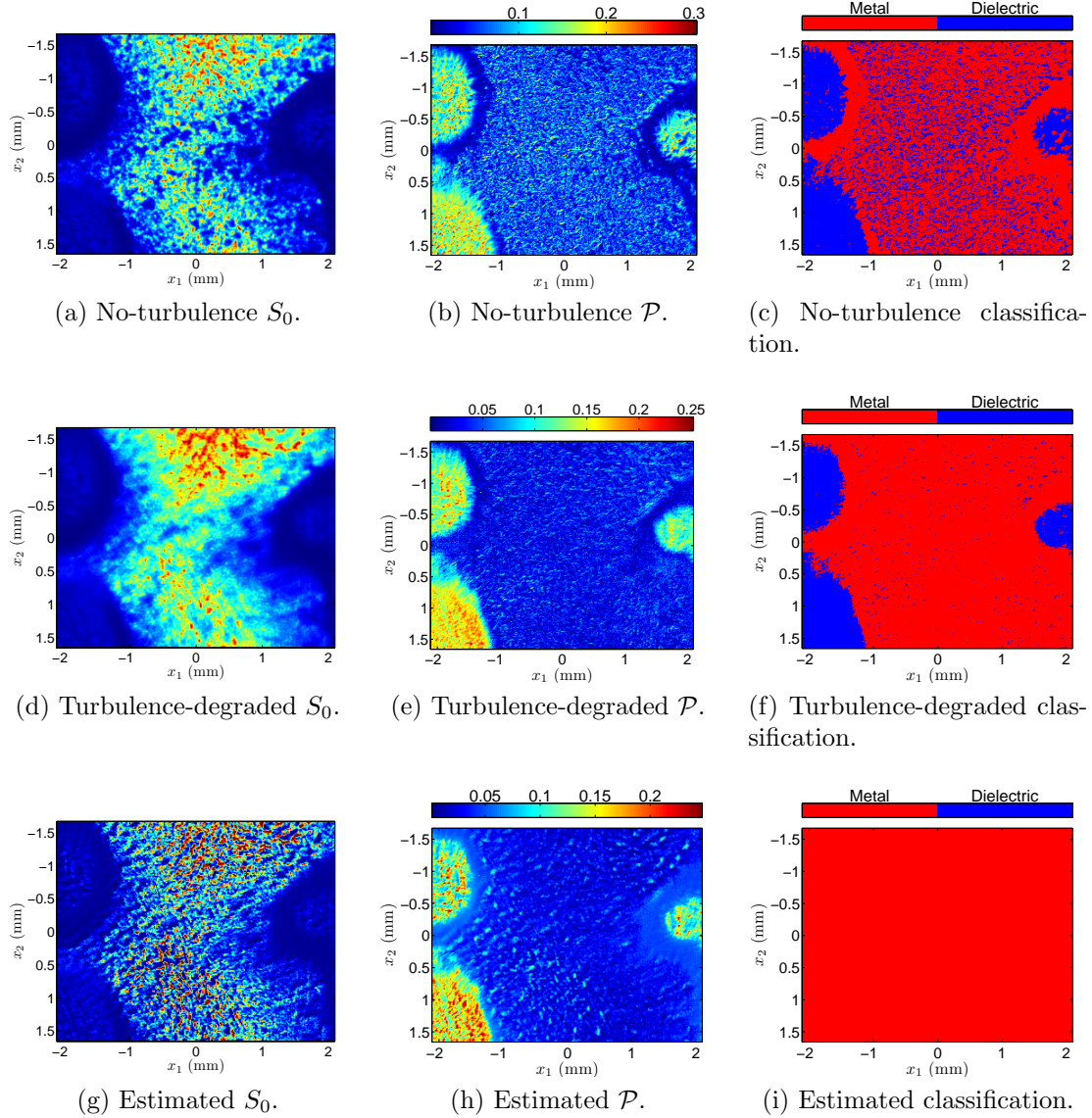
Figure 51. Experimental results of the material-classification algorithm for the painted aluminum ($D/r_0 \approx 7.9$) sample (see Fig. 47). The images depict the right side of the letter s and the left side of the letter t formed using a template. The collection geometry is $\theta_i = \theta_r = 24°$. The dimensions annotated on the figures are object coordinates $\boldsymbol{x} = (x_1, x_2)$ at normal incidence. For the no-turbulence and turbulence-degraded classification results, $\mathcal{P} < 0.08$ implies metal, $\mathcal{P} \geq 0.08$ implies dielectric. The estimated classification result uses the metal and dielectric DOLP priors derived in Section 5.2.2.

155

(a) No-turbulence S_0.

(b) No-turbulence $\mathcal{P}$.

(c) No-turbulence classification.

(d) Turbulence-degraded S_0.

(e) Turbulence-degraded $\mathcal{P}$.

(f) Turbulence-degraded classification.

(g) Estimated S_0.

(h) Estimated $\mathcal{P}$.

(i) Estimated classification.
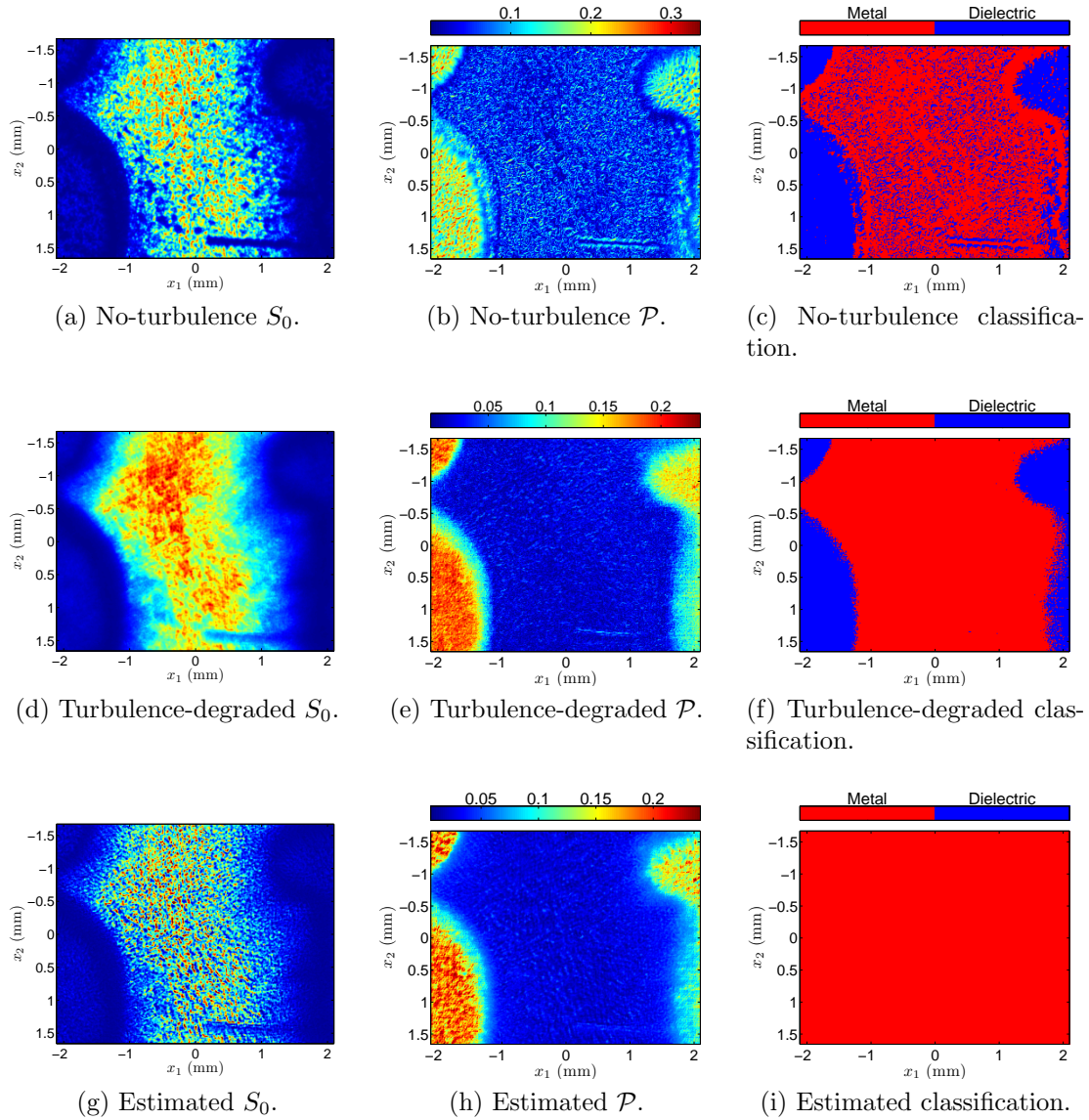
Figure 52. Experimental results of the material-classification algorithm for the painted steel ($D/r_0 \approx 12.9$) sample (see Fig. 47). The images depict the right side of the letter s and the left side of the letter t formed using a template. The collection geometry is $\theta_i = \theta_r = 24°$. The dimensions annotated on the figures are object coordinates $x = (x_1, x_2)$ at normal incidence. For the no-turbulence and turbulence-degraded classification results, $\mathcal{P} < 0.08$ implies metal, $\mathcal{P} \geq 0.08$ implies dielectric. The estimated classification result uses the metal and dielectric DOLP priors derived in Section 5.2.2.

priors derived in Section 5.2.2 (applicable to θ_i, $\theta_r > 30°$). As expected, the algorithm (as currently constituted) poorly classifies dielectric materials for near-normal collection geometries. It is possible to modify the algorithm to perform better in these collection scenarios. The most promising modification is to adaptively update the DOLP priors as more information becomes known about the scene. This can be accomplished by inspecting the histogram of the DOLP estimate and choosing new values for c_2 and c_3 in Eq. (196). This modification has the possibility of extending the region of validity of the algorithm to $\theta_i, \theta_r \approx 15°$ (not experimentally verified). Collection geometries $\theta_i, \theta_r < 15°$ will be difficult to correctly classify even with this modification because of the very weak manner in which natural materials polarize scattered light under these conditions. Although poor classification performance should be expected from the proposed method for near-normal geometries, as a result of the blind-deconvolution algorithm, improved S_0 and $\mathcal{P}$ images are still obtained.

5.4 Conclusion

In this chapter, a material-classification technique using polarimetric imagery degraded by atmospheric turbulence is presented. At the technique's core is the LeMaster and Cain polarimetric blind-deconvolution algorithm (reviewed above) [74]. The algorithm estimates the true object's irradiance S_0, the DOLP $\mathcal{P}$, the AOP α, and the PSF's h_n from turbulence-degraded polarimetric imagery. Added to LeMaster and Cain's algorithm are two novel DOLP priors (derived above), one representative of a dielectric and one representative of a metal. The DOLP estimate (i.e., the estimate resulting from the dielectric DOLP prior or the estimate resulting from the metal DOLP prior) which maximizes the log-likelihood function determines whether the image pixel is classified as a dielectric or a metal. Experimental results of two painted

metal samples are provided to validate the classification technique. The proposed algorithm is found to perform well for off-normal collection geometries $(\theta_i, \theta_r > 30°)$. For near-normal geometries, the algorithm, as expected, poorly classifies dielectric materials. As discussed, it may be possible to alleviate this limitation through adaptive DOLP priors.

VI. Enhanced Material Classification Using Polarimetric Imagery Degraded by Atmospheric Turbulence

T̲he contents of this chapter were submitted to *Optics Letters*, June 2010.

6.1 Introduction

Polarization-based material-classification techniques can generally be divided into two types—active polarimetric [21, 120] and, most relevant to the work presented here, passive [61, 126, 141] polarimetric techniques. In Chapter V, a passive polarimetric material-classification technique was introduced which determines whether an object is composed of dielectric or metallic materials using turbulence-degraded polarimetric imagery. The technique uses a variant of the LeMaster and Cain [74] blind-deconvolution algorithm to recover the first Stokes parameter S_0, the degree of linear polarization $\mathcal{P}$ (DOLP), the angle of polarization α (AOP), and the polarimetric-image point spread functions h_n (PSF's). The dielectric/metal classification decision is based on DOLP maximum-likelihood estimates provided by two DOLP priors (one representative of dielectric materials, the other representative of metallic materials). The DOLP estimate which maximizes the log-likelihood function determines the image pixel's classification.

In this chapter, the existing algorithm in Chapter V is enhanced to provide a more detailed object classification. This is accomplished by redesigning the DOLP priors to include subclasses of materials. For the research presented here, the metal classification is divided into an aluminum group (includes aluminum, copper, gold, and silver) classification and an iron group (includes iron, titanium, nickel, and chromium) classification. This new classification provides functional information about the object which is not provided by existing dielectric/metal classifiers. A discussion of these

new DOLP priors, particularly, the physical motivation behind their mathematical forms, is provided. Experimental results of the enhanced classification technique are also presented and discussed. Note that the enhanced classification algorithm presented here utilizes the same framework as that presented in Chapter V; therefore, all assumptions and limitations stated in Chapter V apply here as well.

6.2 DOLP Priors

Before the aluminum group, iron group, and dielectric DOLP priors can be formed, one must understand how these materials polarize light. To gain the necessary understanding, a polarimetric bidirectional distribution function (see Chapter IV) (pBRDF) is used to predict the DOLP's of the metals making up the aluminum and iron groups as well as a representative sample of dielectric materials. A similar analysis, considering surface roughness and out-of-plane observation, is performed in Chapter V. Figure 53a shows the DOLP's predicted using the pBRDF (see Chapter IV). Note the similarities in DOLP among the materials within each of the three classifications. More importantly, note the differences in DOLP between the different classification groups. As is evident in Fig. 53a, dielectric materials tend to strongly polarize scattered light with DOLP values encompassing the entire possible range, i.e., $0 \leqslant \mathcal{P} \leqslant 1$. Metals, such as aluminum, copper, gold, and silver, tend to polarize scattered light very weakly with $\mathcal{P} \ll 0.1$. Other metals, such as iron, titanium, nickel, and chromium, polarize light more strongly than aluminum group metals, however, not as strongly as dielectric materials. Metals in the iron group have DOLP values which range between $0 \leqslant \mathcal{P} \leqslant 0.3$.

From the DOLP traces depicted in Fig. 53a, priors in the shape of uniform probability densities extending from 0 to 0.07, from 0.07 to 0.3, and from 0.3 to 1 would capture a large majority of the DOLP values shown in Fig. 53a for the aluminum group
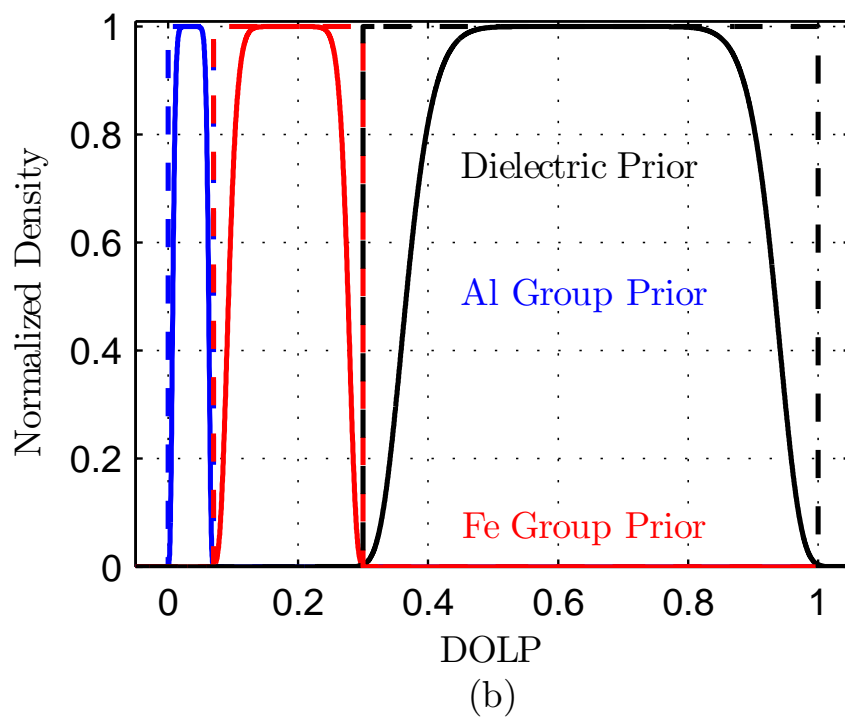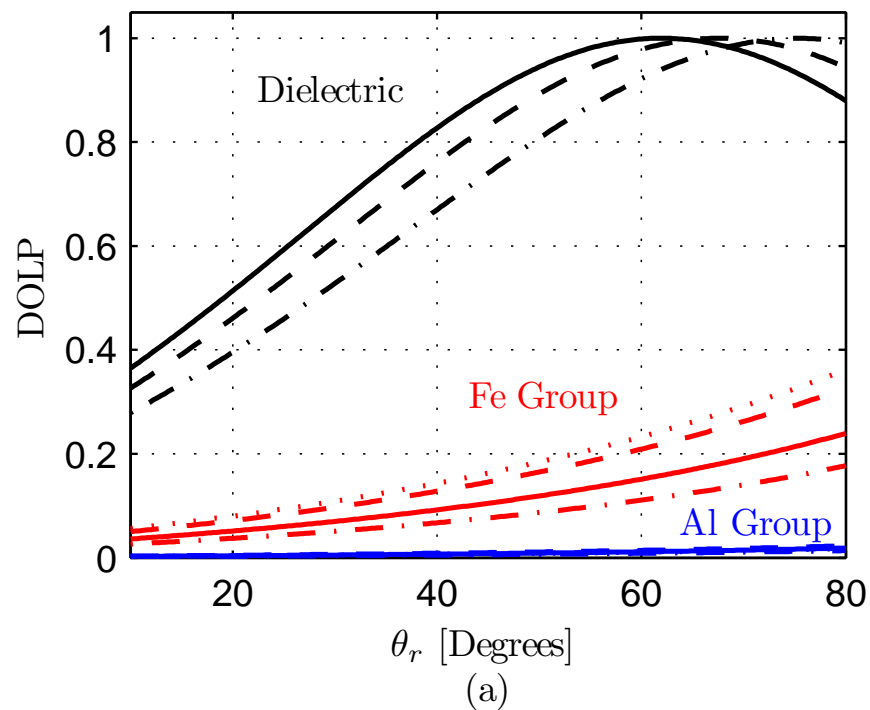
Figure 53. DOLP plots of the aluminum group, iron group, Teflon, glass, and alumina (dielectrics) versus observation angle θ_r (incident angle $\theta_i = 45°$) predicted using a pBRDF (Fig. 53a). The aluminum group, iron group, and dielectric DOLP priors (Fig. 53b).

metals, iron group metals, and dielectric materials, respectively. Unfortunately, the uniform probability density is not differentiable and therefore cannot serve as a prior in the deconvolution algorithm [61]. A differentiable approximation to a uniform distribution is a super-Gaussian distribution, namely,

$$\Pi\left(\mathcal{P}\right) = c_1 \exp\left\{-\left[c_2\left(\mathcal{P} - c_3\right)\right]^m\right\} \tag{198}$$

where c_1 is a constant which ensures the above expression integrates to unity, c_2 is a constant which controls the width of the distribution, c_3 is a constant which controls where the distribution is centered, and m is an even integer (see Chapter V). It is clear from the form of Eq. (198) that the prior density approaches a uniform probability as m approaches infinity. Figure 53b shows plots of the newly-designed aluminum group, iron group, and dielectric DOLP priors. To produce the aluminum group, iron group, and dielectric DOLP prior traces, $c_1 = (1, 1, 1)$, $c_2 = (35, 10.5, 3.4)$, $c_3 = (0.035, 0.185, 0.65)$, and $m = (10, 10, 10)$, respectively. It should be noted that the DOLP relationships between aluminum group metals and iron group metals are applicable to visual and near-infrared optical bands only. Dispersion may cause these relationships to break down for other wavelengths. Having discussed the formulation of the aluminum group, iron group, and dielectric DOLP priors, attention can now be turned to experimental verification of the enhanced classification algorithm.

6.3 Experimental Results

The instrument (see Fig. 47) used to collect the Stokes imagery presented here is a Stokes polarimeter in the OPTECS laboratory at the Air Force Institute of Technology. A detailed description of the instrument can be found in Chapter V. The Stokes images, i.e, S_0, S_1, and S_2, are created from four polarimetric images, analyzer
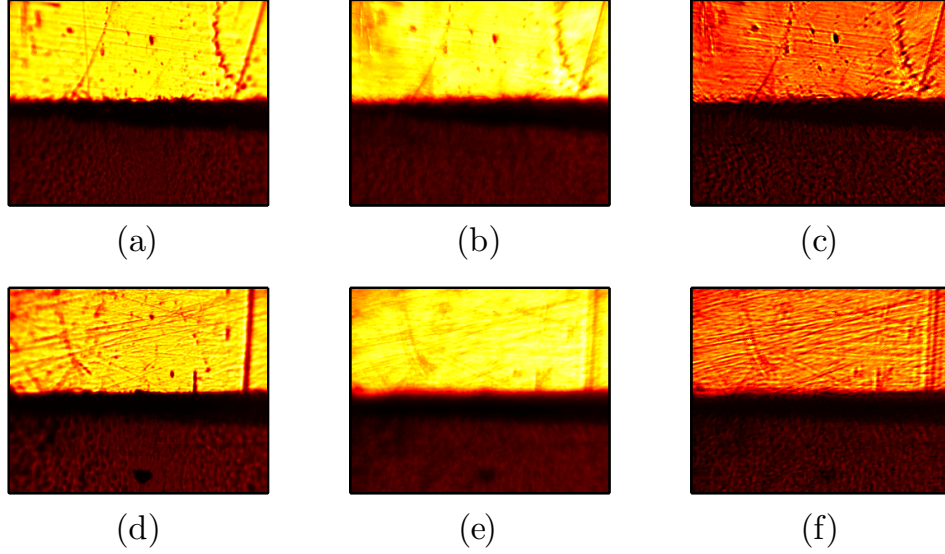
Figure 54. S_0 **correction results of the enhanced material-classification algorithm. Figures 54a and 54d show the no-turbulence images, Figs. 54b and 54e show the turbulence-degraded** S_0 **images, and Figs. 54c and 54f show the corrected** S_0 **images for the painted aluminum and painted steel samples, respectively. The images shown here are collected at** $\theta_i = \theta_r = 55°$**.**

angle $\theta = 0°$, $45°$, $90°$, and $135°$, respectively [47, 50, 132]. Dark-frame images, which are taken with the camera's lens cap on, are also collected and subtracted from the raw polarimetric images prior to converting to Stokes images. The objects imaged in this experiment are a 25.8 cm² aluminum sample and a 25.8 cm² steel sample. A coat of white primer followed lastly by a coat of green paint is applied to half of each sample to produce an object consisting of both dielectric and metallic parts.

Experimental results of the enhanced material-classification algorithm are shown in Figs. 54 and 55. In Fig. 54, Fig. 54a shows the no-turbulence S_0, Fig. 54b shows the turbulence-degraded S_0 ($D/r_0 \approx 7.9$, where D is the diameter of the pupil and r_0 is the atmospheric seeing parameter [44]), and Fig. 54c shows the corrected S_0 (after 250 deconvolution iterations) for the painted aluminum sample. Likewise, Fig. 54d shows the no-turbulence S_0, Fig. 54e shows the turbulence-degraded S_0 ($D/r_0 \approx 12.9$), and Fig. 54f shows the corrected S_0 (after 250 deconvolution iterations) for the painted steel sample. Note that object features lost in the turbulence-degraded S_0 images are

163
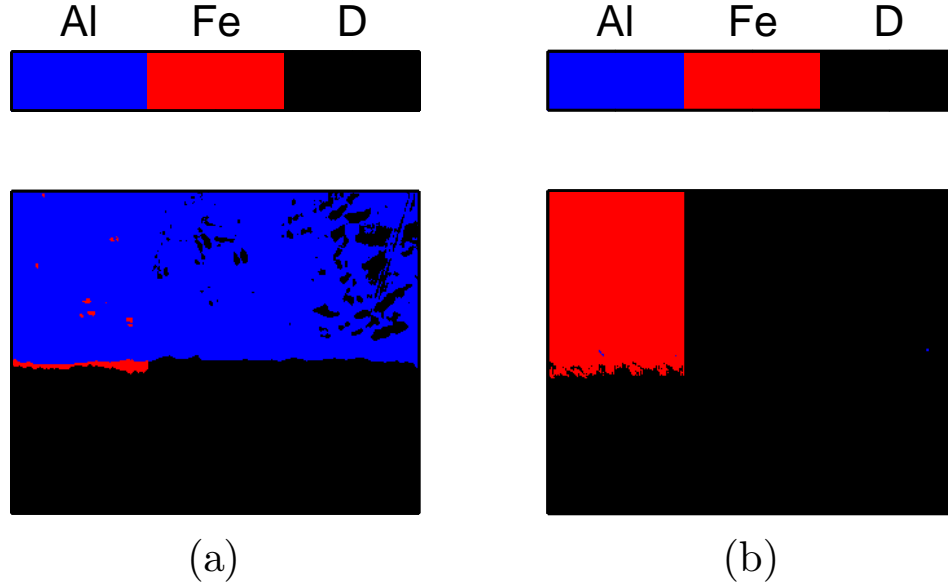
Figure 55. Classification results of the enhanced material-classification algorithm. Figure 55a shows the results for the painted aluminum sample; Fig. 55b shows the results for the painted steel sample.

successfully recovered in the corrected S_0 images.

Figure 55 shows the classification results for the painted aluminum (Fig. 55a) and painted steel (Fig. 55b) samples. Note the excellent classification results for the painted steel sample. Also note that the classification errors for the painted aluminum sample occur at scratches in the metal's surface and at the metal/paint boundary. The classification errors at the scratches occur because more light is scattered in the polarization state parallel to the scratches than the polarization state perpendicular to the scratches. Thus, scattered light from the scratches is polarized more strongly than the surrounding aluminum explaining the incorrect iron classification. This scattering phenomenon is the same used to create wire-grid polarizers and polarimetric edge-detection algorithms. The classification errors at the metal/paint boundary are caused by the manner in which the primer and paint are applied to the metal samples. Masking tape is used to ensure that half of the sample remains bare metal. This unfortunately creates a discontinuity at the metal/tape boundary causing the primer

and paint to be applied unevenly in this region. Removing the tape, after the paint has dried, disbonds the primer/paint layers from the metal substrate. This is the dark region clearly seen in Fig. 54a. The same metal/paint boundary effect occurs for the steel sample results (see Fig. 54d); however, since the algorithm classifies that region as iron, no errors are evident in Fig. 55b.

6.4 Conclusion

In this chapter, the dielectric/metal classifier presented in Chapter V is enhanced to provide a more detailed metal classification. This is accomplished by redesigning the DOLP priors to include an aluminum group (includes aluminum, copper, gold, and silver) classification and an iron group (includes iron, titanium, nickel, and chromium) classification. It is experimentally demonstrated that the algorithm is able to determine whether an object is composed of aluminum, iron, or dielectric materials. This new metal classification provides functional information about the object which is not provided by existing dielectric/metal classifiers.

VII. Material Characterization Using Polarimetric Imagery Degraded by Atmospheric Turbulence

The major developments and results of this chapter were submitted to *Optical Engineering*, June 2010.

7.1   Introduction

Electromagnetic material characterization is the science of determining a material's constituent parameters. At microwave wavelengths, the material parameters of interest are typically complex permittivity and permeability; at optical wavelengths, complex index of refraction is typically the sought material parameter. A search of available literature on the subject yields numerous laboratory material-characterization techniques, such as Brewster's angle [12, 99], prism [28, 29, 58, 88], interferometric [19, 46, 89, 95, 99], and ellipsometric [73, 118, 127] methods. However, very little research exists in material characterization performed remotely, that is, remote-sensing material characterization. The techniques which are available in literature, Refs. [60, 105, 120, 123], use polarimetry to measure the Stokes vector of scattered light from a material's surface. With the measured Stokes vector, the researchers are able to obtain the complex index of refraction of the material via numerical inversion of the theoretical Stokes vector derived using a polarimetric bidirectional reflectance distribution function (pBRDF) [103, 104, 128]. While the experimental material-characterization results presented in the referenced papers are impressive, the researchers utilize diffraction-limited imagery in their material-characterization experiments and do not account for any effects of atmospheric turbulence. The purpose of this chapter is to present a remote-sensing material-characterization technique using polarimetric images degraded by atmospheric turbulence. To the author's

knowledge, no such technique currently exists.

The material-characterization technique presented here (measurement geometry is depicted in Fig. 56) extracts the complex index of refraction (index of refraction and coefficient of extinction) of a material. The method uses a variant of the polarimetric maximum-likelihood blind-deconvolution algorithm developed by LeMaster and Cain [74] (see Chapter V) to recover the true object's irradiance (i.e., the first Stokes parameter), the degree of linear polarization (DOLP) $\mathcal{P}$, and the polarimetric-image point spread functions (PSF's) from turbulence-degraded imagery. The estimated (or corrected) DOLP's $\mathcal{P}^{\mathrm{meas}}$ (at multiple angles of incidence θ_i and angles of reflection, or observation θ_r) are then compared to the theoretical DOLP's $\mathcal{P}^{\mathrm{thy}}$, obtained using a pBRDF [62, 140, 139] (see Chapter IV), and the difference minimized via nonlinear least squares to yield the complex index of refraction and surface roughness parameter, i.e.,

$$\left| \mathcal{P}^{\mathrm{thy}}\left(\eta; \sigma; \theta_{i1}, \theta_{r1}\right) - \mathcal{P}^{\mathrm{meas}}_1 \right| \leqslant \delta$$

$$\left| \mathcal{P}^{\mathrm{thy}}\left(\eta; \sigma; \theta_{i2}, \theta_{r2}\right) - \mathcal{P}^{\mathrm{meas}}_2 \right| \leqslant \delta$$

$$\vdots$$

$$\left| \mathcal{P}^{\mathrm{thy}}\left(\eta; \sigma; \theta_{i\mathrm{N}}, \theta_{r\mathrm{N}}\right) - \mathcal{P}^{\mathrm{meas}}_{\mathrm{N}} \right| \leqslant \delta$$

(199)

where δ is a user-defined tolerance. The proposed material-characterization technique assumes that the object is illuminated with spatially incoherent and unpolarized light (i.e, passive polarimetry) as depicted in Fig. 56. Note that as a result of this assumption, circular polarization can generally be ignored [27]. It should be noted that this assumption is invalid when dealing with circularly dichroic materials which are encountered in biological applications [2, 30]. Another assumption of this work is that the unknown material must be able to produce polarized scatter from unpolarized illumination, i.e., the material must have some diattenuation. This proposed technique is not designed to handle diffuse scatterers or materials which are purely retarding.
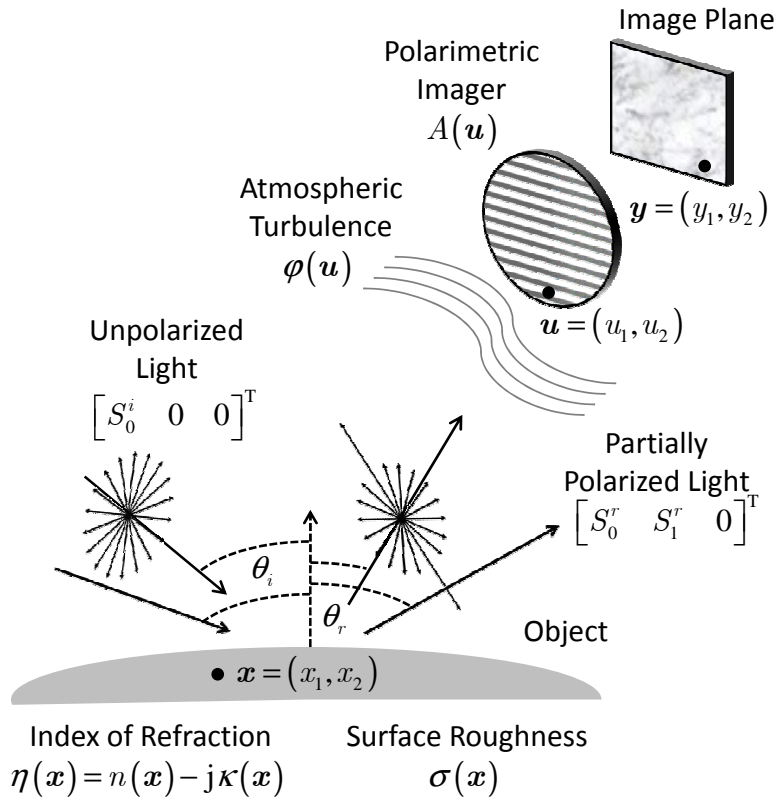
Figure 56. Measurement geometry of proposed material-characterization technique. Unpolarized light with Stokes vector $\begin{bmatrix} S_0^i & 0 & 0 \end{bmatrix}^{\mathrm{T}}$ illuminates an object of complex index of refraction $\eta(x) = n(x) - \mathrm{j}\kappa(x)$ and roughness $\sigma(x)$. Upon reflection, the light is partially polarized with Stokes vector $\begin{bmatrix} S_0^r & S_1^r & 0 \end{bmatrix}^{\mathrm{T}}$, is distorted by atmospheric turbulence with random phase distribution $\varphi(u)$, and is received by a polarimetric sensor of aperture $A(u)$.

168

Lastly, this research assumes that the measurement geometry is known *a priori* (i.e., θ_i and θ_r are known) and that the measured polarimetric images are obtained in the specular plane (defined and explained below). Note that these same assumptions are utilized in the remote-sensing material-characterization references cited above.

In the next section, the theoretical development of the proposed material-characterization technique is discussed. Included in this section are the derivation of the theoretical DOLP and a brief review of the LeMaster and Cain blind-deconvolution algorithm (needed to correct the deleterious effects of atmospheric turbulence). Section 7.3 of this chapter presents experimental results of the material-characterization technique in order to validate the method. Lastly, this chapter is concluded with a summary of the work presented.

7.2   Theoretical Development

Before progressing to the theoretical derivation of the technique, it is important to note that material characterization requires one to solve forward and inverse problems. The forward problem involves finding theoretical expressions for the particular measurement geometry (see Fig. 56). The forward problem of this material-characterization technique is the derivation of the theoretical DOLP (topic of Section 7.2.1). In some rare instances, the forward problem can be algebraically inverted resulting in direct closed-form expressions for the desired parameters in terms of measurable quantities, e.g., Brewster's angle and prism methods. However, in most circumstances (including the one discussed in this chapter), the inverse problem must be solved using numerical techniques such as the Gauss-Newton method, the Levenberg-Marquardt algorithm, etc. [79]. As a consequence of turbulence degradation of the measured data, an additional step must be added to the inverse problem of the material-characterization technique presented here. This added step, deconvo-

lution, is the subject of Section 7.2.2.

7.2.1 The Forward Problem.

The pBRDF chosen to derive the theoretical DOLP is the one described in Refs. [62, 139, 140] and in Chapter IV. Only the details necessary to arrive at a theoretical DOLP expression are presented here. For more information and physical insight, the reader is referred to the aforementioned papers and Chapter IV of this dissertation.

7.2.1.1 Derivation of the Theoretical DOLP.

Recall from Chapter IV that the full pBRDF expression (observation in the specular plane $\phi = \pi$) is [62, 139, 140]

$$
\begin{aligned}
\mathrm{F}_{00}\left(\theta_i, \theta_r, \pi; \sigma; \eta\right) &= \mathrm{F}_{00}^{\mathrm{s}}\left(\theta_i, \theta_r, \pi; \sigma; \eta\right) + \frac{R_s + R_p}{2\pi}\left[1 - \rho_{\mathrm{DHR}}^{\mathrm{s,\,PEC}}\left(\theta_i; \sigma\right)\right] \\
\mathrm{F}_{jk}\left(\theta_i, \theta_r, \pi; \sigma; \eta\right) &= \mathrm{F}_{jk}^{\mathrm{s}}\left(\theta_i, \theta_r, \pi; \sigma; \eta\right) \quad j, k \neq 0
\end{aligned}
\tag{200}
$$

As depicted in Fig. 56, an unpolarized and spatially incoherent light source illuminates an object of complex index of refraction η and roughness σ. Determining the polarization state of the scattered light in this scenario is accomplished using the Stokes/Mueller formalism [112], i.e.,

$$
\begin{bmatrix}
\mathrm{F}_{00} & \mathrm{F}_{01} & 0 \\
\mathrm{F}_{01} & \mathrm{F}_{00} & 0 \\
0 & 0 & \mathrm{F}_{22}
\end{bmatrix}
\begin{bmatrix}
S_0^i \\
0 \\
0
\end{bmatrix}
= S_0^i
\begin{bmatrix}
\mathrm{F}_{00} \\
\mathrm{F}_{01} \\
0
\end{bmatrix}.
\tag{201}
$$

Note that the above expression is only applicable when circular polarization can be ignored and observation is in the specular plane. The theoretical DOLP is readily identified as

$$
\mathcal{P}^{\mathrm{thy}} = \frac{\mathrm{F}_{01}}{\mathrm{F}_{00}}.
\tag{202}
$$

Substituting the applicable elements of Eq. (200) into the above expression and simplifying yields the desired result, i.e.,

$$\mathcal{P}^{\text{thy}}\left(\eta;\sigma;\theta_i,\theta_r\right) = \left(\frac{R_s - R_p}{R_s + R_p}\right)\left\{\frac{\Gamma\left(\theta_i,\theta_r,\pi;\sigma\right)}{\Gamma\left(\theta_i,\theta_r,\pi;\sigma\right) + \left[1 - \rho_{\text{DHR}}^{\text{s, PEC}}\left(\theta_i;\sigma\right)\right]/\pi}\right\} \quad (203)$$

where Γ is

$$\Gamma\left(\theta_i,\theta_r,\phi;\sigma\right) = \frac{G\left(\theta_i,\theta_r,\phi\right)\exp\left[-\tan^2\alpha/\left(2\sigma^2\right)\right]}{8\pi\sigma^2\cos\theta_i\cos\theta_r\cos^4\alpha}. \quad (204)$$

Before discussing the inverse problem, it is important to interpret the theoretical DOLP expression in Eq. (203). The first term on the right hand side of Eq. (203), i.e., $(R_s - R_p)/(R_s + R_p)$, is readily identified as the DOLP of scattered light (unpolarized incident light) from an object with an optically smooth surface [16]. Recall that the microfacet surface model [128] forms the basis of the pBRDF model and by extension Eq. (203). Thus, $(R_s - R_p)/(R_s + R_p)$ physically represents the DOLP of scattered light from a surface composed of optically smooth facets, i.e., microfacets. Note that this is the theoretical expression for the DOLP derived by Thilak *et al.* [123] using the Priest and Germer pBRDF [103, 104]. While it is simple to derive and more importantly invert, the expression does not account for diffuse scattering, which has the physical effect of lowering the DOLP. When viewed in this context, the second term on the right hand side of Eq. (203) represents a diffuse-scattering correction to the DOLP. Consistent with one's intuition, its value varies between 0, for a rough high-σ surface, and 1, for a smooth low-σ surface.

7.2.2 The Inverse Problem.

As previously mentioned, an additional step is required in the inverse problem of the material-characterization technique presented here. This extra step, deconvolution, is necessary because of the degradation of the measured polarimetric data due

to atmospheric turbulence. This subsection provides the necessary background on the deconvolution algorithm utilized in this research. For more information on deconvolution, the reader is referred to Refs. [59, 70, 74, 94, 114] and Chapters III and V of this dissertation.

7.2.2.1 LeMaster and Cain's Polarimetric Blind-Deconvolution Algorithm.

The deconvolution algorithm utilized here is the one developed by LeMaster and Cain [74]. The algorithm, as presented in Ref. [74] and in Chapter III, estimates the polarized and unpolarized image components of a scene, as well as the angle of polarization and polarimetric-image PSF's [44]. For use in the proposed characterization technique, it is more convenient to have the algorithm estimate the first Stokes parameter S_0, the DOLP, and the image PSF's (see Chapter V). Note that the assumptions of unpolarized illumination and observation in the specular plane imply that the angle of polarization is equal to zero. Thus, there is no need to have the algorithm estimate it. In addition to this simple change, LeMaster and Cain's algorithm is modified to include a DOLP prior (defined and discussed in Chapter V) to aid in the DOLP estimate. Note that two DOLP priors are used here—one representative of a dielectric material, the other representative of a metallic material. The DOLP estimate (the one resulting from the dielectric prior or the one resulting from the metallic prior) which maximizes the log-likelihood function is the accepted estimate. For the sake of brevity, only the deconvolution update equations are shown below. The reader is referred to Refs. [61, 74] and Chapters III and V for more detail.

The update equations applicable to the material-characterization technique devel-

oped in this chapter are

$$0 = mc_2^m \mathcal{P}^2 (\mathcal{P} - c_3)^{m-1} - mc_2^m \mathcal{P} (\mathcal{P} - c_3)^{m-1}$$

$$- \mathcal{P} \sum_n \sum_{\boldsymbol{y}} \left(\psi_{un}^{i+1} + \psi_{pn}^{i+1} \right) + \sum_n \sum_{\boldsymbol{y}} \psi_{pn}^{i+1}$$

$$S_0 = \frac{2}{N} \sum_n \sum_{\boldsymbol{y}} \left(\psi_{un}^{i+1} + \psi_{pn}^{i+1} \right) \tag{205}$$

$$h_n(\boldsymbol{z}) = \frac{1}{D_n} \sum_{\boldsymbol{y}} \left[\psi_{un}^{i+1}(\boldsymbol{y}, \boldsymbol{y} - \boldsymbol{z}) + \psi_{pn}^{i+1}(\boldsymbol{y}, \boldsymbol{y} - \boldsymbol{z}) \right]$$

These update equations are derived in the same manner as outlined in Chapter V. The constants of the DOLP priors are $c_1 = 1$, $c_2 = 4$, $c_3 = 0.7$, $m = 10$ for the dielectric DOLP prior and $c_1 = 1$, $c_2 = 7$, $c_3 = 0.15$, $m = 10$ for the metal DOLP prior.

7.2.3   Summary of Material-Characterization Technique.

The material-characterization technique introduced here (shown as a flowchart in Fig. 57) extracts the complex index of refraction of a material using polarimetric imagery degraded by atmospheric turbulence. The technique uses a variant of the LeMaster and Cain [74] blind-deconvolution algorithm to recover S_0, the DOLP $\mathcal{P}$, and the PSF's h_n (described briefly above and in more detail in Chapter V). The estimate for the DOLP is aided by the use of two DOLP priors—one representative of a dielectric material, the other representative of a metallic material. The DOLP estimate which maximizes the log-likelihood function is the accepted DOLP estimate. The deconvolution algorithm is iterated until the stopping criterion is met. Iteration count is used as the stopping criterion in this research. Another stopping criterion based on the variance difference between the estimated and measured images is presented in Ref. [78]. The desired values of n, κ, and σ are found by minimizing the difference between the estimated, or corrected DOLP's (at multiple θ_i and θ_r) and
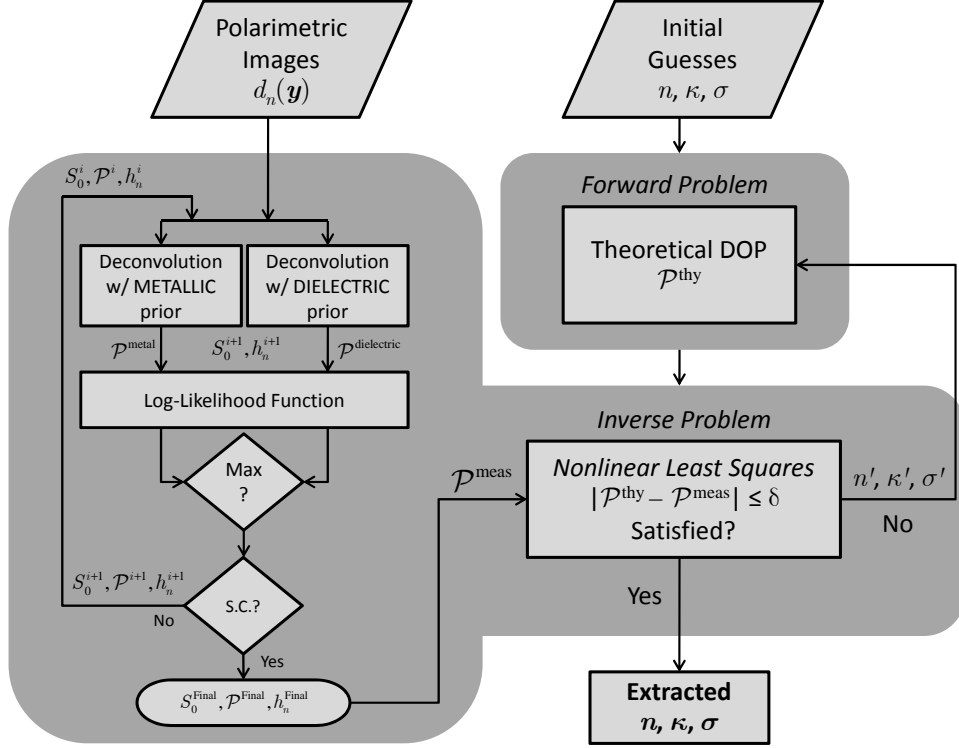
Figure 57. Flowchart of proposed material-characterization algorithm. The ith deconvolution iteration is depicted. S.C. represents the stopping criterion.

the theoretical DOLP's [Eq. (203)] via nonlinear least squares. In the next section, measurement results using the proposed material-characterization algorithm are presented to validate the technique.

7.3 Experimental Verification

7.3.1 Experiment Description and Procedure.

The instrument (see Fig. 47) used to collect the Stokes imagery presented here is the same as that described in Chapter V. For this experiment, the Stokes image formation process (identical to that described in Chapter V) is repeated at seven specular observation geometries, i.e., $\theta_i = \theta_r = 30°$, $35°$, $40°$, $45°$, $50°$, $55°$, and $60°$, to provide the measured DOLP data necessary to extract n and κ. Note that this set of angular measurements makes determining σ difficult. This is demonstrated in
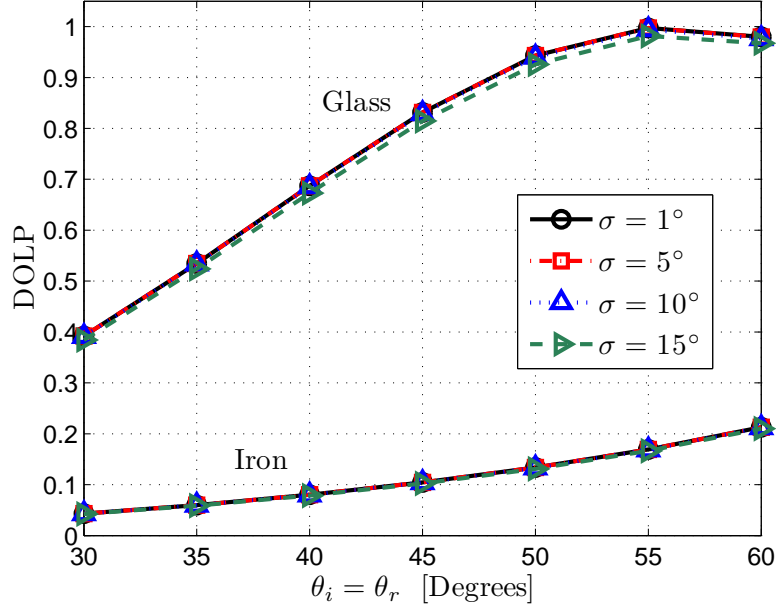
Figure 58. DOLP, demonstrating the effect of σ, of glass ($n = 1.5$, $\kappa = 0$) and iron ($n = 3.6$, $\kappa = 5.9$) predicted at $\theta_i = \theta_r = 30°$, $35°$, $40°$, $45°$, $50°$, $55°$, and $60°$.

Fig. 58 which shows the small effect σ has on the DOLP when observed specularly. A better way to find σ would be to make DOLP measurements by varying θ_r while keeping θ_i constant or vice versa (equivalent due to reciprocity). For this observation scheme to work, however, there must be enough light in the off-specular measurements ($\theta_i \neq \theta_r$) to determine the DOLP. Unfortunately, the Stokes polarimeter utilized here is not sensitive enough to make measurements of this sort. It is for this reason that experimental results employing this observation scheme are not presented. The σ's of the samples characterized in this experiment (shown in Fig. 47) are determined by measuring the width of the specular lobe. While not as accurate as the off-specular scheme described above (results in a per-pixel estimate of σ), this method does result in a mean σ of the sample. For the samples used in this experiment, $\sigma < 1°$, i.e., they are highly specular.

In this experiment, the phase wheel locations are chosen such that the ratio of the aperture diameter D to Fried's parameter r_0 [5, 44, 111] is approximately $D/r_0 \approx 7.9$ and 12.9. For the same reason specified in Chapter V (i.e., to avoid pixel misregistra-

tion due to tilt), the phase wheel is not rotated throughout the data-collection process. In addition to requiring pixel registration during the Stokes image formation process, the material-characterization technique described above requires registration of Stokes images collected over multiple observation angles. This algorithm requirement can result in misregistration due to the fact that as the observation angle changes, the image is stretched or compressed (depending on whether θ_r is increasing or decreasing). This imaging phenomenon is known as the Scheimpflug condition, or keystone distortion [117]. For the algorithm to yield meaningful index-of-refraction values, the misregistration due to keystone distortion must be corrected. For the measurement results presented here, all images are registered to the polarimetric images of the object at $\theta_i = \theta_r = 30°$. This is accomplished by cropping (by the appropriate amount) the polarimetric images collected at the other observation angles and digitally expanding them back to their original size (250×316). It should be noted that tilt, or turbulence misregistration is an issue here as well. It can be mitigated with the use of a tilt sensor and a fast steering mirror or with post-processing image-registration techniques.

The painted aluminum and steel samples used in this experiment (see Fig. 47) were prepared in the same manner as that described in Chapter V. Processing of the raw polarimetric images and initial guesses input into the deconvolution algorithm for S_0, $\mathcal{P}$, and h_n are also the same as that described in Chapter V.

7.3.2 Characterization Results.

Figure 59 shows the no-turbulence, turbulence-degraded, and corrected (after 250 deconvolution iterations) S_0 images at $\theta_i = \theta_r = 30°$ for the painted aluminum and painted steel samples, respectively. Note that in the corrected S_0 images for both the aluminum and steel samples, the algorithm successfully recovers features lost
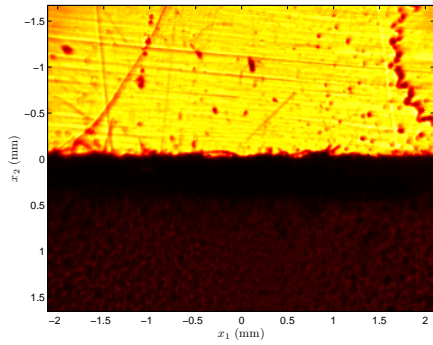
(a) Painted Al, no-turbulence S_0.
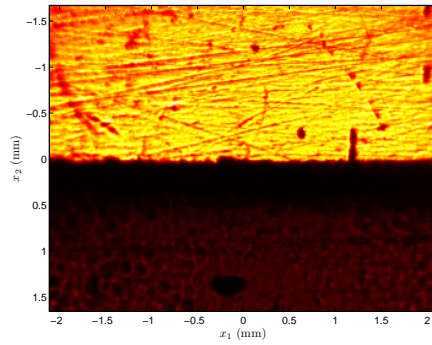

(b) Painted steel, no-turbulence S_0.
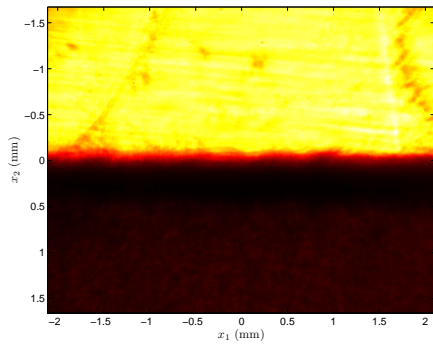
(c) Painted Al, turbulence-degraded S_0.
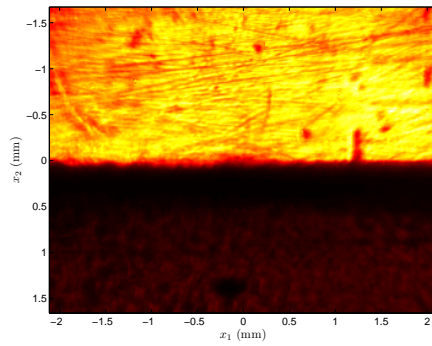

(d) Painted steel, turbulence-degraded S_0.
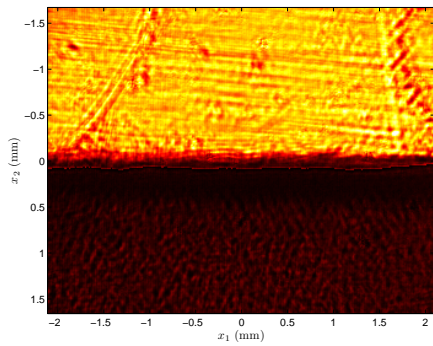
(e) Painted Al, corrected S_0.
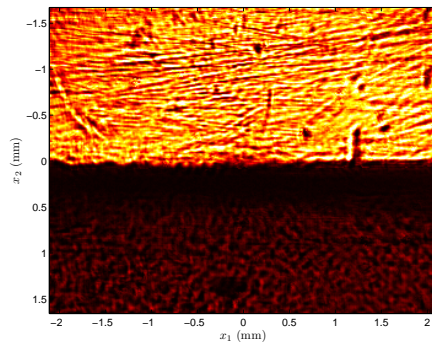
(f) Painted steel, corrected S_0.

Figure 59. S_0 **experimental results for the painted aluminum ($D/r_0 \approx 12.9$) and painted steel ($D/r_0 \approx 7.9$) samples. The S_0 images of the samples are those collected at $\theta_i = \theta_r = 30°$. The dimensions annotated on the figures are object coordinates $x = (x_1, x_2)$ at normal incidence.**

177
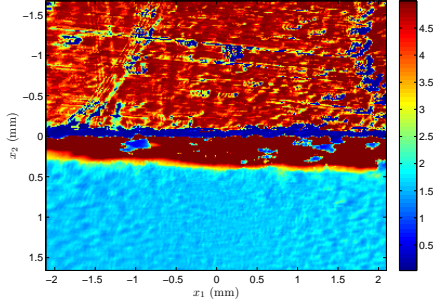
(a) Painted Al, no-turbulence n.
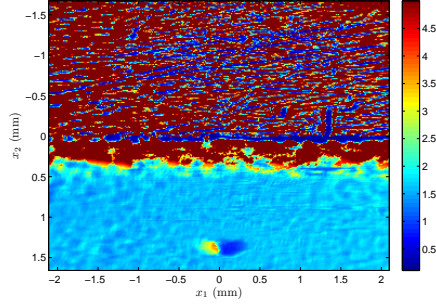
(b) Painted steel, no-turbulence n.
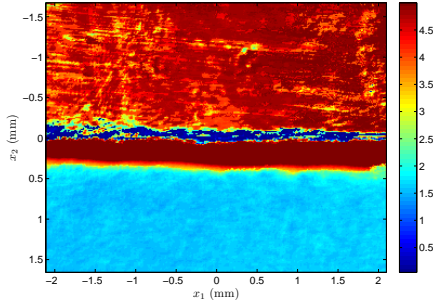
(c) Painted Al, turbulence-degraded n.
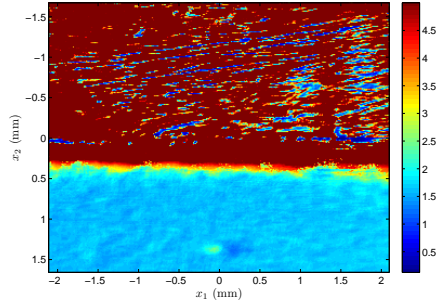
(d) Painted steel, turbulence-degraded n.
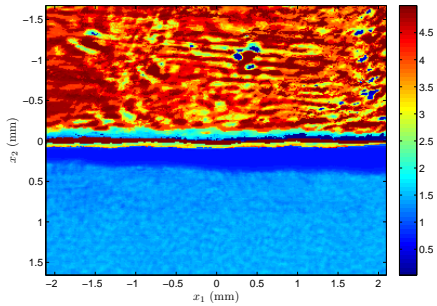
(e) Painted Al, corrected n.
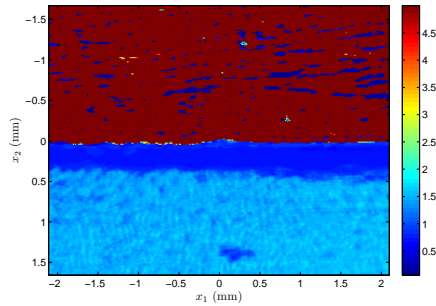
(f) Painted steel, corrected n.

Figure 60. Index of refraction n experimental results for the painted aluminum ($D/r_0 \approx$ 12.9) and painted steel ($D/r_0 \approx 7.9$) samples. The n values for aluminum, steel, and green paint are $n = 1.44$, 3.60, and 1.39, respectively. The dimensions annotated on the figures are object coordinates $x = (x_1, x_2)$ at normal incidence.

178

Table 5. Means and standard deviations of n and κ for the painted aluminum and painted steel samples.

	Aluminum ($n = 1.44$, $\kappa = 16$) Area				Steel ($n = 3.60$, $\kappa = 5.88$) Area			
	$E[n]$	σ_n	$E[\kappa]$	σ_κ	$E[n]$	σ_n	$E[\kappa]$	σ_κ
No Turb.	3.8614	1.487	11.1757	3.7652	3.8649	1.6921	5.7123	1.6088
Turb. $D/r_0 \approx 7.9$	4.1437	1.1708	11.9855	2.8092	4.4741	1.1529	6.3506	1.0067
Turb. $D/r_0 \approx 12.9$	4.2454	1.0718	12.2713	2.7750	4.8632	0.52165	6.7198	0.59269
Corr. $D/r_0 \approx 7.9$	3.9451	1.2605	11.3748	3.1434	4.6241	1.2863	4.6493	1.3366
Corr. $D/r_0 \approx 12.9$	3.9762	1.0008	11.9791	2.2400	4.8465	0.84901	5.0693	1.0472

	Green Paint ($n = 1.39$, $\kappa = 0.34$) Area				Green Paint ($n = 1.39$, $\kappa = 0.34$) Area			
	$E[n]$	σ_n	$E[\kappa]$	σ_κ	$E[n]$	σ_n	$E[\kappa]$	σ_κ
No Turb.	2.2467	1.2717	1.4073	1.4859	2.1424	1.1946	1.1951	1.0491
Turb. $D/r_0 \approx 7.9$	2.2420	1.2777	1.5772	1.9564	2.3459	1.2942	1.4020	1.6017
Turb. $D/r_0 \approx 12.9$	2.3074	1.3033	1.8434	2.5221	2.3819	1.3459	1.7714	2.207
Corr. $D/r_0 \approx 7.9$	1.2832	0.30757	0.68629	0.14007	1.3290	0.40899	0.63531	0.22920
Corr. $D/r_0 \approx 12.9$	1.3586	0.49623	0.77617	0.34729	1.3874	0.67263	0.74994	0.65207

in the turbulence-degraded S_0 images. Figures 60 and 61 show plots of the index of refraction n and the coefficient of extinction κ extracted from the no-turbulence, turbulence-degraded, and corrected DOLP's. Means and standard deviations of the n and κ values are shown in Table 5. Note that the accepted index-of-refraction and coefficient-of-extinction values for aluminum and steel (iron) at 1550 nm are $n = 1.44$, $\kappa = 16.0$ and $n = 3.60$, $\kappa = 5.88$, respectively [76]. No accepted complex index-of-refraction value exists for green paint; however, the results obtained by Thilak *et al.* [123] at 650 nm ($n = 1.39$, $\kappa = 0.34$) and Wellems *et al.* [140] at approximately 9 μm ($n = 1.41$, $\kappa = 0.24$) are consistent. The interior-reflective Newton method is used to extract n and κ [24]. It is a bounded solver, i.e., it searches for the best solution on a specified domain. The bounds chosen for n and κ here are $n \in [0, 5]$ and $\kappa \in [0, 25]$. Note that these bounds encompass a majority of the complex index-of-refraction values one would expect from metals and common dielectric materials at 1550 nm.

Overall, the material-characterization technique performs well. The characterization results for the green paint (dielectric) regions of the samples are especially impressive. The characterization results for the metal regions of the samples are erro-
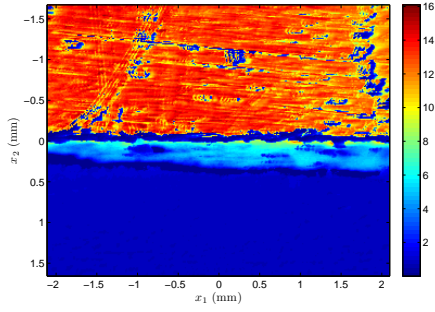
(a) Painted Al, no-turbulence κ.
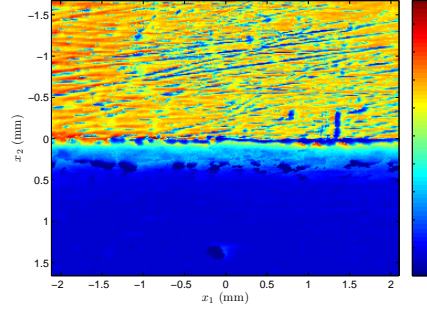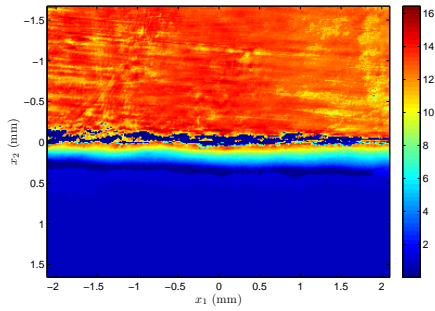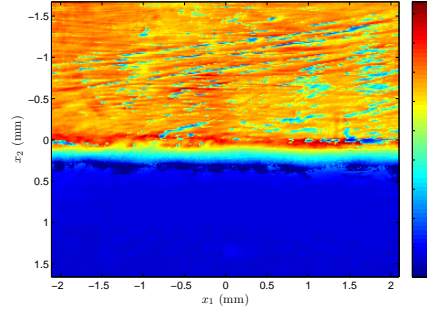
(b) Painted steel, no-turbulence κ.

(c) Painted Al, turbulence-degraded κ.

(d) Painted steel, turbulence-degraded κ.
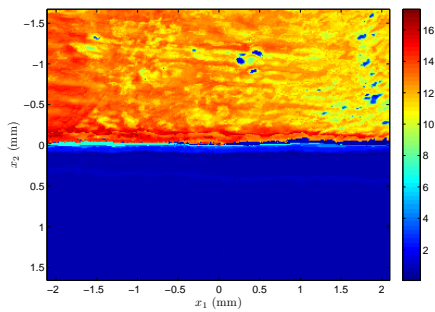
(e) Painted Al, corrected κ.
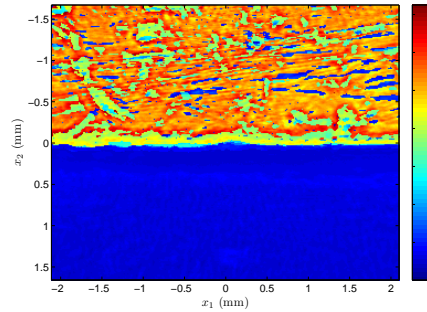
(f) Painted steel, corrected κ.

Figure 61. Coefficient of extinction κ experimental results for the painted aluminum $(D/r_0 \approx 12.9)$ and painted steel $(D/r_0 \approx 7.9)$ samples. The κ values for aluminum, steel, and green paint are $\kappa = 16$, 5.88, and 0.34, respectively. The dimensions annotated on the figures are object coordinates $x = (x_1, x_2)$ at normal incidence.

180

neous. In particular, the n values extracted from the metals are inconsistent with the accepted values. Note, however, that the results for κ are more accurate. There are two main reasons for this metal-characterization error. The first is due to the greater difficulty in measuring the DOLP of light scattered from metal surfaces. This difficulty arises from the fact that over most observation angles the Fresnel reflectances (R_s and R_p) of metals are approximately equal, i.e, $R_s \approx R_p$. This makes measuring the difference in irradiance between the two polarization states difficult and thus leads to greater error (greater noise susceptibility) in the DOLP measurement. Note that the opposite is true for dielectric surfaces. Over most observation angles R_s is several times R_p. It is therefore much easier to discern a difference in irradiance between the two polarization states resulting in a more accurate DOLP measurement. This is clearly evident in the results presented in Table 5. Note that DOLP measurements of metal surfaces made beyond $\theta_i = \theta_r = 80°$ (pseudo-Brewster's angle [65], i.e., max $R_s - R_p$) should help the characterization; however, these near-grazing observation angles are especially difficult in imaging because of keystone distortion. The second possible reason for the error is oxidation. Metallic aluminum reacts with oxygen to form alumina, a dielectric. Likewise, steel (actually, the iron in it) reacts with oxygen to form rust, another dielectric. Thin coatings of alumina and rust on the metal regions of the samples would affect the DOLP of light scattered from those regions and thus affect the index of refraction.

Before concluding, it is worth noting a couple more aspects of the experimental results. In the n and κ images, Figs. 60 and 61, respectively, the scratches in the metal are characterized differently than the metal itself. This erroneous characterization is due to the behavior of electromagnetic waves at edge-like structures. The scratches in the samples scatter more light in the polarization state parallel to the scratches than the polarization orthogonal to the scratches. Thus, scattered light

from the scratches is polarized more strongly than the surrounding metal explaining the mischaracterization. This scattering phenomenon is the same exploited to create wire-grid polarizers and polarimetric edge-detection algorithms. Note that although these features are mischaracterized, they are resolved in the corrected n and κ images after being lost in the turbulence-degraded images. Also, in the corrected n and κ images, a distinct boundary is resolved between the metal and green paint regions of the samples. Note that this occurs as a result of the deconvolution algorithm and is a highly desirable aspect of the proposed material-characterization technique.

7.4 Conclusion

In this chapter, a material-characterization technique using passive polarimetric imagery degraded by atmospheric turbulence is presented. The technique uses a variant of the LeMaster and Cain deconvolution algorithm [74] (discussed briefly above and in more detail in Chapter V) to recover the object S_0, the DOLP $\mathcal{P}$, and the PSF's h_n from turbulence-degraded polarimetric imagery. Nonlinear least squares is then used to find the values of index of refraction n and coefficient of extinction κ which best fit the theoretical DOLP (shown above), derived using a pBRDF [62, 139, 140] (see Chapter IV), to the turbulence-corrected DOLP. Lastly, experimental characterization results of two painted metal samples are provided to verify the proposed technique. It is found that the technique performs well. It recovers object features lost in the turbulence-degraded imagery, provides a clear demarcation between the material types of the samples, and characterizes the dielectric (painted) regions of the samples very accurately. The characterization results for the metal regions of the samples are less accurate with the results for κ being more accurate than n. As discussed, this metal-characterization error is likely due to the inherent difficulty in measuring the DOLP of metal surfaces (i.e., greater noise susceptibility

in the measurement) and possible oxidation of the metal portions of the samples.

The main contribution of the work presented in this chapter is a method to passively characterize materials with imagery degraded by turbulence. Future research in this subject will include extension of the technique to situations where the observation geometry is unknown, out-of-specular-plane observation, and active illumination scenarios.

VIII. Conclusions

In this dissertation, an algorithm is developed to estimate the index of refraction of an unknown object using passive polarimetric images degraded by atmospheric turbulence (see Chapter VII). The algorithm uses a variant of the LeMaster and Cain polarimetric maximum-likelihood blind-deconvolution algorithm to estimate the true object S_0, the degree of linear polarization (DOLP), and the point spread functions (PSF's) from turbulence-degraded polarimetric imagery. The values for the index of refraction n and the coefficient of extinction κ are found by minimizing the difference between the theoretical DOLP (derived using a pBRDF) and the turbulence-corrected DOLP via nonlinear least squares. Experimental characterization results of two painted metal samples are provided to verify the technique. It is found that the characterization technique performs well. It recovers object features lost in the turbulence-degraded imagery, provides a clear demarcation between the material types of the samples, and characterizes the dielectric (painted) regions of the samples very accurately. The characterization results for the metal regions of the samples are less accurate with the results for κ being more accurate than n. As discussed, this metal-characterization error is likely due to the inherent difficulty in measuring the DOLP of metal surfaces (i.e., greater noise susceptibility in the measurement) and possible oxidation of the metal portions of the samples.

In addition to the material-characterization algorithm discussed above, the pBRDF used to solve the forward problem is validated in two ways (see Chapter IV). The first compares predictions made using the pBRDF to MoM solutions of a rough PEC surface. The second compares predictions made using the pBRDF to experimental Mueller matrix results of LabSphere Infragold and flame-sprayed aluminum. It is shown, via these results, that the pBRDF accurately models the physics of the light/material surface interaction. While the pBRDF itself is not new research, it has

never been fully validated until now. Comparing predictions made using the pBRDF to exact electromagnetic solutions of a surface is a novel approach to validating a pBRDF.

Lastly, two material-classification techniques (Chapters V and VI) are developed in this dissertation as well. The first classification algorithm determines whether an object is composed of metal or dielectric materials using turbulence-degraded polarimetric imagery. As is the case for the material-characterization algorithm discussed above, the classification algorithm uses a variant of the LeMaster and Cain deconvolution algorithm to estimate S_0, the DOLP, the AOP, and the PSF's from turbulence-degraded polarimetric imagery. The metal/dielectric classification decision is made depending on which DOLP estimate (the estimate resulting from the dielectric DOLP prior or the estimate resulting from the metal DOLP prior) maximizes the log-likelihood function. Experimental results of two painted metal samples are provided to validate the technique. It is found that the algorithm performs well for off-normal collection geometries. For near-normal geometries, the algorithm, as expected, poorly classifies dielectric materials. As discussed, it may be possible to alleviate this limitation through adaptive DOLP priors (discussed below). The second classification algorithm is an enhanced version of the first. It determines whether an object is composed of aluminum, iron, or dielectric materials. This is accomplished by redesigning the DOLP priors used to make the classification decision. It is experimentally demonstrated that the algorithm is able to determine whether an object is composed of aluminum, iron, or dielectric materials. This new metal classification provides functional information about the object which is not provided by existing dielectric/metal classifiers.

8.1 Future Work

There are several areas of this research that can be investigated further. Listed below are a few examples.

8.1.1 Adaptive DOLP Priors for the Material-Classification Algorithms.

As discussed above (and in the previous chapters), the material-classification algorithms designed in this dissertation perform poorly for near-normal collection geometries. This poor performance is due to the fact that natural material weakly polarize scattered light at near-normal incident angles. This limitation can be alleviated somewhat by adaptively updating the DOLP priors as more information becomes known about the scene. This can be accomplished by inspecting the histogram of the DOLP estimate and choosing new values for the constants in Eqs. (196) and (198) in Chapters V and VI, respectively. This modification has the possibility of extending the region of validity of the algorithm to $\theta_i, \theta_r \approx 15°$. Collection geometries $\theta_i, \theta_r < 15°$ will be difficult to correctly classify even with this modification because of the very weak manner in which natural materials polarize scattered light under these conditions.

8.1.2 Incorporating the Angle of Polarization.

Not really considered in this research is the angle of polarization (AOP). In passive polarimetry, the AOP provides information about the object geometry. Consider an unpolarized source illuminating a material surface observed through a linear polarizer

(LP). The Stokes vector/Mueller matrix representation of this scenario is

$$I\left(\theta\right) = \begin{bmatrix} 1 & 0 & 0 \end{bmatrix} \begin{bmatrix} 1 & \cos 2\theta & \sin 2\theta \\ \cos 2\theta & \cos^2 2\theta & \cos 2\theta \sin 2\theta \\ \sin 2\theta & \cos 2\theta \sin 2\theta & \sin^2 2\theta \end{bmatrix} \begin{bmatrix} F_{00} & F_{01} & F_{02} \\ F_{10} & F_{11} & F_{12} \\ F_{20} & F_{21} & F_{22} \end{bmatrix} \begin{bmatrix} 1 \\ 0 \\ 0 \end{bmatrix} \quad (206)$$

where θ is the LP angle and F_{ij} are the pBRDF components defined in Eq. (177). Carrying out the matrix multiplication results in

$$\mathrm{AOP} = \frac{1}{2}\tan^{-1}\left(\frac{S_2}{S_1}\right) = \gamma_r. \quad (207)$$

Recall from Chapter IV (Fig. 35) that γ_r is the angle between the macroscopic plane of reflection and the scattering plane of the microfacet. It is related to the incident and observation angles by rather complicated expressions:

$$\cos \gamma_r = \left(\cos \alpha - \cos \theta_r \cos \beta\right) / \left(\sin \theta_r \sin \beta\right)$$
$$\cos \alpha = \left(\cos \theta_i + \cos \theta_r\right) / \left(2 \cos \beta\right) \quad . \quad (208)$$
$$\cos 2\beta = \cos \theta_i \cos \theta_r + \sin \theta_i \sin \theta_r \cos \phi$$

When $\phi = 0$ is substituted into the Eq. (208), AOP $= \gamma_r = 0$. Thus, AOP $= 0$ implies observation in the specular plane. While it may be possible to find the observation geometry exactly with the AOP alone (does not appear likely), the AOP (independent of the index of refraction of the material) is still useful as a measure of how far in azimuth ϕ the observer is away from the specular plane. This information can be incorporated into the material-characterization algorithm developed in Chapter VII to extend the technique to out-of-specular-plane observation geometries. Note that θ_i and θ_r still have to be known. Since many remote-sensing platforms are likely to possess a global positioning system or an inertial navigation system onboard,

these angles, at the very least, can be estimated [123].

8.1.3 Active Polarimetry.

As described in the previous chapters, active polarimetry is the measure of the polarization state of scattered light when the source excitation is controlled. A very good example of active polarimetry is ellipsometry [127]. When one considers how powerful a tool ellipsometry is, it becomes apparent that redesigning the algorithms developed in this dissertation to work under active illumination scenarios could provide a great deal more information about the object than the current passive techniques. As with any engineering decision, utilizing active illumination brings with it some complications not encountered in passive polarimetry. First, the mathematical simplifications associated with using a passive source do not apply under active illumination scenarios. For instance, circular polarization cannot be ignored in active polarimetry. Second, active illumination in remote sensing typically utilizes a coherent source such as a laser. This introduces speckle which is not encountered in incoherent imaging. Third, the techniques developed in this research are bistatic in nature, i.e., the source and observer are in different locations. This is important in polarimetry because change in polarization state occurs for off-normal collection geometries (i.e., bistatic measurements). Active illumination in remote sensing is most commonly performed with the source and observer in the same location, i.e., a monostatic measurement. Examples of this include RADAR, SONAR, and LADAR. The fact that a bistatic measurement is necessary to observe a polarization state change does somewhat limit the feasibility of using active polarimetry in the field. Note that there exist a great amount of research dealing with a phenomenon known as enhanced backscatter [8, 7, 18, 67, 77]. Enhanced backscatter occurs when light interacts with a very rough surface and is the result of multiple surface reflections (at least two).

This scattering effect may be exploitable for active polarimetry using coherent illumination. The author does not possess a strong understanding of this phenomenon, and therefore the interested researcher should review the referenced papers as well as the literature (especially work by Ezekiel Bahar) before proceeding. Lastly, since polarization is defined using the object's coordinate system, not knowing the object geometry makes active polarimetry much more difficult than passive polarimetry. For instance, transmitting a $\begin{bmatrix} 1 & 0 & 1 & 0 \end{bmatrix}^{\mathrm{T}}$ beam does not necessarily mean that will be the polarization state which interrogates the object. Passive polarimetry, on the other hand, assumes that the illumination is unpolarized. This assumption implies that no matter the orientation of the target relative to the source, an unpolarized beam interrogates the object. These challenges aside, extending the algorithms developed in this dissertation to work under active illumination scenarios is a rich area of future research.

8.1.4   Field Testing.

Having demonstrated classification and characterization of materials using polarimetric imagery degraded by atmospheric turbulence in the laboratory, the next step is to test the algorithms developed in this dissertation on actual scenes degraded by actual turbulence. Unfortunately, this is not possible using the polarimeter described in the previous chapters. Thus, future field research using the algorithms developed in this dissertation will require a new, compact polarimeter. One suitable for this future polarimetric research is depicted in Fig. 62. The polarimeter shown in the figure is a division of amplitude polarimeter (DoAmP) developed by FluxData, Inc. [37]. Light enters the camera's aperture and is split three ways. The light along each optical path passes through a LP oriented at a certain angle before being sensed by a charged-coupled device (CCD). In this manner, S_0, S_1, and S_2 images can be

Schematic View of 3-CCD Camera

F-Mount Lens

CCD Sensor

CCD Sensor

3-Way Prism Beamsplitter

CCD Sensor

FluxData
Incorporated
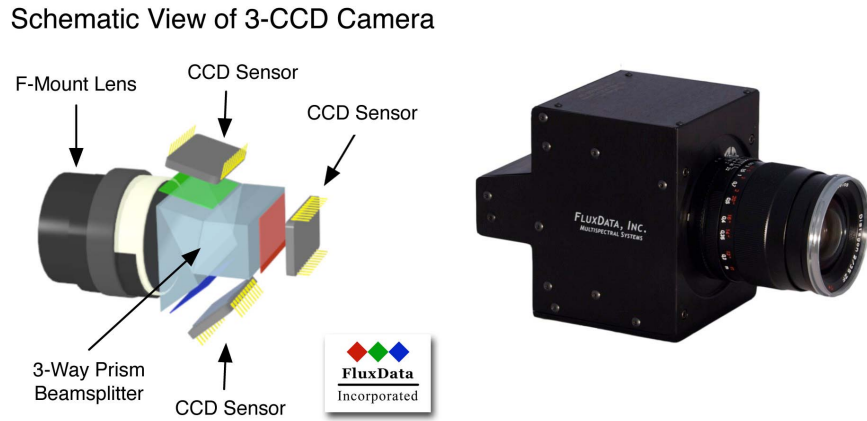
Figure 62. A compact division of amplitude polarimeter (DoAmP) from FluxData, Inc. [37].

obtained simultaneously. The device has a programmable electronic shutter (equivalent to integration time) which can be set to any value between 1 μs and 65 s. The maximum frame rate is 120 Hz; this value does depend on the specified CCD arrays. The polarimeter shown above can easily be incorporated into the existing laboratory configuration for controlled testing or mounted on a tripod and used in the field.

8.1.5 Improvement of the pBRDF.

The accuracy of any material-characterization technique relies heavily on the accuracy of the solution to the forward problem. In this research, the solution to the forward problem, i.e., the theoretical degree of linear polarization, is derived using a geometrical optics pBRDF. As discussed in the previous chapters, geometrical optics is an asymptotic approach to scattering which approximates light as a ray. It does not (in its most basic form) account for wave effects associated with scattering. For instance, geometrical optics predicts that light incident on a smooth surface of size X is scattered completely in the specular direction (i.e., the scattered light possesses no lobing structure) which is only true when the wavelength $\lambda \to 0$ or when X $\to \infty$.

Physical optics, like geometrical optics, is also an asymptotic approach to scattering. It, being based on a more rigorous approximation, more accurately predicts

the light scattered from a surface than does geometrical optics. For instance, physical optics predicts that light incident on a smooth surface of size X is scattered in non-specular directions (that is, the scattered light possesses a lobing structure). The amount of light scattered in the non-specular directions is related to X/λ.

One obvious improvement to the material-characterization algorithm developed in Chapter VII is to replace the geometrical optics pBRDF with a pBRDF based on physical optics. A physical optics pBRDF that can be used to solve the forward problem is the one developed by An and Zeringue [3]. It should be noted that even physical optics breaks down when object or surface features fall below 5λ and edge effects become significant. For these situations, a more rigorous approximation, like the Physical Theory of Diffraction (PTD) [136], can possibly be used to develop a new pBRDF.

8.1.6 Deconvolution Algorithm and Atmospheric Correction.

The deconvolution algorithm used in this research is a close variant of the one published by LeMaster and Cain [74]. One possible improvement is to redesign the algorithm to estimate the ellipticity angle χ along with S_0, the DOP, the AOP α, and the PSF's. In order to make this change, the irradiance received through a quarter-wave plate (QWP) and a LP must be modeled:

$$
I\left(\theta_{\mathrm{LP}}, \theta_{\mathrm{QWP}}\right) = \begin{bmatrix} 1 & 0 & 0 & 0 \end{bmatrix} \mathbf{M}_{\mathrm{LP}}\left(\theta_{\mathrm{LP}}\right) \mathbf{M}_{\mathrm{QWP}}\left(\theta_{\mathrm{QWP}}\right)
$$
$$
\left\{ \mathcal{P} S_0 \begin{bmatrix} 1 \\ \cos 2\alpha \cos 2\chi \\ \sin 2\alpha \cos 2\chi \\ \sin 2\chi \end{bmatrix} + (1 - \mathcal{P}) S_0 \begin{bmatrix} 1 \\ 0 \\ 0 \\ 0 \end{bmatrix} \right\}. \tag{209}
$$

Carrying out the matrix multiplications and simplifying produces

$$I\left(\theta_{\mathrm{LP}}, \theta_{\mathrm{QWP}}\right) = \frac{1}{2}\left(1 - \mathcal{P}\right) S_0 + \frac{1}{2}\mathcal{P}S_0$$

$$\left[1 + \cos 2\chi \cos\left(2\theta_{\mathrm{LP}} - 2\theta_{\mathrm{QWP}}\right)\cos\left(2\alpha - 2\theta_{\mathrm{QWP}}\right) + \sin 2\chi \sin\left(2\theta_{\mathrm{LP}} - 2\theta_{\mathrm{QWP}}\right)\right]$$

$$(210)$$

Note that this expression is very similar to Eq. (185) in Chapter V and thus the same method used in that chapter to derive the update equations can be applied here as well. With this change to LeMaster and Cain's algorithm, the algorithm would now be able to recover any polarization state, or equivalently any Stokes vector. This is a necessary step if one wishes to adapt the algorithms developed in this dissertation to work under active illumination scenarios.

Another possible improvement to LeMaster and Cain's algorithm, in regards to the material-characterization technique derived in Chapter VII, would be to redesign the algorithm to estimate n and κ directly. Attempting to estimate n and κ directly, using the algorithm in its current form, results in very complex coupled update equations. In order for this to work, the algorithm would have to be completely redesigned.

In addition to these possible improvements to the deconvolution algorithm, the techniques developed in this research could be applied to data captured using a polarimeter where the atmospheric distortion is corrected using an adaptive optics system. The OPTECS laboratory already contains all the necessary AO hardware to perform the experiments. Some redesign of the current layout of the optical bench would be required.

Bibliography

[1] Ageorges, Nancy and Chris Dainty. *Laser Guide Star Adaptive Optics for Astronomy*. Kluwer Academic Publishers, Norwell, MA, 2000.

[2] Aïnouz, Samia, Jihad Zallat, Antonello de Martino, and Christophe Collet. "Physical interpretation of polarization-encoded images by color preview". *Opt. Express*, 14(13):5916–5927, 2006. URL `http://www.opticsexpress.org/abstract.cfm?URI=oe-14-13-5916`.

[3] An, Chang-Hyuk and Kyle J. Zeringue. "Polarization scattering from rough surfaces based on the vector Kirchhoff diffraction model". volume 5158, 205–216. SPIE, 2003. URL `http://link.aip.org/link/?PSI/5158/205/1`.

[4] Anderson, Richard. "Matrix description of radiometric quantities". *Appl. Opt.*, 30(7):858–867, March 1991.

[5] Andrews, Larry C. and Ronald L. Phillips. *Laser Beam Propagation Through Random Media*. SPIE Press, Bellingham, WA, 2nd edition, 2005.

[6] Axline, R. M. and Adrian K. Fung. "Numerical computation of scattering from a perfectly conducting random surface". *IEEE Trans. Antennas Propag.*, AP-26(3):482–488, May 1978.

[7] Bahar, E. and M. El-Shenawee. "Vertically and horizontally polarized diffuse double-scatter cross sections of one-dimensional random rough surfaces that exhibit enhanced-backscatter—full-wave solutions". *J. Opt. Soc. Am. A*, 11(8):2271–2285, 1994. URL `http://josaa.osa.org/abstract.cfm?URI=josaa-11-8-2271`.

[8] Bahar, Ezekiel and Mary Ann Fitzwater. "Depolarization and backscatter enhancement in light scattering from random rough surfaces: comparison of full-wave theory with experiment". *J. Opt. Soc. Am. A*, 6(1):33–43, 1989. URL `http://josaa.osa.org/abstract.cfm?URI=josaa-6-1-33`.

[9] Balanis, Constantine A. *Advanced Engineering Electromagnetics*. John Wiley & Sons, Inc., Hoboken, NJ, 1989.

[10] Barrick, D. E. "Theory of HF and VHF propagation across the rough sea—parts I and II". *Radio Sci.*, 6:517–533, 1971.

[11] Beckmann, Petr and André Spizzichino. *The Scattering of Electromagnetic Waves from Rough Surfaces*. Artech House, Inc., Norwood, MA, 1963.

[12] Bell, Guy C. "Refractive index of opaque high-gloss surfaces". *J. Opt. Soc. Am.*, 47(12):1118–1120, December 1957.

[13] Berg, Eric C. and Jeffrey D. Barchers. *ATSBNM: Atmospheric Turbulence Simulator with N Modules and Control System Base User Manual (Ver 2.0)*. Science Applications International Corporation (SAIC), July 2007.

[14] Bickel, William S. and Wilbur M. Bailey. "Stokes vectors, Mueller matrices, and polarized scattered light". *Am. J. Phys.*, 53(5):468–478, May 1985.

[15] Blinn, James F. "Models of light reflection for computer synthesized pictures". *SIGGRAPH 1977 Proceedings*, 192–198. Special Interest Group on Graphics and Interactive Techniques, Computer Graphics, 1977.

[16] Born, Max and Emil Wolf. *Principles of Optics*. Cambridge University Press, New York, NY, 7th edition, 1999.

[17] Breon, F.-M., D. Tanre, P. Lecomte, and M. Herman. "Polarized reflectance of bare soils and vegetation: measurements and models". *IEEE Trans. Geosci. Remote Sens.*, 33(2):487–499, March 1995. ISSN 0196-2892.

[18] Bruce, N. C., A. J. Sant, and J. C. Dainty. "The Mueller matrix for rough surface scattering using the Kirchhoff approximation". *Opt. Commun.*, 88(4-6):471–484, 1992. ISSN 0030-4018. URL `http://www.sciencedirect.com/science/article/B6TVF-46JGWT3-1TH/2/8b6fe4a98d0b9baba0ea61c8cb1175a7`.

[19] Chang, Chang, Erik Anderson, Patrick Naulleau, Eric Gullikson, Kenneth Goldberg, and David Attwood. "Direct measurement of index of refraction in the extreme-ultraviolet wavelength region with a novel interferometer". *Opt. Lett.*, 27(12):1028–1030, June 2002.

[20] Chen, Chao, Yong-qiang Zhao, Li Luo, Dan Liu, and Quan Pan. "Robust materials classification based on multispectral polarimetric BRDF imagery". volume 7384, 73840T. SPIE, 2009. URL `http://link.aip.org/link/?PSI/7384/73840T/1`.

[21] Chen, Hua and Lawrence B. Wolff. "Polarization phase-based method for material classification and object recognition in computer vision". volume 2599, 54–63. SPIE, 1996. URL `http://link.aip.org/link/?PSI/2599/54/1`.

[22] Chen, L. F., C. K. Ong, C. P. Neo, V. V. Varadan, and V. K. Varadan. *Microwave Electronics: Measurement and Materials Characterization.* John Wiley & Sons, Ltd., West Sussex, England, 2004.

[23] Chen, M. F. and S. Y. Bai. "Computer simulation of wave scattering from a dielectric random surface in two dimensions—cylindrical case". *J. Electromagn. Waves Appl.*, 4(10):963–982, 1990.

[24] Coleman, Thomas F. and Yuying Li. "An interior trust region approach for nonlinear minimization subject to bounds". *SIAM J. Optim.*, 6(2):418–445, 1996. URL `http://link.aip.org/link/?SJE/6/418/1`.

[25] Compain, Eric, Stéphane Poirier, and Bernard Drevillon. "General and self-consistent method for the calibration of polarization modulators, polarimeters, and Mueller-matrix ellipsometers". *Appl. Opt.*, 38(16):3490–3502, June 1999.

[26] Cook, Robert L. and Kenneth E. Torrance. "A reflectance model for computer graphics". *SIGGRAPH 1981 Proceedings*, volume 15, 307–316. Special Interest Group on Graphics and Interactive Techniques, Computer Graphics, August 1981.

[27] Coulson, Kinsell L. *Polarization and Intensity of Light in the Atmosphere*. A. Deepak Publishing, Hampton, VA, 1988.

[28] DeBell, A. G., E. L. Dereniak, J. Harvey, J. Nissley, J. Palmer, A. Selvarajan, and W. L. Wolfe. "Cryogenic refractive indices and temperature coefficients of cadmium telluride from 6 μm to 22 μm". *Appl. Opt.*, 18(18):3114–3115, September 1979.

[29] DeFranzo, A. C. and B. G. Pazol. "Index of refraction measurement on sapphire at low temperatures and visible wavelengths". *Appl. Opt.*, 32(13):2224–2234, May 1993.

[30] Demos, Stavros, Harry Radousky, and Robert Alfano. "Deep subsurface imaging in tissues using spectral and polarization filtering". *Opt. Express*, 7(1):23–28, 2000. URL `http://www.opticsexpress.org/abstract.cfm?URI=oe-7-1-23`.

[31] Eckart, C. "The scattering of sound from the sea surface". *J. Acoust. Soc. Am.*, 25:566–570, 1953.

[32] Edwards, David, William Humbert, and Charles Kim. "Influence of sensing geometry on polarimetric reflectance data". *Opt. Eng.*, 47(11):1–8, November 2008.

[33] Ellis, Kenneth K. "Polarimetric bidirectional reflectance distribution function of glossy coatings". *J. Opt. Soc. Am. A*, 13(8):1758–1762, August 1996.

[34] Fetrow, Matthew P., David Wellems, Stephanie H. Sposato, Kenneth P. Bishop, Thomas R. Caudill, Michael L. Davis, and Elizabeth R. Simrell. "Results of a new polarization simulation". volume 4481, 149–162. SPIE, 2002. URL `http://link.aip.org/link/?PSI/4481/149/1`.

[35] FLIR Systems, Inc. *Alpha NIR User's Guide*, 2002.

[36] FLIR Systems, Inc. *Alpha NIR Technical Specifications*, 2004.

[37] FluxData, Inc. "FD-1665 3-CCD Multispectral Camera". URL `http://www.fluxdata.com/wp-content/uploads/FD-1665-brochure.pdf`.

[38] Flynn, David S. and Cliff Alexander. "Polarized surface scattering expressed in terms of a bidirectional reflectance distribution function". *Opt. Eng.*, 34(6):1646–1650, June 1995.

[39] Frehlich, Rod. "Simulation of laser propagation in a turbulent atmosphere". *Appl. Opt.*, 39(3):393–397, January 2000.

[40] Fung, A. K. and M. F. Chen. "Numerical simulation of scattering from simple and composite random surfaces". *J. Opt. Soc. Am. A*, 2(12):2274–2284, December 1985.

[41] Gartley, M. G., S. D. Brown, and J. R. Schott. "Micro-scale surface and contaminate modeling for polarimetric signature prediction". volume 6972, 697213. SPIE, 2008. URL `http://link.aip.org/link/?PSI/6972/697213/1`.

[42] Gartley, Michael G. *Polarimetric Modeling of Remotely Sensed Scenes in the Thermal Infrared*. Ph.D. dissertation, Chester F. Carslon Center for Imaging Science, Rochester Institute of Technology, Rochester, NY, 2007.

[43] Gerchberg, R. W. and W. O. Saxton. "A practical algorithm for the determination of phase from image and diffraction plane pictures". *Optik*, 35(2):237–246, 1972.

[44] Goodman, Joseph W. *Statistical Optics*. John Wiley & Sons, Inc., New York, NY, 2000.

[45] Goodman, Joseph W. *Introduction to Fourier Optics*. Roberts & Company, Englewood, CO, 3rd edition, 2005.

[46] Goodwin, Eric P., John J. Sullivan, Daniel G. Smith, and John E. Greivenkamp. "Dual interferometer system for measuring index of refraction". *Frontiers in Optics*, OFTuC2. Optical Society of America, 2006. URL `http://www.opticsinfobase.org/abstract.cfm?URI=OFT-2006-OFTuC2`.

[47] Goudail, François. "Noise minimization and equalization for Stokes polarimeters in the presence of signal-dependent Poisson shot noise". *Opt. Lett.*, 34(5):647–649, 2009. URL `http://ol.osa.org/abstract.cfm?URI=ol-34-5-647`.

[48] Goudail, François. "Optimization of the contrast in active Stokes images". *Opt. Lett.*, 34(2):121–123, 2009. URL `http://ol.osa.org/abstract.cfm?URI=ol-34-2-121`.

[49] Goudail, François and Arnaud Bénière. "Optimization of the contrast in polarimetric scalar images". *Opt. Lett.*, 34(9):1471–1473, 2009. URL `http://ol.osa.org/abstract.cfm?URI=ol-34-9-1471`.

[50] Goudail, François and Arnaud Bénière. "Estimation precision of the degree of linear polarization and of the angle of polarization in the presence of different sources of noise". *Appl. Opt.*, 49(4):683–693, 2010. URL `http://ao.osa.org/abstract.cfm?URI=ao-49-4-683`.

[51] Goudail, François, Patrick Terrier, Yoshitate Takakura, Laurent Bigué, Frédéric Galland, and Vincent DeVlaminck. "Target detection with a liquid-crystal-based passive Stokes polarimeter". *Appl. Opt.*, 43(2):274–282, January 2004.

[52] Greiner, Michael A., Bradley D. Duncan, and Matthew P. Dierking. "Bidirectional scattering distribution functions of maple and cottonwood leaves". *Appl. Opt.*, 46(25):6485–6494, 2007.

[53] Hapke, Bruce W. "A theoretical photometric function for the lunar surface". *J. Geophys. Res.*, 68(15):4571–4586, 1963.

[54] Harper, E. Y. and F. M. Labianca. "Scattering of sound from a point source by a rough surface progessing over an isovelocity ocean". *J. Acoust. Soc. Am.*, 58(2):349–364, 1975.

[55] He, Xiao D., Kenneth E. Torrance, François. X. Sillion, and Donald. P. Greenberg. "A comprehensive physical model for light reflection". *SIGGRAPH 1991*

Proceedings, volume 25, 175–186. Special Interest Group on Graphics and Interactive Techniques, Computer Graphics, July 1991.

[56] Hecht, Eugene. *Optics*. Pearson Education, Inc., San Francisco, CA, 4th edition, 2002.

[57] Hegedüs, Ramón, András Barta, Balázs Bernáth, Victor Benno Meyer-Rochow, and Gábor Horváth. "Imaging polarimetry of forest canopies: how the azimuth direction of the sun, occluded by vegetation, can be assessed from the polarization pattern of the sunlit foliage". *Appl. Opt.*, 46(23):6019–6032, 2007.

[58] Hoffman, Jeffrey M. and William L. Wolfe. "Cyrogenic refractive indices of ZnSe, Ge, and Si at 10.6 μm". *Appl. Opt.*, 30(28):4014–4016, October 1991.

[59] Holmes, Timothy J. "Blind deconvolution of quantum-limited incoherent imagery: maximum-likelihood approach". *J. Opt. Soc. Am. A*, 9(7):1052–1061, 1992. URL `http://josaa.osa.org/abstract.cfm?URI=josaa-9-7-1052`.

[60] Hong, Sungwook. "Retrieval of refractive index over specular surfaces for remote sensing applications". *J. Appl. Remote Sens.*, 3:033560, 2009. URL `http://link.aip.org/link/?JRS/3/033560/1`.

[61] Hyde, M. W., S. C. Cain, J. D. Schmidt, and M. J. Havrilla. "Material classification of an unknown object using turbulence-degraded polarimetric imagery". *IEEE Trans. Geosci. Remote Sens.*, 49(1), 2011.

[62] Hyde, M. W., J. D. Schmidt, and M. J. Havrilla. "A geometrical optics polarimetric bidirectional reflectance distribution function for dielectric and metallic surfaces". *Opt. Express*, 17(24):22138–22153, 2009. URL `http://www.opticsexpress.org/abstract.cfm?URI=oe-17-24-22138`.

[63] Ishimaru, Akira. *Wave Propagation and Scattering in Random Media*. IEEE Press, New York, NY, 1997.

[64] James, Steven P. *Blind Deconvolution Through Polarization Diversity of Long Exposure Imagery*. Master's thesis, Graduate School of Engineering and Management, Air Force Institute of Technology (AETC), Wright-Patterson AFB OH, March 2009. AFIT/EO/ENG/09-06.

[65] Jordan, D. L., G. D. Lewis, and E. Jakeman. "Emission polarization of roughened glass and aluminum surfaces". *Appl. Opt.*, 35(19):3583–3590, 1996. URL http://ao.osa.org/abstract.cfm?URI=ao-35-19-3583.

[66] Kalshoven, Jr., J.E. and P.W. Dabney. "Remote sensing of the Earth's surface with an airborne polarized laser". *IEEE Trans. Geosci. Remote Sens.*, 31(2):438–446, March 1993. ISSN 0196-2892.

[67] Kim, M.-J., J. C. Dainty, A. T. Friberg, and A. J. Sant. "Experimental study of enhanced backscattering from one- and two-dimensional random rough surfaces". *J. Opt. Soc. Am. A*, 7(4):569–577, 1990. URL http://josaa.osa.org/abstract.cfm?URI=josaa-7-4-569.

[68] Kimes, D. S. "Modeling the directional reflectance from complete homogeneous vegetation canopies with various leaf-orientation distributions". *J. Opt. Soc. Am. A*, 1(7):725–737, 1984.

[69] Krishen, K. "Correlation of radar backscattering cross sections with ocean wave height and wind velocity". *J. Geophys. Res.*, 76:6528–6539, 1971.

[70] Kundur, Deepa and Dimitrios Hatzinakos. "Blind image deconvolution". *IEEE Signal Process. Mag.*, 13:43–64, May 1996.

[71] Kwok, Yue Kuen. *Applied Complex Variables for Scientists and Engineers.* Cambridge University Press, New York, NY, 2002.

[72] LabSphere, Inc. "A guide to reflectance coatings and materials". URL `http://www.labsphere.com/tecdocs.aspx`.

[73] Leberknight, C. E. and Benjamin Lustman. "An optical investigation of oxide films on metals". *J. Opt. Soc. Am.*, 29:59–66, February 1939.

[74] LeMaster, Daniel A. and Stephen C. Cain. "Multichannel blind deconvolution of polarimetric imagery". *J. Opt. Soc. Am. A*, 25(9):2170–2176, August 2008.

[75] Lukin, Vladimir P. and Boris V. Fortes. *Adaptive Beaming and Imaging in the Turbulent Atmosphere.* SPIE Press, Bellingham, WA, 2002.

[76] Luxpop, Inc. URL `http://www.luxpop.com/`.

[77] Macaskill, C. "Geometric optics and enhanced backscatter from very rough surfaces". *J. Opt. Soc. Am. A*, 8(1):88–96, 1991. URL `http://josaa.osa.org/abstract.cfm?URI=josaa-8-1-88`.

[78] MacDonald, Adam, Stephen C. Cain, and Ernest E. Armstrong. "Maximum a posteriori image and seeing condition estimation from partially coherent two-dimensional light detection and ranging images". *Opt. Eng.*, 45(8):086201, 2006. URL `http://link.aip.org/link/?JOE/45/086201/1`.

[79] Madsen, K., H. B. Nielsen, and O. Tingleff. *Methods for Non-Linear Least Squares Problems.* Technical University of Denmark, 2004. URL `http://www2.imm.dtu.dk/pubdb/views/edoc_download.php/3215/pdf/imm3215.pdf`.

[80] Mantravadi, Samuel V., Troy A. Rhoadarmer, and Robert S. Glas. "Simple laboratory system for generating well-controlled atmospheric-like turbulence".

volume 5553, 290–300. SPIE, 2004. URL `http://link.aip.org/link/?PSI/5553/290/1`.

[81] Margarit, G., J. J. Mallorqui, and L. Pipia. "Polarimetric characterization and temporal stability analysis of urban target scattering". *IEEE Trans. Geosci. Remote Sens.*, 48(4):2038–2048, April 2010. ISSN 0196-2892.

[82] Margarit, G., J.J. Mallorqui, and X. Fabregas. "Single-pass polarimetric SAR interferometry for vessel classification". *IEEE Trans. Geosci. Remote Sens.*, 45(11):3494–3502, November 2007. ISSN 0196-2892.

[83] Margarit, G., J.J. Mallorqui, J. Fortuny-Guasch, and C. Lopez-Martinez. "Exploitation of ship scattering in polarimetric SAR for an improved classification under high clutter conditions". *IEEE Trans. Geosci. Remote Sens.*, 47(4):1224–1235, April 2009. ISSN 0196-2892.

[84] Martino, Antonello De, Yong-Ki Kim, Enric Garcia-Caurel, Blandine Laude, and Bernard Drévillon. "Optimized Mueller polarimeter with liquid crystals". *Opt. Lett.*, 28(8):616–618, April 2003.

[85] Matchko, Roy M. and Grant R. Gerhart. "Polarization azimuth angle in daylight scenes". *Opt. Eng.*, 44(2):1–9, February 2005.

[86] Matchko, Roy M. and Grant R. Gerhart. "Polarization measurements using a commercial off-the-shelf digital camera". *Opt. Eng.*, 44(2):1–10, February 2005.

[87] Maxwell, J. R., J. Beard, S. Weiner, D. Ladd, and S. Ladd. *Bidirectional Reflectance Model Validation and Utilization*. Technical Report AFAL-TR-73-303, Air Force Avionics Laboratory, Wright-Patterson Air Force Base, OH, October 1973.

[88] McAlister, E. D., J. J. Villa, and C. D. Salzberg. "Rapid and accurate measurements of refractive index in the infrared". *J. Opt. Soc. Am.*, 46(7):485–487, July 1956.

[89] McCartney, James T. and Sabri Ergun. "Refractive index and thickness of ultrathin sections of coals and graphite by interferometry". *J. Opt. Soc. Am.*, 52(2):197–200, February 1962.

[90] McNairn, H., Jiali Shang, Xianfeng Jiao, and C. Champagne. "The contribution of ALOS PALSAR multipolarization and polarimetric data to crop classification". *IEEE Trans. Geosci. Remote Sens.*, 47(12):3981–3992, December 2009. ISSN 0196-2892.

[91] McNamara, D. A., C. W. I. Pistorius, and J. A. G. Malherbe. *Introduction to the Uniform Geometrical Theory of Diffraction.* Artech House, Inc., Norwood, MA, 1990.

[92] Meyers, Jason P. *Modeling Polarimetric Imaging Using DIRSIG.* Ph.D. dissertation, Chester F. Carslon Center for Imaging Science, Rochester Institute of Technology, Rochester, NY, 2002.

[93] Mian, S. M., A. Y. Hamad, and J. P. Wicksted. "Refractive index measurements using a CCD". *Appl. Opt.*, 35(34):6825–6826, December 1996.

[94] Moon, Todd K. "The expectation-maximization algorithm". *IEEE Signal Process. Mag.*, 13:47–60, November 1996.

[95] Moore, Duncan T. and Danette P. Ryan. "Measurement of the optical properties of gradient index materials". *J. Opt. Soc. Am.*, 68(9):1157–1166, September 1978.

[96] Nicodemus, Fred E. "Radiance". *Am. J. Phys.*, 31:368–377, October 1963.

[97] Nicodemus, Fred E. "Directional reflectance and emissivity of an opaque surface". *Appl. Opt.*, 4(7):368–377, July 1965.

[98] O'Neill, K. "Discrimination of UXO in soil using broadband polarimetric GPR backscatter". *IEEE Trans. Geosci. Remote Sens.*, 39(2):356–367, February 2001. ISSN 0196-2892.

[99] Palik, Edward D. *Handbook of Optical Constants of Solids*. Academic Press, Chestnut Hill, MA, 1998.

[100] Palik, Edward D. *Handbook of Optical Constants of Solids II*. Academic Press, Chestnut Hill, MA, 1998.

[101] Peterson, Andrew F., Scott L. Ray, and Raj Mittra. *Computational Methods for Electromagnetics*. IEEE Press, New York, NY, 1998.

[102] Praks, J., E.C. Koeniguer, and M.T. Hallikainen. "Alternatives to target entropy and alpha angle in SAR polarimetry". *IEEE Trans. Geosci. Remote Sens.*, 47(7):2262–2274, July 2009. ISSN 0196-2892.

[103] Priest, Richard G. and Thomas A. Germer. "Polarimetric BRDF in the microfacet model: theory and measurements". *Proceedings of the 2000 Meeting of the Military Sensing Symposia Specialty Group on Passive Sensors*, 169–181. Infrared Information Analysis Center, August 2000.

[104] Priest, Richard G. and Steven R. Meier. "Polarimetric microfacet scattering theory with applications to absorptive and reflective surfaces". *Opt. Eng.*, 41(5):988–993, May 2002.

[105] Pust, Nathan J., Joseph A. Shaw, and Andrew R. Dahlberg. "Concurrent polarimetric measurements of painted metal and illuminating skylight compared with a microfacet model". volume 7461, 74610X. SPIE, 2009. URL `http://link.aip.org/link/?PSI/7461/74610X/1`.

[106] Reeves, Stanley J. "Fast image restoration without boundary artifacts". *IEEE Trans. Image Process.*, 14(10):1448–1453, October 2005.

[107] Rhoadarmer, Troy A. and J. Roger P. Angel. "Low-cost, broadband static phase plate for generating atmosphericlike turbulence". *Appl. Opt.*, 40(18):2946–2955, 2001. URL `http://ao.osa.org/abstract.cfm?URI=ao-40-18-2946`.

[108] Rhodes, Richard. *Dark Sun: The Making of the Hydrogen Bomb*. Simon & Schuster, New York, NY, 1995.

[109] Rust-Oleum Corporation. "249058 PTOUCH 2X SSPR 6PK White Primer Material Safety Data Sheet", 2009. URL `http://www.rustoleum.com/CBGResourceCenter.asp?sn=ms2&msdsTyp=SKU&msdssku=249058`.

[110] Sandford, B. P. and D. C. Robertson. "Infrared reflectance properties of aircraft paints". *Proceedings of IRIS Targets, Backgrounds and Discrimination*. 1985.

[111] Sasiela, Richard J. *Electromagnetic Wave Propagation in Turbulence: Evaluation and Application of Mellin Transforms*. SPIE Press, Bellingham, WA, 2nd edition, 2007.

[112] Schott, John R. *Fundamentals of Polarimetric Remote Sensing*. SPIE Press, Bellingham, WA, 2009.

[113] Schuler, D.L., Jong-Sen Lee, D. Kasilingam, and G. Nesti. "Surface roughness and slope measurements using polarimetric SAR data". *IEEE Trans. Geosci. Remote Sens.*, 40(3):687–698, March 2002. ISSN 0196-2892.

[114] Schulz, Timothy J. "Multiframe blind deconvolution of astronomical images". *J. Opt. Soc. Am. A*, 10(5):1064–1073, May 1993.

[115] Shaw, Joseph A. "Degree of linear polarization in spectral radiances from water-viewing infrared radiometers". *Appl. Opt.*, 38(15):3157–3165, 1999. URL `http://ao.osa.org/abstract.cfm?URI=ao-38-15-3157`.

[116] Shell, James R. *Polarimetric Remote Sensing in the Visible to Near Infrared.* Ph.D. dissertation, Chester F. Carslon Center for Imaging Science, Rochester Institute of Technology, Rochester, NY, 2005.

[117] Smith, Warren J. *Modern Optical Engineering.* McGraw-Hill, New York, NY, 3rd edition, 2000.

[118] Sullo, Nancy J. and Duncan T. Moore. "Measurement of absolute gradient-index profiles using modulation ellipsometry". *Appl. Opt.*, 23(11):1765–1773, June 1984.

[119] Sun, Yinlong. "Statistical ray method for deriving reflection models of rough surfaces". *J. Opt. Soc. Am. A*, 24(3):724–744, March 2007.

[120] Terrier, Patrick, Vincent Devlaminck, and Jean Michel Charbois. "Segmentation of rough surfaces using a polarization imaging system". *J. Opt. Soc. Am. A*, 25(2):423–430, February 2008.

[121] The Sherwin-Williams Company. "52001 KRYLON® Indoor/Outdoor Paint, Hunter Green Material Safety Data Sheet", 2009. URL `http://www.paintdocs.com/webmsds/webPDF.jsp?SITEID=DBS&UPC=724504020011`.

[122] Thilak, Vimal, David G. Voelz, and Charles D. Creusere. "Image segmentation from multi-look passive polarimetric imagery". volume 6682, 668206. SPIE, 2007. URL `http://link.aip.org/link/?PSI/6682/668206/1`.

[123] Thilak, Vimal, David G. Voelz, and Charles D. Creusere. "Polarization-based index of refraction and reflection angle estimation for remote sensing applications". *Appl. Opt.*, 46(30):7527–7536, October 2007.

[124] Thilak, Vimal, Qingsong Wang, David G. Voelz, and Charles D. Creusere. "Estimation of target geometry from Mueller matrix imagery". volume 6972, 69720S. SPIE, 2008. URL `http://link.aip.org/link/?PSI/6972/69720S/1`.

[125] Thorsos, Eric I. "The validity of the Kirchhoff approximation for rough surface scattering using a Gaussian roughness spectrum". *J. Acoust. Soc. Am.*, 83(1):78–92, January 1988.

[126] Tominaga, Shoji and Akira Kimachi. "Polarization imaging for material classification". *Opt. Eng.*, 47(12):123201, 2008. URL `http://link.aip.org/link/?JOE/47/123201/1`.

[127] Tompkins, Harland G. and Eugene A. Irene. *Handbook of Ellipsometry*. William Andrew, Inc., Norwich, NY, 2005.

[128] Torrance, K. E. and E. M. Sparrow. "Theory for off-specular reflection from roughened surfaces". *J. Opt. Soc. Am.*, 57(9):1105–1114, September 1967.

[129] Touzi, R. "Target scattering decomposition in terms of roll-invariant target parameters". *IEEE Trans. Geosci. Remote Sens.*, 45(1):73–84, January 2007. ISSN 0196-2892.

[130] Toyoshima, Morio, Hideki Takenaka, Yozo Shoji, Yoshihisa Takayama, Yoshisada Koyama, and Hiroo Kunimori. "Polarization measurements through space-to-ground atmospheric propagation paths by using a highly polarized laser source in space". *Opt. Express*, 17(25):22333–22340, 2009. URL `http://www.opticsexpress.org/abstract.cfm?URI=oe-17-25-22333`.

[131] Tyo, J. Scott. "Enhancement of the point-spread function for imaging in scattering media by use of polarization-difference imaging". *J. Opt. Soc. Am. A*, 17(1):1–10, 2000. URL `http://josaa.osa.org/abstract.cfm?URI=josaa-17-1-1`.

[132] Tyo, J. Scott. "Design of optimal polarimeters: maximization of signal-to-noise ratio and minimization of systematic error". *Appl. Opt.*, 41(4):619–630, February 2002.

[133] Tyo, J. Scott, Dennis L. Goldstein, David B. Chenault, and Joseph A. Shaw. "Review of passive imaging polarimetry for remote sensing applications". *Appl. Opt.*, 45(22):5453–5469, August 2006.

[134] Tyo, J. Scott, Sergio J. Johnson, Zhipeng Wang, and Brian G. Hoover. "Designing partial Mueller matrix polarimeters". volume 7461, 74610V. SPIE, 2009. URL `http://link.aip.org/link/?PSI/7461/74610V/1`.

[135] Tyson, Robert K. *Principles of Adaptive Optics*. Academic Press, Chestnut Hill, MA, 2nd edition, 1998.

[136] Ufimtsev, Pyotr Ya. *Fundamentals of the Physical Theory of Diffraction*. John Wiley & Sons, Inc., Hoboken, NJ, 2007.

[137] Van Trees, Harry L. *Detection, Estimation, and Modulation Theory: Part I*. John Wiley & Sons, Inc., New York, NY, 2001.

[138] Watkins, David S. *Fundamentals of Matrix Computations*. John Wiley & Sons, Inc., New York, NY, 2nd edition, 2002.

[139] Wellems, D., M. Serna, S. H. Sposato, M. P. Fetrow, K. P. Bishop, S. A. Arko, and T. R. Caudill. "Spectral polarimetric BRDF model and comparison to

measurements from isotropic roughened glass". *Workshop on Multi/Hyperspectral Sensors, Measurements, Modeling and Simulation*. U.S. Army Aviation and Missile Command, Huntsville, AL, November 2000.

[140] Wellems, David, Steve Ortega, David Bowers, Jim Boger, and Matthew Fetrow. "Long wave infrared polarimetric model: theory, measurements and parameters". *J. Opt. A: Pure Appl. Opt.*, 8(10):914–925, 2006. URL `http://stacks.iop.org/1464-4258/8/914`.

[141] Wolff, Lawrence B. "Polarization-based material classification from specular reflection". *IEEE Trans. Pattern Anal. Mach. Intell.*, 12(11):1059–1071, November 1990.

[142] Wolff, Lawrence B. "Polarization camera for computer vision with a beam splitter". *J. Opt. Soc. Am. A*, 11(11):2935–2945, November 1994.

[143] Wolff, Lawrence B., Todd A. Mancini, Philippe Pouliquen, and Andreas G. Andreou. "Liquid crystal polarization camera". *IEEE Trans. Rob. Autom.*, 13(2):195–203, April 1997.

[144] Wolff, L.B. and T.E. Boult. "Constraining object features using a polarization reflectance model". *IEEE Trans. Pattern Anal. Mach. Intell.*, 13(7):635–657, July 1991. ISSN 0162-8828.

[145] Xia, Jinjun and Gang Yao. "Angular distribution of diffuse reflectance in biological tissue". *Appl. Opt.*, 46(26):6552–6560, 2007.

[146] Yariv, Amnon and Pochi Yeh. *Optical Waves in Crystals: Propagation and Control of Laser Radiation*. John Wiley & Sons, Inc., Hoboken, NJ, 2003.

[147] Zhao, Yongqiang, Quan Pan, and Hongcai Zhang. "Material classification based on multi-band polarimetric images fusion". volume 6240, 624007. SPIE, 2006. URL `http://link.aip.org/link/?PSI/6240/624007/1`.

[148] Zonios, George, Ioannis Bassukas, and Aikaterini Dimou. "Comparative evaluation of two simple diffuse reflectance models for biological tissue applications". *Appl. Opt.*, 47(27):4965–4973, 2008.

Vita

Milo W. Hyde IV received the B.S. degree in computer engineering from the Georgia Institute of Technology, Atlanta, in 2001 and the M.S. degree in electrical engineering from the Air Force Institute of Technology, Wright-Patterson Air Force Base, Dayton, OH, in 2006. He is currently working toward the Ph.D. degree in electrical engineering with the Air Force Institute of Technology. From 2001 to 2004, he was a Maintenance Officer with the F-117A Nighthawk, Holloman Air Force Base, Alamogordo, NM. From 2006 to 2007, he was a government researcher with the Air Force Research Laboratory, Wright-Patterson Air Force Base. His current research interests include electromagnetic material characterization, guided-wave theory, scattering, and optics. He is a member of IEEE, SPIE, and OSA.

REPORT DOCUMENTATION PAGE

Form Approved
OMB No. 0704–0188

1. REPORT DATE *(DD–MM–YYYY)*	2. REPORT TYPE	3. DATES COVERED *(From — To)*
16–09–2010	Doctoral Dissertation	Sep 2007 — Sep 2010

4. TITLE AND SUBTITLE

DETERMINING THE INDEX OF REFRACTION
OF AN UNKNOWN OBJECT
USING PASSIVE POLARIMETRIC IMAGERY
DEGRADED BY ATMOSPHERIC TURBULENCE

5a. CONTRACT NUMBER

5b. GRANT NUMBER

F1ATA0035J001

5c. PROGRAM ELEMENT NUMBER

6. AUTHOR(S)

Milo W. Hyde IV, Capt, USAF

5d. PROJECT NUMBER

ENGJON219

5e. TASK NUMBER

5f. WORK UNIT NUMBER

7. PERFORMING ORGANIZATION NAME(S) AND ADDRESS(ES)

Air Force Institute of Technology
Graduate School of Engineering and Management (AFIT/EN)
2950 Hobson Way
WPAFB OH 45433-7765

8. PERFORMING ORGANIZATION REPORT NUMBER

AFIT/DEE/ENG/10-12

9. SPONSORING / MONITORING AGENCY NAME(S) AND ADDRESS(ES)

Air Force Office of Scientific Research
Kent Miller
3875 Randolph St., Suite 348
Arlington, VA 22203
(703) 696-8573, kent.miller@afosr.af.mil

10. SPONSOR/MONITOR'S ACRONYM(S)

AFOSR/NE

11. SPONSOR/MONITOR'S REPORT NUMBER(S)

12. DISTRIBUTION / AVAILABILITY STATEMENT

APPROVED FOR PUBLIC RELEASE; DISTRIBUTION UNLIMITED

13. SUPPLEMENTARY NOTES

14. ABSTRACT

In this research, an algorithm is developed to estimate the index of refraction of an unknown object using passive polarimetric images degraded by atmospheric turbulence. The algorithm uses a variant of the maximum-likelihood blind-deconvolution algorithm developed by LeMaster and Cain to recover the true object (i.e., the first Stokes parameter), the degree of linear polarization, and the polarimetric-image point spread functions. Nonlinear least squares is then used to find the value of the complex index of refraction which best fits the theoretical degree of linear polarization, derived using a polarimetric bidirectional reflectance distribution function, to the turbulence-corrected degree of linear polarization. To verify the proposed material-characterization algorithm, experimental results of two painted metal samples are provided and analyzed. Possible uses of this novel algorithm include intelligence-gathering and nondestructive inspection/evaluation applications such as corrosion and crack detection/characterization.

15. SUBJECT TERMS

Atmospheric turbulence; blind deconvolution; material characterization; material classification; polarimetry; refractive index; remote sensing; scattering

16. SECURITY CLASSIFICATION OF:			17. LIMITATION OF ABSTRACT	18. NUMBER OF PAGES	19a. NAME OF RESPONSIBLE PERSON
a. REPORT	**b. ABSTRACT**	**c. THIS PAGE**			Maj Jason D. Schmidt
U	U	U	U	232	**19b. TELEPHONE NUMBER** *(include area code)* (937) 255-3636, x7224; jason.schmidt@afit.edu

Standard Form 298 (Rev. 8–98)
Prescribed by ANSI Std. Z39.18